Development and Characterization of Low Pt-Loaded Membrane Electrode Assemblies with Focus on Performance and Durability

Von der Fakultät Energie-, Verfahrens- und Biotechnik der Universität Stuttgart zur Erlangung der Würde eines Doktor-Ingenieurs (Dr.-Ing.) genehmigte Abhandlung

Vorgelegt von
Krishan Talukdar
Aus Chattogram, Bangladesh

Hauptberichter: Prof. Dr. rer. nat. K. Andreas Friedrich
Mitberichter: Prof. Dr. Andrea Casalegno
Tag der mündlichen Prüfung: 09.12.2020

Universität Stuttgart
Institut für Gebäudeenergetik, Thermotechnik und Energiespeicherung

2020

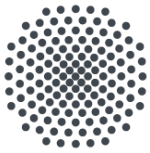

University of Stuttgart
Germany

IGTE

Institut für Gebäudeenergtik,
Thermotechnik und Energiespeicherung

DLR

Deutsches Zentrum
für Luft- und Raumfahrt
German Aerospace Center

I would rather have questions that can't be answered
than answers that can't be questioned.

Richard P. Feynman

Acknowledgement

First and foremost, I would like to thank my *Doktorvator* Prof. K. Andreas Friedrich. I want to express my heartfelt gratitude to him for giving me the opportunity to pursue my PhD research with DLR-DAAD research fellowship at the German Aerospace Center (DLR). I really appreciate his kind support during last four years with scientific discussions, suggestions, and guidance to enlighten my way to the field of electrochemistry. I would also like to convey my sincere appreciation to Prof. Andrea Casalegno for being the external advisor of my thesis. I would like to thank DLR-DAAD to fund my PhD for four years.

I want to thank my *Betreuer* Dr. Mathias Schulze and Dr. Pawel Gazdzicki for their relentless effort to guide me through the years. I also want to thank Dr. Stefan Helmly to mentoring me in the initial years of my PhD.

I also wish to express my gratitude to my DLR colleagues, especially Dr. Mitzel Jens, Dr. Daniel Garcia, Dr. Thomas Jahnke, Dr. Norbert Wagner, Dr. Wang Li, Dr. Srikanth Santhanam for their support in scientific aspect. I am very grateful to Siegfried Graf, Werner Seybold, Ina Plock, Dr. Noriko Sata for their technical support. I am grateful to Prof. Renate Hiesgen, Tobias Morawietz, and Michael Handl from University of Applied Sciences Esslingen for SEM and AFM measurements.

I am indebted to my master thesis students: Sofia Delgado and Md Asaduzzaman Ripan. I cordially thank them for their great contribution in the experiment and simulation.

Now, I will express my heartfelt gratitude to the most important woman of my life, my mother Shima Talukdar, from whom I learned to dream. Her unparalleled effort and struggle made me who I am today. Obviously, I thank my father Pradip Kumar Talukdar who teaches me how to be humble, and always motivates me to achieve knowledge. I am also grateful to my sister Kristy Talukdar to whom I am always a hero.

Last but not the least, my heartfelt thanks goes to my beloved wife Mukti Dhar, who always encourages me to move forward. Her support and unwavering love always motivate me to keep away from stress. Eventually, I would like to express gratitude to my family and all friends for supporting me all along.

Declaration

I hereby want to confirm that this submitted dissertation has been written by me, and no other sources or materials have been used in this process except the indicated. I have acknowledged and properly referenced the published work of others. This work contains partial experimental contribution from supervised MSc thesis students, but the idea of all the work and experiments were designed by myself.

Erklärung

Ich möchte hiermit bestätigen, dass diese eingereichte Dissertation von mir geschrieben wurde und keine anderen Quellen oder Materialien in diesem Prozess verwendet wurden, außer den angegebenen. Ich habe die veröffentlichten Arbeiten anderer anerkannt und ordnungsgemäß referenziert. Diese Arbeit enthält teilweise experimentelle Beiträge von betrueten Studenten; aber die Idee der gesamten Arbeit sowie die Experimente sind von mir selbst entworfen.

Krishan Talukdar

Stuttgart, den 09.12.2020

Abstract

For many applications of polymer electrolyte membrane fuel cell (PEMFC), the loading attributed to platinum as catalyst is still too high for this technology to penetrate into the mass market. However, this high loading of platinum is still necessary to achieve the performance and service life targets. Therefore, reducing the loading of precious group metals is a major challenge to low temperature PEM fuel cell community. The performance of the membrane electrode assembly (MEA) with low Pt loading depends on the optimization of numerous parameters like catalyst activity, proton conductivity of ionomer, ionomer to catalyst ratio, diffusion media, operating conditions, and last but not the least the microstructure of the electrode, which is determined by the coating method. An efficient electrode with low platinum loading and durable performance requires a thin but porous catalyst layer, in which the catalyst particles and ionomer are homogenously distributed with a large surface area.

The fundamental goal of this dissertation is to understand the relationships between structural properties and performance, and to derive strategies for a goal oriented development. In the first part of the study, PEMFC electrodes were fabricated with the same Pt loading by means of diverse coating techniques. Current-voltage curves, electrochemical analysis, and physical characterizations are evaluated to interpret the influence of microstructure caused by the coating methods on performance and durability. In order to obtain different catalytic layer structures, the electrodes were produced using six different coating techniques with the same Pt loading. The selected coating techniques are wet spraying, screen printing, inkjet printing, dry spraying, doctor-blade and drop casting. Similar drying conditions were maintained after all the wet coating processes. The physical and electrochemical characterizations of the individual catalyst layers (CL) were investigated under identical operating conditions. The results show that wet spraying and screen printing showed the highest performance due to the low proton resistance. The lowest efficiencies were observed in doctor-blade and drop-cast techniques, which are associated with particularly low protonic conductivity. Microstructure investigation by focus-ion-beam scanning electron

microscope analysis were used to determine transport properties such as porosity, permeability, diffusivity and inverse tortuosity by image analysis in GeoDict. A comparison of peak power density and effective transport parameters shows that an increase in permeability, diffusivity and porosity correlates strongly with increasing power. A dimensionless classification of the transport properties of the MEA with a point system and their summation can describe the observed performance very well. Consequently, the measured and analyzed transport parameters seem to be sufficient for predicting the performance of a membrane electrode assembly (MEA). This can help to optimize coating techniques and thus increase MEA performance together with service life. Furthermore, the dry coating technology developed at DLR was improved in order to produce MEAs nearly 50 % more efficient than before.

Additionally, the effect of ionomer with diverse side chain length as well as the significance of membrane thickness is also studied for long and short term application upon load cycling test. This research further provides a deep insight into the importance of ionomer and its microstructure both in the electrode and the membrane in PEM fuel cell, which influences the performance and also the long term stability. After 600 hours of load cycle operation with the cells, roughly 120 mV of drastic degradation was observed owing to the higher gas crossover through thinner membrane, while the performance can be increased approximately 16 % due to the shorter side chain of ionomer.

Another important result of this work is the investigation of the influence of the drying process of MEA production on the electrode microstructure, i.e. the open porosity, the ionomer distribution and the size of the reactive interface. An unconventional drying method known as freeze drying, shows three-fold improvement in the porosity and promising ionomer distribution in CL. Consequently, this can reduce the transport limitations and improve the peak power density about 34 % compared to the conventional drying technique. Furthermore, a transient 2D physical continuum model was applied and simulations were performed to numerically investigate the influence of different drying methods on PEM fuel cell performance. Both experimental and simulation data emphasize the fact that the sublimation of the catalyst layer improves the architecture by optimizing porosity, permeability and tortuosity. These above-mentioned properties of the microstructure of the catalytic layer significantly

improve water management and diffusion properties, which has an impact on performance and reduced mass transport limitation.

This work is able to identify important process engineering relationships between the microstructure of CL and its performance. In addition, promising manufacturing processes, drying methods and operating conditions were found, which should allow a targeted improvement of CL performance in the next step.

Zusammenfassung

Für viele Anwendungen sind die Beladungen mit Pt als Katalysator in Polymerelektrolytmembran-Brennstoffzellen (PEMFC) nach wie vor zu hoch, um die Durchdringung dieser Technologie in den Massenmärkten zu erreichen. Diese Beladungen sind allerdings zurzeit noch notwendig, um die Leistungs- und Lebensdauerziele zu erreichen. Daher ist die Reduzierung der Beladung mit Edelmetallen eine große Herausforderung für die Entwickler von Niedertemperatur-PEM-Brennstoffzellen. Die Leistungsfähigkeit der Membran-Elektroden-Einheit (MEA) mit niedrigen Beladungen basiert auf der Optimierung von zahlreichen Parametern, wie Katalysatoraktivität, Protonenleitfähigkeit des Ionomers, Ionomer-Katalysator-Verhältnis, Diffusionsmedien, Betriebsbedingungen und nicht zuletzt die Mikrostruktur der Elektrode, die durch die Beschichtungsmethode bestimmt wird. Eine effiziente Elektrode mit geringer Platinbeladung und dauerhafter Leistung erfordert eine dünne, aber poröse Katalysatorschicht, bei der die Katalysatorpartikel und das Ionomer homogen mit einer großen Oberfläche verteilt sind.

Grundsätzliches Ziel dieser Dissertation ist es, die Beziehung zwischen Struktur und Leistungsfähigkeit im Elektrodendesign zu verstehen und entsprechend für eine rationale Entwicklung zu nutzen. Im ersten Teil der Studie wurden PEMFC-Elektroden mit gleicher Pt Beladung durch verschiedene Beschichtungstechniken hergestellt. Strom-Spannungskurven sowie elektrochemische und physikalische Charakterisierungen wurden im gleichen Betriebszustand ausgewertet, um den Einfluss der Mikrostruktur bzw. der Beschichtungsverfahren auf die endgültige Leistung und Lebensdauer zu verstehen. Um unterschiedliche katalytische Schichtstrukturen zu erhalten, wurden die Elektroden mit sechs verschiedenen Beschichtungstechniken mit der gleichen Pt-Beladung hergestellt. Die ausgewählten Beschichtungstechniken sind Nasssprühen, Siebdruck, Tintenstrahldruck, Trockensprühen, Rakelauftrag und Fallguss. Ähnliche Trocknungsbedingungen wurden nach den allen Nassbeschichtungsprozessen beibehalten. Die physikalischen und elektrochemischen Charakterisierungen der einzelnen Katalysatorschichten (CL) wurden unter identischen

Betriebsbedingungen untersucht. Die Ergebnisse zeigen, dass Nasssprühen und Tintenstrahldruck aufgrund des geringen Protonenwiderstandes die höchste Leistungsfähigkeit zeigten. Die niedrigsten Leistungsfähigkeiten wurden bei den Rakel- und Fallgusstechniken beobachtet, die mit einer besonders niedrigen protonischen Leitfähigkeit einhergeht. Die Untersuchung der Mikrostruktur mittels Rasterelektronenmikroskop mit Ionenstrahltiefenanalyse wurde verwendet, um Transporteigenschaften wie Porosität, Permeabilität, Diffusivität und inverse Tortuosität mittels Bildanalyse in GeoDict zu bestimmen. Ein Vergleich der Spitzenleistungsdichte und der effektiven Transportparameter zeigt, dass eine Zunahme der Permeabilität, Diffusivität und Porosität in hohem Maße stark mit zunehmender Leistung korreliert. Eine Klassifizierung der Transporteigenschaften der MEA mit dimensionslosen Kennzahlen und ihre Summation kann die beobachtete Leistungsfähigkeit sehr gut beschreiben. Folglich scheinen die gemessenen und analysierten Transportparameter ausreichend für die Vorhersage der Leistungsfähigkeit einer Membran-Elektrodeneinheit (MEA) zu sein. Dies kann dazu beitragen, die Beschichtungstechniken zu optimieren und damit die MEA-Leistung zusammen mit der Lebensdauer zu erhöhen. Darüber hinaus wurde die am DLR entwickelte Trockenbeschichtungstechnik verbessert, um MEAs 50 % leistungsfähiger als bisher herzustellen.

Darüber hinaus wurde die Wirkung von Ionomer mit unterschiedlicher Seitenkettenlänge auch für den lang- und kurzfristigen Einsatz bei Lastwechselversuchen untersucht. Diese Forschungsarbeit liefert auch einen tiefen Einblick in die Bedeutung des Ionomers und seiner Mikrostruktur sowohl in der Elektrode als auch in der Membran in der PEM-Brennstoffzelle, was die Leistungsfähigkeit beeinflusst aber auf die Langzeitstabilität. Nach 600 Stunden Lastzyklusbetrieb der Zellen wurden aufgrund des höheren Gasübergangs durch die dünnere Membran etwa 120 mV höherer Degradation beobachtet, während die Leistung aufgrund der kürzeren Seitenkette des Ionomers um etwa 16% gesteigert werden kann.

Ein weiteres wichtiges Ergebnis dieser Arbeit ist die Untersuchung des Einflusses des Trocknungsvorganges der MEA-Herstellung auf die Elektrodenmikrostruktur, d.h. die offene Porosität, die Ionomerverteilung und die Größe der reaktiven Grenzfläche. Ein unkonventionelles Trocknungsverfahren, die Gefriertrocknung, zeigt eine dreifach

höhere Porosität und eine homogene und feine Ionomerverteilung in der CL. Folglich können dadurch die Transportlimitierungen herabsetzt und die Spitzenleistungsdichte im Vergleich zur konventionellen Trocknungstechnik um 34 % verbessert werden. Außerdem wurde ein transientes 2D physikalisches Kontinuumsmodell angewendet und es wurden Simulationen durchgeführt, um den Einfluss verschiedener Trocknungsmethoden auf die PEM-Brennstoffzellenleistung numerisch zu untersuchen. Sowohl die Experimental- als auch die Simulationsdaten zeigen, dass die Sublimationstrocknung der Katalysatorschicht die Architektur durch Optimierung von Porosität, Permeabilität und Tortuosität verbessert. Diese oben genannten Eigenschaften der Mikrostruktur der katalytischen Lage verbessern signifikant die Wassermanagement- und Diffusionseigenschaften, was sich auf die Leistung und die reduzierte Stofftransportbegrenzung auswirkt.

Diese Arbeit konnte wichtige verfahrenstechnische Zusammenhänge zwischen der Mikrostruktur der CL und ihrer Leistungsfähigkeit identifizieren. Zusätzlich konnten erfolgsversprechende Herstellverfahren, Trocknungsverfahren und Betriebsbedingungen gefunden werden, die es im nächsten Schritt erlauben sollten, Leitungsfähigkeiten der CL zielgerichtet zu verbessern.

List of publications

This is a cumulative thesis, which is based on five scientific articles listed following,

Article I: Understanding the important parameters of Electrode Fabrication in Polymer Electrolyte Membrane Fuel Cell.
Krishan Talukdar, Patrick Sarkezi-Selsky, Khrystyna Yezerska, Oleg Sergeev, Pawel Gazdzicki, K. Andreas Friedrich.
Submitted

Article II: Enveloping of catalyst powder by ionomer for dry spray coating in polymer electrolyte membrane fuel cells.
Krishan Talukdar, Stefan Helmly, Mathias Schulze, Daniel G. Sanchez, Michael Handl, Renate Hiesgen, Jürgen Kraut, K. Andreas Friedrich.
Journal of Power Sources 424 (2019) 82-90

Article III: Comparative investigation into the performance and durability of long and short side chain ionomers in Polymer Electrolyte Membrane Fuel cells.
Krishan Talukdar, Pawel Gazdzicki, K. Andreas Friedrich.
Journal of Power Sources 439 (2019) 227078

Article IV: Minimizing mass transport loss in proton exchange membrane fuel cell by freeze drying of cathode catalyst layer.
Krishan Talukdar, Sofia Delgado, Tiago Lagarteira, Pawel Gazdzicki, K. Andreas Friedrich.
Journal of Power Sources 427 (2019) 309-31

Article V: Experimental and Numerical Study on Catalyst Layer of Polymer Electrolyte Membrane Fuel Cell Prepared with Diverse Drying Methods.
Krishan Talukdar, Md Asaduzzaman Ripan, Thomas Jahnke, Pawel Gazdzicki, Tobias Morawietz, K. Andreas Friedrich.
Journal of Power Sources 461 (2020) 228169

Table of Content

Abbreviation

Alkaline fuel cell	AFC
Atomic force microscopy	AFM
Accelerated stress test	AST
Brunauer-Emmett-Teller	BET
The British Petroleum company plc	BP
Catalyst coated membrane	CCM
Counter electrode	CE
Catalyst layer	CL
Constant phase element	CPE
Critical pigment volume concentration	CPVC
Cyclic voltammetry	CV
German Aerospace Center	DLR
Department of Energy, USA	DOE
Electrochemical active surface area	ECSA
Energy-dispersive X-ray spectroscopy	EDX
Electrochemical impedance spectroscopy	EIS
Equivalent weight	EW
Focus ion beam scanning electron microscopy	FIB-SEM
Fourier transform infrared spectroscopy	FTIR
Gas channels	GC
Gas diffusion electrode	GDE
Greenhouse gas	GHG
Hydrogen evolution reaction	HER
Internal combustion engine	ICE
Ion exchange capacity	IEC
Linear sweep voltammetry	LSV
Long side chain	LSC
Short side chain	SSC
Membrane electrode assembly	MEA

Molten carbonate fuel cell	MCFC
Natural gas	NG
Oxygen evolution reaction	OER
Phosphoric acid fuel cell	PAFC
Proton exchange membrane or polymer electrolyte membrane	PEM
Platinum group metals	PGM
Pigment volume concentration	PVC
Quantitative nano-mechanical tapping mode	QNM™
Rotating disk electrode	RDE
Reference electrode	RE
Reversible hydrogen electrode	RHE
Chemical reaction	rxn
Scanning electron microscopy	SEM
Standard hydrogen electrode	SHE
Standard temperature and pressure	STP
Turnover frequency	TOF
Ultra-high vacuum	UHV
Working electrode	WE
X-ray photoelectron spectroscopy	XPS

Symbol definition and unit

Description	Symbols	Unit
Active surface area	A	cm^2
Transfer coefficient	α	/
Anode transfer coefficient	α_a	/
Cathode transfer coefficient	α_c	/
Liquid transport coefficient	α_l	$mol^2\ J^{-1}\ m^{-1}\ s^{-1}$
Vapor transport coefficient	α_v	$mol^2\ J^{-1}\ m^{-1}\ s^{-1}$
activity of species	a^i	/
Tafel slope	β	$mV\ dec^{-1}$
Double layer capacitance	C_{DL}	$F\ m^{-3}$
Saturated concentration of O_2 in the electrolyte	C_0	$mol\ cm^{-3}$
Molar concentration of species i	c^i	$mol\ m^{-3}$
Molar concentration of species I in phase α	c_α^i	$mol\ m^{-3}$
Reactant surface concentration	C_R^*	$mol\ cm^2$
Diffusion coefficient of O_2 in the solution	D_0	$cm^2\ s^{-1}$
Diffusion coefficient of species κ in phase α	D_α^κ	$m^2\ s^{-1}$
Knudsen diffusion coefficient of component κ	$D_{Knudsen,g}^\kappa$	$m^2\ s^{-1}$
Diffusive flux density	d_α^κ	$mol\ m^{-2}\ s^{-1}$
Electrical potential	E	V
Thermodynamic equilibrium potential	E_0	V
Equilibrium potential of reaction i	$E^{0,i}$	V
Activation energy of reaction i	E_{act}^i	$J\ mol^{-1}$
Faraday's constant	F	$C\ mol^{-1}$
Change in Gibbs free energy of reaction	ΔG	$J\ mol^{-1}$
Change in enthalpy of reaction	ΔH	$J\ mol^{-1}$
Cell current	I	A
Current density	i	$A\ cm^{-2}$
Molar flux	J	$mol\ s^{-1}\ m^{-1}$

Exchange current density	j_0	A cm^{-2}
Intrinsic permeability	K	m^2
Rate constant of reaction	κ^i	/
Relative permeability of phase	$\kappa_{r\alpha}$	/
Number of phases	M	/
Molar mass of component κ	M^κ	kg mol^{-1}
Number of component	N	/
Number of transferred electrons	n	/
Normal vector	$\vec{n}$	/
Overpotential	η	V
Activation overpotential	η_{act}	V
Nernst potential	η_{Nernst}	V
Ohmic overpotential	η_{ohm}	V
Pressure	p	Pa
Partial pressure of species	$P_{species}$	Pa
Heat	Q	J
Source and sink term	q	/
Universal gas constant (8.314 $J\ K^{-1}\ mol^{-1}$)	R	J K^{-1} mol^{-1}
Charge transfer resistance	R_{Ct}	Ω
Mass transport or diffusion resistance	R_{diff}	Ω
Roughness	R_a	nm
Interfacial resistance	R_{int}	S m^{-1}
Resistance due to water films	R_l	S m^{-1}
Integrated volumetric reaction rate	$\hat{r}$	mol $m^{-3}s^{-1}$
Volumetric reaction rate of reaction i	r^i	A m^{-3}
Entropy	S	J K^{-1}
Saturation of phase α	S_α	/
Fraction of expanded channels	S_{ch}	/
Maximum heat flux	S_Ψ	W m^{-2}
Temperature	T	°C
Time	t	s
Cell temperature	T_{cell}	°C

Internal energy	U	J
Mass specific internal energy of phase α	u_α	J kg^{-1}
Ion mobility	u^i	m^2 V^{-1} s^{-1}
Velocity	v	m s^{-1}
Volume	V	m^3
Cell voltage	U_{cell}	V
Velocity of phase α	v_α	m s^{-1}
Stoichiometric coefficient of species i	υ^i	-
Work	W	J
Molar work	w	J mol^{-1}
mole fraction of component κ in phase α	x_α^κ	/
Real part of impedance	Z'	Ω cm^{-2}
Imaginary part of impedance	Z''	Ω cm^{-2}
BET surface area	S_{BET}	m^2 g^{-1}
Thickness of the ionomer film	δ_{ion}	m
Effectiveness factor for the platinum loading	ϵ	/
Heat conductivity	λ	W m^{-1} K^{-1}
Chemical potential of H_2O	μ^{H_2O}	J mol^{-1}
Dynamic viscosity of phase α	μ^α	Pa s
Potential	Φ	V
Porosity	ϕ	/
Volume fraction of phase i	ϕ_i	/
Peltier coefficient of reaction i	Π^i	V
Flux term	Ψ	/
Permeation coefficient of species κ	ψ^κ	mol s^{-1} m^{-1} Pa^{-1}
Mass density of phase i	ρ_i	kg m^{-3}
Molar density of phase i	$\rho_{mol,\alpha}$	mol m^{-3}
Mass density of the solid matrix	ρ_s	kg m^{-3}
Conductivity	σ	S m^{-1}
Surface tension	$\sigma^{surface}$	N m^{-1}
Contact angle	θ	/
Storage term	ξ	/

1 Introduction

1.1 Background

Fossil fuels became one of the greatest utilities for the human civilization from the beginning of the industrial revolution, and they are still the major source of energy supply even in the mid of 21st century. Due to the growing energy demand caused by population growth, the intensive burning of fossil fuels amplifies greenhouse gas (GHG) emission and drastic deforestation leads to global warming, which has never been seen before in human history. According to the "BP statistical review of world Energy 2018", the following graph shows an alarming course of global energy consumption within only the last few decades. Thus, alternative, renewable energy carriers are urgently needed to satisfy human energy demand and at the same time lower emission of GHG [1].

One of the most environmental friendly solutions to escape from this complicated situation is to divert our energy consumption from fossil fuels to chemical energy carriers such as hydrogen and related electrochemical energy conversion devices such as fuel cell. Fuel cell is an electrochemical device that transforms chemical energy of a fuel and an oxidizing agent into electricity through a redox reaction. In particular, proton exchange membrane fuel cell (PEMFC) is one of the many kind of fuel cells, which generates electrochemical energy very efficiently from renewable or non-renewable source to the stationary or mobile application without emitting GHGs that harms our environment [2–4]. The principle difference between battery and fuel cell is that a battery provides electrical energy that is stored previously in it as chemical energy, whereas fuel cell instantly converts chemical energy of an externally fed fuel into electrical energy.

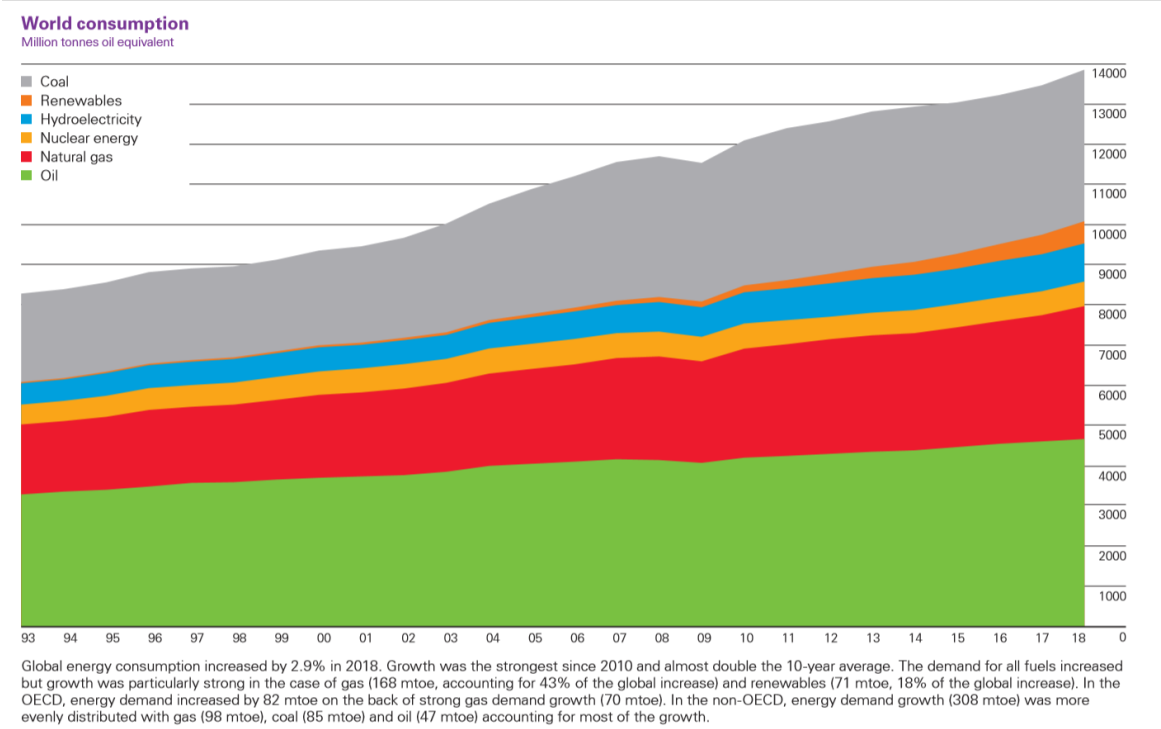

Figure 1: Statistics showing world consumption of global energy from 1993 to 2018. Reproduced from [1].

PEMFC is an electrochemical engine, which uses in the simplest form H_2 as a fuel, and a proton conducting solid membrane as an electrolyte to produce electricity at a temperature ranges from 60 °C to 200 °C. Temperature range 60 °C to 90 °C is associated with low temperature PEMFC, whereas 120 °C to 200 °C is associated with high temperature PEMFC [5]. Hydrogen produced using renewable energy is a so called clean energy carrier which can be produced by electrolysis of water. The following scheme is reconstructed from the special report of European Commission's community research magazine, which demonstrates the scenario of hydrogen sources and applications in a nutshell [6]. In addition, the distinct fuel reactants for various fuel cells and their consecutive applications also have been depicted. Certainly, hydrogen is considered by many a key solution to 21st century's energy demand, which enables green and efficient manufacturing of power as well as heat from a wide spectrum of primary energy sources.

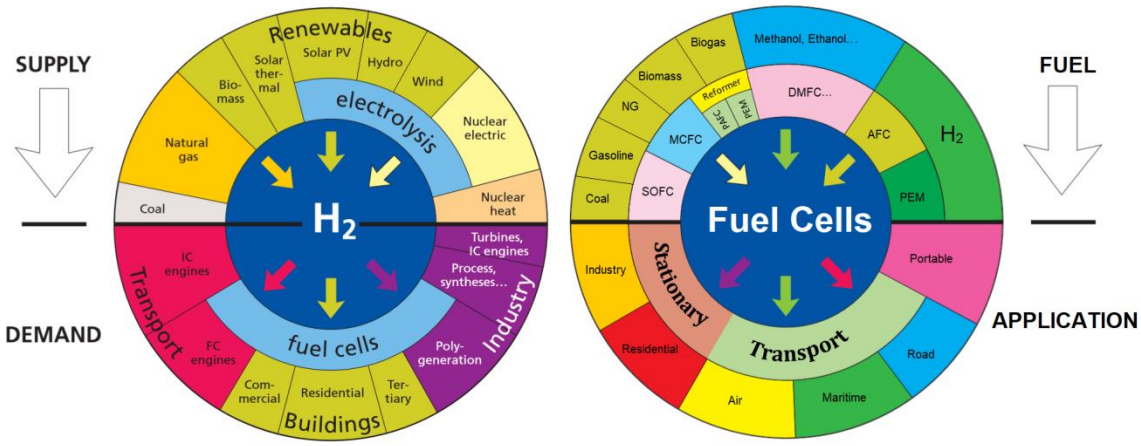

Figure 2: A schematic diagram of primary energy sources together with energy converters, applications of hydrogen with distribution of FC technologies and available fuels as well as their applications. Reproduced from [6].

1.2 Motivation

PEMFC involves hydrogen oxidation reaction (HOR) at the anode along with oxygen reduction reaction (ORR) at the cathode to produce electricity, and both of the reactions are catalyzed by platinum which is a precious metal [7,8]. Plenty of researches are carrying out investigations all over the world to reduce or replace the precious metal catalyst from the PEMFC, but so far platinum and its alloyed catalysts are still on top considering activity, selectivity and stability [9]. Due to the limited resource and erratic price of platinum, catalyst of PEMFC becomes the primary obstacles for its feasibility to commercialization. The following graph is a cost breakdown of PEMFC stack components presented by US DOE [10].

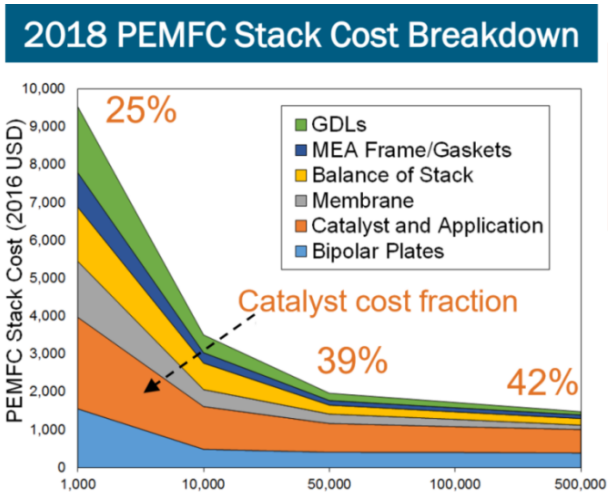

Figure 3: Distribution of expenditure from individual component of PEMFC stack. Reproduced from [10].

Therefore, it is very important to reduce the loading of platinum especially in cathode catalyst layer which contains 80 % to the loading, while at the same time enhance the activity along with durability [11,12]. On that ground, the motivation of my research is to reduce the loading of precious metal in the catalyst layer while characterizing as well as understanding the influence of CL microstructure and other parameters on the performance. Additionally, an investigation of other component such as membrane and ionomer (used in the electrode) also has been performed to achieve a high performance PEMFC in short and long term application. Furthermore, the drying step of MEA fabrication techniques, which is frequently overlooked in the community is studied and developed in this work.

1.3 Thesis outlines

This doctoral thesis initially investigated the effect of catalyst layer (CL) microstructure on performance by applying several coating techniques for MEA fabrication. In particular, this work explored how different CL structure contributes to the different voltage loss of the cell performance. In this context, the powder preparation technique of dry spray coating method, which was invented by DLR, has been improved by nearly 50 %. Afterwards, this work concentrates on selecting other components such as membrane and ionomer in the electrode to yield higher performance and increases longevity. In broad lines, this research work targets to the fundamental challenges of the commercialization of PEM fuel cell by taking into account the application of low Pt loading in MEA while increasing the performance and durability. Eventually, an MEA fabrication method from catalyst ink suspension has been developed by implementing sublimation technique. Along with the experiments, a numerical model and simulation also has been conducted to get further insight, how the optimized porous structure improves ionomer network and reduces the mass transfer limitations, which consequently increase performance as well as improve water management.

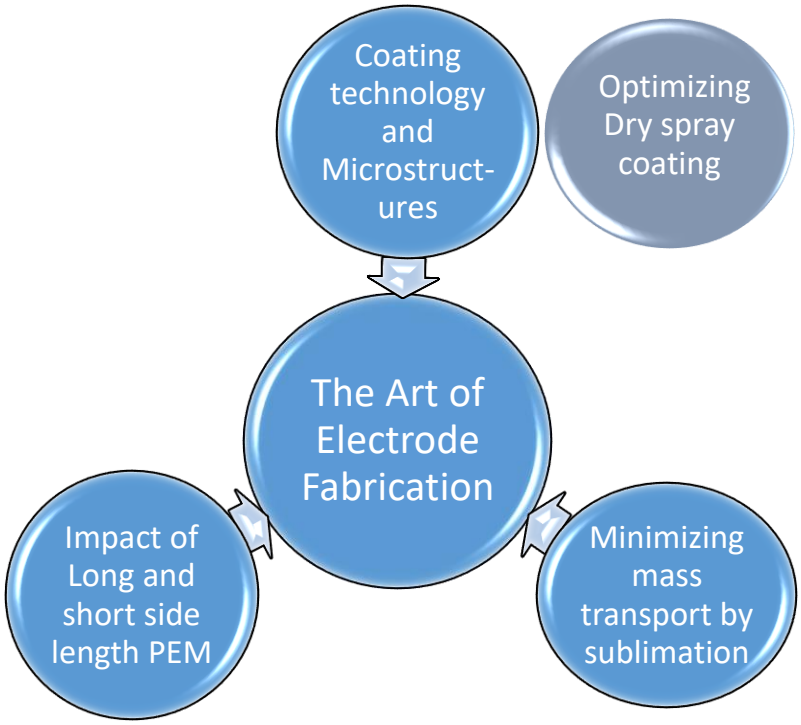

Scheme 1: Outline of this thesis in a nutshell

2 Fundamentals

2.1 PEMFC Principle

Polymer Electrolyte membrane fuel cell is an electrochemical device where chemical energy can be converted into electrical energy by an electrochemical reaction. Fuel cell as a device was first invented by Sir William Robert Grove in 1839 [13]. At present, the leading application of PEMFC has been individual transportation with environmental friendly cars which are zero emission if H_2 are produced from renewable sources. Leading motor companies work on PEMFC for fuel cell electrical vehicles (FCEV) considering its high power density and outstanding dynamic characteristics compared to other FCs. Additionally, aircraft application (e.g. the HY4 fuel cell airplane developed by DLR), distributed/stationary and portable power generation are also alternative applications of PEMFC [3].

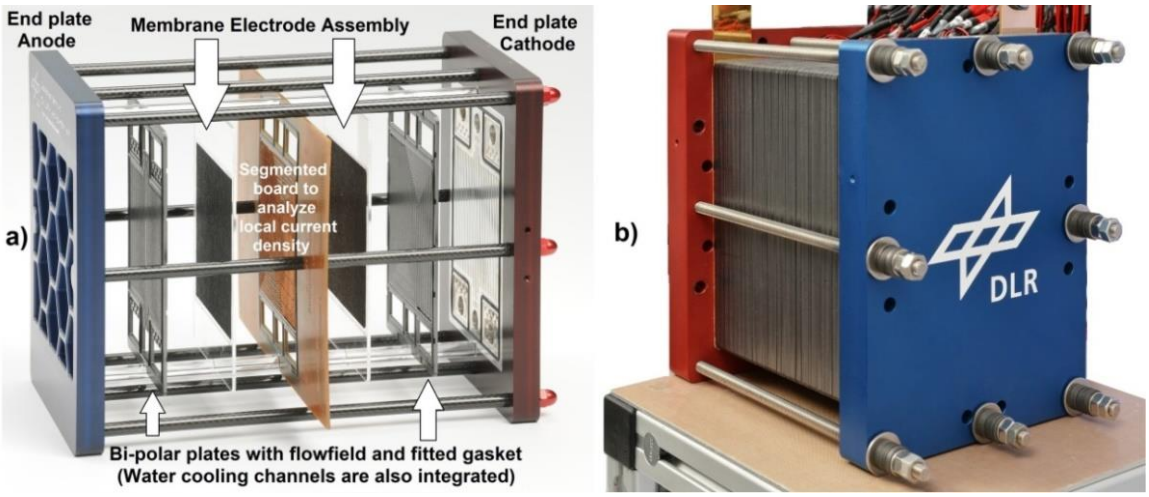

Figure 4: a) Exploded cell view of a DLR PEMFC stack configured with segmented board, b) a finished PEMFC stack produced by DLR ready to operate.

Fig. 4 and 5 demonstrates the key components and configuration of PEM fuel cell in which oxidative and reductive half-cell reactions are kept separate. A simple PEM fuel cell incorporates three major units: An MEA (membrane electrode assembly) along with two bipolar plates**,** which connect MEA in series. This series of bi-polar plates provide adequate media distribution with flow field, separate anode and cathode reaction chamber as well as provide a good electronical conductivity acting as current collector. Also cooling can be accomplished by the bipolar plate in many designs. These bipolar plates are sealed towards the atmosphere with the MEA with appropriate seal or gaskets. The heart of PEMFC is the membrane electrode assembly or MEA where the electrochemical reaction takes place. The design of the individual components are comprehended by considering the stack performance related to operating conditions, fuel and oxidant composition, water management, and finally yet importantly the cost effectiveness [14,15].

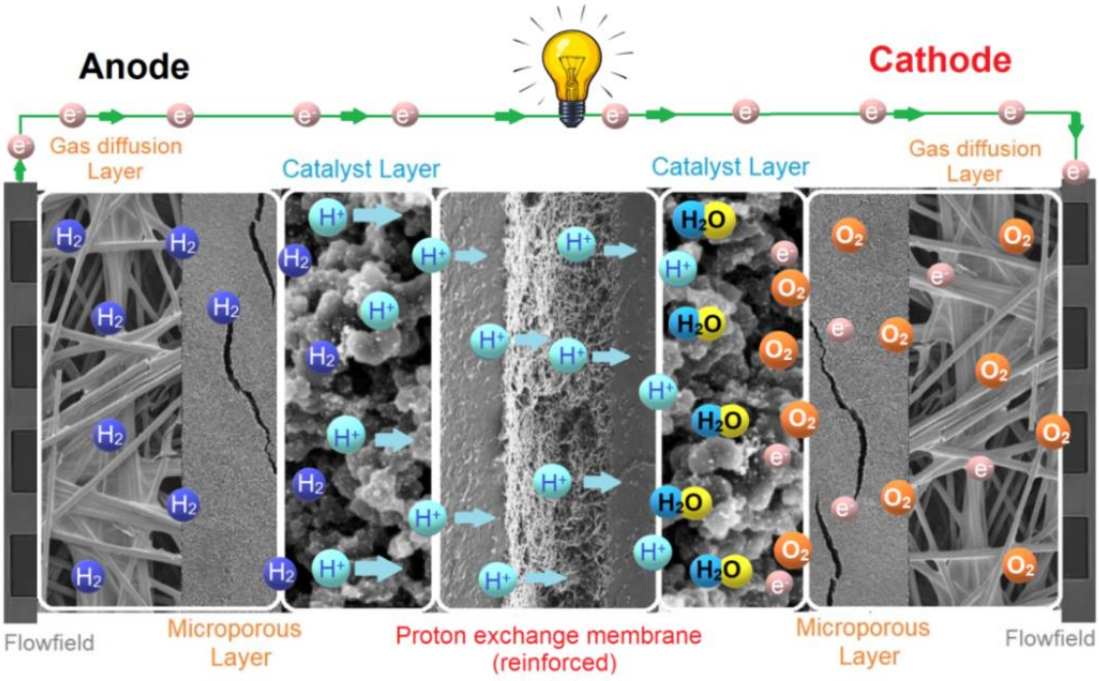

Figure 5: Layout of a membrane electrode assembly of PEMFC. The components are represented by SEM images those are not the same scale and only used as a schematic representation.

The MEAs are electrochemical cells in which a pair of catalyst layers and a pair of diffusion media on both sides is sandwiched with an electrolyte membrane in-between. The principle task of an MEA is to accommodate the electrochemical reaction along with transport of proton, gas, water, heat, and finally and most importantly to regulate

efficiently the flow of electrons liberated from the oxidation reaction site (the anode) to the reduction reaction site (cathode). Generally, this is accomplished by isolating anodic reaction chamber from cathodic reaction chamber by using a membrane, which only conducts (H^+) protons. An external circuit transports electron from anode to cathode. The membrane should stay in hydrated condition to conduct solvated protons. Due to this limitation of working temperature, operating temperature of low temperature PEMFC remains below 100 °C, typically 60 to 90 °C [16,17].

The overall electrochemical reaction in a PEMFC is following,

$$H_2 + \frac{1}{2}O_2 \rightleftharpoons H_2O + \text{electricity} + \text{heat} \quad (2.1.1)$$

Anodic: $H_2 \rightleftharpoons 2H^+ + 2e^-$ or hydrogen oxidation reaction (HOR) (2.1.2)

Cathodic: $\frac{1}{2}O_2 + 2H^+ + 2e^- \rightleftharpoons H_2O$ or oxygen reduction reaction (ORR) (2.1.3)

At the anode, gaseous hydrogen is dissociated, also electrochemically oxidized yielding protons as well as electrons, and protons are being transported through the polymer electrolyte membrane, which is also known as proton exchange membrane. The electrons travel through an external circuit to produce electricity, eventually consumed by oxygen, and all combines to water in cathode. This reaction is an exothermic process and produces heat as a byproduct [2,18]. The aforementioned reaction 2.1.1 (forward) is thermodynamically favored and thus spontaneous, since the free energy of the reactants is more than the products.

2.2 Polymer Electrolyte Membrane

Polymer electrolyte membrane is the centre feature of the MEA, which transport protons as well as hinders electron conduction. This electrolyte not only used as membrane (as a separator), but also being integrated with catalyst in the catalyst layer (CL) to improve the proton conductivity through CL [19]. The electrolyte or ionomer composed of polytetrafluroethylene (PTFE) backbone that is hydrophobic and perfluroalkyl ether side chains terminated with (SA) sulfonic acid group that is hydrophilic fragment. When the membrane is hydrated, water molecules stabilize the dissociated proton derived from the SA group [20]. The hydrophobic-hydrophilic behaviour of polymer backbone and sulfonic acid group causes natural phase separation in hydrated ionomer. This phase separation is responsible for the unique capability of proton transport [21].

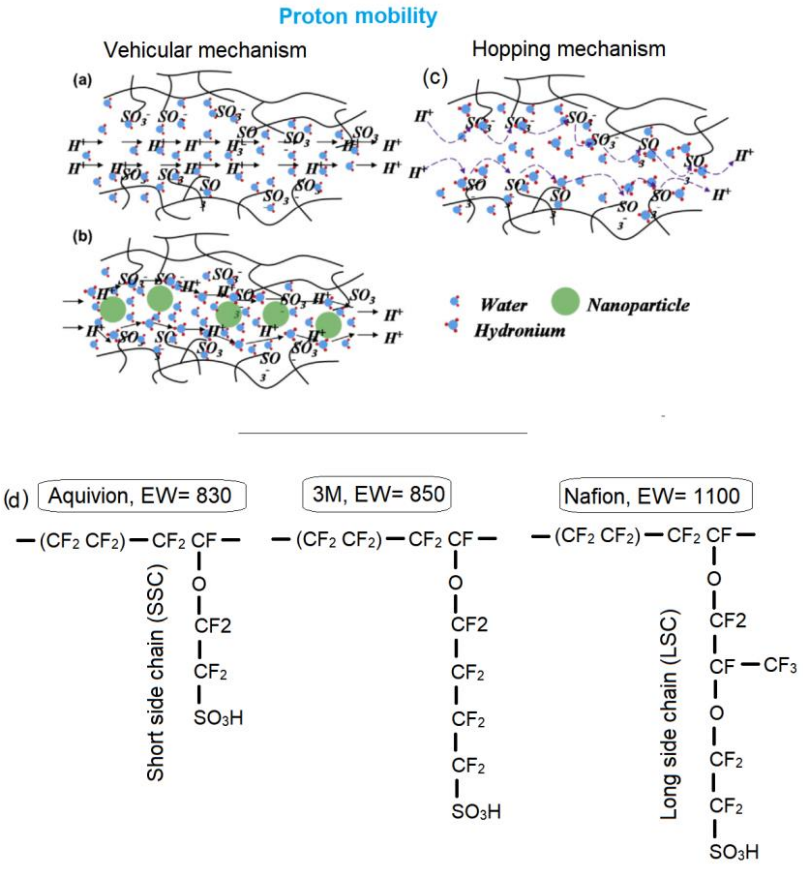

Figure 6: The Schematic diagram of the proton conduction in (a) bulk membranes and (b) polymer/ nano-particle composite membranes by vehicular mechanism, (c) hopping mechanism, (d) chemical structures of ionomers with different length of side chains.

Nafion® is the most widely used electrolyte in PEM fuel cell. Aquivion®, 3M™, Flavion® etc. are also used as membrane including ionomer dispersion. The basic difference among these ionomer is the length of side chain, which determines the vital properties of ionomer that is equivalent weight (EW). The EW (g $mole^{-1}$) of an ionomer is the weight of the polymer necessary to yield 1 mole of exchangeable protons, which is also the inverse of the (IEC) ion exchange capacity (mmole g^{-1}) [22]. Generally, more the IEC (or less EW) of ionomer, the more water uptake or proton conductivity it carries. The chemical structures of ionomers are demonstrated in fig. 6 d.

The state of the art proton conductivity of PEM membrane is in between 0.12 to 0.26 S cm^{-1} [23]. Higher proton conductivity is expected to gain higher current density of cell, and the proton conductivity of the ionomer can be explained through two principle mechanisms: “vehicular” and “hopping”. The schematics of the proton conduction mechanism in both bulk membrane and nano particle composites are illustrated with fig. 6 a, b and c, which are reconstructed from [2,24,25].

Along with proton mobility and water content, water retention capacity and permeation phenomena also have a critical influence in determining the performance of fuel cell. Besides, literatures have shown that when ionomers absorb water, ionic materials redistribute themselves so that the spacing between the clusters increases, but their number density declines [26]. Moreover, membrane durability is also a very important factor impacting fuel cell lifetime. The structural and compositional variations between SSC and LSC ionomers influence their specific features. The absence or presence of the pendant perfluoroether group can significantly determine the chemical stability of ionomers. Similarly, CF3 group and side chain length regulates the glass transition temperature at a given EW [22]. To increase the mechanical stability, PTFE reinforcement is used as a layer inside the membrane (Fig. 5). In addition, radical attack is one of the most detrimental phenomena for the ionomer that causes breaking of weaker functional group and/ or side chain of the ionomer. Recently, radical scavengers like Ce composites are used to minimise this degradation effect of the membrane due to radical attack.

2.3 Thermodynamics

Thermodynamics of the PEMFC is the key to understand the energy conversion process.

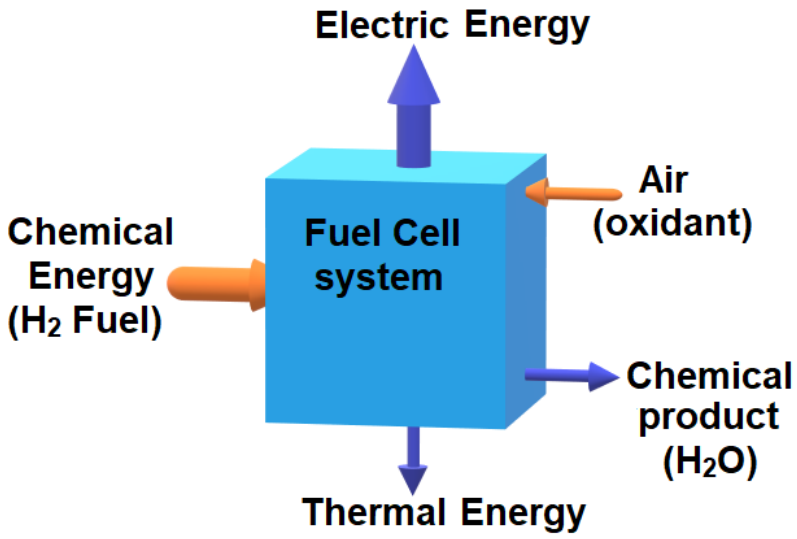

Figure 7: Thermodynamic energy conversion system of fuel cell

A fuel cell is an electrochemical device that transforms the Gibbs free enthalpy that originates from a combustion reaction of a fuel and oxidant. The highest work output obtained from the (2.1.1) reaction is the difference in free energy between the reactant and product. The Gibbs free energy is taken into account as it is the key to the potential of reaction. Though the reaction produces some amount of heat due to the exothermic process, the amount is much less than the direct combustion of oxygen and hydrogen. If enthalpy is S, temperature is *T*, volume is V, pressure is *P* and electric work is W_{elec}, then the original differential expression of Gibbs free energy *G* is,

$$dG = -S\,dT + Vdp - dW_{elec} \tag{2.3.1}$$

For constant temperature and pressure, the variation in standard free energy change of fuel cell reaction is indicated by the equation 2.3.2, which can be transformed to equation 2.3.3

$$dG = -dW_{elec} \tag{2.3.2}$$

$$\Delta G = -nFE \tag{2.3.3}$$

Where ΔG is the difference in Gibbs free energy, E is reversible potential, n is the sum of electrons transferred, and F is Faraday constant. In the standard states of reactant and product, the theoretical equilibrium potential E° is obtained by the following equation.

$$E^0 = -\frac{\Delta G^0}{nF} \quad (2.3.4)$$

ΔG value corresponding to reaction 2.1.1. is -229 kJ mol^{-1}, F= 96500 C g^{-1} mol^{-1}, n=2 electron, resulting the determined value of $E°$ is 1.229 V (reversible cell potential).

- Reversible cell potential variation with temperature:

The final derivation of how to express the variation of reversible cell potential as a function of temperature is following, where ΔS is the change of entropy.

$$\left(\frac{dE}{dT}\right)_p = \frac{\Delta S}{nF} \quad (2.3.5)$$

If we define E_T as the reversible cell potential at an arbitrary temperature T and at constant pressure p, E_T can be calculated by,

$$E_T = E^0 + \frac{\Delta S}{nF}(T - T°) \quad (2.3.6)$$

- Reversible cell potential variation with pressure:

The variation of the reversible cell potential with pressure is following, where ΔV is the change of volume (in mole), where R is the gas constant, and Δn_g represents change in total number of moles of gas in the reaction.

$$\left(\frac{dE}{dp}\right)_T = -\frac{\Delta V}{nF} = -\frac{\Delta n_g RT}{nFp} \quad (2.3.7)$$

- Reversible cell potential variation with concentration:

The alteration of the reversible cell potential with chemical activity (chemical concentration, composition, etc.) is given by the Nernst equation:

$$E = E^0 - \frac{RT}{nF} \ln \frac{\Pi a_{products}^{v_i}}{\Pi a_{reactant}^{v_i}} \quad (2.3.8)$$

For a system with an arbitrary number of product as well as reactant species denotes as Π, and where a is activity of each species by its corresponding stoichiometric coefficient (v_i). [27,28].

2.4 Overpotentials

It is evident that the open circuit voltage (OCV) of the PEMFC is less than the theoretical standard potential or reversible cell potential. We encounter voltage losses due to several effects, and this loss of voltage is called overpotential of the system. Some potential loss occurs due to the crossover of fuel gas through membrane and mixed potential [29]. In particular, there are three kinds of overpotential occurs in PEMFC, and they are activation polarization or kinetic loss, ohmic polarization or charge transport loss and concentration polarization or mass transport loss [30,31].

The cell voltage is provided by

$$U_{cell} = U^0 - \eta_{act} - \eta_{ohm} - \eta_{Conc} \quad (2.4.1)$$

Where, U^0 is theoretical voltage, η_{act} is kinetic overpotential, η_{ohm} is ohmic overpotential, and η_{Conc} is concentration or mass transport overpotential.

- **Kinetic overpotential**:

Fuel cell reaction associates the transfer of electron between chemical species to the electrode surface and vice versa. As each electrochemical half reaction (hydrogen oxidation reaction HOR and oxygen reduction reaction OER) involves transfer of electron, hence current generated from the cell is a magnitude of the reaction rate. Notably, the exchange current density j_0 plays a significant role to understand the kinetics and electrocatalysis of the reaction. The exchange current density is the current of net electrochemical reaction at the equilibrium state.

For the forward reaction, $i_1 = nfC_R^* f_1 \, e^{-\Delta G_1^{\ddagger}/(RT)}$ (2.4.2)

And for the reverse reaction, $i_2 = nfC_P^* f_2 \, e^{-\Delta G_2^{\ddagger}/(RT)}$ (2.4.3)

Where $n$is the number of transferred electron f is the decay rate of the species, $\Delta G^{\ddagger}$ is the size of the energy barrier, C_R^* is the reactant surface concentration (mol cm^{-2}) of reactant and C_P^* is the reactant surface concentration of product.

At thermodynamic equilibrium the forward and reverse reaction are in balance, and there are no net current. So $i_1 = i_2 = j_0$ (2.4.4)

However, reaction kinetics consistently inflicts an exponential loss on a PEMFC's i–V curve as demonstrated in fig. 8. Actually, there are four fundamental means to increase exchange current density j_0, which is a proportional factor to the performance. They are:

1. By increasing the reactant concentration c_R^*
2. By decreasing the activation barrier $\Delta G^{\ddagger}$
3. Increasing the temperature T, and
4. Enhancing the number of probable reaction sites (reaction interface roughness).

In a electrochemical reaction, j_0 exchange current density is very much analogous to the rate constant. The effective exchange current density is a function of concentration, temperature, pressure, catalyst loading and catalyst specific surface area. With a reference exchange current density at a given temperature and pressure, the effective current density at any pressure and temperature is following [32],

$$j_0 = j_0^{ref}\ a_c L_c \left(\frac{P_r}{P_r^{ref}}\right)^{\gamma} \exp\left[-\frac{E_C}{RT}\left(1-\frac{T}{T_{ref}}\right)\right] \qquad (2.4.5)$$

Where, j_0 is effective exchange current density, j_0^{ref} is reference exchange current density, a_c is catalyst specific area, L_c catalyst loading, is P_r reactant partial pressure, P_r^{ref} reference pressure, γ pressure dependency co-efficient, E_C activation energy, T_{ref} reference temperature. It is worth mentioning that the product $a_c L_c$ is also termed as electrode roughness.

The foundation equation of the reaction kinetics in electrocatalysis is known as Butler-Volmer Equation, which comprises both of the oxidation and reduction reaction.

$$i = j_0\ \left\{\exp\left[\frac{\alpha_a nF\eta}{RT}\right] - \exp\left[\frac{\alpha_c nF\eta}{RT}\right]\right\} \qquad (2.4.6)$$

Here i is the current density, j_0 = exchange current density, n = no of electrons transferred, α = transfer coefficient (anodic or cathodic), F = faraday's constant 96,485 C mol^{-1}, η = overpotential, R = gas constant and T = temperature. It is a balance between both way reactions. Further the equilibrium shifts to one direction or other, one of these terms will cancel out, eventually ends up with one significant term of the equation. And it is known as Tafel equation, a more simplified way of stating Butler-Volmer eq., when the reverse reaction is neglected and the overpotential is large.

$$i_a = j_0 \exp\left[\frac{\eta}{b}\right] \quad (2.4.7)$$

$$i_c = j_0 \exp\left[-\frac{\eta}{b}\right] \quad (2.4.8)$$

Where, i_a and i_c are the current density of anode and cathode respectively, and b is the Tafel slope, which determines the activity of electrocatalyst. This can be expressed as following equation of linear slope [33].

$$\eta_{act} = a + b \log i \quad (2.4.9)$$

where, $a = -\frac{RT}{\alpha n F} \ln j_0$ and $b = \frac{RT}{\alpha n F}$

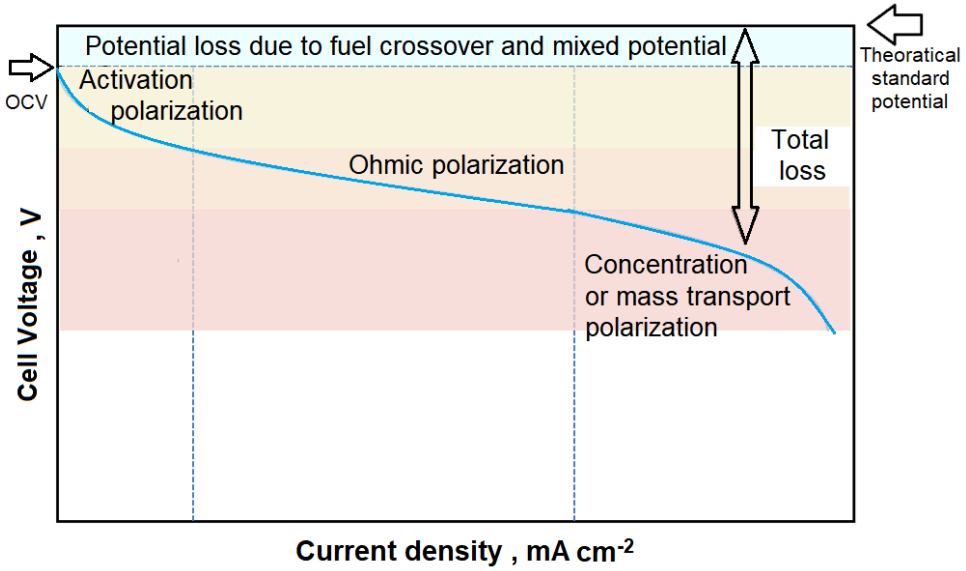

Figure 8: Distribution of dominating over potential zone in overall PEMFC performance

- **Ohmic overpotential**:

Ohmic loss is attributed to the resistance against the flow of electron through the whole circuit including the MEA as well as the flow of proton through electrolyte. For instance, the electrical resistance causes from the insufficient compression of the MEA with bi-polar plates (which means contact resistance), thickness of electrode along with diffusion media, electrical conductivity of bi-polar plates and the complete circuit. However, proton conductivity of membrane contributes the major part of the ohmic resistance. Additionally, proton conductivity throughout the electrode also plays a role

in the contribution of ohmic resistance. There is a linear relation between applying currents and voltage losses due to the internal resistances. It can be recognized from the fig. 8, where we can see a linear behavior of ohmic polarization. The ohmic polarization, R_{ohmic}, can be given as [34]:

$$R_{ohmic} = R_{ionic} + R_{electric} + R_{contact} \quad (2.4.10)$$

Where R_{ionic} , $R_{electronic}$ and $R_{contact}$ represent proton resistance, electronic resistance and contact resistance respectively. If σ is conductivity, L is length, and A is area, R_{ionic} is following,

$$R_{ionic} = \frac{L}{\sigma A} \quad (2.4.11)$$

- **Concentration overpotential**:

To yield uninterrupted production of electricity, fuel and oxidant must be supplied continuously to the reaction zone, and simultaneously the products have to be eliminated so as to avoid restraining the power production. The process of continuous supply of reactants and removing products is tagged as fuel cell "mass transport" in fig. 8. The primary concentration of the reactant gases has an influence on consumption and OCV; however, the concentration will decline until they reach to a certain point when the amount of reactant gases reaching to the electrode-electrolyte interface is equal to the rate of consumption. Then instantly, the concentration will reach to zero, and the attainable current density reaches to the maximum point, which is known as the limiting current density i_l. Considering the initial concentration C_1 at zero current, gradually the concentration drops to C_2 at a current density i, and finally drops to zero at the limiting current density i_l, the relation can be written as following [35,36]:

$$\frac{C_2}{C_1} = 1 - \frac{i}{i_l} \quad (2.4.12)$$

Integrating the above mention equation in Butler-Volmer equation, concentration polarization can be written as:

$$\eta_{conc} = -\frac{RT}{nF} \ln\left\{1 - \frac{i}{i_l}\right\} \quad (2.4.13)$$

So, in order to improve the FC performance especially at higher current density, it is required to maximize reactant transport to the active-site and get rid of products at once.

2.5 Literature Survey

Greszler et al. stated back on 2012 that Pt loading is inversely proportional to the O_2 transport resistance [37]. Moreover, high Pt-loading allows PEM fuel cell the advantages of a longer lifespan including more effectiveness and stability. However, the research and improvement of electro-catalysts with low loading of Pt remains significantly important since such progress will substantially minimize the cost of MEA, and decrease the PEMFC weight as well as volume [38,39]. In recent years, extensive efforts have been put into designing electrodes with low Pt loading but with high power density and stability. For instance, according to Kriston et al., due to the decreasing catalyst utilization or accessibility, the active area decreases with increasing Pt loading [40]. Major progress to enhance performance and to reduce the Pt loading has been made probable by: (i) adopting Pt supported on large surface-area carbon as a substitute of pure Pt black [41]; (ii) impregnating proton conducting ionomer into the CL of the either GDE or the CCM [42–44]. Some research findings are stated below:

- In case of gas diffusion media, thicker the microporous layer comparing to carbon paper thickness, smaller the diffusion resistance [45].
- It is possible to reduce Pt loading by increasing its activity and surface area.

Pt catalyst loading may be curtailed by a number of ways such as i) Pt particles can be supported over higher surface area carbon support (graphitized) [46], ii) fabricating core shell nanoparticles together with non-Pt metal as core and Pt metal as shell [47–50], iii) alloying the Pt with transition metals [51–55], and inner transition metals / rare earth metals (La, Ce, Pr, Nd, Gd, Sm, Eu etc.) [56–59]. This finding further motivated researchers to work on non-Pt based electro-catalyst/nonmetallic (metal-free) catalysts, whose electrochemical activity competes with the traditional Pt/C catalysts. The investigation is intensified since last decade, and large number of scientists have proposed new ideas for designing active ORR catalyst, mostly with the transitional metals-based catalyst (Fe, Co, Mn, Ni, etc.) along with non-metallic ORR catalyst (metal-free catalysts) [60–63].

- (LSC) Low / solid surface area carbon support (Vulcan) has higher ECSA but lower ORR mass activity than (HSC) high surface area carbon (Ketjen). ECSA retention capacity is higher with increasing porosity. There is a tendency of ionomer to fill pores smaller than 4 nm, and hence the carbon pores $\leq$ 4 nm is very critical [64,65].

- Electrode should be well-balanced between thickness and porosity. Contact and better electronic conductivity are facilitated by thin electrode, but it loses the porosity. Contrarily, porous electrode shows better diffusion properties, however exhibits higher contact resistance and ohmic resistance compared to the thinner one [66,67].
- The proton resistance of the membrane increases with the thickness. However, the influence of the membrane thickness is trivial, if the membrane is ≤ 25 µm [68].
- Thickness and high tortuosity of ionomer in electrode is inversely proportional to the proton conductivity. High humidification of electrode reduces the O_2 diffusion resistance. However, Park et al. stated that the excessive swelling of the ionomer causes larger O_2 diffusion resistance. So, the equivalent weight of ionomer and resulting water uptake should be optimized appropriately. The average thickness of ionomer over particle or agglomerates in commercial electrode is 7 to 13 nm. Thinner than 4 nm ionomer causes laminar bilayer and reduces proton conductivity. The critical thickness of Nafion® film over catalyst surface is 0.2 µm. Ionomer layer thicker than this causes diffusion problem. Moreover, roughness factor is also inversely proportional to electrode transport resistance [37,66,67,69–73]. A schematic diagram reactive interface in cathode catalyst layer is illustrated in fig. 9.

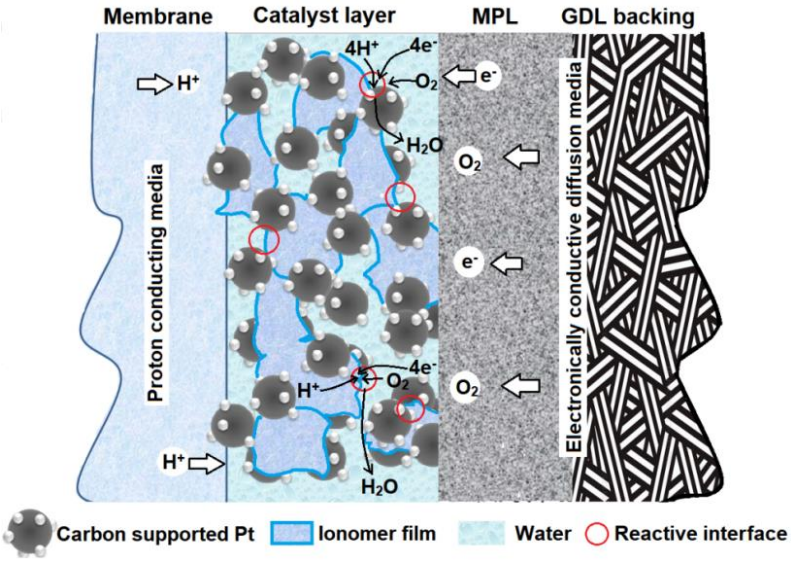

Figure 9: Scheme of cathode catalyst layer reactive interface

- Regarding the ionomer loading, less the Pt content higher will be the ionomer ratio, and Shashikumar et al. experimentally showed that ionomer loading should increase as Pt loading decrease. Consequently, for electrode with 0.5, 0.25, 0.1 mg cm^{-2} Pt-loading, the highest performance was achieved at 20, 40 and 50 % loading of ionomer respectively. However, distribution of ionomer is more important than

homogeneity to have higher performance. Especially, the proton resistivity of the cathode has strong dependency on the ionomer at lower I/C ratio. It is calculated by several groups that oxygen transport resistance through the ionomer coating over Pt/C agglomerates is a rate determining step of the CCL activity in a normal operating FC conditions. Moreover, it is proposed that limitations of the oxygen transport through the ionomer could be inhibiting by decreasing the ionomer film thickness, and increasing the thickness of CL. Nevertheless, expanding the porosity of the CL, lessening the ionomer thickness and employing thicker CL reduce the effective proton conductivity. This causes inadequate proton conductivity also non-uniform voltage in the CL leading to loss of performance. Considering this phenomenon, an effective strategy would be to increase the permeability of oxygen in the ionomer to maintain satisfactory current-voltage or polarization performance with lower loading of Pt [67,74–78].

- Performance of CL and catalyst utilization principally depends on the ionomer content and their distribution throughout the CL. This ionomer catalyst interaction varies with materials (Pt/C/ionomer), solvent, composition and condition. And these have consequential effects on following properties like: agglomeration, phase segregation, pore space morphology and stability [79][80]. Typically, smaller agglomerate size, larger pore diameter and higher oxygen pressure increases the effectiveness factor of catalyst utilization. Eikerling and his group defines “the effectiveness factor of Pt utilization as the apparent rate of current conversion exhibited by a specific catalyst layer design divided by the ideal rate obtained if all Pt atoms were used equally in electrochemical reactions at the specified electrode overpotential and externally provided reactant concentrations” [81]. Therefore, low to medium coverage of ionomer film is advantageous to the optimized interplay of proton and oxygen supply [82]. Low operating current and high operating temperature facilitates the Pt utilization [81]. ECSA value increases with decreasing Pt particle size in carbon supported catalyst [83]. Nevertheless, higher Pt loading does not always ensure higher performance. Inhomogeneous thickness (thick layer) of ionomer often blocks the accessibility of both the exterior and interior Pt in carbon support, and consequently reduce the ECSA [84].
- Compression of the diffusion media is one of the most critical parameters, which plays a significant role in the mass transport behavior of a MEA. The optimum compression of the MEA is 14 % inside the bipolar plate, and the optimum pressure of the fuel cell bipolar plate to the MEA is 1-1.5 MPa [85].

2.6 Principle of Freeze Drying Technique

Freeze drying is a process consisting the consecutive removal of liquid solvent from a dispersion or a solution in the form of a solid (ice) phase by means of vacuum sublimation [86]. Freeze-drying is extensively used method for drying along with increasing the stability of numerous pharmaceutical and food products. Additionally, this technique has also been considered improving the long term stability of colloidal nanoparticles. Freeze-drying technique is divided into three fundamental steps: solidification or freezing, primary-drying or sublimation, and secondary-drying, which includes desorption of unfrozen water [87].

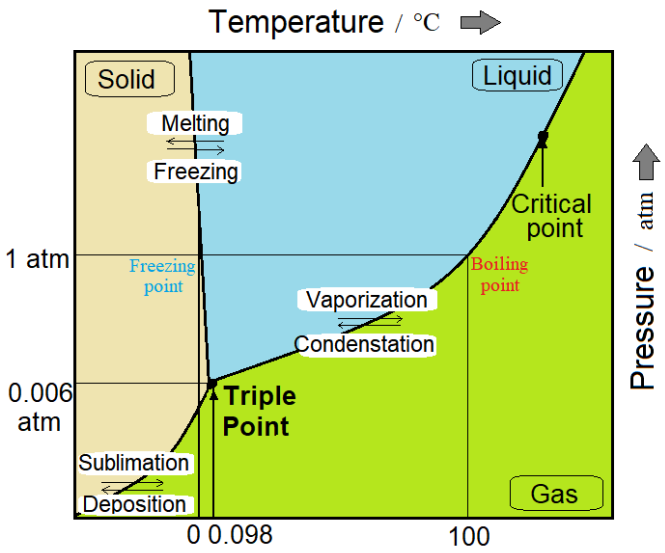

Figure 10: Phase diagram of water with triple point as well as critical point [88].

Freezing step involves the cooling of the solvent liquid into stable ice crystals. The material should be cooled down below to its triple point to ensure that only sublimation rather than melting will occur.

Primary drying step involves sublimation of solid solvent by means of reduced pressure below the triple point. A small amount of heat (still keeping the temperature below triple point) is provided as a latent heat of sublimation to increase the sublimation rate.

Secondary drying step involves removal of rest of the solvent, which is bound to the product. The temperature of the product now being raised since all of the free solid ice solvent has been already evaporated by sublimation.

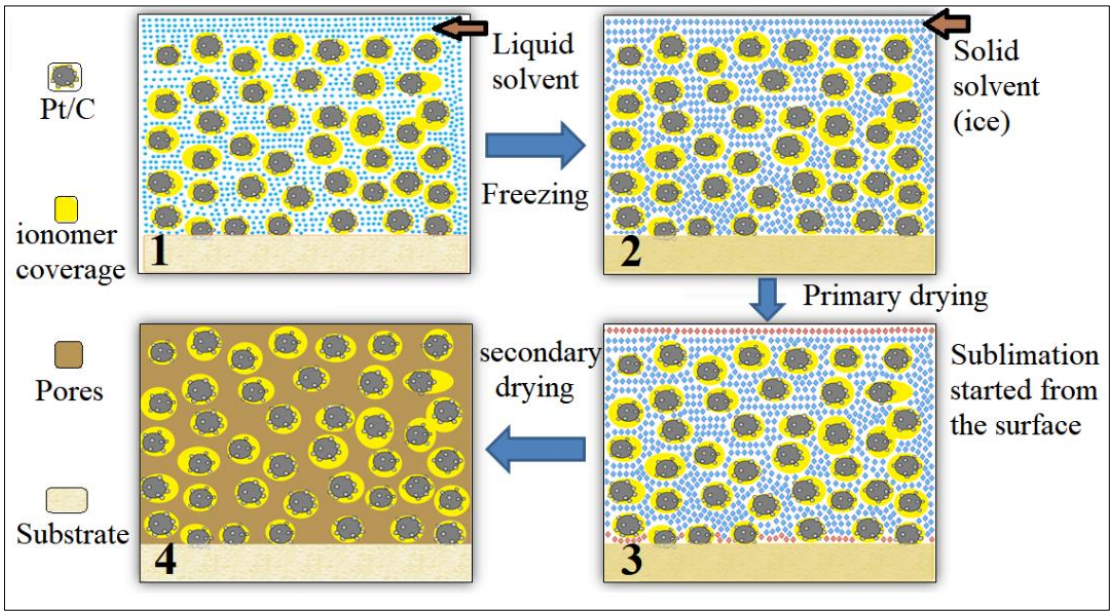

Figure 11: Schematic diagram regarding principle of freeze drying freeze dryer

Phase diagram of water is illustrated in fig. 10. In this research work (article IV, V), freeze drying technique has been practiced to remove the solvent from the catalyst layer after coating. This unique drying method is substantially able to increase the porosity and ionomer distribution of the catalyst layer while drying the substrate [89,90]. Fig. 11 demonstrates a schematic diagram attributed to the step by step mechanism of freeze drying. It starts with a substrate coated with liquid ink dispersion. Later it is cooled enough to convert all the liquid solvent into the ice crystal. Then the vacuum triggers the sublimation from the surface of the product. Slowly, all the solid ice evaporates, leaving the solid content as it is. Eventually the temperature is raised to evaporate the available physically or chemically bonded water from the layer.

In addition, fig. 15 c) shows an in-house freeze dryer built within DLR equipped with a solvent trap to retrieve the solvent and reuse it. Therefore, this drying technique is also an environment friendly method where the vapor of solvent need not to be discharged into the air.

3 Methods

3.1 Different catalyst layer preparation methods

Classification of catalyst coating method is demonstrated in table 1.

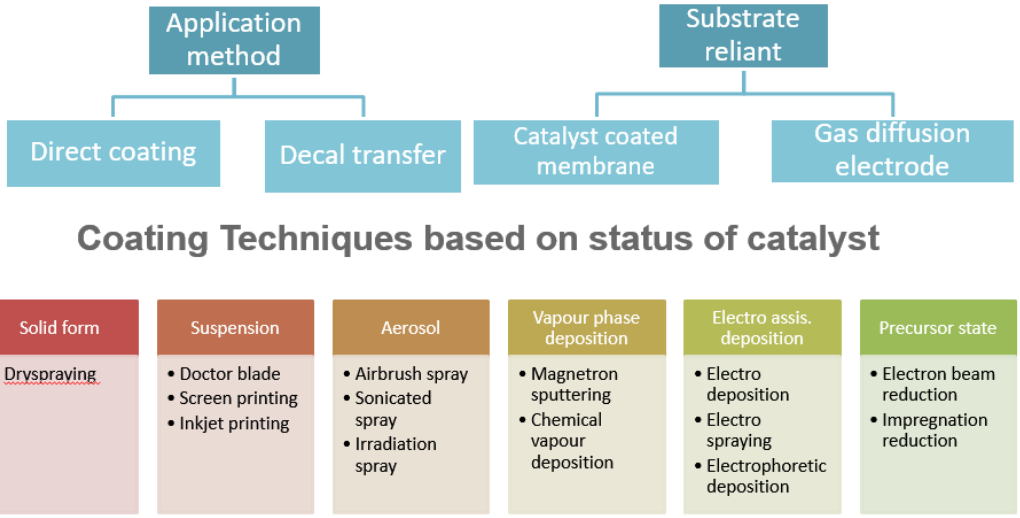

Table 1: Demonstrates a classification coating methods based on certain factors.

The MEA fabrication methods utilized in this work are mentioned below.

3.1.1 Dry Spray Method: The DLR research group has developed a dry layer preparation method to fabricate catalyst layers bound with either PTFE or Nafion®. Coating is executed onto either membrane or GDL by means of spraying the atomized dry mixture of Nitrogen stream. Afterwards, the membrane and the electrodes are arranged cautiously and hot-pressed. This is a very environmental friendly and fast MEA production process, where there is no requirement of any toxic solvent and drying step. Fig 12 a) displays a schematic diagram of dry spray MEA formulation process.

3.1.2 Air brush Method: Carbon supported catalyst is mixed with distilled water, ionomer and convenient solvent. This catalyst ink is then sprayed with air brush by

nitrogen gas flow onto the membrane or GDL. The substrate is kept over a heated suction plate, so that the substrate is firmly attached and the solvent can evaporate from the surface of the heated substrate. This is a very widely used and economic fabrication technique for MEA formulation. This method can be manually driven or can be also used with automation. Fig. 12 b) depicts an experimental setup of an airbrush method. Spray gun plays a vital role to control the size of aggregate on the substrate.

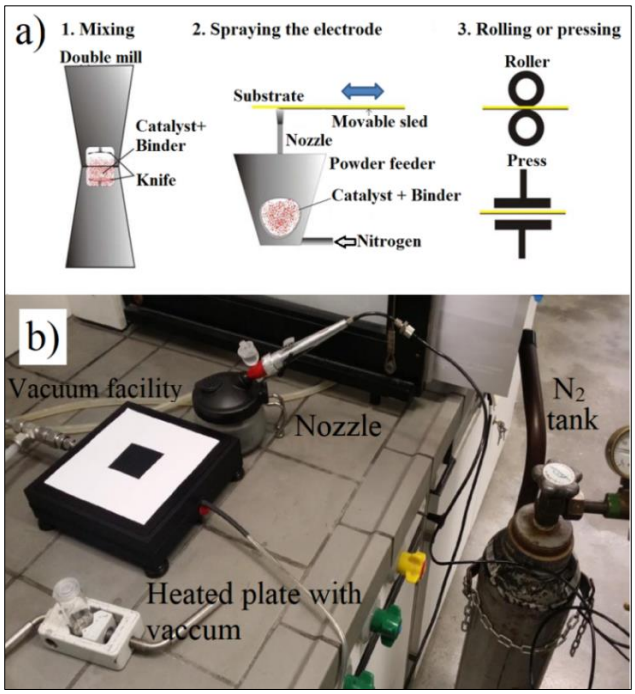

Figure 12: a) Schematic diagram of dry spraying method with solid powder (article II), b) image attributed to an experimental setup of airbrush coating technique (article I, III).

3.1.3 Screen printing method: In the screen printing coating technique the catalyst suspension is applied to the GDL or membrane through a mesh or screen. This also has a suction facility to fix the substrate. The viscous catalyst suspension is pushed over the screen, which is placed over substrate, and consequently the ink is coated on the substrate through the screen. The screen or the mesh is the crucial factor to control the thickness of the CL and the distribution of the coating. Fig. 13 a) shows an image of an automatic screen printing device.

3.1.4 Drop casting method: Drop casting is a very rudimentary way of coating a catalyst layer. The catalyst ink is prepared as suspension and loaded in a micropipette. The ink is then disposed dropwise from the micropipette, and being deposited on the

substrate. It is a very fast fabrication method to produce MEA with small active area. Fig. 13 b) shows a schematic diagram of drop casting. This technique is not very efficient to make a catalyst layer with bigger active area.

3.1.5 Doctor blade method: In this coating process carbon supported Pt catalyst suspension is coated on the membrane or GDL by doctor blading technique. It is a metering blade drawn across the surface of the substrate with viscous catalyst ink suspension. The thickness of the layer can be optimized by controlling the height of the blade, which is scaled precisely. Doctor blade is also a widely used and fast MEA fabrication technique. Fig. 13 c) displays a table (left) used for doctor blading with suction as well as heating facility, and the doctor-blade (right), which can be adjusted.

3.1.6 Ink-jet printing method: Inkjet printing is a sophisticated deposition technique to fabricate PEM fuel cell electrodes. It is a high resolution piezoelectric printer that is operated based on an on demand continuous ink jetting, and one is represented in fig. 13 d). Inkjet printer can achieve thicknesses and Pt loadings as low as 1.5 μm and 0.025 mg cm^{-2} respectively. The type of solvent, ion concentration and pH dictate the ink stability as well as the size of particle aggregate, which in turn will decide the applicability, jetting efficiency and performance of the ink [91].

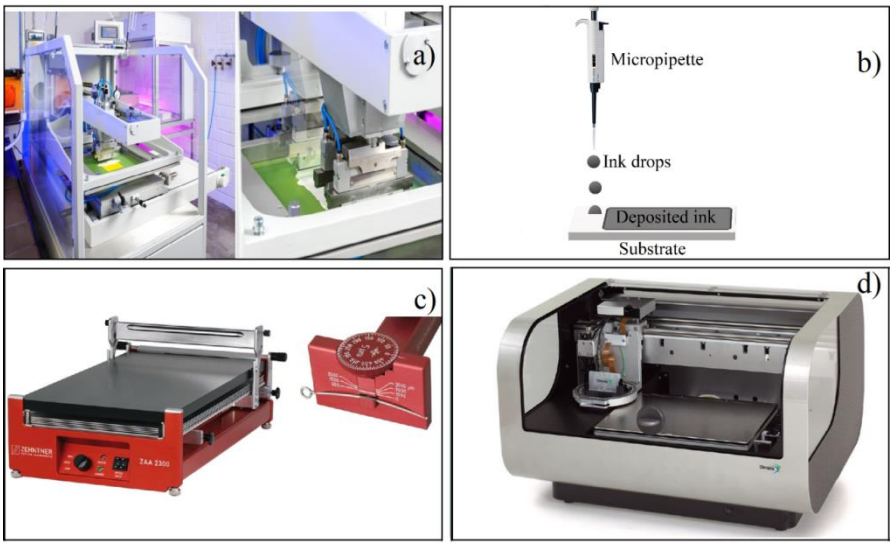

Figure 13: Images of suspension coating techniques a) Screen printing (article I, IV, V), b) drop casting (article I), c) doctor blading (article I), d) inkjet printing (article I).

3.2 Numerical Modelling: paradigm and assumptions

In order to determine the performance and electrochemical behavior of a PEMFC, a fuel cell test station with control of all relevant parameters including the possibility of applying EIS is necessary. The experimental procedure requires a lot of equipment and installation including storage place, supply gas, heater, humidifier, sensor and computerized data acquisition. The complete procedure is expensive, and a person requires proper training as well as resources to get familiar with the procedure that makes it a time consuming job as well. On the contrary, numerical modelling provides a platform to gain predictive capability to design and optimize a fuel cell without literally constructing or testing it. Consequently, numerical process reduces the cost and associated time with many trials necessary for empirical optimization of the cell. Additionally, it is not required for a person to have extensive laboratory training and resources to physically characterize the fuel cell. Admitting that also detailed simulations are time consuming, the associated expense is only the computational resources. Moreover, a validated as well as verified numerical model can be applied to determine a broad range of distinctive designs without any supplementary cost of software and hardware. Therefore, it is evident that, applying numerical models and simulation in the PEMFC research is a very advantageous method of characterization.
The numerical model, which has been used to conduct the research work, is an in-house model constructed within the NEOPARD-X framework developed by Futter et al. [92]. NEOPARD-X stands for **N**umerical **E**nvironment for the **O**ptimization of **P**erformance **A**nd **R**eduction of **D**egradation of **X**, where **X** represents an electrochemical energy conversion device. The framework is based on Dune as well as on DUMU^{X}. Furthermore, Dune PDE-Lab, UG, Multidomain, Multidomaingrid and SuperLU are required as well. Explaining the description of this framework is beyond the scope of this research work, but interested reader may obtain the detailed information in an review [92]. The model was applied in my thesis to the structural and transport properties of the developed electrodes.

3.2.1 Model Assumptions

The schematic of the working process is demonstrated in fig. 14 and the following sections are giving a summary of the fundamentals of the model not implying that the

equations were derived in my work. The PEMFC model used in this research work is established on the following assumptions:

- The gas diffusion layers, catalyst layers, and membrane are considered homogeneous media with active transport properties.
- In the GCs as well as in the porous layers, identical transport processes such as convection, diffusion and capillary transport are considered.
- The fluid is assumed incompressible.
- In the porous domains, fluid phases are locally in chemical equilibrium.
- Porous electrodes and membrane hold a local chemical equilibrium at the interface.
- Local thermal equilibrium exists in the system.
- The inlet gases behave ideal.

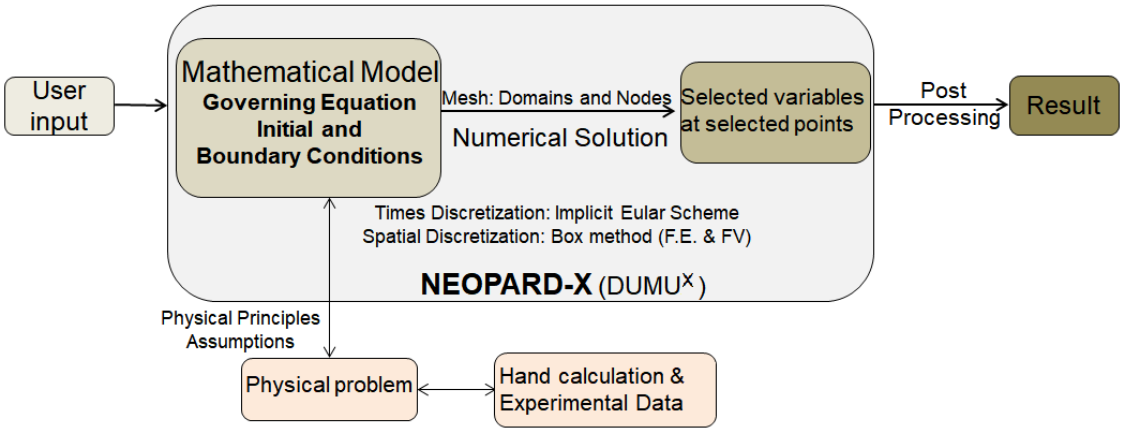

Figure 14: Schematic of our approach to the numerical modelling (article V)

3.2.2 Governing Equations

In fluid dynamics, the flow can be explained by mass, momentum, and energy balance equations. Considering finite control volume, the balance equations are derived using the transport theorem of Reynolds [93]. Let us consider that, *E* is an arbitrary property (e.g. mass, momentum, energy), which can be obtained by integrating the scalar quantity *e* moving with velocity *v* within a subdomain Ω,

$$E = \int_{\Omega} e \, d\Omega \tag{3.2.1}$$

For the change of *E* in the domain Ω over the time- interval *dt*,

$$\frac{dE}{dt} = \int_{\Omega} \frac{\partial e}{\partial t} d\Omega + \int_{\Gamma} e \, (v \times n) d\Gamma \tag{3.2.2}$$

when $\vec{n}$ serving as the unit normal vector of the boundary. Due to the conservation requirements, *E* can be changed due to the sink/ source in **Ω**. v is gas velocity.

$$\frac{dE}{dt} = \int_{\Omega} \frac{\partial e}{\partial t} d\Omega + \int_{\Gamma} e\,(v \times n) d\Gamma = \int_{\Omega} q^{e}\, d\Omega \qquad (3.2.3)$$

generally, the conservation equation can be presented as,

$$\frac{\partial \xi^{e}}{\partial t} + \nabla \times \Psi^{e} - q^{e} = 0 \qquad (3.2.4)$$

First term of the equation 3.2.4 represents the storage term, which is basically the temporal derivative of quantity *e*, the second term represents the partial derivative of the flux term where the operator ∇ represents the partial derivative in Cartesian coordinates and the last one stands for source and sink of quantity *e*.

Mass-Transport: According to our focus on mass transport, the governing equation can be written as follows by considering a FC system with M different phases and N components,

$$\xi^{\kappa} = \phi \sum_{\alpha=1}^{\mathrm{M}} (\rho_{mol,\alpha} x_{\alpha}^{\kappa} S_{\alpha}) \qquad (3.2.5)$$

Where $\rho_{mol,\alpha}$ represents the molar density of phase α, x_{α}^{κ} denotes the molar fraction of component κ of phase α, and S_{α} is the phase saturation.

$$\Psi^{\mathrm{K}} = -\sum_{\alpha=1}^{\mathrm{M}} (\rho_{mol,\alpha} x_{\alpha}^{\kappa} v_{\alpha} + d_{\alpha}^{\mathrm{K}}) \qquad (3.2.6)$$

Here d_{α}^{K} stands for the diffusive flux density of component κ in phase α, and v_{α} is the phase velocity, which can be estimated based on the multi-phase Darcy approach [94]:

$$v_{\alpha} = -\frac{k_{r\alpha}}{\mu_{\alpha}} K \nabla P_{\alpha} \qquad (3.2.7)$$

In the above equation, $k_{r\alpha}$ is the relative permeability of phase α, *K* denotes intrinsic permeability and P_{α} and μ_{α} represent pressure and mass specific internal energy of phase α respectively. Though the phase relative permeability is considered as $\kappa_{r\alpha} = s_{\alpha}^{2.5}$ for each of the porous layers, the exponent usually varies from 2-3 [95]. The relative permeability is considered equivalent to the phase saturation in case of the GCs.

Applying Leverett approach [96], considering S_{Ψ} is maximum heat flux (need not to be equal to unity) the capillary pressure P_c can be calculated as a function of liquid saturation, permeability, material wettability and porosity. For contact angels $\theta < 90°$

$$P_c = \sigma^{surface}\cos(\theta)\left(\frac{K}{\phi}\right)^{-\frac{1}{2}} \cdot [1.417(1-S_\Psi) - 2.12(1-S_\Psi)^2 + 1.263(1-S_\Psi)^3] \quad (3.2.8)$$

For contact angles θ > 90°:

$$P_c = \sigma^{surface}\cos(\theta)\left(\frac{K}{\phi}\right)^{-\frac{1}{2}} \cdot [1.417S_\Psi - 2.12{S_\Psi}^2 + 1.263{S_\Psi}^3] \quad (3.2.9)$$

The values 1.417, 2.12 and 1.263 are empirical constants. In both equations, $\sigma^{surface}$ stands for surface tension. For each of the porous layer, the capillary pressure saturation, porosity, intrinsic permeability, and the properties of wetting may differ. But the phase pressures must exhibit a local mechanical equilibrium at the interface between two layers to maintain continuity.

According to Stefan-Maxwell equation [97], the molar flux density ∇x_α can be calculated as:

$$\nabla x_\alpha = \sum_{j=1}^{N} \frac{C_\alpha^i C_\alpha^j}{C_\alpha^2 D_{eff,\alpha}^i}\left(\frac{d_\alpha^j}{C_\alpha^j} - \frac{d_\alpha^i}{C_\alpha^i}\right) \quad (3.2.10)$$

Where C_α^i and C_α^j are the molar concentration of species *i* and *j* in phase α, and consecutively d_α^i and d_α^j represent diffusive flux density of species *i* and *j* in phase α. $D_{eff,\alpha}^\kappa$ is the effective diffusion coefficient, which is determined based on binary diffusion coefficient, D_α^κ.

The diffusion coefficients in the porous medium can be written with the help of Bruggemann-correction as,

$$D_{pm,\alpha}^\kappa = (\phi S_\alpha)^{1.5} D_\alpha^\kappa \quad (3.2.11)$$

In case of the liquid phase,

$$D_{eff,l}^\kappa = D_{pm,l}^\kappa \quad (3.2.12)$$

In the gas phase, Knudsen diffusion occurs and $D_{eff,\alpha}^\kappa$ is calculated with a Bosanquet approximation due to the pore sizes of CLs and MPLs,

$$D_{eff,g}^\kappa = \left(\frac{1}{D_{pm,g}^\kappa} + \frac{1}{D_{Knudsen,g}^\kappa}\right)^{-1} \quad (3.2.13)$$

where, $$D_{Knudsen,g}^\kappa = r_{pore}\frac{2}{3}\sqrt{\frac{8RT}{\pi M^\kappa}} \quad (3.2.14)$$

Here, $D^{\kappa}_{Knudsen,g}$ represents Knudsen diffusion coefficient of component κ in the gaseous phase, M^{κ} denotes molar mass of component κ and R, T and r_{pore} express ideal gas constant, temperature and pore radius respectively.

Water management is a critical issue for PEMFC. At higher current density, there will be some contribution from liquid water in certain locations across the modeling domain, and consecutively this effects strongly to the numerical efficiency [98]. To get a numerical approach which may be helpful to handle the above mentioned problem [98], the Karush-Kuhn-Tucker (KKT) can be reformulated as nonlinear complimentary problem (NCP) combined with the balance equations (3.2.5 and 3.2.6) to hold a local phase equilibrium in between gas and liquid phase inside the PEMFC. There might be two cases, where in one case, a certain phase is missing, and in other case a certain phase is present. For the first case, where the certain phase is missing, the saturation must be zero.

$$\forall \alpha : S_{\alpha} = 0 \rightarrow \sum_{\kappa=1}^{N} x_{\alpha}^{\kappa} \leq 1 \tag{3.2.15}$$

Though the saturation is zero, the summation of all molar fractions of that certain phase might be smaller than unity as well. For the second case, the saturation must be larger than zero as well as the summation of all molar fractions yields unity.

$$\forall \alpha : \sum_{\kappa=1}^{N} x_{\alpha}^{\kappa} = 1 \rightarrow S_{\alpha} > 0 \tag{3.2.16}$$

From equations (3.2.15) and (3.2.16), the expression can be formulated as:

$$\forall \alpha : S_{\alpha} \left(1 - \sum_{\kappa=1}^{N} x_{\alpha}^{\kappa}\right) = 0 \tag{3.2.17}$$

By considering the solution as a nonlinear complementary function f^{NCP},

$$f^{NCP}(a, b) = \min\{ S_{\alpha}, 1 - \sum_{\kappa=1}^{N} x_{\alpha}^{\kappa} \} \tag{3.2.18}$$

To fulfill $f^{NCP}(a, b) = 0$, condition $a \geq 0 \wedge b \geq 0 \wedge a.b = 0$ is used. The source and sink term for mass transport can be written as:

$$q^{\kappa} = \pm \frac{r^{i}}{nF} \tag{3.2.19}$$

The calculated value depends either on production or consumption of the species. Here r^{i} represents the volumetric reactions rate of reaction *i* (HOR or ORR).

Charge-Transport: Applying Ohm's law, proton transportation can be described in the catalyst layers. Though electrical double layers are being used to store protons, the storage term can be written as:

$$\xi^{H^+} = -C_{DL}(\Phi_{elec} - \Phi_{ion}) \quad (3.2.20)$$

Where C_{DL} is the double layer capacitance, Φ_{elec} and Φ_{ion} represent electrode potential and ionic potential respectively.

The flux term is, $\Psi^{H^+} = -\sigma_{eff}^{H^+} \nabla \Phi_{ion}$ (3.2.21)

Though the only driving force is the ionic potential, the water activity plays a vital role in proton conductivity. A material-dependent empirical relation has been implemented to evaluate the influence of water activity on proton transport. Here, the water activity range has been divided into two domains by a separating the value $a_{trans}^{H_2O}$. Different exponential relations have been implemented for each of the two domains by maintaining a continuity of the function for $a^{H_2O} = a_{trans}^{H_2O}$ [99]:

$$f_1(a^{H_2O}) = A \cdot \exp(B a^{H_2O}) \quad (3.2.22)$$

$$f_2(a^{H_2O}) = A \cdot \exp\left[(B - C)\, a_{trans}^{H_2O}\right] \exp\left(C a^{H_2O}\right) \quad (3.2.23)$$

$$\sigma_{eff,CL}^{H^+} = \min(f_1, f_2) \quad (3.2.24)$$

Here, *A* is the amount of conductivity in the catalyst layer as well as prefactor, and other two parameters *B* and *C* are fitting parameters. Except PEM, electron transfers through all the porous layers of the fuel cell. Alike protons, the electrical double layers may be used to store electrons also. So equation (3.20) can be used to describe both of discharging and charging of the double layers. The flux term can be described by using Ohm's law as:

$$\Psi^{e^-} = \sigma_{eff}^{e^-} \nabla \Phi_{elec} \quad (3.2.25)$$

Unlike proton transport, gradient of electrode potential is the only driving force here. The source and sink terms for charge transport can be directly expressed as the volumetric reaction rate of hydrogen oxidation reaction (HOR) or oxygen reduction reaction (ORR):

$$q^{H^+} = r^{HOR} = \frac{P^{H_2}}{P_{ref}^{H_2}} ECSA_{Anode} i^{0,HOR} \cdot \left[exp\left(\frac{\alpha^f n F \eta^{HOR}}{R T}\right) - exp\left(-\frac{\alpha^r n F \eta^{HOR}}{R T}\right)\right] \quad (3.2.26)$$

Where $$ECSA = \frac{\epsilon\, 3 m_{pt}}{r_{pt}\, \rho_{pt}\, d_{CL}} \quad (3.2.27)$$

Here, m_{pt} is the mass of loading, r_{pt} is the average radius, $\rho_{pt}$is the density of Pt, and d_{CL} is the thickness of the electrode

and $q^{e^-} = r^{ORR} = \frac{-R\kappa^{ORR} + \sqrt{4ECSA_{eff}^2\, n^2\, F^2\, c_g^{O_2} + R^2(\kappa^{ORR})^2}}{2n\, F\, ECSA_{eff}}\, \kappa^{ORR}$ (3.2.28)

Where $ECSA_{eff} = (1 - \theta^{Ptox})\, EC$(when θ^{Ptox} is oxide coverage) (3.2.29)

and $$k^{ORR} = \begin{cases} high\ voltage\ regime: \\ ECSA_{eff} i_{high}^{0,ORR} \left(c_{g,ref}^{O_2}\right)^{-\frac{1}{2}} \\ \cdot \left[exp\left(\frac{\alpha_{high}^{f} nF\eta^{ORR}}{RT}\right) - exp\left(\frac{-\alpha_{high}^{r} nF\eta^{ORR}}{RT}\right)\right] \\ low\ voltage\ regime: \\ ECSA_{eff} i_{low}^{0,ORR} \left(c_{g,ref}^{O_2}\right)^{-\frac{1}{2}} \\ \cdot \left[exp\left(\frac{\alpha_{low}^{f} nF\eta^{ORR}}{RT}\right) - exp\left(\frac{-\alpha_{low}^{r} nF\eta^{ORR}}{RT}\right)\right] \end{cases} \quad (3.2.30)$$

Comparing with transition overpotential, two voltage regimes have been defined by $\eta_{trans}^{ORR} = 0.76\ V$:

If $\Phi_{elec} - \Phi_{ion} \geq \eta_{trans}^{ORR}$ => high voltage regime

If $\Phi_{elec} - \Phi_{ion} < \eta_{trans}^{ORR}$ => low voltage regime

The model calculates the oxygen transport resistance, through the ionomer film, as the combined effects of the resistance due to the oxygen diffusion through the ionomer film and the interfacial resistance.

$$R = R_{diff} + R_{int} \quad (3.2.31)$$

where, diffusion resistance: $R_{diff} = \frac{\delta_{ion}}{D_{ion}^{O_2}}$ (3.2.32)

and interfacial resistance: $R_{int} = B\ \exp(Ca^{H_2O})$ (3.2.33)

Here, *B* and *C* are fitting parameters describing the relative humidity dependence of the resistance and δ_{ion} is the thickness of the ionomer film.

The effective diffusion coefficient for oxygen in Nafion® is calculated as [100]:

$$D_{ion}^{O_2} = 4.38 \times 10^{-6} \exp\left(\frac{-2.5 \times 10^4}{RT}\right) \quad (3.2.34)$$

4 Materials and Characterization Techniques

4.1 Chemicals and devices:

Materials used in this thesis work are mentioned in the following table.

Material	Specification	Supplier	Function	Used in Article
Nafion® XL	27.94 µm thick	Ionpower (DuPont)	Membrane	I, II, III, IV, V
Dispersion: Nafion® D521	≥0.92 meqg^{-1} 5 wt% (Alcohol-water)	Ionpower (DuPont)	Catalyst binder	I, II, III, IV, V
Nafion® D1021	10 wt% (Aqueous)	Sigma Aldrich Ionpower (DuPont)	Catlalyst binder	IV, V
Aquivion® membrane	Eq wt. 790 geq^{-1}, 11 µm	Solvay, (non-commercial)	Membrane	III
Aquivion® dispersion	Eq wt. 833 geq^{-1} (Aqueous)	Solvay, (non-commercial)	Catalyst binder	III
Gas diffusion Layer	With microporous Layer	SGL Carbon GmbH	Diffusion media	I, II, III, IV, V
Gasket	1. PTFE 206 µm 2. Iceqube 35 FC-PO	1. Bohlender 2. Quintech/ Freunderberg	Sealing	I II, III, IV, V
Bipolar Plate	Graphite Gold plated SS	Electrochem DLR	Cell component	I, II,V III,IV,V
Screen	Polyster mesh FL-190 5-10 µm and 12-15 µm	Koenen	Screen printing	IV, V
Pt/ C catalyst	40wt % Pt over Vulcun Xc72	Johnson Mathey	Electro-catalyst	I, II, III, IV, V
Ultra-pure water	HPLC garde	Alfa Aesar	Solvent	I, II, III, IV, V
Isopropyl Alcohol	99.9 %	VWR	Solvent	I, II, III, IV, V
Cyclohexanol	99 %	Alfa Aesar	Solvent	IV, V

Glycerol	99 %	Alfa Aesar	Solvent	IV
Air	99.9 %	DLR compressor	Oxidant	I, II, III, IV, V
H_2, N_2	99.5 %	VWR	Reactant and Purging gas	I, II, III, IV, V

Table 2: Information about the chemicals used in this dissertation

Device	Function	Supplier	Article
Bath sonication **Probe sonication**	Mixing	Elma 50/60 Hz Hielscher UP 200S 40 Hz	I, II, III, IV,V IV,V
Cryogenic Mill	Pulverizing	6850 Freeze mill, Spex Certipep	I, II
Hot press	MEA fabrication	Vogt	I, II, III
Screen printer	Coating	Aurel 9000	I, IV, V
Ball mill	Mixing	Fritsch, Pulverisette 7	IV, V
Plastic air spray gun	Coating	Herpa	I, III

Table 3: List of the devices used in this research to prepare MEAs

MEAs were dried according to the individual studies in the following drying methods. Three types of drying methods have been applied, and fig. 15 shows the dryers used in the laboratory.

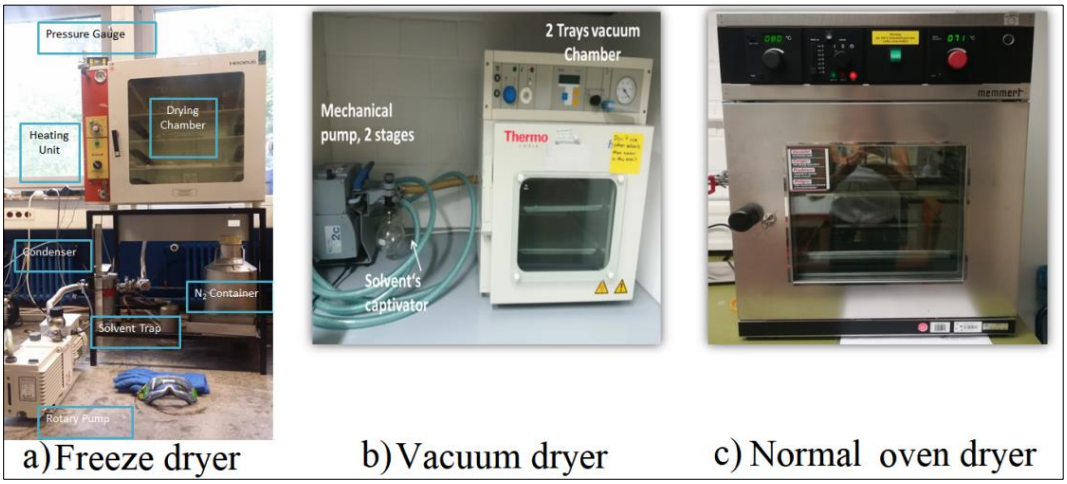

Figure 15: Images of a) freeze dryer (article IV, V), b) vacuum dryer (article IV,V), c) oven dryer (article I, II, III, IV, V)

4.2 MEA Formulation and Operating Conditions

MEAs used in article I, II, III were hot pressed according to the fig. 16 a) in the hot press device shown in fig 16. b) at 165 °C and 700 N cm^{-2} for 5 minutes.

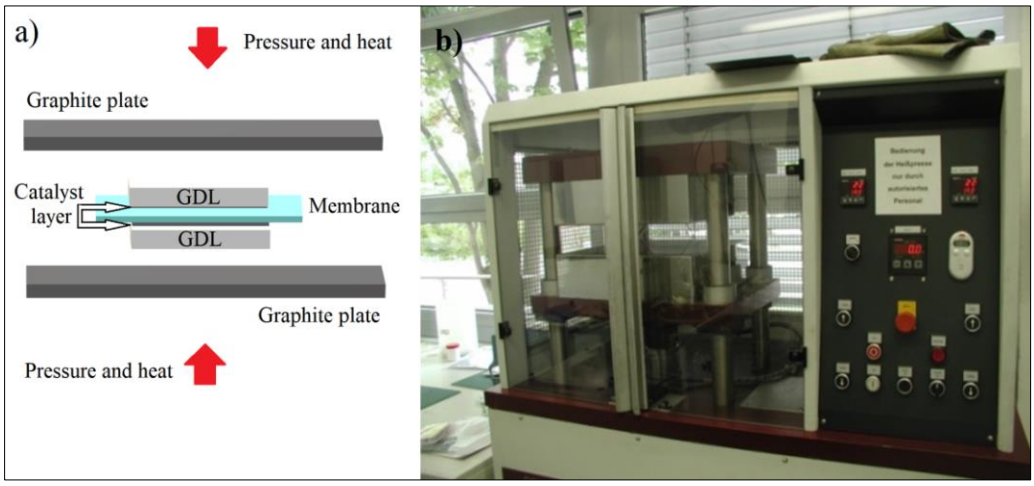

Figure 16: a) Orientation of hot pressing, b) the hot press device (article I, II, III)

All the MEAs were tested in the in-house built test benches by DLR. Two test facilities: 1 cm^2 active area (article I, II, III) and 25 cm^2 active area (article III, IV, V) cells were used to electrochemically characterize the MEAs. The test benches, controlled by programmable logic controller (PLC), allow automatic control of the input and output conditions, such as the pressure, temperature, flow rate of gases, and humidity of reactants. Humidification was controlled by the associated humidifier in the test facilities. Heating unit, sensors and mass flow controller were used to control the operating conditions and stoichiometry, which are mentioned in details in the concerning articles. The smaller active area test bench has anode and cathode flow 25 ml min^{-1} and 75 ml min^{-1} respectively, whereas bigger active area test bench has anode and cathode flow 500 ml min^{-1} and 2000 ml min^{-1}. Load capacity of the test benches are 3A and 50 A respectively. The operating temperature was 80 ºC and the gas outlet pressure was kept constant at 1.5 bar (absolute). Relative humidity and stoichiometric flow has been changed according to the requirement of the study. Fig. 17 a) and b) shows the testing facilities and fig. 17 c) displays the potentiostat device which was operated to measure electrochemical impedance measurements.

4.3 Electrochemical Characterization

Polarization study

Polarization curves were performed with the load attached to the test bench which can be operated in either galvano-static or potentio-static mode. Before making polarization measurement, all the the MEAs were well conditioned (break-in procedure) in both potentiostatic and galvanostatic modes.

a) 1 cm^2 Test bench b) 25 cm^2 test bench c) Potentiostat

Figure 17: Test benches and the EIS device used in the scope of this study.

Impedance Evaluation

Electrochemical Impedance Spectroscopy was performed for all of the MEAs by a Zahner potentiostat (Zahner Zennium with PP241 load) and the Thales software. Nyquist and Bode plots were determined in three different current densities at 0.1, 0.5 and 1 A cm^{-2}, in the frequency range from 100 mHz to 100 KHz with appropriate amplitude. To ascertain a linear EIS measurement, the amplitude was chosen accordingly. Anode acts as a reference and counter electrode, but cathode acts as a working electrode. Nyquist plot is constructed with negative imaginary impedance in the Y axis and the real impedance in the X axis. On the other hand, the bode plot

consists three components: impedance with phase angel in the Y axis and the frequency in the X axis.

Ionic Impedance

The ionic impedance of the electrode was also evaluated with special EIS measurement. In order to characterize ionic impedance, very low but equal amount of hydrogen and nitrogen gas were fed into anode and cathode with 100% humidification. To avoid the contribution from ORR charge transfer, cathode compartment is purged with nitrogen during the measurement. Consequently, the charging of the catalyst's double layer against the ionic resistance of CL becomes dominating factor. Ionic impedance was measured in 1 V potentiostatic condition with 10 mV amplitude from 500 mHz to 100 KHz frequency. At high frequencies a Warburg-like response (45° slope) is observed, corresponding to ion conductivity in the catalyst layer. At low frequencies, the impedance plot curves up to a limiting capacitance response (vertical) which corresponds to the total capacitance and resistance of the catalyst layer. The ionic resistance, R_{ionic}, can be obtained from the length of the Warburg-like region projected onto the real impedance (Z') axis (= $R_{ionic}/3$) with the help of transmission line model.

Cyclic Voltammetry

Cyclic voltammograms (CVs) were obtained at 1.5 bar pressure with 20 mV s^{-1} slew rate between 60 mV to 1 V to measure the electrochemical active surface area for each of the cathodes. To measure cathode CV, minimum but equal amount of H_2 and N_2 gas are fed with 100 % humidification. The cathode side of the MEA is triggered by a sweep of voltage (0 to 1 V) where the coulombic charge for hydrogen adsorption is used to calculate the active surface area of platinum considering the charge needed to adsorb a monolayer of adsorbed H^+ on polycrystalline platinum. Thereupon it is possible to obtain the electrochemical surface area (ECSA) of the cathode through the following equation:

$$\mathrm{ECSA} = \frac{q_{Pt}}{\Gamma \cdot L} \qquad (4.3.1)$$

Where q_{Pt} refers to the hydrogen adsorption charge density retrieved from each CV; Γ is equal to 210 $\mu C \cdot cm^{-2}_{Pt}$ and represents the charge required to reduce a monolayer of protons on Pt. Finally, L represents the Pt loading in the electrode. Pt utilization was

calculated from the ratio between the ECSA and the theoretical surface area (TSA) of the catalyst provided by the catalyst supplier. TSA is calculated as follows:

$$TSA = \frac{6}{(\rho \cdot d)} \qquad (4.3.2)$$

Where ρ is the density of platinum (21.4×10^6 g m^{-3}), d is the mean diameter of the Pt particle provided from the supplier (4.5 nm).

Linear Sweep Voltammetry

At the scan rate of 2 mV s^{-1}, the working electrode is scanned against linear voltage change with respect to the counter or reference electrode. In order to determine the hydrogen crossover, also to identify the existence of pinhole or short circuits across the cell, the output of the working electrode current vs. voltage is used. During the whole process, nitrogen is supplied at the cathode side until the OCV used to be stable around 80 mV.

Segmented board

The locally resolved current density measurements were performed with the 25 cm^2 cell using DLR's segmented bipolar plate (SC) based on printed circuit board (PCB) technology with integrated temperature sensors. This device allows us to gain insight into the heterogeneity of current distribution in the cell. Especially, this technique is very useful for identifying local degradation processess. The study of local processes, which are influenced by heterogeneous water management, can be also measured successfully.

4.4 Physical Characterization

Scanning Electron Microscopy (SEM)

To observe the cross section of MEAs with scanning electron microscopy (SEM), specimens were prepared by cutting a 1×1 cm^2 from MEAs. After placing the sample inside the SEM sample holder, the fractures were made by emerging the sample into liquid Nitrogen. The measurement was carried out in a Zeiss UltraPlus, providing an electron beam range of 2.0 to 10 kV that allows the analysis of the surface and cross section of the different MEAs. Combined with SEM measurements, an energy dispersive x-ray spectroscopy (EDX) peltier cooled Si (Li) detector allowed the quantification of the chemical elements.

Porosimetry analysis

BET: Brunauer–Emmett–Teller (BET) measurements were performed using the Dollimore/Heal method for surface area determination of the approached catalyst powders. The samples are dried here, under vacuum conditions at 60 °C for 3 h, with liquid nitrogen and positioned inside a Sorptomanic 1195 chamber.

MIP: To determine the pore size distribution of the catalyst composite mercury intrusion porosimetry (MIP) has been performed at 25 °C. This porosimetric characterization is based on the properties of non-wetting liquids inside capillaries. An optimum pressurized chamber is applied to stimulate penetration of mercury into the pores of the sample.

Atomic force microscopy (AFM)

Atomic force microscopy is a device which can characterize the topography, deformation and conductivity of a surface with tapping method. Unlike SEM, the greatest advantage of this technique is, AFM is capable of detecting the ionomer distribution of surface without destroying the thin ionomer film with electric beam. A Multimode 8 AFM (Bruker, Karlsruhe) device was used as AFM. Conductive adhesive tape was used to glue the MEAs samples over an AFM steel disc and to electrically connect the surface of the sample. Platinum/iridium coated AFM tips (NCHStPt, Nanoworld) were used in tapping mode with additional recorded current that gets averaged by a lock-in amplifier (PF-TUNA, Bruker). The 9 μm^2 measurements were

recorded with 768 x 768 pixels at a scan rate of 0.326 Hz. Images with 4 μm² were cropped out of the measured areas.

Thermogravimetric Analysis

After obtaining completely dried electrodes, both GDEs and CCMs were weighted for Pt loading calculation purposes. To determine the precise Pt loading of the CCM samples, thermogravimetric analysis (TGA) of catalyst-coated membranes was performed with a thermal gravimetric analyzer (NETZSCH STA 449 C) and a DSC/TG platinum pan; the samples were heated from room temperature to 1100 °C with a heating rate of 1 K min^{-1} under air atmosphere.

X-ray photoelectron spectroscopy (XPS)

For x-ray photoelectron spectroscopy (XPS) characterization, photoemission spectra were recorded using a hemispherical electron energy analyzer in an ultrahigh vacuum chamber of a base pressure of 4.10^{-10} mbar (Thermo Scientific ESCALAB250). The fresh GDE was measured first, and then the gas diffusion layer (GDL) was delaminated by hand from the operated active layer to access the interface between catalyst layer (CL) and microporous layer (MPL) in addition to the GDL backing surface. Only samples with no apparent material transfer from the detached component were analyzed.

Focus Ion Beam Scanning Electron Microscopy (FIBSEM)

Samples were cut into squares of size 1 × 1 cm^2 from the CCM or MEA, and in case of MEA gas diffusion layer has been delaminated manually. After placing the sample inside the SEM sample holder, the fracture was made by emerging the sample in liquid nitrogen. The measurements were carried out in 1.5 KV EHT with a 30 KV FIB probe. By 20×20μm cut area with standard image resolution 1024×720 pixel The Thickness of each cut is 150 nm. The FIB-SEM images were taken with a Zeiss Scanning Electron Microscope (Neon 40 ESB Crossbeam).

Infrared spectroscopy (IR)

Infrared spectroscopy has been performed to characterize the bonding of the ionomer from 0 to 4000 wavenumber cm^{-1} with Bruker Hyperion 306 (Vertex 80 V).

4.5 Boundary Condition and Discretization of Model

4.5.1 Initial and Boundary Conditions

Based on our model assumptions these following parameters hold continuity at the interface: flux density, primary variables, protonic current density, ionic potential, species partial pressure, energy fluxes and temperature.

Initial conditions:

The primary conditions for anode, cathode and interfaces are given in the table below:

Initial variable	Anode	PEM/Anode	Cathode/ PEM	Cathode
P_g	$P_{g,out,anode}$	-	-	$P_{g,out,cathode}$
S_l	0	-	-	0
$x_g^{H_2O}$	$RH_{anode}P_{sat}^{H_2O}/P_g$	-	-	$RH_{cathode}P_{sat}^{H_2O}/P_g$
$x_g^{O_2}$	0	-	-	$0.21\left(1-x_{g,cathode}^{H_2O}\right)$
$x_g^{N_2}$	-	-	-	$0.79\left(1-x_{g,cathode}^{H_2O}\right)$
$x_g^{H_2}$	$1-x_{g,anode}^{H_2O}$	-	-	0
T	T_{init}	T_{init}	T_{init}	T_{init}
Φ_{ion}	0	0	0	0
Φ_{elec}	0	-	-	$\Phi_{elec,init}$
μ^{H_2O}	-	$RTln(P_{g,anode}^{H_2O}/P_{sat}^{H_2O})$	$RTln(P_{g,cathode}^{H_2O}/P_{sat}^{H_2O})$	-
P^{H_2}	-	$x_g^{H_2}P_{g,anode}$	$x_g^{H_2}P_{g,cathode}$	-
P^{O_2}	-	$x_g^{O_2}P_{g,anode}$	$x_g^{O_2}P_{g,cathode}$	-

Table 4: Initial conditions at the interfaces between electrolyte and electrodes.

Boundary conditions:

Boundary conditions were actuated at the inlet-outlet and current collectors of the simulation. For the conservation equation of the molar flux densities of H_2 and O_2 at the inlets, Neumann condition is considered, and Faraday's law is used to determine the values. Here λ is denoted as conductivity.

$$\Psi^{\kappa} = \frac{\lambda^{flux,\kappa_I}}{nFA_{inlet}} n \qquad (4.5.1)$$

If the integrated cell-current is less than a provided minimum value, then the formulation will be as follows:

$$\Psi^{\kappa} = \frac{\lambda^{flux,\kappa}\max(I_{min},I)}{nFA_{inlet}} n \qquad (4.5.2)$$

Dirichlet condition is stated to specify the mole fraction of all remaining values of mass balances from the sub-domain. Other boundary conditions at the inlet are:

$T = T_{inlet}$

$i_{ion} = 0$

$i_{elec} = 0$

$S_l = 0$

In case of outlet, all mass conservative equations are set as outflow boundary-conditions except the equation of the gradients. The gradients required to be constant across the boundary to implement the outflow boundary-condition, which suggests diffusion may not occur in through-plane direction, and the phases have to be mixed properly. Adding the longer tubes at the outlets of the modeling domain helps to solve this issue. However, the length of these tubes should be selected in such a fashion that the phases mix accurately before reaching the outlet boundary. For the gas pressure, a Dirichlet boundary condition is fixed instead of the remaining mass balance equation. Other outflow boundary conditions are:

$P_g = P_{g,outlet}$

$T = T_{outlet}$

$i_{ion} = 0$

$i_{elec} = 0$

For the applied temperature, a Dirichlet condition is set for cathode and anode. The electrode potential of anode is:

$\Phi_{elec} = 0$

when the cell operation mode defines the boundary condition for the cathode. In potentiostatic approach, the Dirichlet condition is applied and the values are calculated as: Φ_{elec} = the cell voltage

Neumann condition is used for the galvanostatic mode where the electric current density is determined using the desired cell current density and the cell area in agreement with:

$$i_{elec} = \frac{I}{A_{cell} n} \qquad (4.5.3)$$

4.5.2 Discretization

There are two categories of systems, one is discrete system and another is continuous system. Discrete system consists of finite number of algebraic constitutive equations, whereas continuous system consists of differential equations. To exactly solve a differential equation, which fulfills all boundary conditions, a discrete idealization is required. Therefore, a continuous system is required to be reduced to a discrete system using different discretization methods such as finite volume method, finite element method, finite difference method, fully implicit Euler scheme or fully explicit Euler scheme.

Differential equation for a continuous system is valid for the whole domain. So the number of unknown variable is not known, therefore, each point needs to determined, which becomes an unknown function (Fig. 18 a).

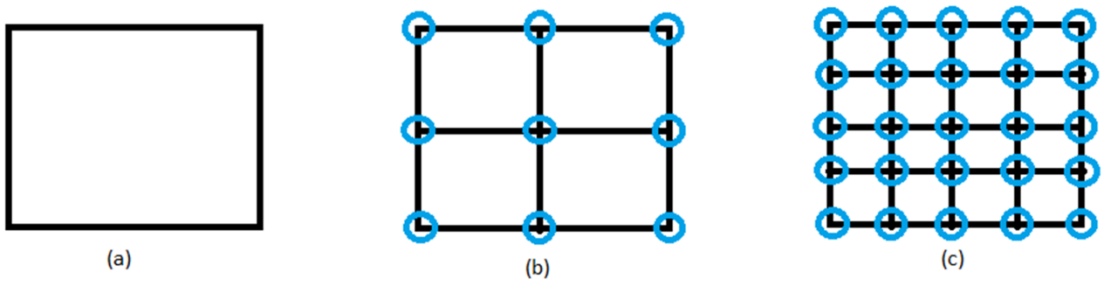

Figure 18: a) whole domain, b) discretized domain, and c) more refined (discretized) domain

Instead of determining the unknown variable at each point, the problem can be reduced to determine the unknown variable at selected locations (Fig. 18 b and c). The unknown variable at other locations can be determined using interpolation. Discretization makes the whole process more flexibility by giving a platform to determine a finite number values rather than a function.

The equations presented in previous section, required to be discretized according to time and space. Box method [101] has been chosen considering spatial discretization along with fully implicit Euler scheme for time discretization.

Box Method

Though the representation of the box method has been taken from the DuMu^X handbook, an interested individual is requested to go through to know more in details [102]. Schematic of spatial discretization of box method is provided in fig. 19.

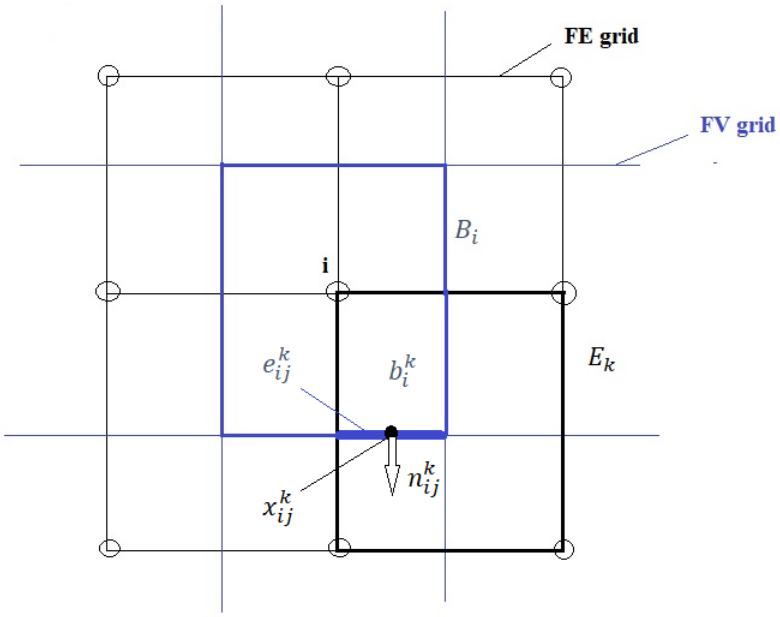

Figure 19: Schematic of spatial discretization of box method (reproduced from [102])

The box method couples the benefit of both of the finite-volume (FV) method as well as the finite-element (FE) method. Because of this combination, the method is locally mass conservative as well as allows application of unstructured grids. The whole domain, Ω, is primarily discretized by a finite-element grid consisting of node i with a corresponding elements E_k, and then a secondary finite-volume grid is constructed, which creates a box B_i by adding the midpoints and barycenters. The box B_i, around node i, is divided into four subcontrolvolumes (scv's) by finite-element grids, where the subcontrolvolumes are belong to the corresponding elements created by finite-element grids. e_{ij}^k is one of the subcontrolvolumefaces (scvf) between the scv's b_i^k and b_j^k , including it's length $|e_{ij}^k|$, which is required for the discretization. x_{ij}^k and n_{ij}^k represent the integration point on e_{ij}^k and the outer normal vector respectively.

Due to the combination of FE and FV, box method calculates the fluxes at the integration points using FE gradients as well as maintains a balance of fluxes beyond the scvf's with FV method.

The discrete form of the balance equation (equation 3.2.2), derived from Reynolds transport theorem, can be written as:

$$f(u) = \int_\Omega \frac{\partial u}{\partial t} d\Omega + \int_\Omega \nabla.\Psi \, d\Omega - \int_\Omega q \, d\Omega = 0 \qquad (4.5.4)$$

First term, $\int_\Omega \frac{\partial u}{\partial t} d\Omega$, represents the change of the unknown field u over time, second term, $\int_\Omega \nabla.\Psi \, d\Omega$, denotes the fluxes over the interfaces and the last one, $\int_\Omega q \, d\Omega$, is the source and sink term. At the integration point, an approximation $\tilde{u}(x_{ij}^k)$ of u is considered as:

$$\tilde{u}(x_{ij}^k) = \sum_i N_i(x_{ij}^k) \, . \, \hat{u}_i \qquad (4.5.5)$$

Where $N_i(x_{ij}^k)$ is the linear basis function and $\hat{u}_i$ represents the nodal value.

And the gradient of $\tilde{u}(x_{ij}^k)$,

$$\nabla\tilde{u}(x_{ij}^k) = \sum_i \nabla N_i(x_{ij}^k) \, . \, \hat{u}_i \qquad (4.5.6)$$

At each scvf, the expression will result as:

$$f\left(\tilde{u}(x_{ij}^k)\right) . \, n_{ij}^k \, . \, |e_{ij}^k| \qquad (4.5.7)$$

Here, $f\left(\tilde{u}(x_{ij}^k)\right)$, n_{ij}^k and $|e_{ij}^k|$ represent flux due to the gradient of $\tilde{u}(x_{ij}^k)$, outer normal vector and length of the scvf respectively.

Due to the approximation of *u*, equation (4.4) does not fulfill exactly and a residual ϵ is produced.

$$f(\tilde{u}) = \epsilon \neq 0 \qquad (4.5.8)$$

Like FE method, the box method follows the principle of weighted residuals. Implying the principle of weighted residuals:

$$\int_\Omega w_j \epsilon \, d\Omega \stackrel{!}{=} 0 \qquad \text{with } \sum_j w_j = 1 \qquad (4.5.9)$$

Where w_j is a weighting function.

Implementing equation (4.5.9) into equation (4.5.4) yields:

$$\int_\Omega w_j \frac{\partial \tilde{u}}{\partial t} d\Omega + \int_\Omega w_j [\nabla.\Psi(\tilde{u}) \, d\Omega] - \int_\Omega w_j q \, d\Omega = \int_\Omega w_j \epsilon \, d\Omega \stackrel{!}{=} 0 \qquad (4.5.10)$$

The first term of the above equation, $\int_\Omega w_j \frac{\partial \tilde{u}}{\partial t} d\Omega$, can be rewritten as:

$$\int_\Omega w_j \frac{\partial \tilde{u}}{\partial t} d\Omega = \int_{B_i} \frac{\partial \tilde{u}}{\partial t}\, d\Omega = \frac{d}{dt} \int_{B_i} \sum_i \hat{u}_i N_i \, d\Omega = \sum_i \frac{\partial \hat{u}_i}{\partial t} \int_{B_i} N_i \, d\Omega \quad (4.5.11)$$

After implementing the Green-Gauss theorem and product rule, the second term of equation (4.5.10) results as:

$$\int_\Omega w_j [\nabla . \Psi(\tilde{u})\, d\Omega] = \int_{\partial\Omega} \left[w_j \Psi(\tilde{u})\right] n \, d\Gamma_\Omega - \int_\Omega \nabla w_j \Psi(\tilde{u}) d\Omega \quad (4.5.12)$$

In box method, the weighting functions, w_j, are chosen as the piece-wise constant functions, i.e.

$$w_j(x) = \begin{cases} 1 \; x \in B_i \\ 0 \; x \notin B_i \end{cases} \quad (4.5.13)$$

Where B_i is the control volume box. Based on the assumption that, the storage capacity is reduced to the nodes, a mass lumping technique is applied to replace the integrals $M_{i,j}$ = $\int_{B_i} N_i \, d\Omega$ by the mass lumping term M_{ij}^{lump} as follows:

$$M_{ij}^{lump} = \begin{cases} \int_{B_i} w_j \, d\Omega = \int_{B_i} N_i \, d\Omega = V_i & if \;\; i = j \\ 0 & if \; i \neq j \end{cases} \quad (4.5.14)$$

Where V_i denotes the volume of box B_i.

Putting all the values in equation (4.5.10), we obtain:

$$\sum_i \frac{\partial \hat{u}_i}{\partial t} \int_{B_i} N_i \, d\Omega + \int_{\partial B_i} \Psi(\tilde{u}) \, . \, n \, d\Gamma_{B_i} - \int_{B_i} w_j q \, d\Omega \stackrel{!}{=} 0 \quad (4.5.15)$$

With w_j =1, the discrete form of equation (4.5.4):

$$V_i \frac{\partial \hat{u}_i}{\partial t} + \int_{\partial B_i} \Psi(\tilde{u}) n \, d\Gamma_{B_i} - V_i \, . \, q = 0 \quad (4.5.16)$$

4.5.3 Time Discretization

Stability is a basic requirement of the efficiency of a numerical solution. Therefore in transient problems, it is important to integrate every term of a differential equation over a time step to analysis the stability of the solution. For the time discretization, the mathematical model used an implicit Euler scheme.

Domain of dependence plays a vital role to make a solution more stable and the prerequisites are: it has to be finite as well as contains the boundary conditions completely. In case of an implicit method, both of the prerequisites are fulfilled automatically and therefore, the implicit solution is unconditionally stable. Implicit euler scheme is a first order scheme, which simplifies as:

$$\frac{\partial \hat{u}_i}{\partial t} = \frac{\hat{u}_i^{n+1} - \hat{u}_i^n}{t^{n+1} - t^n} = \frac{\hat{u}_i^{n+1} - \hat{u}_i^n}{\Delta t} \quad (4.5.17)$$

Where the length of the time step, Δt, is adaptive and n denotes the time level. To get the solution at t^{n+1}, equation (4.5.16) can be expressed as:

$$V_i \frac{\hat{u}_i^{n+1} - \hat{u}_i^n}{\Delta t} + \int_{\partial B_i} \Psi(\tilde{u}^{n+1}) n \, d\Gamma_{B_i} - V_i \cdot q^{n+1} = 0 \quad (4.5.18)$$

A heuristic time step estimator, which is based on the value of Newton iterations, is used to determine the time step size. In this process, expected number of iterations is set as well as tolerance limit is defined, and time step is determined using these values.

Parameter	Unit	Source	Spatial Parameter	Unit	Source
$d_{CL,cathode,FD}$= 14.58×10^{-6}	m	measured	K_{MPL}= 4.0×10^{-15}	m^2	fitted
$d_{CL,cathode,VD}$= 12.67×10^{-6}	m	measured	$\emptyset_{GDL}$= 0.62		estimated
$d_{CL,cathode,OD}$= 11×10^{-6}	m	measured	$\emptyset_{MPL}$= 0.75		fitted
			$\emptyset_{CL,FD}$= 0.24		estimated
ORR, i_{ref}^0= $1.0e^{-4}$	A m^{-2}	fitted	$\emptyset_{CL,VD}$= 0.21		estimated
			$\emptyset_{CL,OD}$= 0.18		estimated
$ECSAm_{Pt,anode}$ = $m_{Pt,cathode}$ = $3.5e^{-3}$	Kg m^{-2}	measured	$r_{pore,MPL}$= 45×10^{-9}	m	fitted
$ECSA_{FD}$= $7e^6$	$m^2\,m^{-3}$	measured	$r_{pore,CL}$= 2.5×10^{-8}	m	estimated
$ECSA_{VD}$= $5.6e^6$	$m^2\,m^{-3}$	measured	λ_{GDL}= 0.60	W $m^{-1}\,k^{-1}$	[103]
$ECSA_{OD}$= $5.25e^6$	$m^2\,m^{-3}$	measured	λ_{MPL}= 0.33	W $m^{-1}\,k^{-1}$	[104]
			λ_{CL}= 0.3	W $m^{-1}\,k^{-1}$	fitted

Table 5: Model parameters and spatial parameters used in the numerical method [92].

The applied model parameters for numerical simulation have been listed in table 5 and 6 after modification from the work of Futter et al.

Parameter	Unit	Source	Parameter	Unit	Source
Catalyst Layer Conductivity					
Freeze and vacuum drying			Oven drying		
A= 1.0× 10^{-2}	S m^{-1}	fitted	A= 0.80× 10^{-2}	S m^{-1}	fitted
B= 3.0		fitted	B= 3.0		fitted
C= 5.0		fitted	C= 5.0		fitted
Ionomer Film Model					
Freeze and vacuum drying			Oven drying		
A= 0.0	S m^{-1}	fitted	A= 0.0	S m^{-1}	fitted
B= 2.5×10^{5}	s m^{-1}	fitted	B= 2.2648×10^{4}	s m^{-1}	fitted
C= -5.0		fitted	C = -1.5		fitted

Table 6 : Model parameters used in the numerical method [92]

Detailed methods and the applied parameters of the simulation are addressed in the Article V (section 8.5).

5 Conclusion

5.1 General Conclusion

This cumulative doctoral thesis integrates an thorough investigation to design an efficient membrane electrode assembly for PEMFC application. In this work, selection of ionomer (in both electrode and electrolyte application), and the influence of catalyst layer fabrication technique along with the effect of drying technique have been taken into account. Therefore, the objective of this work is to select optimized materials, and to develop a feasible fabrication process for our system to make it accessible to the interested industry.

Increasing the platinum utilization to reduce the cost of MEA fabrication is one of the few challenges we accepted, and reported that this is significantly associated with the catalyst layer manufacturing approach. Article I of this cumulative dissertation encompasses the study concerning the influential parameters, which are involved in the catalyst layer fabrication process. Furthermore, the measures which should be taken care of also acknowledged in the primary study. It is really intriguing to speculate, to what degree a coating technique alone can decide the fate of the electrode by virtue of agglomerate formation, platinum utilization, ionomer distribution, porosity, tortuosity, permeability, diffusion co-efficient, etc.

In Article II the improved procedure for catalyst powder preparation for the coating techniques named “dry spray”, which was invented at DLR, has been reported. Application of dry Nafion® powder was the limitation to produce electrode with smaller aggregates and homogenous ionomer distribution. Incorporating the liquid ionomer dispersion with the catalyst, and cryo-milling it afterwards to prepare dry powder

unfolds the new opportunity to partially coat the catalyst aggregates with thin film of ionomer, which contributes to a better outcome.

Article III elucidates the influence of the side chain length of ionomer on short and long-term application. This particular study demonstrates a comprehensive analogy between Aquivion® (short side chain) and Nafion® (long side chain) both as membrane and catalyst additives in the CL layer. Experimental data shows, thin membrane has the tendency to degrade faster due to higher crossover and vigorous mechanical stress. In addition, the short side chain ionomer has better proton conductivity and performance for the short term application. However, due to abundant weaker CO- bond, and less fluorine content compared to its alternative, electrodes prepared with Aquivion® deteriorates faster.

Eventually, Article IV of this thesis work investigated the influence of the drying step of the CL manufacturing process on CL structure and PEMFC operation, which has not fully received attention from the PEMFC community yet. We have encountered a significant influence of drying mechanism on the CL preparation derived from suspension coating techniques. Freeze drying or lyophilisation not only provides higher porosity and surface area into the CL, but also improves the ionomer distribution through the CL. Reduced pore electrolyte resistance and enhanced diffusion capacity due to porous architecture result in higher performance with declined mass transport limitation. Additionally, in Article V, a numerical approach with a “transient 2D physical model for single cell” has been executed to simulate this phenomenon. The simulation yields a very good agreement with the experimental results, and the fit accurately explains how the improved oxygen transport behaviour triggers the performance. Optimizing the thickness of ionomer film by specific drying method and increasing the CL thickness by improving its porosity can negate the limitations in the transport of oxygen through the ionomer. Even though increased porosity, thicker electrode and very thin ionomer film hamper the charge transfer, higher permeability and diffusibility of oxidant in the reacting interface counterbalance the adverse effect.

This is reasonable to presume that there are still many scopes for further investigation, which were not addressed in this work but important to CL manufacturing. However, gathering all the information from the literature and the laboratory experience regarding MEA fabrication, following improvements are possible to design a low platinum loaded

MEA with higher performance and durability. A combined schematic of the studies is illustrated in fig. 20.

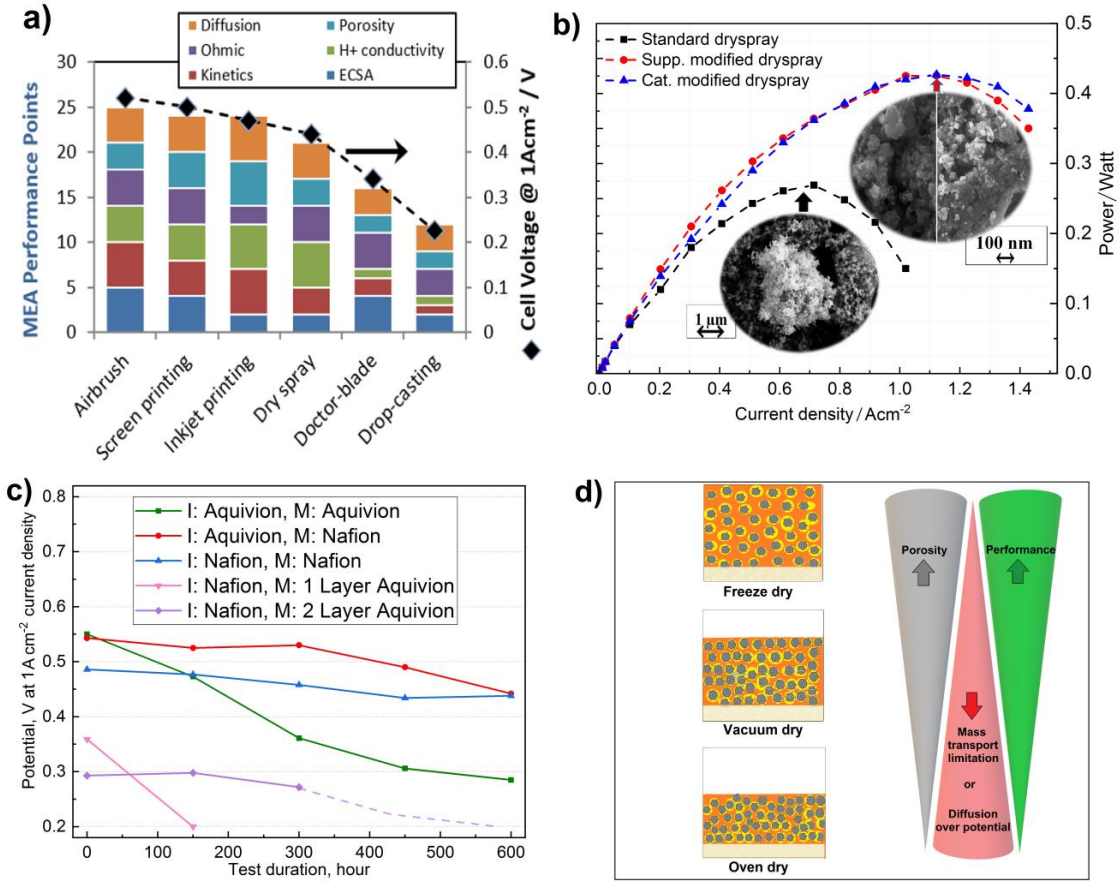

Figure 20: A synoptic illustration attributed to the findings of this dissertation; a) Article I: distribution of MEA performance limitation factors associated to differently prepared MEAs, b) Article II: improvement of dry spray technology by applying liquid ionomer dispersion, c) Article III: performance of ionomer with different side chain length with function of time, d) Article IV, V: improvement of electrode preparation by adapting freeze drying techniques.

Fig. 20 a) demonstrates the distribution of MEA performance points attributed to different coating methods along with their individual voltage values at 1 A cm^{-2}. With this MEA performance point, the individual limiting factors of the CLs have been comprehensibly investigated, which correlates between their microstructures and their specific performances. Furthermore, fig. 20 b) illustrates the improvement of ionomer distribution in dry catalyst layer by wet mixing, which consecutively escalates the performance of MEA prepared with dry spray coating technique. Additionally, fig. 20 c)

displays the voltage deterioration of the MEAs prepared with the combination of long and short side chain ionomers with respect to time. This study reveals the higher degradation rate due to the thinner membrane. Eventually, fig. 20 d) shows a schematic of three CLs dried with three different drying techniques in the left panel. Moreover, it also exhibits the positive effect of the freeze drying technique on porosity as well as gas diffusion properties of CL, which consequently improves the performance of the MEAs.

5.2 Synopsis

Aforementioned studies and experiences advocate us to discuss possible improvements in low Pt loaded MEA to achieve higher performance and durability.

- In this dissertation, I have investigated various parameters for characterizing CL properties such as CL thickness, porosity, tortuosity, ionomer distribution and proton conductivity through CL. Additionally, active surface area of catalyst and their utilization were also determined from the electrochemical characterization. Electrochemical impedance spectroscopy also reveals the possible contribution of different overpotentials involved in the electrode. Optimizing the above mentioned extrinsic as well as intrinsic characteristics play a significant role to design an efficient and durable CL that is also comprehensible from the prediction of the modelling as well as its simulated results. However, the limiting current study has not been performed in this work, which can foresee the pressure dependent and pressure independent resistances of oxygen diffusion in the catalyst layer [105]. Nevertheless, isolating the transport resistance through ionomer-water film from the total transport limitation is still a challenge in the community. Diffusion through water and thin ionomer films can be determined by Henry's Law, yet there is no general agreement on its relevance [106–108]. Even though a lot of research is taking place all around the globe to simulate this phenomenon in CL [109], a bridge between the experimental parameters and the prediction of modelling is still required.

- The most widely used ionomer in PEMFC application is perfluorosulfonic acid, which is made of hydrophobic perfluorinated backbone along with perfluoropolyether as side chains that terminates in a sulfonic acid group. The ratio of both monomers determines the equivalent weight, proton conductivity as well as water uptake. Therefore, ionomers with short side chain (SSC) appeared to be more stable at lower equivalent weight with higher proton conductivity and water uptake [110]. The structural and compositional divergence between SSC and LSC ionomers regulates their specific characteristics. At a given polymeric EW, the SSC-membranes are associated with higher heat of fusion than LSC-membranes. Moreover, SSC retains its semi-crystalline behavior even at low EW, and the absence of the CF_3 group as well as the shorter side chain yield a polymer of higher glass transition temperature at a given EW [22,111]. However, one of the works in this monograph shows SSC ionomer in the

electrode experiences higher rate of degradation in the long term of application due to having higher concentration of CO functional group, which is weak and more susceptible to radical attack. This loss of stability can be compensated by using SSC as membrane and LSC as ionomer additives in CL, or stabilization of the SSC ionomer by incorporating more competent radical scavengers.

- Freeze drying techniques of CL shows a promising improvement in CL properties by improving the porosity and transport behavior. This method can be further optimized to regulate the thickness and porosity of the CL by adjusting the amount of solvent and the rate of cooling as well as drying [112]. Nevertheless, uncontrolled sublimation often generates excessive porosity which in turn increases the tortuosity and reduces the performance of electrode. Moreover, this extreme condition of drying sometime causes unwanted brittleness of the ionomer and realignment of PTFE backbone (if liq. N_2 is used for cooling). However, cooling with mild condition can improve these demerits, but increase the drying time. In addition, our model predicts that even though increased porosity, thicker electrode and very thin ionomer film hamper the charge transport within the CL (very thin film of ionomer hinders the in-plane proton conductivity), the higher permeability and diffusibility of oxidant in the reacting interface counterbalances the overall performance. Both numerical and experimental perspectives emphasize on the fact that the drying technique plays a significant role in PEMFC performance due to its influence on the porosity and the distribution along with the thickness of the ionomer layer through the CL.
- Meeting the DOE target 2020 with 0.125 mg cm^{-2} Pt loading to reach 300 mA cm^{-2} at 0.8V or 1 W cm^{-2} peak power density at 1.5 bar for 5000 cycles is still a challenge [113]. Implementing the improvements in MEA, which are mentioned in this dissertation will facilitate to gain higher performance and durability at low catalyst loading. Nevertheless, the performance shown in this dissertation still does not meet the target, but contributes to the development of important parameters, which should be taken care of. Interestingly, using only the state of the art components does not confirm the highest possible fuel cell performance; whereas, a wide spectrum of parameters (such as hot pressing, compression, break-in condition etc.) are also involved in the performance and durability of PEMFC. A combination of up-to-date materials and synergic optimization of various parameters are required to attain the DOE or EU target of PEMFC.

6 General Outlook

Possibly, this doctoral thesis is one of the building blocks of the growing pool of knowledge regarding PEMFC research, which is very crucial to understand and design an efficient as well as durable electrode. But, certainly a huge prospect of research is still required to meet the ultimate goal of the mass commercialization of the PEMFC. Deeper understanding of the catalyst layer coating technology is still mandatory to deal with the challenges like controlling the architecture of the microstructure by aggregate size, distribution of ionomer, etc. An appropriate pore network model can assist the engineers to optimize the parameters according to the transcendent electrode design. From the perspective of this study, it is essential to examine the durability of freeze dried electrode in a long term degradation test. An interpretation of the water management through the pores of the freeze dried CL needs to be addressed. Moreover, investigation of the limiting current study by means of varying oxygen concentration will give a significant clue to perceive the quantitative concentration limitation. The model of the CL should accommodate the drying effect more deeply, considering the rate of evaporation and rate of deposition along with the thermal conductivity of individual materials. The study of ionomers should be conducted with the setup, where the fluorine emission from the exhaust water line can be determined. This inspection will confirm the contribution as well as the distribution of the chemical degradation occurring in the membrane electrode assembly.

Finally, polymer electrolyte membrane fuel cell is still an open ended research due to its dependence on numerous variables and parameters, which are all inter connected. Moreover, understanding the reactive interface and the role of ionomer in the CL is still a great challenge in the PEMFC community that need to be addressed.

7 Bibliography

[1] BP Statistical Review of World Energy Statistical Review of World, Ed. BP Stat. Rev. World Energy. (2019) 10. https://www.bp.com/content/dam/bp/business-sites/en/global/corporate/pdfs/energy-economics/statistical-review/bp-stats-review-2019-full-report.pdf.

[2] S.J. Peighambardoust, S. Rowshanzamir, M. Amjadi, Review of the proton exchange membranes for fuel cell applications, Int. J. Hydrogen Energy. 35 (2010) 9349–9384. doi:10.1016/j.ijhydene.2010.05.017.

[3] Y. Wang, K.S. Chen, J. Mishler, S.C. Cho, X.C. Adroher, A review of polymer electrolyte membrane fuel cells: Technology, applications, and needs on fundamental research, Appl. Energy. 88 (2011) 981–1007. doi:10.1016/j.apenergy.2010.09.030.

[4] R.S. Khurmi, R.S. Sedha, Material Science, 5th ed., S. Chand & Company Ltd, 2014, 2019.

[5] R.E. Rosli, A.B. Sulong, W.R.W. Daud, M.A. Zulkifley, T. Husaini, M.I. Rosli, E.H. Majlan, M.A. Haque, A review of high-temperature proton exchange membrane fuel cell (HT-PEMFC) system, Int. J. Hydrogen Energy. 42 (2017) 9293–9314. doi:10.1016/j.ijhydene.2016.06.211.

[6] Hydrogen Energy and Fuel Cells, A vision of our future, Security. (2003) 11–12. https://ec.europa.eu/research/energy/pdf/hydrogen-report_en.pdf.

[7] J.K. Nørskov, T. Bligaard, A. Logadottir, J.R. Kitchin, J.G. Chen, S. Pandelov, U. Stimming, Trends in the exchange current for hydrogen evolution, J. Electrochem. Soc. 152 (2005) 0–3. doi:10.1149/1.1856988.

[8] P.N. Ross, J. Lipkowski, Electrocatalysis, Band 3 von, John Wiley & Sons, 1998,

New York, 1998. https://books.google.de/books/about/Electrocatalysis.html?id=HZowkmoF4ngC&redir_esc=y.

[9] J.Z. Xin Chen Dingguo Xia, Zheng Shi, Electrocatalysis in Fuel Cells: A Non- and Low- Platinum Approach, Springer London, 2013. https://books.google.de/books?id=4V5DAAAAQBAJ.

[10] D. Papageorgopoulos, Fuel Cell R&D Overview, 2019. https://www.hydrogen.energy.gov/pdfs/review19/plenary_fuel_cell_papageorgopoulos_2019.pdf.

[11] Z. Qi, A. Kaufman, Low Pt loading high performance cathodes for PEM fuel cells, J. Power Sources. 113 (2003) 37–43. doi:10.1016/S0378-7753(02)00477-9.

[12] T.R. Ralph, G.A. Hards, J.E. Keating, S.A. Campbell, D.P. Wilkinson, M. Davis, J. St-Pierre, M.C. Johnson, Low cost electrodes for proton exchange membrane fuel cells: Performance in single cells and Ballard stacks, J. Electrochem. Soc. 144 (1997) 3845–3857. doi:10.1149/1.1838101.

[13] G. Wand, FUEL CELL HISTORY , PART ONE George Wand, Fuel Cells Today. (2006). https://www.ogniwa-paliwowe.info/Fuel_Cell_History_1.pdf.

[14] V. Mehta, J.S. Cooper, Review and analysis of PEM fuel cell design and manufacturing, J. Power Sources. 114 (2003) 32–53. doi:10.1016/S0378-7753(02)00542-6.

[15] T.A.Z. Shimson Gottesfeld, Advances in Electrochemical Sciences and Engineering, Wiley-VCH, Weinheim, Germany, 1997. doi:10.1017/CBO9781107415324.004.

[16] B. Bladergroen, H. Su, S. Pasupathi, V. Linkov, Overview of Membrane Electrode Assembly Preparation Methods for Solid Polymer Electrolyte Electrolyzer, Electrolysis. (2012). doi:10.5772/52947.

[17] Y. Shao, G. Yin, Z. Wang, Y. Gao, Proton exchange membrane fuel cell from low temperature to high temperature: Material challenges, J. Power Sources. 167

(2007) 235–242. doi:10.1016/j.jpowsour.2007.02.065.

[18] Chapter 1: Introduction, in: Fuel Cell Fundam., John Wiley & Sons, Ltd, New Jersey, USA, 2016: pp. 1–24. doi:10.1002/9781119191766.ch1.

[19] S. Litster, G. McLean, PEM fuel cell electrodes, J. Power Sources. 130 (2004) 61–76. doi:10.1016/j.jpowsour.2003.12.055.

[20] T. Shimoaka, C. Wakai, T. Sakabe, S. Yamazaki, T. Hasegawa, Hydration structure of strongly bound water on the sulfonic acid group in a Nafion membrane studied by infrared spectroscopy and quantum chemical calculation, Phys. Chem. Chem. Phys. 17 (2015) 8843–8849. doi:10.1039/c5cp00567a.

[21] C. Yin, Z. Wang, Y. Luo, J. Li, Y. Zhou, X. Zhang, H. Zhang, P. Fang, C. He, Thermal annealing on free volumes, crystallinity and proton conductivity of Nafion membranes, J. Phys. Chem. Solids. 120 (2018) 71–78. doi:10.1016/j.jpcs.2018.04.028.

[22] Deborah Jones, Perfluorosulfonic Acid Membranes for Fuel Cell and Electrolyser Applications | Sigma-Aldrich, Merck. (n.d.). https://www.sigmaaldrich.com/technical-documents/articles/materials-science/perfluorosulfonic-acid-membranes.html#ref.

[23] Z. Rao, B. Tang, P. Wu, Proton Conductivity of Proton Exchange Membrane Synergistically Promoted by Different Functionalized Metal–Organic Frameworks, ACS Appl. Mater. Interfaces. 9 (2017) 22597–22603. doi:10.1021/acsami.7b05969.

[24] B.R. Breslau, I.F. Miller, A Hydrodynamic Model for Electroosmosis, Ind. Eng. Chem. Fundam. 10 (1971) 554–565. doi:10.1021/i160040a003.

[25] W.H.J. Hogarth, J.C. Diniz Da Costa, G.Q. Lu, Solid acid membranes for high temperature (>140 ° C) proton exchange membrane fuel cells, J. Power Sources. 142 (2005) 223–237. doi:10.1016/j.jpowsour.2004.11.020.

[26] J.A. Elliott, S. Hanna, A.M.S. Elliott, G.E. Cooley, The swelling behaviour of perfluorinated ionomer membranes in ethanol/water mixtures, Polymer (Guildf). 42 (2001) 2251–2253. doi:10.1016/S0032-3861(00)00538-3.

[27] Chapter 2: Fuel Cell Thermodynamics, in: Fuel Cell Fundam., John Wiley & Sons, Ltd, New Jersey, USA, 2016: pp. 25–76. doi:10.1002/9781119191766.ch2.

[28] E. Principles, Thermodynamics of Fuel Cells, Green Energy Technol. 12 (2011) 25–36.

[29] T. Bednarek, G. Tsotridis, Issues associated with modelling of proton exchange membrane fuel cell by computational fluid dynamics, J. Power Sources. 343 (2017) 550–563. doi:10.1016/j.jpowsour.2017.01.059.

[30] L. Wang, Development and investigation of oxygen evolution reaction catalysts for proton exchange membrane electrolyzers, University of Stuttgart, 2018. http://dx.doi.org/10.18419/opus-10359.

[31] J. césar garcía Navarro, On The Mass Transport Phenomena In Proton Exchange Membrane Water Electrolysis, Der Fakultät Energie- , Verfahrens- und Biotechnik der Universität Stuttgart zur Erlangung der Würde eines Doktors der Ingenieurwissenschaften (Submitted), University of Stuttgart, 2019.

[32] F. Barbir, PEM Fuel Cells, Elsevier, California, USA, 2013. doi:10.1016/C2011-0-06706-6.

[33] Chapter 3: Fuel Cell Reaction Kinetics, in: Fuel Cell Fundam., John Wiley & Sons, Ltd, New Jersey, USA, 2016: pp. 77–116. doi:10.1002/9781119191766.ch3.

[34] Chapter 4: Fuel Cell Charge Transport, in: Fuel Cell Fundam., John Wiley & Sons, Ltd, New Jersey, USA, 2016: pp. 117–166. doi:10.1002/9781119191766.ch4.

[35] J. Larminie, A. Dicks, Fuel cell systems explained: Second edition, J. Wiley, New Jersey, USA, 2013. doi:10.1002/9781118878330.

[36] Chapter 5: Fuel Cell Mass Transport, in: Fuel Cell Fundam., John Wiley & Sons, Ltd, New Jersey, USA, 2016: pp. 167–202. doi:10.1002/9781119191766.ch5.

[37] T.A. Greszler, D. Caulk, P. Sinha, The impact of platinum loading on oxygen transport resistance, J. Electrochem. Soc. 159 (2012) 831–840.

doi:10.1149/2.061212jes.

[38] T. Van Cleve, S. Khandavalli, A. Chowdhury, S. Medina, S. Pylypenko, M. Wang, K.L. More, N. Kariuki, D.J. Myers, A.Z. Weber, S.A. Mauger, M. Ulsh, K.C. Neyerlin, Dictating Pt-Based Electrocatalyst Performance in Polymer Electrolyte Fuel Cells, from Formulation to Application, ACS Appl. Mater. Interfaces. 11 (2019) 46953–46964. doi:10.1021/acsami.9b17614.

[39] A. Esmaeilifar, S. Rowshanzamir, M.H. Eikani, E. Ghazanfari, Synthesis methods of low-Pt-loading electrocatalysts for proton exchange membrane fuel cell systems, Energy. 35 (2010) 3941–3957. doi:https://doi.org/10.1016/j.energy.2010.06.006.

[40] Á. Kriston, T. Xie, D. Gamliel, P. Ganesan, B.N. Popov, Effect of ultra-low Pt loading on mass activity of polymer electrolyte membrane fuel cells, J. Power Sources. 243 (2013) 958–963. doi:10.1016/j.jpowsour.2013.05.078.

[41] V. Yarlagadda, M.K. Carpenter, T.E. Moylan, R.S. Kukreja, R. Koestner, W. Gu, L. Thompson, A. Kongkanand, Boosting Fuel Cell Performance with Accessible Carbon Mesopores, ACS Energy Lett. 3 (2018) 618–621. doi:10.1021/acsenergylett.8b00186.

[42] N. Pramounmat, C.N. Loney, C.O. Kim, L. Wiles, K.E. Ayers, A. Kusoglu, J.N. Renner, Controlling the Distribution of Perfluorinated Sulfonic Acid Ionomer with Elastin-like Polypeptide, ACS Appl. Mater. Interfaces. 11 (2019) 43649–43658. doi:10.1021/acsami.9b11160.

[43] S. Srinivasan, E.A. Ticianelli, C.R. Derouin, A. Redondo, Advances in solid polymer electrolyte fuel cell technology with low platinum loading electrodes, J. Power Sources. 22 (1988) 359–375. doi:10.1016/0378-7753(88)80030-2.

[44] E.A. Ticianelli, Methods to Advance Technology of Proton Exchange Membrane Fuel Cells, J. Electrochem. Soc. 135 (2006) 2209. doi:10.1149/1.2096240.

[45] Andrew Wonga and Aimy Bazylaka, Investigating the effect of non-uniform microporous layer intrusion on oxygen transport in dry and partially saturated polymer electrolyte membrane fuel cell gas diffusion layers, in: ECS transaction, 2017: pp. 175–186. doi:10.1017/CBO9781107415324.004.

[46] S.G. Peera, A. Arunchander, A.K. Sahu, Platinum nanoparticles supported on nitrogen and fluorine co-doped graphite nanofibers as an excellent and durable oxygen reduction catalyst for polymer electrolyte fuel cells, Carbon N. Y. 107 (2016) 667–679. doi:https://doi.org/10.1016/j.carbon.2016.06.021.

[47] M. Oezaslan, F. Hasché, P. Strasser, Pt-based core-shell catalyst architectures for oxygen fuel cell electrodes, J. Phys. Chem. Lett. 4 (2013) 3273–3291. doi:10.1021/jz4014135.

[48] L. Bu, N. Zhang, S. Guo, X. Zhang, J. Li, J. Yao, T. Wu, G. Lu, J.-Y. Ma, D. Su, X. Huang, Biaxially strained PtPb/Pt core/shell nanoplate boosts oxygen reduction catalysis., Science. 354 (2016) 1410–1414. doi:10.1126/science.aah6133.

[49] Y. Xiong, L. Xiao, Y. Yang, F.J. DiSalvo, H.D. Abruña, High-Loading Intermetallic Pt3Co/C Core–Shell Nanoparticles as Enhanced Activity Electrocatalysts toward the Oxygen Reduction Reaction (ORR), Chem. Mater. 30 (2018) 1532–1539. doi:10.1021/acs.chemmater.7b04201.

[50] Contents: Fuel Cells 2/2010, Fuel Cells. 10 (2010) 215–216. doi:10.1002/fuce.201090002.

[51] K. Jayasayee, J.A.R. Van Veen, T.G. Manivasagam, S. Celebi, E.J.M. Hensen, F.A. de Bruijn, Oxygen reduction reaction (ORR) activity and durability of carbon supported PtM (Co, Ni, Cu) alloys: Influence of particle size and non-noble metals, Appl. Catal. B Environ. 111–112 (2012) 515–526. doi:https://doi.org/10.1016/j.apcatb.2011.11.003.

[52] F. Hasché, M. Oezaslan, P. Strasser, Activity, structure and degradation of dealloyed ptni3 nanoparticle electrocatalyst for the oxygen reduction reaction in pemfc, J. Electrochem. Soc. 159 (2012) 24–33. doi:10.1149/2.030201jes.

[53] X. Huang, Z. Zhao, L. Cao, Y. Chen, E. Zhu, Z. Lin, M. Li, A. Yan, A. Zettl, Y.M. Wang, X. Duan, T. Mueller, Y. Huang, ELECTROCHEMISTRY. High-performance transition metal-doped Pt(3)Ni octahedra for oxygen reduction reaction., Science. 348 (2015) 1230–1234. doi:10.1126/science.aaa8765.

[54] T. Chen, Y. Xu, S. Guo, D. Wei, L. Peng, X. Guo, N. Xue, Y. Zhu, Z. Chen, B. Zhao, W. Ding, Ternary Heterostructural Pt/CNx/Ni as a Supercatalyst for Oxygen Reduction., IScience. 11 (2019) 388–397. doi:10.1016/j.isci.2018.12.029.

[55] Q. Li, L. Wu, G. Wu, D. Su, H. Lv, S. Zhang, W. Zhu, A. Casimir, H. Zhu, A. Mendoza-Garcia, S. Sun, New approach to fully ordered fct-FePt nanoparticles for much enhanced electrocatalysis in acid., Nano Lett. 15 (2015) 2468–2473. doi:10.1021/acs.nanolett.5b00320.

[56] V.R. Stamenkovic, B. Fowler, B.S. Mun, G. Wang, P.N. Ross, C.A. Lucas, N.M. Markovic, Improved oxygen reduction activity on Pt3Ni(111) via increased surface site availability., Science. 315 (2007) 493–497. doi:10.1126/science.1135941.

[57] B.A. Kakade, H. Wang, T. Tamaki, H. Ohashi, T. Yamaguchi, Enhanced oxygen reduction reaction by bimetallic CoPt and PdPt nanocrystals, RSC Adv. 3 (2013) 10487–10496. doi:10.1039/C3RA40920A.

[58] W. Li, W. Zhou, H. Li, Z. Zhou, B. Zhou, G. Sun, Q. Xin, Nano-stuctured Pt–Fe/C as cathode catalyst in direct methanol fuel cell, Electrochim. Acta. 49 (2004) 1045–1055. doi:https://doi.org/10.1016/j.electacta.2003.10.015.

[59] I.E.L. Stephens, A.S. Bondarenko, L. Bech, I. Chorkendorff, Oxygen Electroreduction Activity and X-Ray Photoelectron Spectroscopy of Platinum and Early Transition Metal Alloys, ChemCatChem. 4 (2012) 341–349. doi:10.1002/cctc.201100343.

[60] S.G. Peera, T.G. Lee, A.K. Sahu, Pt-rare earth metal alloy/metal oxide catalysts for oxygen reduction and alcohol oxidation reactions: an overview, Sustain. Energy Fuels. 3 (2019) 1866–1891. doi:10.1039/c9se00082h.

[61] A. Kongkanand, M.F. Mathias, The Priority and Challenge of High-Power Performance of Low-Platinum Proton-Exchange Membrane Fuel Cells, J. Phys. Chem. Lett. 7 (2016) 1127–1137. doi:10.1021/acs.jpclett.6b00216.

[62] A.A. Gewirth, J.A. Varnell, A.M. DiAscro, Nonprecious Metal Catalysts for Oxygen Reduction in Heterogeneous Aqueous Systems, Chem. Rev. 118 (2018)

2313–2339. doi:10.1021/acs.chemrev.7b00335.

[63] Y. Wang, J. Li, Z. Wei, Transition-metal-oxide-based catalysts for the oxygen reduction reaction, J. Mater. Chem. A. 6 (2018) 8194–8209. doi:10.1039/C8TA01321G.

[64] Y. Liu, C. Ji, W. Gu, J. Jorne, H.A. Gasteiger, Effects of catalyst carbon support on proton conduction and cathode performance in PEM fuel cells, J. Electrochem. Soc. 158 (2011) 614–621. doi:10.1149/1.3562945.

[65] E. Padgett, V. Yarlagadda, M.E. Holtz, M. Ko, B.D.A. Levin, R.S. Kukreja, J.M. Ziegelbauer, R.N. Andrews, J. Ilavsky, A. Kongkanand, D.A. Muller, Mitigation of PEM fuel cell catalyst degradation with porous Carbon supports, J. Electrochem. Soc. 166 (2019) F198–F207. doi:10.1149/2.0371904jes.

[66] M.S. Wilson, J.A. Valerio, S. Gottesfeld, Low platinum loading electrodes for polymer electrolyte fuel cells fabricated using thermoplastic ionomers, Electrochim. Acta. 40 (1995) 355–363. doi:https://doi.org/10.1016/0013-4686(94)00272-3.

[67] S. Holdcroft, Fuel cell catalyst layers: A polymer science perspective, Chem. Mater. 26 (2014) 381–393. doi:10.1021/cm401445h.

[68] A. Kongkanand, M.F. Mathias, The Priority and Challenge of High-Power Performance of Low-Platinum Proton-Exchange Membrane Fuel Cells, J. Phys. Chem. Lett. 7 (2016) 1127–1137. doi:10.1021/acs.jpclett.6b00216.

[69] Z. Xie, X.S. Zhao, J. Gazzarri, Q. Wang, T. Navessin, S. Holdcroft, Identification of dominant transport mechanisms in PEMFC cathode catalyst layers operated under low RH, ECS Trans. 25 (2009) 1187–1192. doi:10.1149/1.3210673.

[70] Y.-C. Park, K. Kakinuma, H. Uchida, M. Watanabe, M. Uchida, Effects of short-side-chain perfluorosulfonic acid ionomers as binders on the performance of low Pt loading fuel cell cathodes, J. Power Sources. 275 (2015) 384–391. doi:https://doi.org/10.1016/j.jpowsour.2014.10.149.

[71] Y.-C. Park, H. Tokiwa, K. Kakinuma, M. Watanabe, M. Uchida, Effects of

carbon supports on Pt distribution, ionomer coverage and cathode performance for polymer electrolyte fuel cells, J. Power Sources. 315 (2016) 179–191. doi:https://doi.org/10.1016/j.jpowsour.2016.02.091.

[72] T. Morawietz, M. Handl, C. Oldani, K.A. Friedrich, R. Hiesgen, Quantitative in Situ Analysis of Ionomer Structure in Fuel Cell Catalytic Layers, ACS Appl. Mater. Interfaces. 8 (2016) 27044–27054. doi:10.1021/acsami.6b07188.

[73] K. Shinozaki, J.W. Zack, S. Pylypenko, B.S. Pivovar, S.S. Kocha, Oxygen reduction reaction measurements on platinum electrocatalysts utilizing rotating disk electrode technique II. influence of ink formulation, catalyst layer uniformity and thickness, J. Electrochem. Soc. 162 (2015) F1384–F1396. doi:10.1149/2.0551512jes.

[74] A. Orfanidi, P. Madkikar, H.A. El-Sayed, G.S. Harzer, T. Kratky, H.A. Gasteiger, The key to high performance low pt loaded electrodes, J. Electrochem. Soc. 164 (2017) F418–F426. doi:10.1149/2.1621704jes.

[75] G. Sasikumar, J.W. Ihm, H. Ryu, Optimum Nafion content in PEM fuel cell electrodes, Electrochim. Acta. 50 (2004) 601–605. doi:10.1016/j.electacta.2004.01.126.

[76] Y. Liu, C. Ji, W. Gu, D.R. Baker, J. Jorne, H.A. Gasteiger, Proton conduction in PEM fuel cell cathodes: Effects of electrode thickness and ionomer equivalent weight, J. Electrochem. Soc. 157 (2010) 1154–1162. doi:10.1149/1.3435323.

[77] Y. Liu, M.W. Murphy, D.R. Baker, W. Gu, C. Ji, J. Jorne, H.A. Gasteiger, Proton conduction and oxygen reduction kinetics in PEM fuel cell cathodes: Effects of ionomer-to-carbon ratio and relative humidity, J. Electrochem. Soc. 156 (2009) 970–980. doi:10.1149/1.3143965.

[78] Y. Tabe, M. Nishino, H. Takamatsu, T. Chikahisa, Effects of cathode catalyst layer structure and properties dominating polymer electrolyte fuel cell performance, J. Electrochem. Soc. 158 (2011) 1246–1254. doi:10.1149/1.3624606.

[79] M.H. Eikerling, What else determines the activity of Platinum in PEM Fuel Cells ?, Oral Present. Tennessee Univ. (2011).

[80] K. Malek, M. Eikerling, Q. Wang, T. Navessin, Z. Liu, Self-Organization in Catalyst Layers of Polymer Electrolyte Fuel Cells, J. Phys. Chem. C. 111 (2007) 13627–13634. doi:10.1021/jp072692k.

[81] Z. Xia, Q. Wang, M. Eikerlitig, Z. Liu, Efffectiweness factor of Pt utilization in cathode catalyst layer of polymer electrolyte fuel cells, Can. J. Chem. 86 (2008) 657–667. doi:10.1139/V08-053.

[82] E. Sadeghi, A. Putz, M. Eikerling, Effects of ionomer coverage on agglomerate effectiveness in catalyst layers of polymer electrolyte fuel cells, J. Solid State Electrochem. 18 (2014) 1271–1279. doi:10.1007/s10008-013-2268-z.

[83] P.G. Corradini, F.I. Pires, V.A. Paganin, J. Perez, E. Antolini, Effect of the relationship between particle size, inter-Particle distance, and metal loading of carbon supported fuel cell catalysts on their catalytic activity, J. Nanoparticle Res. 14 (2012). doi:10.1007/s11051-012-1080-5.

[84] K. Talukdar, S. Helmly, M. Schulze, D.G. Sanchez, M. Handl, R. Hiesgen, J. Kraut, K.A. Friedrich, Enveloping of catalyst powder by ionomer for dry spray coating in polymer electrolyte membrane fuel cells, J. Power Sources. (2019) 82–90. doi:10.1016/j.jpowsour.2019.03.093.

[85] M.B. Sassin, Y. Garsany, B.D. Gould, K.E. Swider-Lyons, Fabrication Method for Laboratory-Scale High-Performance Membrane Electrode Assemblies for Fuel Cells, Anal. Chem. 89 (2017) 511–518. doi:10.1021/acs.analchem.6b03005.

[86] F. Franks, Freeze-drying of bioproducts: Putting principles into practice, Eur. J. Pharm. Biopharm. 45 (1998) 221–229. doi:10.1016/S0939-6411(98)00004-6.

[87] W. Abdelwahed, G. Degobert, S. Stainmesse, H. Fessi, Freeze-drying of nanoparticles: Formulation, process and storage considerations, Adv. Drug Deliv. Rev. 58 (2006) 1688–1713. doi:10.1016/j.addr.2006.09.017.

[88] S.N. Tkachev, R.M. Nasimov, V.A. Kalinin, Phase diagram of water in the vicinity of the triple point, J. Chem. Phys. 105 (1996) 3722–3725. doi:10.1063/1.472191.

[89] Z. Xia, S. Wang, L. Jiang, H. Sun, F. Qi, J. Jin, G. Sun, Rational design of a highly efficient Pt/graphene-Nafion® composite fuel cell electrode architecture, J. Mater. Chem. A. 3 (2015) 1641–1648. doi:10.1039/c4ta05399k.

[90] K. Talukdar, S. Delgado, T. Lagarteira, P. Gazdzicki, K.A. Friedrich, Minimizing mass-transport loss in proton exchange membrane fuel cell by freeze-drying of cathode catalyst layers, J. Power Sources. 427 (2019) 309–317. doi:10.1016/j.jpowsour.2019.04.094.

[91] S. Shukla, Experimental analysis of inkjet printed polymer electrolyte fuel cell electrodes, University of Alberta, 2016. http://www.esdlab.mece.ualberta.ca/pdfs/Shukla_Shantanu_PhD_Thesis.pdf.

[92] G.A. Futter, P. Gazdzicki, K.A. Friedrich, A. Latz, T. Jahnke, Physical modeling of polymer-electrolyte membrane fuel cells: Understanding water management and impedance spectra, J. Power Sources. 391 (2018) 148–161. doi:10.1016/j.jpowsour.2018.04.070.

[93] F.M. White, Fluid Mechanics, 5th ed., McGraw Hill, NewYork, USA, 2002. http://library.aceondo.net/ebooks/Physics/_Fluid_Mechanics.pdf.

[94] Rainer Helmig, Multiphase Flow and Transport Processes in the Subsurface, A Contribution to the Modeling of Hydrosystems Autoren, Springer-Verlag, Berlin-Heidelberg, 1997. https://www.springer.com/de/book/9783642645457.

[95] T. Rosén, J. Eller, J. Kang, N.I. Prasianakis, J. Mantzaras, F.N. Büchi, Saturation dependent effective transport properties of PEFC gas diffusion layers, J. Electrochem. Soc. 159 (2012) 536–544. doi:10.1149/2.005209jes.

[96] M.C.L. (Humble O. and R. Co.), Capillary Behavior in Porous Solids, Soc. Pet. Eng. 142 (1941) 152–169. doi:10.1515/crll.1958.200.129.

[97] E.N.L. R. Byron Bird, Warren E. Stewart, Transport Phenomena, 2nd ed., John Willey and Sons, New Jersey, USA, 2006. doi:10.1017/CBO9781107415324.004.

[98] A. Lauser, C. Hager, R. Helmig, B. Wohlmuth, A new approach for phase transitions in miscible multi-phase flow in porous media, Adv. Water Resour. 34

(2011) 957–966. doi:10.1016/j.advwatres.2011.04.021.

[99] B.P. Setzler, T.F. Fuller, A physics-based impedance model of proton exchange membrane fuel cells exhibiting low-frequency inductive loops, J. Electrochem. Soc. 162 (2015) F519–F530. doi:10.1149/2.0361506jes.

[100] W. Sun, B.A. Peppley, K. Karan, An improved two-dimensional agglomerate cathode model to study the influence of catalyst layer structural parameters, Electrochim. Acta. 50 (2005) 3359–3374. doi:https://doi.org/10.1016/j.electacta.2004.12.009.

[101] R. Huber, R. Helmig, Node-centered finite volume discretizations for the numerical simulation of multiphase flow in heterogeneous porous media, Comput. Geosci. 4 (2000) 141–164. doi:10.1023/A:1011559916309.

[102] Dumux Handbook,version 2.11, 2000. file:///C:/Users/talu_kr/Desktop/ref/dumux-handbook-2.11.pdf.

[103] A. Pfrang, D. Veyret, G. Tsotridis, Computation of Thermal Conductivity of Gas Diffusion Layers of PEM Fuel Cells, Intechopen, Convect. Conduct. Heat Transf. (2011). doi:10.5772/23657.

[104] O.S. Burheim, G.A. Crymble, R. Bock, N. Hussain, S. Pasupathi, A. Du Plessis, S. Le Roux, F. Seland, H. Su, B.G. Pollet, Thermal conductivity in the three layered regions of micro porous layer coated porous transport layers for the PEM fuel cell, Int. J. Hydrogen Energy. 40 (2015) 16775–16785. doi:10.1016/j.ijhydene.2015.07.169.

[105] D.R. Baker, D.A. Caulk, K.C. Neyerlin, M.W. Murphy, Measurement of Oxygen Transport Resistance in PEM Fuel Cells by Limiting Current Methods, J. Electrochem. Soc. 156 (2009) B991. doi:10.1149/1.3152226.

[106] A.K. Srouji, L.J. Zheng, R. Dross, D. Aaron, M.M. Mench, The role of water management on the oxygen transport resistance in polymer electrolyte fuel cell with ultra-low precious metal loading, J. Power Sources. 364 (2017) 92–100. doi:10.1016/j.jpowsour.2017.07.036.

[107] M. Ebara, H. Fukuda, H. Saisho, The copper/zinc ratio in patients with hepatocellular carcinoma, J. Gastroenterol. 38 (2003) 104–105. doi:10.1007/s005350300016.

[108] U.A. Paulus, T.J. Schmidt, H.A. Gasteiger, R.J. Behm, Oxygen reduction on a high-surface area Pt/Vulcan carbon catalyst: A thin-film rotating ring-disk electrode study, J. Electroanal. Chem. 495 (2001) 134–145. doi:10.1016/S0022-0728(00)00407-1.

[109] K. Malek, T. Mashio, M. Eikerling, Microstructure of Catalyst Layers in PEM Fuel Cells Redefined: A Computational Approach, Electrocatalysis. 2 (2011) 141–157. doi:10.1007/s12678-011-0047-0.

[110] S. Shahgaldi, I. Alaefour, X. Li, The impact of short side chain ionomer on polymer electrolyte membrane fuel cell performance and durability, Appl. Energy. 217 (2018) 295–302. doi:10.1016/j.apenergy.2018.02.154.

[111] A. Ghielmi, P. Vaccarono, C. Troglia, V. Arcella, Proton exchange membranes based on the short-side-chain perfluorinated ionomer, J. Power Sources. 145 (2005) 108–115. doi:10.1016/j.jpowsour.2004.12.068.

[112] F. Franks, T. Auffret, Freeze-drying of Pharmaceuticals and Biopharmaceuticals: Principles and Practice, Royal Society of Chemistry, 2007. https://books.google.de/books?id=NnEoDwAAQBAJ.

[113] DOE Technical Targets for Polymer Electrolyte Membrane Fuel Cell Components, Energy.Gov. (n.d.). https://www.energy.gov/eere/fuelcells/doe-technical-targets-polymer-electrolyte-membrane-fuel-cell-components.

List of Tables

List of Figures

8 Scientific Articles

I. Understanding the important parameters of Electrode Fabrication in Polymer Electrolyte Membrane Fuel Cell.
Krishan Talukdar, , Patrick Sarkezi-Selsky, , Khrystyna Yezerska, Oleg Sergeev, Pawel Gazdzicki, K. Andreas Friedrich.
Submitted

II. Enveloping of catalyst powder by ionomer for dry spray coating in polymer electrolyte membrane fuel cells.
Krishan Talukdar, Stefan Helmly, Mathias Schulze, Daniel G. Sanchez, Michael Handl, Renate Hiesgen, Jürgen Kraut, K. Andreas Friedrich.
Journal of Power Sources 424 (2019) 82-90

III. Comparative investigation into the performance and durability of long and short side chain ionomers in Polymer Electrolyte Membrane Fuel cells.
Krishan Talukdar, Pawel Gazdzicki, K. Andreas Friedrich.
Journal of Power Sources 439 (2019) 227078

IV. Minimizing mass transport loss in proton exchange membrane fuel cell by freeze drying of cathode catalyst layer.
Krishan Talukdar, Sofia Delgado, Tiago Lagarteira, Pawel Gazdzicki, K. Andreas Friedrich.
Journal of Power Sources 427 (2019) 309-31

V. Experimental and Numerical Study on Catalyst Layer of Polymer Electrolyte Membrane Fuel Cell Prepared with Diverse Drying Methods. **Krishan Talukdar**, Md Asaduzzaman Ripan, Thomas Jahnke, Pawel Gazdzicki, Tobias Morawietz, K. Andreas Friedrich.
Journal of Power Sources 461 (2020) 228169

Understanding the Important Parameters of Electrode Fabrication for Polymer Electrolyte Membrane Fuel Cell

Krishan Talukdar[*a], Patrick Sarkezi-Selsky*[a], Khrystyna Yezerska*[b], Oleg Sergeev*[b], Pawel Gazdzicki*[a] and K. Andreas Friedrich*[a,c]

[a]German Aerospace Center (DLR), Institute of Engineering Thermodynamics, Pfaffenwaldring 38-40, 70569 Stuttgart, Germany
[b]German Aerospace Center (DLR), Institute of Networked Energy System, Carl-von-Ossietzky-Str. 15, 26129 Oldenburg
[c]University of Stuttgart, Institute of Building Energetics, Thermal Engineering and Energy Storage (IGTE), Pfaffenwaldring 31, 70569 Stuttgart, Germany

Microstructure and electrochemical properties of the cathode catalyst layer (CL) of a polymer electrolyte membrane fuel cell (PEMFC) have great impact on the performance and durability of the cell. In this work, intrinsic properties of PEMFC electrodes such as porosity, permeability, diffusivity, and inverse tortuosity are determined for disparate catalyst layers by analysis of FIB-SEM images using GeoDict®. Moreover, this study explains how properties of the cathode CL influence cell overall performances. To obtain different CL structures the electrodes were prepared with six different coating techniques with the same Pt loading each yielding a unique CL structure. The coating techniques are: air-brush, screen-printing, inkjet printing, dry-spray, doctor-blade and drop cast. Physical and electrochemical characterizations of the individual catalyst layers (CL) are investigated in identical conditions with the same drying processes and same operation conditions. One of the major goals of this article is to identify the parameters that influence the properties of catalyst layers significantly, and should be of particular importance when tailoring electrodes for PEMFC application. This is considered an important step in a more rational development of catalyst layers.

Corresponding author: e-mail: krishan.talukdar@dlr.de Phone: +49-711-6862-567

Keywords: PEMFC, MEA preparation, catalyst coating, microstructure of catalyst layer, electrode design

1. Introduction

In the quest to reduce greenhouse gas emissions (GHG), green hydrogen (generated using electricity from renewable energies) represents a promising energy carrier with a particularly low CO_2 foot print. Polymer electrolyte membrane fuel cell (PEMFC) that uses green hydrogen as fuel is considered the key technology to reduce GHG emissions [1-3]. PEMFCs have higher storage capacity as well as higher power-to-weight-ratio compared to batteries, and are emission-free in contrast to internal combustion engines [4, 5]. However, the biggest obstacle of this technology towards market penetration is the presently high cost caused mainly by still low production volume and the usage of expensive materials (platinum) as catalyst [6-8]. Moreover, mass transport limitations occurring at high current density and at low Pt loadings as well as degradation of the electrodes are still major obstacles in terms of performance and longevity [9-11]. Hence, optimizing electrodes remain a great challenge and requires better understanding of the relation between the electrode properties and structure and the cell behavior.

To design an efficient low platinum loaded electrode with durable performance, it is required to have an active catalyst with higher stability and large surface area. In addition, ionomer in contact with the catalyst is necessary to enable ionic conductivity, improve stability and increased reaction inter-phase [12-14]. Forming a porous catalyst layer requires a coating process of the catalyst on the substrate, either on the membrane (catalyst coated membrane, CCM) or on the gas diffusion layer (gas diffusion electrode, GDE). This coating process of the catalyst layer is one of the most critical steps of the MEA production process as it determines the properties of the catalyst layer. This manufacturing step is accountable for the secondary pores as well as the microstructure of the catalyst layer, which finally influences cell performance [15]. In this context, catalyst layer should have optimized porosity (35-50 %) and thickness (4-10 μm) with appropriate water management capacity [16-24]. Although plentiful articles have been published with respect to optimization of catalyst layer structure by numerical models, few experimental investigations are available [17, 25, 26]. It is due to the involvement of numerous parameters and variables, which are interdependent and thus difficult to discriminate in PEMFC operation as well as characterization.

In recent times, extensive endeavors focused on electrode design with low Pt loading yet with high power density and stability. For instance, according to Kriston et al., due to the decreasing catalyst utilization or accessibility, the active area decreases with increasing Pt loading [27]. However, this relation does not apply to very low or ultra-low Pt loading [16]. Major progress to

enhance performance and to reduce the Pt loading has been made possible by: (i) adopting Pt that is supported on large surface-area carbon as a substitute of pure Pt black [28]; (ii) impregnating proton conducting ionomer into the CL of either GDE or the CCM [29, 30].

Pt catalysts dispersed on low solid surface area carbon (SC) support has higher ECSA but lower ORR mass activity than on high surface area carbon (HSC) support in the CL. ECSA retention capacity is higher with increasing porosity. There is a tendency of ionomer to not fill pores smaller than 4 nm, and hence the carbon pores ≤ 4 nm are very critical [22, 31, 32]. Electrode should be well-balanced between thickness and porosity. Electrical contact and conductivity are facilitated by thin electrodes, but at the expense of porosity. Contrarily, porous electrode shows better diffusion properties, however exhibits higher contact resistance or ohmic resistance compared to thin one [33, 34]. Influence of membrane thickness becomes less dominant if the membrane is thinner than 25 µm [35]. Thickness and high tortuosity of ionomer in electrode is inversely proportional to the proton conductivity. High humidification of electrode reduces the O_2 diffusion resistance. However, Park et al. [36, 37] stated that the excessive swelling of the ionomer causes larger O_2 diffusion resistance. So, the equivalent weight of ionomer and resulting water uptake should be optimized appropriately. The average thickness of ionomer over particle or agglomerates in commercial electrode is 6 to 14 nm [10, 16, 35, 38]. Thinner ionomer layers than 4 nm are associated to a laminar bilayer with reduced proton conductivity [39]. The critical thickness of Nafion® film over catalyst surface is 0.2 µm. Ionomer layer thicker than this is reported to cause diffusion limitations [40]. Moreover, roughness factor is also inversely proportional to electrode transport resistance [37, 41-43]. Regarding platinum loading, the less the Pt content the higher will be the ionomer - Pt ratio. Shashikumar et al. [44] showed experimentally that ionomer loading should increase as Pt loading decreases to maintain high performance. In his experiment using electrodes with 0.5, 0.25, and 0.1 mg/cm2 Pt-loading, the highest performance was achieved at 20, 40 and 50 wt.% loading of ionomer, respectively. Ionomer to carbon (I/C) ratio should be the same for all kind of carbon content. Especially, the proton resistivity of the cathode has strong dependency on the ionomer at lower I/C ratio. It is calculated by several groups that oxygen transport resistance through the ionomer coating over Pt/C agglomerates is a rate determining step of the cathode catalyst layer (CCL) activity in a normal operating FC condition [10, 16]. Moreover, it is proposed that limitations of the oxygen transport through the ionomer can be mitigated by decreasing the ionomer film thickness, and increasing the thickness of CL. Nevertheless, expanding the porosity of the CL, reducing the ionomer thickness and employing thicker CL reduce the effective proton conductivity. This causes inadequate proton conductivity, and possibly also non-uniform potential distribution in the CL leading to accelerated degradation. Considering this phenomenon, an effective strategy

would be to increase the permeability of oxygen in the ionomer to maintain satisfactorily high cell voltages at high current density with lower loading of Pt [34, 45-50]. In general, it can be stated that high performance of MEAs have been achieved by empirical variation of coating parameters but a rational approach in this regard is still missing.

In this work, catalyst layers were fabricated using different coating techniques like dry-spray [51, 52], airbrush [53-55], screen-print [56, 57], doctor-blade [58], drop-cast, inkjet-printing [59, 60] yielding different microstructures that were determined using electron microscopy. Subsequently, the MEAs were characterized electrochemically to understand the relation between electrochemical performance and microstructure. To make a comprehensive comparison, we produced membrane electrode assemblies (MEA) with same Pt loading by means of same drying procedure for wet methods, and tested them in same operating conditions. Different in-situ and ex-situ characterizations were performed to determine the important parameters of the catalyst layers for performance. In this regard, we have used air-brush, screen-printing, inkjet printing, dry-spraying, doctor-blade and drop casting coating techniques to prepare CLs and eventually construct respective MEAs. A drastic variation in the performances was observed when characterizing different MEAs, where the only difference among them is the coating method. It is observed that one property, e.g. ECSA does not suffice to evaluate a catalyst layer due to the complexity of interactions. This work does not aim at providing a high performance of an individual coating techniques but aims at providing a methodology for their evaluation and uses the different coating techniques to prepare CLs with different structures and properties. This article demonstrates how different coating mechanism results to different microstructure of CL and influence the transport and charge transfer limitations accordingly. It is a step into a more rational development effort for catalyst layers.

2. Materials and Methods

2.1 Ink Preparation

All MEAs prepared in this study are symmetrical, i.e. they consist of identically prepared anode and cathode catalyst layers. However, as the loading on anode is also 0.3 mg cm^{-2}, only the contribution from cathode dominates the over potentials. The catalyst layers were prepared by different coating techniques as CCMs or GDEs. List of commercial devices utilized to prepare catalyst ink/ powder and test MEAs are provided in table 1. The specification of the MEAs prepared using the different coating techniques along with recipes of the individual catalyst suspension are summarized in table 2.

Table 1: List of commercial devices used in this study.

Device	Function	Supplier
Sonication	Mixing	Elma 50/60 Hz
Cryogenic Mill	Pulverizing	6850 Freeze Mill, Spex Certipep
Hot Press	MEA Assembly	Vogt
Ball Mill	Mixing	Fritsch, Pulverisette 7
Single Cell Hardware	Single Cell Test	Electrochem
Potentiostat	EIS Analysis	Zahner Zennium with PP241 Load

It should be highlighted that MEA preparation was not optimized to obtain highest performance for the individual coating techniques. Rather, the coating techniques were used to prepare MEAs with different cathode microstructure and study the effect of structure on performance limitations. Catalyst powder (HiSPEC 4000 with 40 wt% Pt from Johnson Matthey) was purchased from Fuel Cell Store, and Nafion® XL membrane (28 µm) as well as Nafion® ionomer (5 wt. % dispersion in alcohol-water, eq. wt 1100) were bought from DuPont. For all MEAs the catalyst-to-ionomer ratio was kept at 70:30 (weight based), whereas the ionomer/ carbon ratio is 0.71. Other solvents like ultra-pure (U.P.) water, glycerol, isopropanol and all gases were purchased from VWR. GDLs (25BC Sigracet®) are from SGL Carbon, and Teflon gaskets (205 µm) were purchased from Bohlender. Individual solvent amount is calculated from the weight-based mass ratio with catalyst (Cat). The solvent amount is administered in terms of the weight of the solid catalyst powder. HiSPEC 4000- 40 wt% catalyst and 5 wt% Nafion ionomer were used for catalyst to ionomer ratio was 70:30. The Pt loading for anode and cathode catalyst layer was 0.3 ± 0.01 mg cm^{-2} in every MEA. HPLC grade Ultra-pure (UP) water was purchased from VWR.

Table 2: Summery of the MEAs prepared using different coating techniques for anode catalyst layers and cathode catalyst layer

Method	MEA type	Solvent 1	Solvent 2	Mixing process	Thickness of Electrode, µm	ECSA, $m^2 g^{-1}$
Dry spray	CCM	none	none	Cryo-mill, knife mill	12 ± 4	10
Air brush	GDE	UP water: Cat × 100	Isopropanol: Cat × 100	Ultrasonication	7.5 ± 2	38
Screen print	GDE	UP water: Cat × 5	none	Ultrasonication, roller ball mill	8 ± 2	32
Doctor blade	GDE	UP water: Cat × 3.75	Isopropanol: Cat × 1.75	Ultrasonication	7 ± 2	28
Drop cast	GDE	UP water: Cat × 118	none	Ultrasonication	10 ± 2	11
Inkjet print	GDE	Isopropanol: Cat × 60.8	Glycerol: Cat × 13.33	Ultrasonication	18± 4	8

2.2 Electrode Preparation

It is worth mentioning that, every ink dispersion media is adapted to their individual coating techniques, that results slight changes of solvents. Therefore, different ionomer-catalyst-solvent interaction is expected which is plays significant role to their physical and electrochemical properties. However, this is a requirement for individual coating techniques, as each coating techniques handles different viscosities of ink. Major properties of the different CL preparation techniques, which are used in this study, are provided in the following [61-63]. The electrode fabrication techniques mentioned here do not acquire state of the art performances mentioned in the literature, which requires optimization of each techniques individually, and that is not the scope of this work. Since, it is convenient to calibrate the loading of Pt over GDLs swiftly, which also shows good performances [64], GDEs were prepared in all cases accept from the dry spray as it allows membrane as substrate.

i) Dry Spray Method: Dry spraying method was developed at DLR [51, 52]. Atomized dry catalyst mixture with nitrogen stream coating is sprayed onto the membrane at room temperature. A stainless steel (s.s.) frame was applied to coat the anode first, and then the membrane along with the s.s. frame was flipped carefully to coat on the cathode side. Afterwards, the CCM and the GDL are arranged cautiously and hot-pressed. CCMs were prepared by dry spray because with catalyst powder membrane shows better adhesion capacity than GDL. This dry or powder spray technique is a very fast and environmental friendly MEA production method, where any kind of toxic solvent is avoided. Fig. 1 a) demonstrates a dry or powder spray MEA fabrication device in DLR facility.

ii) Air brush Method: Catalyst with carbon support is mixed with distilled water, ionomer, and another convenient solvent (Isopropanol)[53, 54]. With a spray nozzle, the highly diluted catalyst suspension is then sprayed onto the GDL by means of nitrogen gas flow [55]. GDL or membrane is kept over a suction plate with heating facility, and the temperature is maintained to 105 °C to evaporate the solvent from the surface of the substrate. Fig. 1 b) shows the experimental setup (with a plastic spray gun from Herpa) of an airbrush coating facility used in this work. The nozzle of spray gun and the air pressure plays a very significant role to determine the size of aggregates.

iii) Screen printing method: Screen printing is an automatic coating method to deposit catalyst suspension over GDL or membrane through a mesh or screen[56, 57]. A suction facility is also available in this method to fix the substrate at room temperature. Viscous catalyst suspension is pushed by a couple of squeezes through the screen, which is placed over a substrate. The screen or the mesh is a critical component to control the thickness of the CL and the distribution

of the catalyst suspension. Fig. 1 c) depicts an Aurel screen printer with the meshes from Koenen, which are operated in DLR to fabricate MEAs.

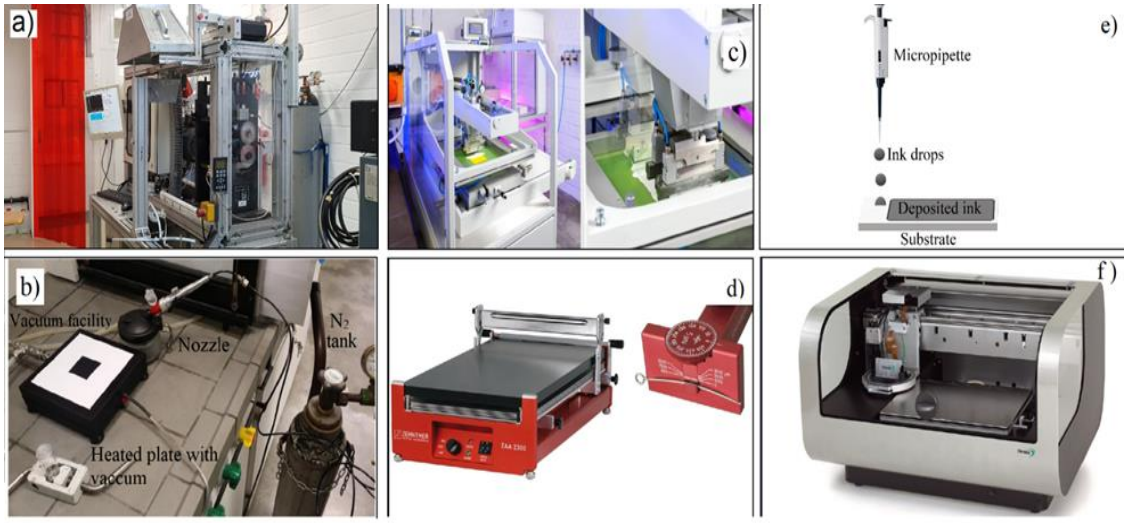

Figure 1: Coating techniques used to fabricate catalyst layer in this study (d[85], f[86])

iv) Doctor blade method: Carbon supported Pt catalyst suspension is coated on the substrate by doctor blading technique in this coating process. A metering blade (applicator) is used to draw across the substrate with viscous slurry at room temperature [58]. Thickness of the CL can be optimized by controlling the elevation of the blade, which is accurately scaled to 85 microns. It is also a widely used, economical and swift MEA fabrication technique, which is displayed in Fig. 1 d) along with a doctor-blade (right) and an adjustable table (Zehntner ZAA 2300). This device also has heating and suction facility.

v) Drop casting deposition: Drop casting deposition is a rudimentary method of coating. The catalyst suspension is prepared and picked up in a micropipette. The catalyst ink is then dropwise disposed from micropipette over a substrate at room temperature. This is a very easy and quick method to fabricate CL with a small active area. Fig. 1 e) demonstrates a schematic of a drop casting technique (pipette drop deposition). This technique was applied to observe the extreme downfall of the coating techniques, moreover, as very small size of CL were prepared to electrochemical and physical characterization.

vi) Inkjet printing: This is a very sophisticated printing method to fabricate PEMFC electrodes; it allows coating of structures, but it is a slow method not suitable for high throughput applications. Inkjet is a piezoelectric printer with high resolution, and it can be operated (ink jet continuously) on demand [59, 60]. An inkjet printer is shown in Fig. 1 f). The ion concentration, nature of solvent and pH dictates the stability of suspension as well as the size of particle aggregates in the catalyst suspension. Consequently, the ink properties are responsible for the

jetting efficiency, the applicability and performance of the CL. We have used a Fujifilm Dimatix DMP 2850 printer with a 10 picolitre cartridge with substrate temperature 60 °C. 100 µm distance was maintained between the printhead and substrate. The jetting voltage was 20V, and the drop spacing to print electrode in this study was 5 µm.

2.3 MEA Preparation

Apart from drysprayed CCMs, all the other GDEs are furthered dried in normal drying oven at 70 °C for 6 hours. After preparation of the catalyst layer the MEA components were assembled by 5 minutes hot pressing at 140 °C and at 650 N cm^{-2} or 6500 kPa pressure. 2 sets of MEAs were prepared by each coating methods and characterized thereby. All fuel cell tests were performed with a commercial cell from Electrochem., which is made of two graphite bipolar-plates with flow-field and a pair of gold coated stainless steel as current collector. Cell specifications are stated in table 3. One of the most important factors in the assembly of PEMFCs is to set the appropriate compressive stress to the cell to balance the conflicting demands of mitigating gas leaks and decreasing contact resistance without damaging the porous components so that optimal performance is obtained [65]. The amount of compression on the GDL affects the contact resistance, the GDL porosity, and the fraction of the pores occupied by liquid water, which, in turn, affect the performance of a PEMFC [66]. In our experiment, we have 20 % compression in gas diffusion media while operating the cell in bipolar plate after clamping. The compression was determined by measuring the thickness of MEA before and after the hot-press.

2.4 Physical Characterization

Scanning electron microscopy: To observe the cross section of MEAs with scanning electron microscopy (SEM), specimens were prepared by cutting approximately 0.3 × 0.3 cm^2 from GDL or CCM. The surfaces of the samples are carefully installed with a carbon tape in the SEM sample holder. The measurement was carried out with a Zeiss UltraPlus, providing an electron beam of 5 kV that allows the analysis of the surface without destroying the ionomer.

Focus Ion Beam Scanning Electron Microscopy (FIB-SEM): Samples were cut into squares of 0.5 × 0.5 cm^2 from the MEA after delaminating the gas diffusion layer manually. After placing the sample inside the FIB-SEM sample holder, the fracture was made by emerging the sample into liquid nitrogen. Measurements were carried out at 1.5 KV EHT with a 30 KV FIB probe. By 20×20 µm cut area the measurements were performed with standard image resolution of 1024×720

pixels. The thickness of each cut is 150 nm. The FIB-SEM images were taken with a Zeiss scanning electron microscope (Neon 40 ESB Crossbeam).

Single Cell test: The MEAs for single cell characterization were tested in an in-house developed test bench. In our test bench, we have two bubbler humidifiers for both anode and cathode gas inlet; moreover, the pressure of the system is regulated after the cell. We have very minute pressure drop before the cell (5 mbar). The MEA test specifications and operating conditions of the experiment are stated in table 3. We started to condition each MEA with 100 % RH (relative humidity), however all the MEAs were tested at 50 % RH to avoid the flooding issue. 1.5 bar absolute pressure was maintained in fuel cell experiments.

Table 3 : MEA test conditions and cell specifications.

Operating conditions and specifications for the single cell test facility			
Teflon gasket thickness			205 micron
MEA compression within bipolar plates, 5mm screws 4 pieces			2 Nm each
Flow channel (Graphite)			Two inlet points and triple channel serpentines
Active area (SI Fig. 7)			1 cm^2
Anode stoichiometry	1.6	Cathode stoichiometry	2.5
Anode outlet pressure	1.5 bar absolute	Cathode outlet pressure	1.5 bar absolute
Anode humidification	50 % RH	Cathode humidification	50 % RH
Humidifier temperature, cell inlet temperature			80 °C, 85 °C
Cell temperature			80 °C

2.5 Electrochemical Characterization

Break-in and polarization curve: After starting the test bench operation each MEA was conditioned in potentiostatic mode at 0.6 V for 1 hour at 100 % RH. Subsequently, humidification was reduced to 50 % RH and further operation was performed in galvanostatic mode for 6 hours with a stepwise increase of current density to 250, 500 and 1000 mA cm^{-2}. Break-in step is considered completed if voltage change is lower than 10 mV h^{-1} at a current density of 1000 mA cm^{-2}. Polarization curve was recorded using a load (Hoecherl and Hackl GmbH) in galvanostatic mode. The cell voltage was monitored as function of the current density with a dwell time of 3 min and with increments of 25 mA cm^{-2} (range: 0 to 100 mA cm^{-2}) followed by steps of 100 mA cm^{-2} (range: 100 mA cm^{-2} to until cell voltage drops to ~200 mV. 2 sets of data has been recorded for each measurement, and the average value has been represented here. The test conditions used for characterization of MEAs are stated in Table 3. It should be stressed that the MEAs are deliberately not operated under differential conditions in order to obtain contribution from

different loss mechanisms to the performance of MEAs. Under differential conditions higher performances would be observed but then the microstructures would not be evaluated with regard to real operation conditions of a MEA.

Impedance Analysis: Electrochemical Impedance Spectroscopies (EIS) were performed for all MEAs and the equivalent circuits are simulated by the Thales software from ZAHNER-Elektrik GmbH & Co. KG. Nyquist and Bode plots were determined within the frequency range from 100 mHz to 100 KHz in three different current densities at 0.1, 0.5 and 1 A cm^{-2} with appropriate (5 to 10 % of current) amplitudes. The measurement regime was linearized by stabilizing the cell for 10 minutes prior to EIS measurement. Anode functions as a reference and counter electrode, whereas cathode acts as a working electrode. Nyquist plots are formulated with the real impedance in the X axis and imaginary impedance in the Y axis. However, the bode plot consists of three components: impedance with phase angle in Y axis and frequency in X axis.

Ionic Conductivity: The ionic impedance of the electrodes was also evaluated by EIS using electrochemical test stations from ZAHNER-elektrik GmbH & Co. KG. In order to characterize ionic impedance, 12 ml min^{-1} of nitrogen and hydrogen gas were fed into cathode and anode with 100% humidification. To avoid the contribution from ORR charge transfer, cathode compartment is purged with nitrogen during the measurement. Consequently, the charging of the catalyst's double layer with the ionic resistance of CL becomes dominant. Ionic impedance was measured in 1 V potentiostatic condition with 10 mV amplitude from 500 mHz to 100 KHz frequency. A Warburg-like response (45° slope) is observed at high frequencies, corresponding to the ionic conductivity (both for electron and proton) in the catalyst layer [67, 68]. At low frequencies, the impedance plot curves up to a limiting capacitance response (vertical) which corresponds to the total capacitance of the catalyst layer. The ionic resistance, Rionic, can be obtained from the length of the Warburg-like region projected over the real impedance (Z´) axis (= Rionic/3) with the aid of transmission line model.

Cyclic Voltammetry: Cyclic voltammograms (CVs) were obtained at 1.5 bar pressure and 80 °C with 20 mV s^{-1} slew rate between 60 mV to 1 V. The electrochemical active surface area for each of the cathodes can be measured by calculating the adsorption (used in this work) or desorption of the hydrogen on Pt surface. To measure cathode CV, minimum but equal amount of H2 and N2 gas (12 ml min^{-1}) were fed with 100 % humidification to anode and cathode. The cathode side of the MEA is triggered by a sweep of potentials (60 mV to 1 V) where the coulombic charge for hydrogen desorption was used to calculate the active surface area of platinum considering the charge needed to adsorb or desorb a monolayer of H^+ on polycrystalline platinum [69].

Thereupon it is possible to obtain the electrochemical surface area (ECSA) of the cathode through the following equation:

$$ECSA = q\_Pt/(\Gamma \cdot L) \quad (I)$$

Where, qPt is the charge density (C cm^{-2} electrode) obtained from the CV experiment; the charge required to reduce a monolayer of protons on Pt, Γ = 210 µC cm^{-2} and the Pt content or loading in the electrode, L in gPt cm^{-2} electrode.

3. Results and Discussion

Current-voltage (I-V) polarization curves in fig. 2 a) show the individual performances of the MEAs prepared with different coating techniques. The open circuit voltages (OCV) are around 920 mV. With slightly increasing current density (up to 0.1 A cm^{-2}) the differences of the performances become obvious due to very different kinetic activity of the MEAs. Clearly the airbrush electrode showed the smallest kinetic losses and highest ECSA (see Table 2), whereas drop casted MEA and inkjet printed MEA exhibit strongest kinetic limitations. It is very interesting that even though performances of drop cast and inkjet printed MEAs are substantially lower than the one of dry sprayed MEA, the ECSA of these three MEAs are very similar (compare Table 2). This clearly suggests that ECSA is only one factor determining electrode kinetics he inkjet printed MEA, on the other hand, has a low slope in the linear region > 0.5 A cm^{-2} and therefore outperforms the dry-sprayed MEA for current densities > 0.75 A cm^{-2}. This behavior was also reported by the Shukla et. al. [70]. It is worth mentioning that, the ECSA value demonstrated in this study is not state of the art mentioned in the literatures due to the fact that these coating techniques and catalyst ink were not in their fully optimized state[71, 72].

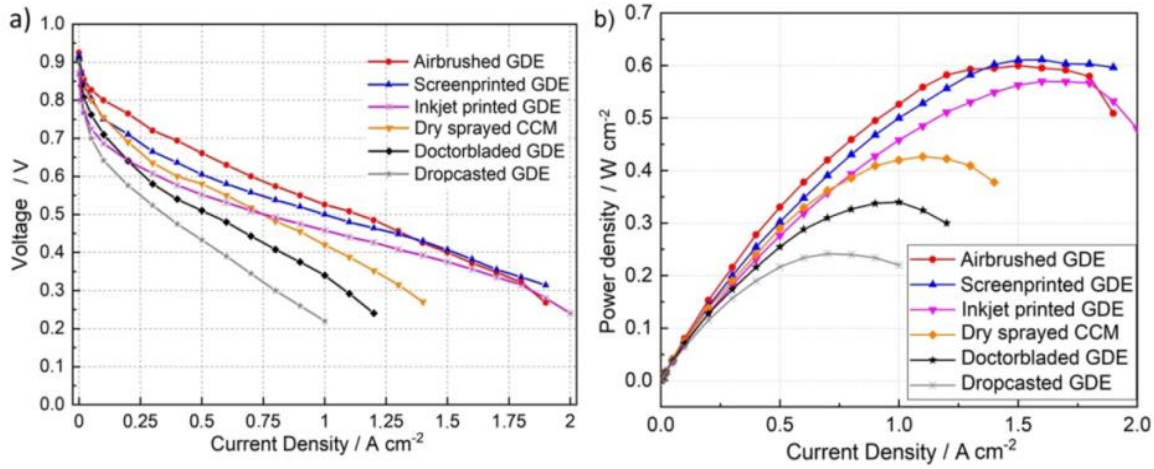

Figure 2: a) I-V curves of the different MEAs prepared with different coating methods, b) power curves of the different MEAs. Pt Loading: 0.3 mg cm^{-2}, temperature 80 °C, 50 % RH, Pressure 1500 mbar absolute, Stoichiometry λ_{H2} 1.6, λ_{air} 2.5.

Penetration of the catalyst suspension into the MPL during coating mainly causes this reduction of ECSA. MEA formulated with doctor-blade methods show poor performance in kinetic region as well. At high current density > 1.5 A cm^{-2} airbrushed, screen-printed and inkjet-printed MEA shows largely linear characteristics; all other MEAs suffer ohmic and substantial mass transport losses. According to power density curve in fig. 2 b), drop-casted MEA shows very poor performance all along. Due to fast kinetics of the anode catalyst layer (for all MEAs anode CL is identical to cathode CL) the losses are clearly ascribed to the cathode catalyst layer. In the following paragraphs, we will try to evaluate the reasons of the diverse performance yet similar loading of platinum in the differently prepared electrodes.

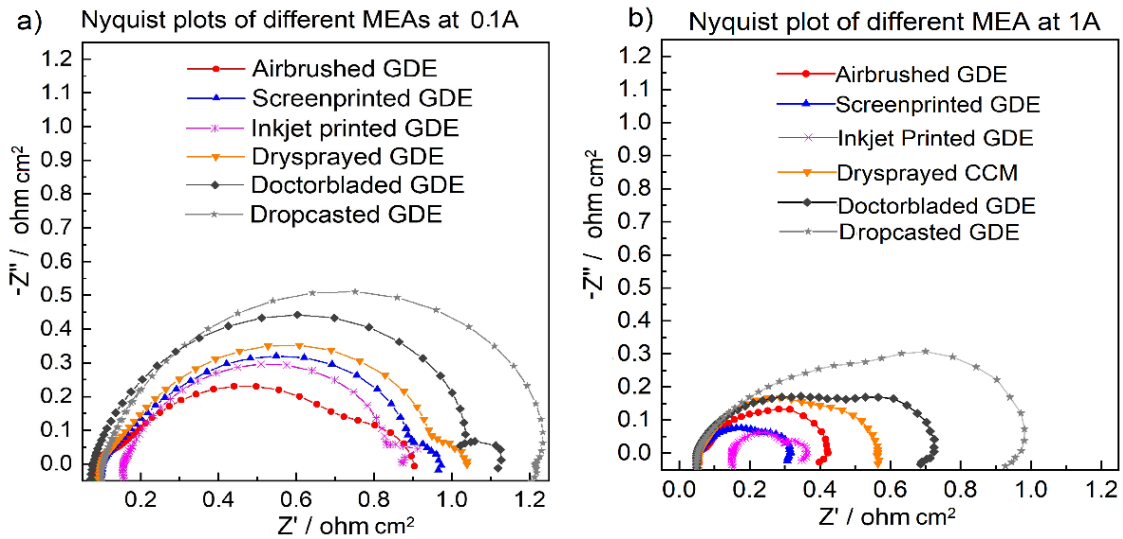

Figure 3: Nyquist plot of the different MEAs recorded at a) 100 mA cm^{-2} and b) 1 A cm^{-2}.

Electrochemical impedance spectroscopy analysis is a suitable tool to diagnose the different contributions to the voltage loss in the MEAs. Moreover, EIS is a suitable nondestructive in-situ technique, which analyzes polarization behavior with individual time constants. Figure 3 shows Nyquist plots which consist of plotting real impedance in X axis and the negative imaginary impedance in Y axis, and the frequency value decreases from left side of X axis to the right side. Fig. 3 a) displays a Nyquist plot at low current density (0.1 A cm^{-2}), where the kinetics overpotential is dominating. Fig. 3 b) demonstrates a Nyquist plot at high current density (1 A cm^{-2}) with predominant diffusion or mass transport polarization limitation. At low current density a very minute contribution of anode activation in high frequency region of the graphs is present. However, in some cases this contribution is suppressed (not visible due to very large kinetic overpotential arc) when the cathode charge transfer resistance is very high, and the semicircle of cathode charge transfer overlaps with the anode charge transfer. In this case, the first big semi-circles are responsible for kinetic impedance, and clearly highlight the catalyst

performance of the electrodes. Larger kinetic impedances can be explained by lower utilization, or more precisely lower effectiveness of the catalyst layer. This phenomenon suggests that even though we have a similar loading of platinum in all electrodes, the access to Pt surface is limited due to different microstructures of the coating methods. Individual coating techniques causes noticeable changes in the microstructure and the ionomer distribution in the catalyst layer, and consequently yields diverse results. At high current density (Fig. 3 b), the second semi-circle became enlarged, which is responsible for diffusion related impedance originated mostly from electrode and GDL [73, 74]. Due to the maneuvering of 1 cm^2 we may neglect the contribution of diffusion coming from channels. Interestingly the inkjet-printed MEA shows the lowest diffusion impedance, which is also reflected in a superior performance in the polarization curves at high current densities. However, in both fig. 3 a) and b), inkjet-printed electrode shows a very high ohmic resistance (X axis intercepts). This is due to the high number of layers (28 layers) we needed to coat to achieve 0.3 mg cm^{-2} Pt loading. Table 2 provides the distribution of thicknesses for all CCMs or GDEs. The 28 layers (20 ± 4 µm) apparently provide a larger interfacial resistance in the electrode. As a consequence, the rather low slope of the polarization curve observed at > 0.5 A cm^{-2} in fig. 2 a) indicates that mass transport resistance, and kinetic charge transfer are particularly low for the inkjet printed MEA, and it can even be postulated that ohmic resistance is reduced at high current densities (Fig. 3 b). Nevertheless, a lower kinetic performance is a typical behavior from inkjet printed MEAs [60, 70]. On the other hand, dry sprayed, doctor

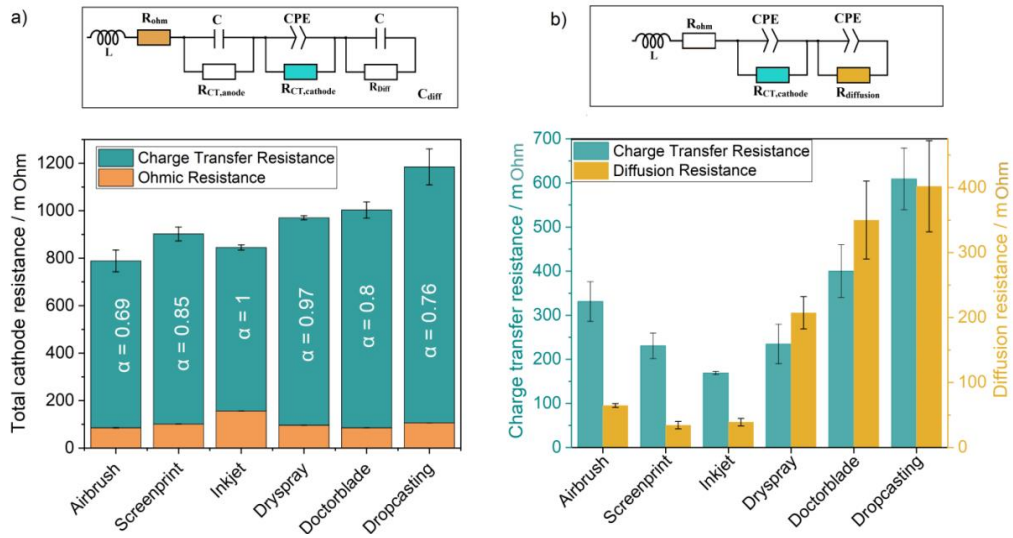

Figure 4: Equivalent circuit of the Nyquist plot from a) low current density: Constant phase element (CPE) is used to replicate cathode charge transfer; whereas capacitance is applied for anode activation and diffusion as their contributions are minimal. Bars are the added-up values of the R_{ohm} and R_{CT}. The phase angle of the CPE, α is depicted in the bar. b) High current density: activation RC element (for anode) is removed as anode contribution is negligible, and CPE is used (within RQ circuit) for both charge transfer and diffusion phenomenon as they dominate at high current density. The error bars correspond to the fitting error attributed to the individual component.

bladed and drop casted GDE display increasingly larger arc related to mass transport losses, which is expected as the I-V curve bend down at higher current densities. Airbrush and screen printed MEAs show an intermediate behavior regarding transport losses.

Fig. 4 shows the equivalent circuits and their associated significant values after simulation. In all cases the error of simulation has been limited to approximately 3 % after fitting. We have used a single model concept but two complementary equivalent circuits according to the contribution of elements in different current densities. In the equivalent circuit (E.C.) the first component is an inductor which was considered for a good fitting as its contribution from wiring influences high frequency time constants. The next element of the E.C. is a resistance, which represents ohmic losses of the circuit as well as the cell. At low current density, we experience a little contribution from anode charge transfer and no significant diffusion limitation. Figure 4 a) demonstrates an E.C. appropriate for low current density where ohmic (indicated as orange) along with cathode charge transfer (indicated as turquoise blue) dominates and represented by a RQ element (resistance with constant phase element). The individual phase angle or α value of different MEAs is mentioned in the bar. However, the anode kinetics and concentration loss, which are very limited in this domain are represented with simple RC (resistance with capacitance) element. A simple RC element also has been integrated to simulate the very limited contribution of diffusion. However, RC elements can also be considered as RQ elements, where the alpha value of the constant phase element is “1”. On the contrary, at high current density the anode contribution is negligible due to the dominating cathode charge transfer and mass transfer effects. Hence, the first RC element (for anode charge transfer) is eliminated from the E.C., which is portrayed in fig. 3 b). However, due to higher diffusion limitation at high current density, a diffusion element (RQ) is used in series together with the RQ circuit that represents mass transfer. In our study, this E.C. with diffusion element is necessary to understand transport limitations of differently prepared electrodes at high current density. Nevertheless, the individual error bars determined in the fitting from individual component in the E.C. are also given in both fig. 4 a) and b). At low current density, ohmic resistance and cathode charge transfer resistance contribute most significantly to the voltage loss of the cell as demonstrated in fig. 4 a). The inkjet printed MEA shows higher ohmic resistance compared to other MEAs in the simulated E.C. fitting (Fig. 4 a), which is also acknowledgeable from Nyquist plots we received from the experiments. This is due to the higher number of catalyst layer required to apply on the substrate to obtain 0.3 mg cm^{-2} Pt loading. Apart from that, other MEAs show more or less similar ohmic behavior that we can also presume from the X axis intersection at high frequency zone in the Nyquist plot. However, aside from the inkjet printer, we can see a gradual increase

in charge transfer resistance from airbrush to drop casting. From both of the polarization curve and Nyquist plot, we can assume that, even though the performance of the inkjet printed MEA is poor in the kinetic region, it improves gradually with increasing current density due to the superior charge transfer properties of cathode. We observe the same phenomenon also by comparing both E.C. simulations in fig. 4. For inkjet printed electrode we have the alpha value "1", which suggests an ideal RC (with capacitance) element, and the charge transfer resistance is also lowest comparing to electrodes prepared with other MEA preparation techniques. On the other hand, E.C. at high current density demonstrates slightly different trend. In accordance with the previous study at low current density screen printed, inkjet printed and airbrushed MEA shows very low diffusion resistance consecutively. However, the diffusion resistance increases drastically from dry sprayed MEA to doctor bladed MEA and finally reaches at the highest in drop casted MEA. The trend is following: screen printing ≤ inkjet < airbrush < dry spray < doctor blade < drop casting. Besides, the RQ element attributed to the charge transfer overpotential shows that the dry-spray and the screen-printed MEA exhibit an analogous resistance, which are lower than airbrushed MEA. Here, electrode prepared with the inkjet printed method appeared with lowest charge transfer resistance. It can be speculated that the higher values of diffusion resistance in dry spray, doctor blade and drop cast technique is due to the larger agglomerates and ionomer films formed during coating with large tortuosity factors for the reactant gases. In summary, the time constant regarding the diffusion resistance or mass transport phenomenon influences the performance to a great extent at higher current density.

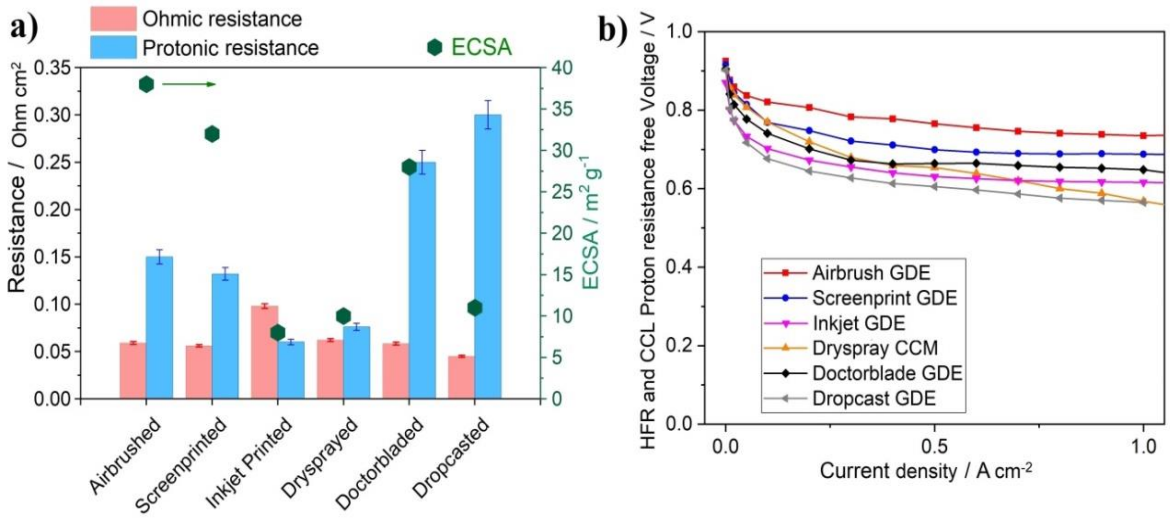

Figure 5: a) Dual axis bar chart of ohmic and protonic impedance of different catalyst layers with ionic conductivity measurement by EIS, and scatter plot of the electrochemical active surface area value from the hydrogen desorption measurement of different cathode catalyst layers with cyclic voltammogram; b) I-V polarization curves at 50 % RH with cell voltage, which is corrected by high frequency resistance (HFR) and protonic resistance (Rp) through cathode catalyst layer.

Fig. 5 a) exhibits a partial scatter plot (for 2nd axis) constructed from the electrochemical active surface area values of the different cathode electrodes. We have noticed an uncommon behavior of inkjet printed and dry sprayed electrode in this case. The measured ECSA value of the aforementioned electrodes provides a very low active surface area, although having a relatively good cell performance. The cyclic voltammetry curves of the MEAs from where the ECSA were measured are included in SI fig. 5. This anomaly shows that ECSA is not the determining factor for performance but only one parameter among many others. However, typical ECSA values for CL with 0.3 mgcm^{-2} are in the range 40-80 m^2 g^{-1} according to literatures [75-78]. The ECSA reported in our paper are in the range 10-40 m^2 g^{-1}, which is substantially lower. However, the intention was to obtain CLs with a broad ECSA variation to analyze the impact on performance. The ionomer microstructure plays an important role for the effectiveness of the catalyst layer which can be high even with low accessible catalyst area. For the dry sprayed MEAs we speculate that due to the bigger agglomerate size ECSA is low. Furthermore, inkjet printed cathode has a high number of individual layers, which might also lead to a coverage of catalyst particles with thicker ionomer film, again leading to low ECSA. Ionic conductivities are measured and illustrated in fig. 4 with a bar chart. Ohmic resistance in the CL is similar to total ohmic resistance of the MEA. Here, the drop casted CL shows the lowest ohmic resistance, since it is prepared directly from a single layer, which is very compact and thin. Furthermore, proton conductivity is high in case of airbrush and screen-printed CL, when inkjet printed and dry sprayed CL show the highest proton conductivity through the electrode. Conversely, doctor bladed and drop casted CL possesses very low proton conductivity that is predicted from the performance and proton conductivity measurement by EIS.

Table 4: Chart of characteristic points between actual polarization curves and IR-free polarization curves derived from the differently prepared but similar Pt loaded MEAs tested in 1 cm^2 cell.

	Actual performance			HFR and Rp free performance		
	Peak Power Density, W cm^{-2}	Current Density at 0.6 V, A cm^{-2}	Voltage at 1 A cm^{-2}, V	Peak Power Density, W cm^{-2}	Current Density at 0.8 V, A cm^{-2}	Voltage at 1 A cm^{-2}, V
Airbrush	0.6	0.7	0.53	1.26	0.23	0.735
Screenprint	0.61	0.52	0.5	1.27	0.067	0.688
Inkjet print	0.57	0.33	0.46	1.10	0.011	0.616
Dryspray	0.43	0.4	0.42	0.67	0.061	0.568
Doctorblade	0.34	0.27	0.34	0.74	0.032	0.648
Dropcast	0.24	0.17	0.22	0.56	0.011	0.565

Fig. 5 b) and table 4 illustrate polarization curves with HFR and Rp corrected voltages. These curves show performances excluding the loss contributions associated to electronic and protonic transport. Dry sprayed MEA still shows a declining performance loss due to the bigger agglomerate size in the catalyst layer. Moreover, poor initial performance of inkjet printed MEA prevails up to 1 A cm^{-2} and does not deteriorate much thereafter [60]. Nevertheless, the sequence of performance is more or less analogous with the real polarization curves. Table 4 reports the numerical values of the significant characteristic points derived from the actual pol curves and the IR-corrected pol curves. Peak power and voltage at 1 A current are exhibited in both cases. It is noted that current densities at 0.8 V are given for IR free performance, however, current densities at 0.6 V are given for actual performances some of the MEAs IR-free performances do not reach down to this value.

In this work, each fabrication method uses slightly different solvents or solid-solvent ratio, therefore there might be slightly different ionomer-catalyst-solvent interactions. However, this matter is not discussed here, as the effect will intricate the correlation. Scanning electron microscopy images in fig. 6 illustrate the microstructure of the CL surface. Catalyst layer surfaces from different preparation techniques are depicted at 500 x magnification. The SEM image of airbrush (Fig. 6 a) clearly exhibits a very porous electrode, which however also consists of a few random agglomerates.

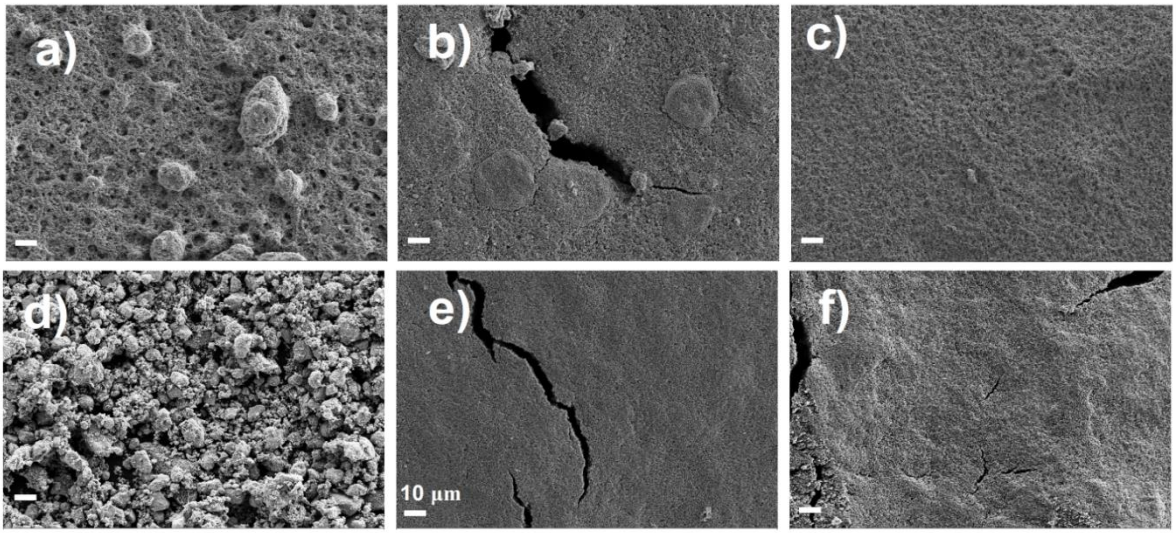

Figure 6: SEM images of 6 different catalyst layer surfaces (pristine) prepared through individual coating methods. The magnification is 500 x, and the white scale bar represents 10 µm; a) airbrush, b) screen print, c) inkjet print, d) dry-spray, e) doctor-blade, e) drop-cast.

When the solvent during the spraying process does not completely evaporate before reaching the substrate, these types of agglomerates could form on the surface of the substrate. This issue can be avoided by improving the spraying nozzle (adapting narrower and finer opening) or applying more volatile solvent. Fig. 6 f) also shows a very compact CL prepared with the drop-

casting method. These last two methods have in common that they consist of a single compact coated layer without micro pores on their surface. This phenomenon is clearly highlighted by the large diffusion resistance of doctor blade and drop casted electrodes. Moreover, the drop casted CL has a very uneven surface (from manual deposition of droplets), which is also a probable cause for its weak ohmic efficiency due to poor contact. Therefore, in this work the overall MEA performance of both doctor blade and drop cast coating technique (Fig. 6/7 e and f) is poorer compared to other coating methods. Fig. 6 b) demonstrates a CL prepared with screen printing, which shows a smooth surface but with large cracks in the CL. These cracks and some hidden droplet type areas are caused by the screen. In fig. 6 c), we can see a very smooth CL, which was prepared with inkjet printer. CL fabricated by inkjet printer is the most homogeneous among the all fabricated CLs. A very rough and agglomerated surface of individual aggregates is shown in fig 6 d) for dry powder spraying. We assume every individual body is a mixture of Pt/C and ionomer in this case. Fig. 6 e) depicts a doctor bladed CL surface, which looks very homogeneously coated besides some small cracks, but very compact layer (i.e. larger structures of several microns are not visible in contrast to fig. 6 a) or d)). This study does not discuss the effect of the cracks in the MPL or CL any further as it will open an additional discourse.

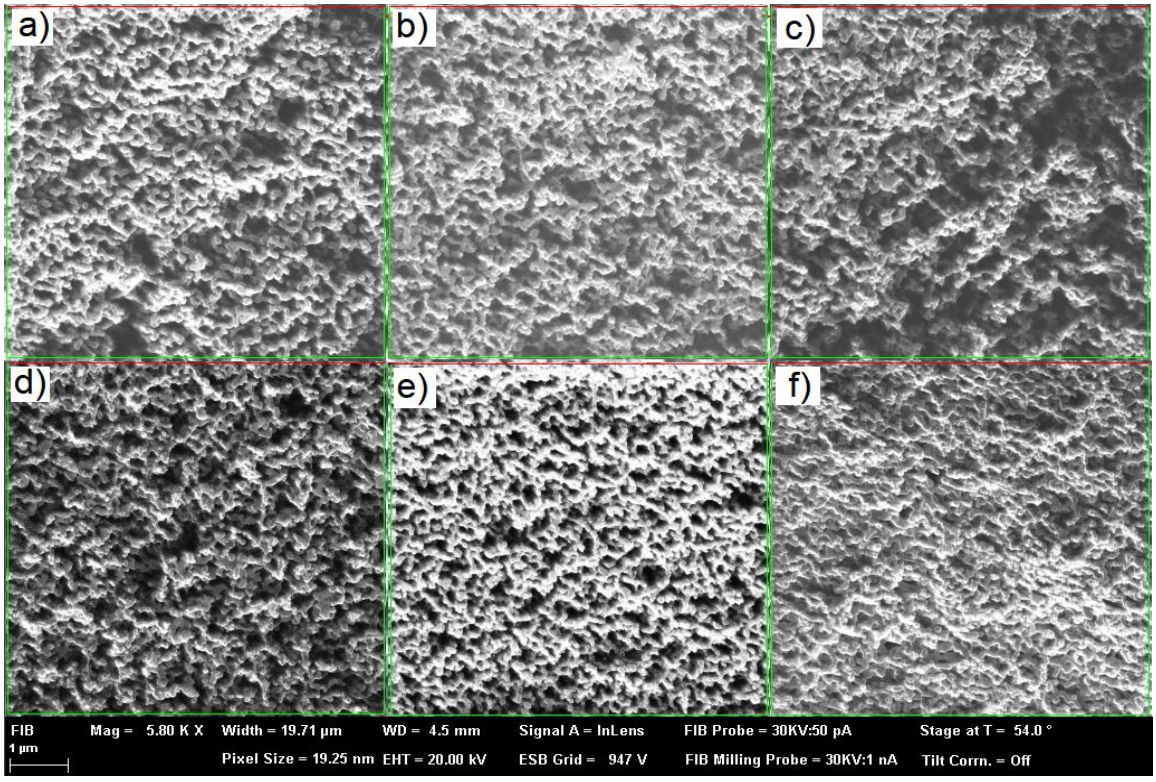

Figure 7: FIB-SEM images of 6 different catalyst layer surfaces prepared through individual coating methods. a) airbrush, b) screen print, c) inkjet print, d) dry-spray, e) doctor-blade, f) drop-casting. The image resolution in each scan is 19.25 nm per pixel.

The definition of the following parameters would be useful to understand the correlations. Porosity: it is the measure of void spaces in a material; permeability: it is the ability for fluids (liquid or gas) to flow through the material; diffusivity: this is a measure of the rate at which particle or fluids can diffuse or spread; tortuosity: it is a property of path of fluid or particle being tortuous (having turns or twisted).

In addition to the SEM analysis of the samples, the microstructures were further analyzed by microstructure reconstruction and analysis using FIB-SEM image data. For this 2D image slices from FIB-SEM with a resolution of 19.25nm were first postprocessed using the open-source software Fiji [79]. After removal of artificial shifts, proper image alignment to 2D image stack and brightness correction the image data was further postprocessed with GeoDict®[80]. The quality of the image data was then enhanced by application of a smoothening filter followed by a sharpening filter. The 2D image stack was then transformed into a 3D image with a voxel resolution of 19.25 nm using trilinear interpolation. The microstructure reconstruction was then finalized by a binarization procedure using the Otsu method [81]. The resulting binarized microstructure was then used as an input geometry for GeoDict® to determine its effective transport parameters such as porosity, diffusivity, tortuosity and permeability. This workflow of microstructure reconstruction from FIB-SEM data and subsequent derivation of effective transport parameters was the same for all samples, and is described in detail in the Supp Info.

Table 5: Median pore sizes as determined by GeoDict® for the reconstructed CL microstructures based on FIB-SEM image data.

	Airbrush	Doctorblade	Dryspray	Inkjet	Screenprint
D50 / nm	344.26	298.227	352.89	404.883	420.881
$\boldsymbol{Kn = \frac{\lambda_{air}(T = 20°C)}{D50}}$	0.1975	0.228	0.1927	0.1679	0.1616

Table 5: Median pore sizes as determined by GeoDict® for the reconstructed CL microstructures based on FIB-SEM image data.Table shows the media pore diameters as determined by GeoDict® for the reconstructed microstructures for the different samples. It can be seen, that for all samples the average pore is larger compared to literature values [23, 82]. By relating the mean free path length ($\lambda_{air}(T = 20°C) = 68nm$) to these average pore sizes one can see that diffusive transport within the microstructures is not anymore fully dominated by Knudsen diffusion $Kn \to 0$, but resides more in the transitional regime between Knudsen $Kn \to 0$ and bulk diffusion $Kn \to \infty$. This was considered for the diffusivity simulations in GeoDict® by determining the effective diffusivity as the harmonic average of the Knudsen and bulk diffusivity

(Bosanquet approximation [83]. More details on the determination of the diffusivity are provided in the Supp. Info. [84-86].

Table 6 demonstrates a classification based on pseudo-quantitative assessment of the MEAs those are mentioned in this manuscript. A synopsis of limitations, which contributes to the voltage loss, can be estimated from this table. It is important to note that information from different characterization techniques mentioned in this study (apart from polarization curve) has been converged in this table into a uni-free simplified classification. The two left columns show the characteristics or performance functions divided in three segments according to three fundamental factors of voltage loss: kinetics, ohmic and diffusion.

Table 6: Subjective representation of the intrinsic characteristics of different MEAs (○○○○○ Very high, ○○○○ high, ○○○ medium, ○○ low, ○ very low), with weighting factor. Calculation is provided in the supporting information.

MEA Characteristics		Airbrush	Screen printing	Inkjet printing	Dry spray	Doctor-blade	Drop-casting
Kinetic	ECSA	●●●●●	●●●●	●●	●●	●●●●	●●
	Kinetic performance	●●●●●	●●●●	●●●●●	●●●	●●	●
Ohmic	CL Proton conductivity	●●●●	●●●●	●●●●●	●●●●●	●	●
	Ohmic efficiency	●●●●	●●●●	●●	●●●●	●●●●	●●●
Diffusion	Porosity	●●●	●●●●	●●●●●	●●●	●●	●●
	Diffusion properties	●●●●	●●●●●	●●●●●	●●●●	●●●	●●●
	Total mpp	25	25	24	21	16	12

In the top row the different MEA preparation techniques applied in this study are given. In the table 6, the higher the number of dots in each box, the larger is the efficacy (positive effect) on certain function or characteristics that is mentioned in the left-first column. Since we were not able to analyze the FIB-SEM images for the drop-casted CCL's, we therefore assumed the porosity of drop-casted sample to be comparable to that of the doctor-blade sample. Considering other parameters and the performance, this approximation is in-line with our previous studies. We used the numerical value from ECSA, charge transfer of cathode (from E.C.), protonic impedance, ohmic resistance, porosity and the diffusion resistance (from E.C.) respectively to construct this table. At first, for each characteristic (row), we summed up the numerical (experimental) values belonging to individual MEAs. Then, we calculated the

percentage of the individual characteristics for each MEA based on the summation. Next, we determine the median of the percentage from each characteristic. Finally, by considering the percentage of increase or decrease from the median, we referred a scale on this, and the scale attributes to the number of dots. As an example, if our median represents 3 dots, 10 % increase from the median means 4 dots, and 20 % increase from the median means 5 dots. On the contrary, if there is a 10 % reduction from our median value, it is attributed to 2 dots, and 20 % reduction attributes to a single dot. The sum of these points for each MEA (vertical summation of dots in the Table 6) is used for classification and named as MEA performance point (mpp). The scales percentages, which are applied to determine the dots, are also mentioned in the supporting information (SI Table 2). If we consider a single point for each dot in the table, we obtain the following mpp - Airbrush: 25, screen print: 25, inkjet: 24, dry spray: 21, doctor blade: 16, drop cast: 12. Certainly, this classifiction of different electrodes is well harmonized with the final performance or I-V curve demonstrated in Fig. 2 a).

Fig. 8 (a) links the measured peak power density of the different MEA samples to their effective transport parameters (porosity, permeability, diffusivity, inverse tortuosity. The drop-casted CCL was very thin after delamination of the GDL; as a result, the number of FIB-SEM images was not high enough for a reasonable microstructure reconstruction and further analysis with GeoDict. Based on this correlation we can see that an increase in the porosity, permeability, diffusivity and a decrease in tortuosity promotes higher performance. Moreover, it is clearly highlighted in

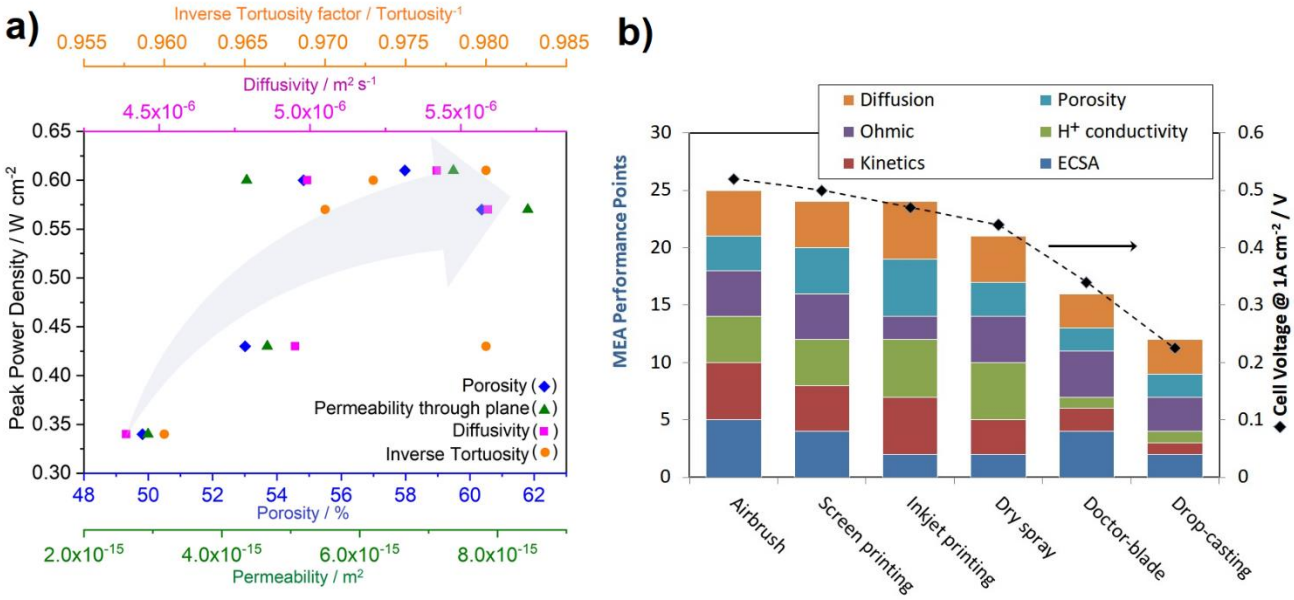

Figure 8: (a)Effective transport parameters from FIB-SEM analysis with GeoDict and their influence on the measured peak power density derived from different coating techniques. The grey arrow is a guide to the eye, (b) Cell voltage at 1 A cm^{-2} versus M performance points (mpp). Determination of mpp (see Table 6) is provided in the text.

Fig. 8 (a) that there is a threshold value after which the performance does not increase further. However, reducing the tortuosity similarly increases performance to a certain degree, and reducing from the optimum value certainly reduces the performance.

Apparently, the cell voltage at 1 A cm^2 is proportional to mpp as shown in fig. 8 (b). In fig. 8 (b) membrane performance point (mpp) of each MEA is plotted along with their voltage at 1 A cm^{-2} current density (second Y axis). All the MEAs prepared with different coating techniques are indicated with their names. Here we can observe a very good correlation between the defined characteristics and the voltage loss in the operated MEAs. Additionally, this correlation is closely compliant to other current densities also. Consequently, this study also shows a very good agreement with the I-V graph or polarization curve. The indicated analysis will help individual readers to make an outline of this investigation, and assist individuals to tailor PEM electrode according to their available resources. Therefore, in this article it is clearly highlighted that it is possible to make a linear relation (suppl. Info SI fig. 6) between the parameters of coating techniques and the performance of the PEMFC even if all properties are equally weighted in this classification.

4. Conclusion

The overall objective of the present work is to evaluate the effect of CL properties on PEMFC performance limitations and to study the effect of fabrication methods of catalyst layer for PEMFC applications. In this context parameters that influence significantly PEMFC operation were identified, which should be taken care of when tailoring cathode CL. Breaking this down to further details, the electrochemical and physical properties of the individual coating techniques, namely airbrush, screen printing, inkjet printing, dry-spraying, doctor-blade, and drop casting were assessed. It is evident that the microstructure of the CL and its intrinsic properties contribute significantly to the transport limitation and as a consequence to the overall performance. This paper also shows the correlation of structural and electrochemical properties of catalyst layer with cell performance.

The results demonstrate that the airbrushed and the screen-printed electrode had highest performance due to the low ohmic and diffusion resistance along with enhanced proton conductivity through CL. The lowest performance was observed for the doctor-blade and drop-casting techniques and the relevant contributions were identified, e.g. particularly low protonic

conductivity. Microstructure investigations illustrate that the airbrush CL exhibited a very porous electrode, which however also consisted of random agglomerates. Intrinsic CL transport properties, such as porosity, permeability, diffusivity, and inverse tortuosity were calculated by analysis of FIB-SEM images using GeoDict®. A comparison of peak power density and effective transport parameters of the CL shows that an increase in permeability, diffusivity and porosity correlates strongly with increasing performance. A threshold value for these individual properties was identified, after which the performance does not increase any further. A dependency between the CL properties obtained by using the different coating techniques and the performance of the PEMFC is apparent. This may help to optimize coating techniques, and therefore to increase MEA performance along with lifetime.

However, it is worth mentioning that none of the six coating methods used in this study have been optimized to yield the highest performance. In other literatures, readers can come across very high MEA performance with the stated techniques, if they are well optimized. Moreover, poor control of humidification or water management within the MEA can cause substantial loss and instability in voltage, which is not reported in this essay. A further investigation regarding limiting current study to determine the oxygen transport resistance will be carried out in upcoming studies.

5. Acknowledgements

Krishan Talukdar acknowledges financial support by DLR.DAAD research fellowship. The authors thank Siegfried Graf for building up and maintaining the fuel cell test benches and Ina Plock for her technical support with SEM images.

6. References

[1] I. Staffell *et al.*, "The role of hydrogen and fuel cells in the global energy system," *Energy & Environmental Science,* 10.1039/C8EE01157E vol. 12, no. 2, pp. 463-491, 2019.

[2] B. C. Steele and A. Heinzel, "Materials for fuel-cell technologies," *Nature,* vol. 414, no. 6861, pp. 345-52, Nov 15 2001.

[3] G. Renouard-Vallet, M. Saballus, G. Schmithals, J. Schirmer, J. Kallo, and K. A. Friedrich, "Improving the environmental impact of civil aircraft by fuel cell technology: concepts and technological progress," *Energy & Environmental Science,* vol. 3, no. 10, p. 1458, 2010.

[4] A. Bauen and D. Hart, "Assessment of the environmental benefits of transport and stationary fuel cells," *Journal of Power Sources,* vol. 86, no. 1-2, pp. 482-494, 3 2000.

[5] S. J. Peighambardoust, S. Rowshanzamir, and M. Amjadi, "Review of the proton exchange membranes for fuel cell applications," *International Journal of Hydrogen Energy,* vol. 35, no. 17, pp. 9349-9384, 9 2010.

[6] D. Papageorgopoulos, "<plenary_fuel_cell_papageorgopoulos_2019.pdf>," *Fuel Cell R&D Overview,* 2019.

[7] S. T. Thompson and D. Papageorgopoulos, "Platinum group metal-free catalysts boost cost competitiveness of fuel cell vehicles," *Nature Catalysis,* vol. 2, no. 7, pp. 558-561, 2019.

[8] R. Chenitz *et al.*, "A specific demetalation of Fe–N4 catalytic sites in the micropores of NC_Ar + NH3 is at the origin of the initial activity loss of the highly active Fe/N/C catalyst used for the reduction of oxygen in PEM fuel cells," *Energy & Environmental Science,* vol. 11, no. 2, pp. 365-382, 2018.

[9] R. O'Hayre and F. B. Prinz, "The Air/Platinum/Nafion Triple-Phase Boundary: Characteristics, Scaling, and Implications for Fuel Cells," *Journal of The Electrochemical Society,* vol. 151, no. 5, pp. A756 11 K. Karan, Interesting Facets of Surface, Interfacial, and Bulk Characteristics of Perfluorinated Ionomer Films, Langmuir, , DOI:10.1021/acs.langmuir.8b03721., 2004.

[10] K. Karan, "Interesting Facets of Surface, Interfacial, and Bulk Characteristics of Perfluorinated Ionomer Films," *Langmuir,* vol. 35, no. 42, pp. 13489-13520, Oct 22 2019.

[11] H. Liu, W. K. Epting, and S. Litster, "Gas Transport Resistance in Polymer Electrolyte Thin Films on Oxygen Reduction Reaction Catalysts," *Langmuir,* vol. 31, no. 36, pp. 9853-8, Sep 15 2015.

[12] N. L. Garland, D. C. Papageorgopoulos, and J. M. Stanford, "Hydrogen and Fuel Cell Technology: Progress, Challenges, and Future Directions," *Energy Procedia,* vol. 28, pp. 2-11, 2012.

[13] E. A. Ticianelli, C. R. Derouin, A. Redondo, and S. Srinivasan, "Methods to Advance Technology of Proton Exchange Membrane Fuel Cells," *Journal of The Electrochemical Society,* vol. 135, no. 9, pp. 2209-2214, 2019.

[14] J.-H. Wee, K.-Y. Lee, and S. H. Kim, "Fabrication methods for low-Pt-loading electrocatalysts in proton exchange membrane fuel cell systems," *Journal of Power Sources,* vol. 165, no. 2, pp. 667-677, 2007.

[15] Y. Yoon, "Effect of pore structure of catalyst layer in a PEMFC on its performance," *International Journal of Hydrogen Energy,* vol. 28, no. 6, pp. 657-662, 6 2003.

[16] J. Huang, Z. Li, and J. Zhang, "Review of characterization and modeling of polymer electrolyte fuel cell catalyst layer: The blessing and curse of ionomer," *Frontiers in Energy,* vol. 11, no. 3, pp. 334-364, 2017.

[17] K. Malek, T. Mashio, and M. Eikerling, "Microstructure of Catalyst Layers in PEM Fuel Cells Redefined: A Computational Approach," *Electrocatalysis,* vol. 2, no. 2, pp. 141-157, 2011.

[18] G. S. Harzer, A. Orfanidi, H. El-Sayed, P. Madkikar, and H. A. Gasteiger, "Tailoring Catalyst Morphology towards High Performance for Low Pt Loaded PEMFC Cathodes," *Journal of The Electrochemical Society,* vol. 165, no. 10, pp. F770-F779, 2018.

[19] D. R. Baker, D. A. Caulk, K. C. Neyerlin, and M. W. Murphy, "Measurement of Oxygen Transport Resistance in PEM Fuel Cells by Limiting Current Methods," *Journal of The Electrochemical Society,* vol. 156, no. 9, pp. B991 29 K. Talukdar, S. Delgado, T. Lagarteira, P. Gazdzicki and K. A. Friedrich, Minimizing mass-transport loss in proton exchange membrane fuel cell by freeze-drying of cathode catalyst layers, J. Power Sources, 2019, 427, 309–317., 2009.

[20] K. Talukdar, S. Delgado, T. Lagarteira, P. Gazdzicki, and K. A. Friedrich, "Minimizing mass-transport loss in proton exchange membrane fuel cell by freeze-drying of cathode catalyst layers," *Journal of Power Sources,* vol. 427, pp. 309-317, 2019.

[21] M. Ji and Z. Wei, "A Review of Water Management in Polymer Electrolyte Membrane Fuel Cells," *Energies,* vol. 2, no. 4, pp. 1057-1106, 2009.

[22] V. Yarlagadda *et al.*, "Boosting Fuel Cell Performance with Accessible Carbon Mesopores," *ACS Energy Letters,* vol. 3, no. 3, pp. 618-621, 2018.

[23] Z. Yu, R. N. Carter, and J. Zhang, "Measurements of Pore Size Distribution, Porosity, Effective Oxygen Diffusivity, and Tortuosity of PEM Fuel Cell Electrodes," *Fuel Cells,* vol. 12, no. 4, pp. 557-565, 2012.

[24] K. Talukdar, M. A. Ripan, T. Jahnke, P. Gazdzicki, T. Morawietz, and K. A. Friedrich, "Experimental and numerical study on catalyst layer of polymer electrolyte membrane fuel cell prepared with diverse drying methods," *Journal of Power Sources,* vol. 461, 2020.

[25] G. A. Futter, P. Gazdzicki, K. A. Friedrich, A. Latz, and T. Jahnke, "Physical modeling of polymer-electrolyte membrane fuel cells: Understanding water management and impedance spectra," *Journal of Power Sources,* vol. 391, pp. 148-161, 2018.

[26] R. Vetter and J. O. Schumacher, "Free open reference implementation of a two-phase PEM fuel cell model," *Computer Physics Communications,* vol. 234, pp. 223-234, 2019.

[27] Y. Shao, G. Yin, Z. Wang, and Y. Gao, "Proton exchange membrane fuel cell from low temperature to high temperature: Material challenges," *Journal of Power Sources,* vol. 167, no. 2, pp. 235-242, 2007.

[28] S. G. Peera, A. Arunchander, and A. K. Sahu, "Platinum nanoparticles supported on nitrogen and fluorine co-doped graphite nanofibers as an excellent and durable oxygen reduction catalyst for polymer electrolyte fuel cells," *Carbon,* vol. 107, pp. 667-679, 10 2016.

[29] Z. S. J. Z. Xin Chen Dingguo Xia, *Electrocatalysis in Fuel Cells: A Non- and Low- Platinum Approach,* . Springer, London 2013.

[30] R. O. H. PhD, S. W. C. PhD, W. C. PhD, and F. B. P. PhD, "Fuel Cell Fundamentals, Chapter 1: Introduction," John Wiley & Sons, Inc, 2016, pp. 1-24.

[31] Y. Liu, C. Ji, W. Gu, J. Jorne, and H. A. Gasteiger, "Effects of Catalyst Carbon Support on Proton Conduction and Cathode Performance in PEM Fuel Cells," *Journal of The Electrochemical Society,* vol. 158, no. 6, 2011.

[32] E. Padgett *et al.*, "Mitigation of PEM Fuel Cell Catalyst Degradation with Porous Carbon Supports," *Journal of The Electrochemical Society,* vol. 166, no. 4, pp. F198-F207, 2019.

[33] M. S. Wilson, J. A. Valerio, and S. Gottesfeld, "Low platinum loading electrodes for polymer electrolyte fuel cells fabricated using thermoplastic ionomers," *Electrochimica Acta,* vol. 40, no. 3, pp. 355-363, 1995/02/01/ 1995.

[34] H. Steven, "Fuel Cell Catalyst Layers: A Polymer Science Perspective " *J Chemistry of Materials,* vol. 26, pp. 381-393, 7 2014.

[35] A. Kongkanand and M. F. Mathias, "The Priority and Challenge of High-Power Performance of Low-Platinum Proton-Exchange Membrane Fuel Cells," *J Phys Chem Lett,* vol. 7, no. 7, pp. 1127-37, Apr 7 2016.

[36] Y.-C. Park, K. Kakinuma, H. Uchida, M. Watanabe, and M. Uchida, "Effects of short-side-chain perfluorosulfonic acid ionomers as binders on the performance of low Pt loading fuel cell cathodes," *Journal of Power Sources,* vol. 275, pp. 384-391, 2015/02/01/ 2015.

[37] Y.-C. Park, H. Tokiwa, K. Kakinuma, M. Watanabe, and M. Uchida, "Effects of carbon supports on Pt distribution, ionomer coverage and cathode performance for polymer electrolyte fuel cells," *Journal of Power Sources,* vol. 315, pp. 179-191, 5 2016.

[38] N. Pramounmat *et al.*, "Controlling the Distribution of Perfluorinated Sulfonic Acid Ionomer with Elastin-like Polypeptide," *ACS Appl Mater Interfaces,* vol. 11, no. 46, pp. 43649-43658, Nov 20 2019.

[39] T. Morawietz, M. Handl, C. Oldani, K. A. Friedrich, and R. Hiesgen, "Quantitative in Situ Analysis of Ionomer Structure in Fuel Cell Catalytic Layers," *ACS Appl Mater Interfaces,* vol. 8, no. 40, pp. 27044-27054, Oct 12 2016.

[40] K. R. Cooper, "IN SITU PEM FUEL CELL ELECTROCHEMICAL SURFACE AREA AND CATALYST UTILIZATION MEASUREMENT," *Fuel Cell Magazine,* 2009.

[41] H. J. Kim, K. Talukdar, Y. H. Kim, Y. Park, H.-C. Lee, and S.-J. Choi, "Study of Semi-Interpenetrating Networks in Nafion®/Polyacrylamide Proton Conducting Membranes," *Journal of Nanoelectronics and Optoelectronics,* vol. 10, no. 4, pp. 569-573, 8 2015.

[42] K. Shinozaki, J. W. Zack, S. Pylypenko, B. S. Pivovar, and S. S. Kocha, "Oxygen Reduction Reaction Measurements on Platinum Electrocatalysts Utilizing Rotating Disk Electrode Technique," *Journal of The Electrochemical Society,* vol. 162, no. 12, pp. F1384-F1396, 2015.

[43] A. Goshtasbi, P. García-Salaberri, J. Chen, K. Talukdar, D. G. Sanchez, and T. Ersal, "Through-the-Membrane Transient Phenomena in PEM Fuel Cells: A Modeling Study," *Journal of The Electrochemical Society,* vol. 166, no. 7, pp. F3154-F3179, 2019.

[44] G. Sasikumar, J. W. Ihm, and H. Ryu, "Dependence of optimum Nafion content in catalyst layer on platinum loading," *Journal of Power Sources,* vol. 132, no. 1-2, pp. 11-17, 2004.

[45] A. Orfanidi, P. Madkikar, H. A. El-Sayed, G. S. Harzer, T. Kratky, and H. A. Gasteiger, "The Key to High Performance Low Pt Loaded Electrodes," *Journal of The Electrochemical Society,* vol. 164, no. 4, pp. F418-F426, 2017.

[46] S. Paul, S.-J. Choi, and H. J. Kim, "Enhanced Proton Conductivity of a Zn(II)-Based MOF/Aquivion Composite Membrane for PEMFC Applications," *Energy & Fuels,* vol. 34, no. 8, pp. 10067-10077, 2020/08/20 2020.

[47] G. Sasikumar, J. W. Ihm, and H. Ryu, "Optimum Nafion content in PEM fuel cell electrodes," *Electrochimica Acta,* vol. 50, no. 2-3, pp. 601-605, 2004.

[48] Y. Liu, C. Ji, W. Gu, D. R. Baker, J. Jorne, and H. A. Gasteiger, "Proton Conduction in PEM Fuel Cell Cathodes: Effects of Electrode Thickness and Ionomer Equivalent Weight," *Journal of The Electrochemical Society,* vol. 157, no. 8, p. B1154, 2010.

[49] Y. Liu *et al.*, "Proton Conduction and Oxygen Reduction Kinetics in PEM Fuel Cell Cathodes: Effects of Ionomer-to-Carbon Ratio and Relative Humidity," *Journal of The Electrochemical Society,* vol. 156, no. 8, p. B970, 2009.

[50] Y. Tabe, M. Nishino, H. Takamatsu, and T. Chikahisa, "Effects of Cathode Catalyst Layer Structure and Properties Dominating Polymer Electrolyte Fuel Cell Performance," *Journal of The Electrochemical Society,* vol. 158, no. 10, 2011.

[51] K. Talukdar *et al.*, "Enveloping of catalyst powder by ionomer for dry spray coating in polymer electrolyte membrane fuel cells," *Journal of Power Sources,* vol. 424, pp. 82-90, 2019.

[52] G. E *et al.*, "Dry layer preparation and characterisation of polymer electrolyte fuel cell components " *Journal of Power Sources,* vol. 86, pp. 352-362, 3 2000.

[53] M. S. Wilson and S. Gottesfeld, "High Performance Catalyzed Membranes of Ultra-low Pt Loadings for Polymer Electrolyte Fuel Cells," *Journal of The Electrochemical Society,* vol. 139, no. 2, pp. L28-L30, 1992/02/01 1992.

[54] W. M. Mosdale R., Srinivasan S. , "In Fabrication of electrodes for proton exchange membrane fuel cells using a spraying method and their performance evaluation," in *The Electrochemical Society*, Pennington, 1994, p. 179: NJ.

[55] K. Talukdar, P. Gazdzicki, and K. A. Friedrich, "Comparative investigation into the performance and durability of long and short side chain ionomers in Polymer Electrolyte Membrane Fuel Cells," *Journal of Power Sources,* vol. 439, 2019.

[56] F. J. RodrÍguez, P. J. Sebastian, O. Solorza, and R. PÉrez, "Mo–Ru–W chalcogenide electrodes prepared by chemical synthesis and screen printing for fuel cell applications," *International Journal of Hydrogen Energy,* vol. 23, no. 11, pp. 1031-1035, 1998/11/01/ 1998.

[57] C. S. Kim, Y. G. Chun, D. H. Peck, and D. R. Shin, "A novel process to fabricate membrane electrode assemblies for proton exchange membrane fuel cells," *International Journal of Hydrogen Energy,* vol. 23, no. 11, pp. 1045-1048, 1998/11/01/ 1998.

[58] A. Saab, F. Garzon, and T. Zawodzinski, "Determination of Ionic and Electronic Resistivities in Carbon/Polyelectrolyte Fuel-Cell Composite Electrodes," *Journal of The Electrochemical Society,* vol. 149, pp. A1541-A1546, 12/01 2002.

[59] S. Towne, V. Viswanathan, J. Holbery, and P. Rieke, "Fabrication of polymer electrolyte membrane fuel cell MEAs utilizing inkjet print technology," *Journal of Power Sources,* vol. 171, no. 2, pp. 575-584, 2007/09/27/ 2007.

[60] S. Shukla, K. Domican, K. Karan, S. Bhattacharjee, and M. Secanell, "Analysis of Low Platinum Loading Thin Polymer Electrolyte Fuel Cell Electrodes Prepared by Inkjet Printing," *Electrochimica Acta,* vol. 156, pp. 289-300, 2 2015.

[61] B. Bladergroen, H. Su, S. Pasupathi, and V. Linkov, "Overview of Membrane Electrode Assembly Preparation Methods for Solid Polymer Electrolyte Electrolyzer," in *Electrolysis*, 2012.

[62] A. Strong, C. Thornberry, S. Beattie, R. Chen, and S. R. Coles, "Depositing Catalyst Layers in Polymer Electrolyte Membrane Fuel Cells: A Review," *Journal of Fuel Cell Science and Technology,* vol. 12, no. 6, p. 064001, 12 2015.

[63] V. Mehta and J. S. Cooper, "Review and analysis of PEM fuel cell design and manufacturing," *Journal of Power Sources,* vol. 114, no. 1, pp. 32-53, 2003.

[64] J. Liu *et al.*, "Understanding the Role of Interfaces for Water Management in Platinum Group Metal-Free Electrodes in Polymer Electrolyte Fuel Cells," *ACS Applied Energy Materials,* vol. 2, no. 5, pp. 3542-3553, 2019/05/28 2019.

[65] M. B. Sassin, Y. Garsany, B. D. Gould, and K. Swider-Lyons, "Impact of Compressive Stress on MEA Pore Structure and Its Consequence on PEMFC Performance," *Journal of The Electrochemical Society,* vol. 163, no. 8, pp. F808-F815, 2016.

[66] C. Simon, F. Hasché, and H. A. Gasteiger, "Influence of the Gas Diffusion Layer Compression on the Oxygen Transport in PEM Fuel Cells at High Water Saturation Levels," *Journal of The Electrochemical Society,* vol. 164, no. 6, pp. F591-F599, 2017.

[67] M. C. Lefebvre, "Characterization of Ionic Conductivity Profiles within Proton Exchange Membrane Fuel Cell Gas Diffusion Electrodes by Impedance Spectroscopy," *Electrochemical and Solid-State Letters,* vol. 2, no. 6, 1999.

[68] G. Li and P. G. Pickup, "Ionic Conductivity of PEMFC Electrodes," *Journal of The Electrochemical Society,* vol. 150, no. 11, 2003.

[69] P. C. Fortunato Migliardini, "CV and EIS Study of Hydrogen Fuel Cell Durability in Automotive Applications," *Int. J. Electrochem. Sci.,* vol. 8, pp. 11033-11047, 2013.

[70] S. Shukla, K. Domican, and M. Secanell, "Analysis of Kinetic Parameters and Effect of Pt Loading on Cell Performance of PEFC Electrodes Prepared by Inkjet Printing," *ECS Transactions,* vol. 69, no. 17, pp. 761-772, 10 2015.

[71] A. Pozio, M. De Francesco, A. Cemmi, F. Cardellini, and L. Giorgi, "Comparison of high surface Pt/C catalysts by cyclic voltammetry," *Journal of Power Sources,* vol. 105, no. 1, pp. 13-19, 2002/03/05/ 2002.

[72] I. Takahashi and S. S. Kocha, "Examination of the activity and durability of PEMFC catalysts in liquid electrolytes," *Journal of Power Sources,* vol. 195, no. 19, pp. 6312-6322, 2010/10/01/ 2010.
[73] L. G. P. Boillat, F.N. Büchi, T.J. Schmidt, "Use and misuse of electrochemical impedance spectroscopy in PEFC research," presented at the 236th ECS Meeting, Atlanta GA, USA, 2019.
[74] E. M and K. A.A, "Electrochemical impedance of the cathode catalyst layer in polymer electrolyte fuel cells," *J. Electroanal. Chem.,* vol. 475, pp. 107-123, 10 1999.
[75] M. B. Sassin, Y. Garsany, B. D. Gould, and K. E. Swider-Lyons, "Fabrication Method for Laboratory-Scale High-Performance Membrane Electrode Assemblies for Fuel Cells," *Anal Chem,* vol. 89, no. 1, pp. 511-518, Jan 3 2017.
[76] S. Shukla, D. Stanier, M. S. Saha, J. Stumper, and M. Secanell, "Analysis of Inkjet Printed PEFC Electrodes with Varying Platinum Loading," *Journal of The Electrochemical Society,* vol. 163, no. 7, pp. F677-F687, 2016.
[77] H. A. Gasteiger, S. S. Kocha, B. Sompalli, and F. T. Wagner, "Activity benchmarks and requirements for Pt, Pt-alloy, and non-Pt oxygen reduction catalysts for PEMFCs," *Applied Catalysis B: Environmental,* vol. 56, no. 1-2, pp. 9-35, 2005.
[78] J. P. Owejan, J. E. Owejan, and W. Gu, "Impact of Platinum Loading and Catalyst Layer Structure on PEMFC Performance," *Journal of The Electrochemical Society,* vol. 160, no. 8, pp. F824-F833, 2013.
[79] J. Schindelin *et al.*, "Fiji: an open-source platform for biological-image analysis," *Nat Methods,* vol. 9, no. 7, pp. 676-82, Jun 28 2012.
[80] (2020). *Geodict*. Available: https://www.math2market.com/
[81] N. Otsu, "A Threshold Selection Method from Gray-Level Histograms," *IEEE Transactions on Systems, Man, and Cybernetics,* vol. 9, no. 1, pp. 62-66, 1 1979.
[82] D. Y. K. C.S. Kong, H. K. Lee, Y. G. Shul, T.H. Lee, "Influence of pore-size distribution of diffusion layer on mass-transport problems of proton exchange membrane fuel cells," *Journal of Power Sources,* vol. 108, 2002.
[83] W. G. Pollard and R. D. Present, "On Gaseous Self-Diffusion in Long Capillary Tubes," *Physical Review,* vol. 73, no. 7, pp. 762-774, 04/01/ 1948.
[84] H. Babovsky, "On Knudsen flows within thin tubes," *Journal of Statistical Physics,* vol. 44, no. 5, pp. 865-878, 1986/09/01 1986.
[85] P. Thevenaz, U. E. Ruttimann, and M. Unser, "A pyramid approach to subpixel registration based on intensity," *IEEE Trans Image Process,* vol. 7, no. 1, pp. 27-41, 1998.
[86] D. Sage and M. Unser, "Teaching image-processing programming in Java," *IEEE Signal Processing Magazine,* vol. 20, no. 6, pp. 43-52, 11 2003.

Understanding the Important Parameters of Electrode Fabrication for Polymer Electrolyte Membrane Fuel Cell

Krishan Talukdar[*a], *Patrick Sarkezi-Selsky*[a], *Khrystyna Yezerska*[b], *Oleg Sergeev*[b], *Pawel Gazdzicki*[a] *and K. Andreas Friedrich* [a,c]

Supporting Information:

Workflow of Geodict analysis:

1. FIB-SEM imaging and image postprocessing

FIB-SEM images were recorded along the depth of the CL in steps of 150 nm and had a pixel resolution of 19.25 nm. The CL material in-between the subsequent image slices was scratched using a focused ion beam. The resulting 3D image stacks from FIB-SEM were then further post-processed using the open-source software Fiji [79]. To remove artificial shifts the images were first aligned using the plugin StackReg [85]. In a second step brightness of the 2D image slices was adjusted with the plugin Local Normalization [86]. From this point on all further image processing and analysis was done using GeoDict®[80]. The 3D image stacks were smoothened with a non-local means filter and then sharpened. Subsequently additional 2D image slices were reconstructed in-between the recorded 2D FIB-SEM images (every 150 nm) by using trilinear interpolation to arrive at a through-plane resolution of 19.25 nm. At last the 3D image stacks were binarized using the Otsu method [81]. The resulting binarized microstructures were then used as input to GeoDict® simulations to derive effective transport parameters for the different CL samples.

2. Simulation of effective transport parameters using GeoDict®

2.1 Porosity

Since a binarized microstructure solely contains voxelized information on the distribution of two phases (pore, solid) the porosity is derived straightforward as the ratio of the number of void voxels to solid voxels

$$\Phi = \frac{n_{pore}}{n_{solid}}. \tag{A1}$$

2.2 Pore size distribution

The pore size distributions were determined by using the GeoDict® tool *Granulometry*. In this method spheres of ascending sizes are created and tested if they still fit into pore spaces. In this way a maximum spherical radius is determined for each of the pores. The pore size distribution is then derived as the number of pores whose size can be approximated by a given spherical radius. The calculation in GeoDict® was conducted using a histogram bin size of 2 voxel and periodic boundary conditions for the in-plane direction of the material.

2.3 Diffusivity

Diffusivity D is a parameter describing the relation between the molar flux j of a species and its concentration gradient ∇c

$$j = -D\nabla c = -D\frac{\Delta c}{L}. \tag{A2}$$

Depending on the Knudsen number $Kn = \frac{\lambda}{L}$ (λ: mean free path length, L: char. length) species transport within porous media is dominated by particle-particle

interactions (bulk diffusion: $Kn \to \infty$), or particle-wall interactions (Knudsen diffusion: $Kn \to 0$), or in the transition regime ($Kn \cong 1$) between bulk and Knudsen diffusion.

2.3.1 Bulk diffusion ($Kn \to \infty$)

Bulk diffusivity D^{bulk} was calculated by simulating a concentration gradient of $\frac{\Delta c}{L} = 1\, {mol}/{l}$ along the thickness of the porous medium and solving eq. (2) for $\nabla^2 c = 0$. In the simulations symmetric boundary conditions are used in normal flow direction and periodic boundary conditions in tangential flow direction.

2.3.2 Knudsen diffusion ($Kn \to 0$)

Knudsen diffusivity D^{Kn} was calculated by simulating molecule movement within the porous medium by using a random walk method [84]. With the average distance $\langle x^2 \rangle$ between two wall collisions the diffusivity after t timesteps is then derived as

$$D^{Kn} = \frac{\langle x^2 \rangle}{2t}. \tag{A3}$$

2.3.3 Transition regime ($Kn \cong 1$)

The diffusivity for the transition regime was calculated by harmonic averaging of the bulk and Knudsen diffusivity values (Bosanquet approximation [83])

$$D = \left(\frac{1}{D^{Kn}} + \frac{1}{D^{bulk}}\right)^{-1}. \tag{A4}$$

2.4 Tortuosity

Tortuosity values were calculated based on the results of the diffusivity simulations and according to the relation of tortuosity τ to porosity Φ and relative diffusivity d^*

$$\tau = \frac{\Phi}{d^*}. \tag{A5}$$

Whereas the relative diffusivity d^* itself is defined as the ratio

$$d^* = \frac{D}{d_0} \tag{A6}$$

of diffusivity to the self-diffusion coefficient $d_0 = \frac{1}{3}\lambda\bar{v}$ (λ: mean free path length, $\bar{v}$: mean thermal velocity).

2.5 Permeability

Stokes flow was simulated by imposing a small pressure gradient of $\frac{\Delta \mathrm{p}}{L} = 0.02Pa$ across the thickness of the binarized CL microstructure. Based on the resulting net flux per area q and dynamic viscosity μ value the permeability κ could then be derived using D'Arcy's law

$$\kappa = -\frac{q\mu}{\nabla p} = -\frac{q\mu}{\frac{\Delta \mathrm{p}}{L}}. \tag{A7}$$

In the simulations symmetric boundary conditions were used, both in normal and tangential direction, to eliminate surface effects.

All GeoDict® simulations were conducted at $T = 20°C$ using oxygen as the fluid in the pore space ($\mu = 1.834e^{-5}\frac{kg}{ms}, \lambda = 68nm, \bar{v} = 464\frac{m}{s}$).

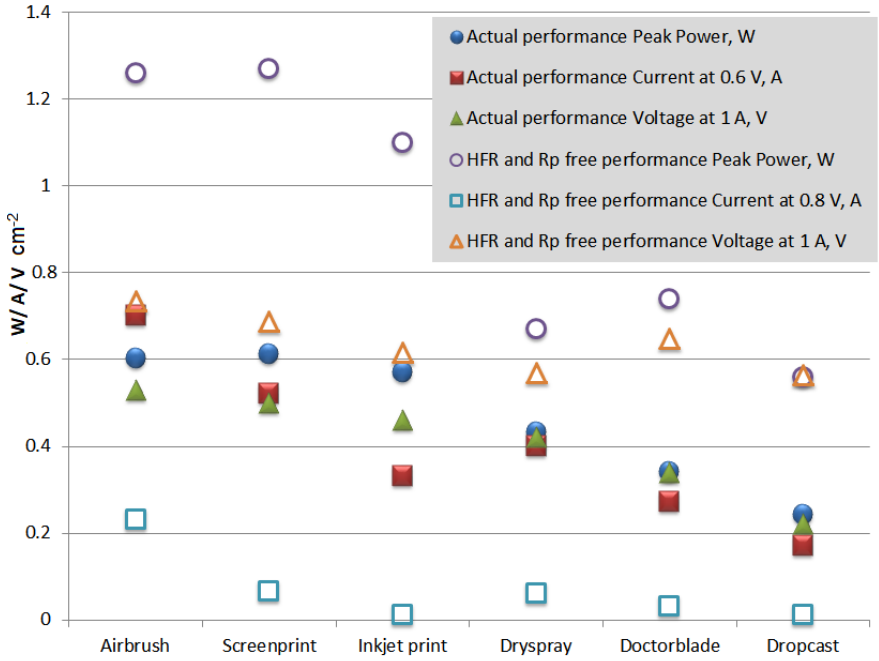

SI Figure 1: Characteristic points between actual polarization curves and IR-free polarization curves derived from the differently prepared but similar Pt loaded MEAs tested in a 1 cm^2 cell.

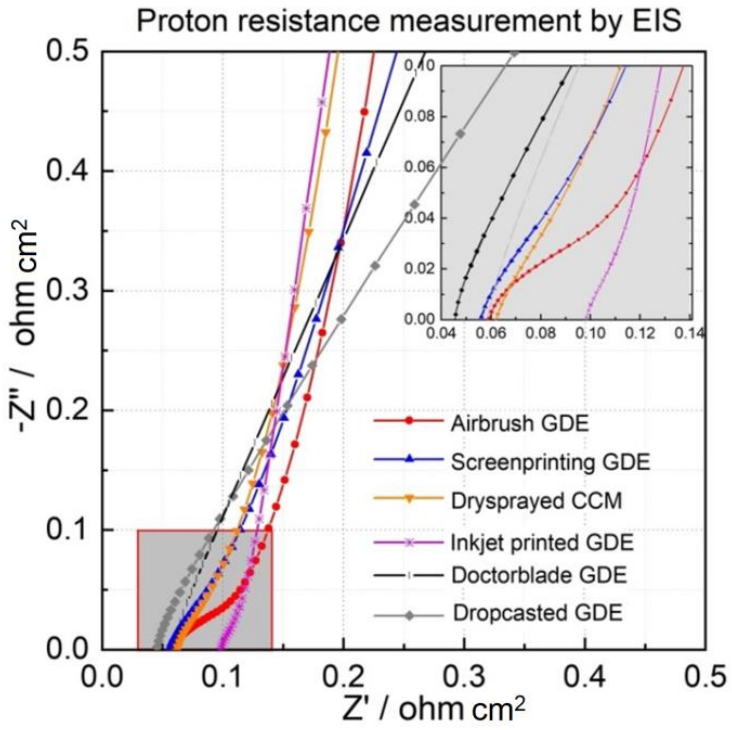

SI Figure 2: Proton resistance through CL measurement of differently prepared CLs with EIS in H_2 / N_2 atmosphere.

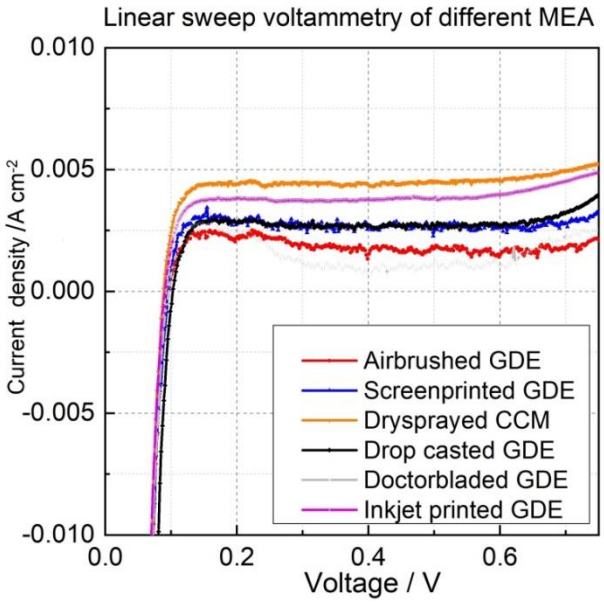

SI Figure 3: Linear sweep voltammetry of the MEAs fabricated with six different coating techniques.

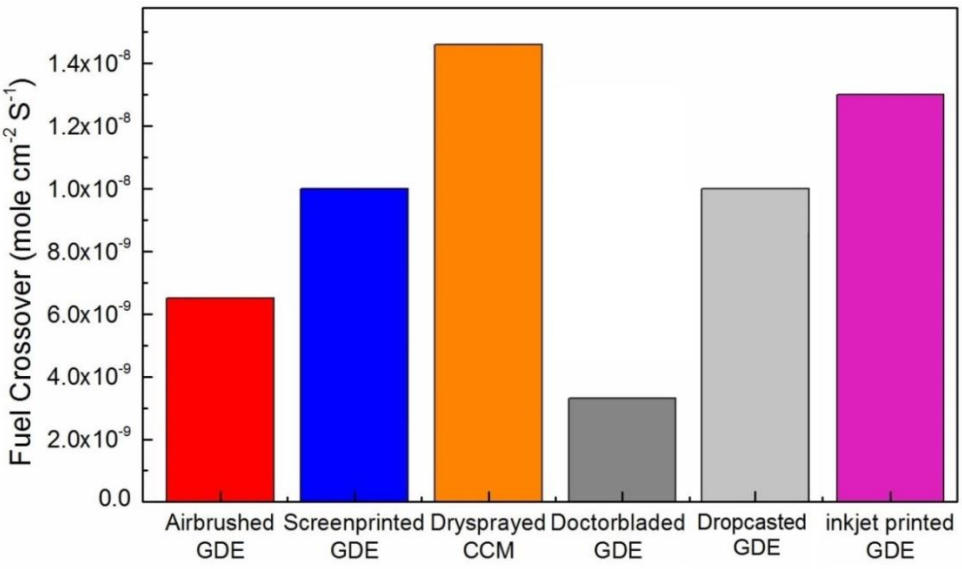

SI Figure 4: Fuel crossover determined from the crossover current derived by linear sweep voltammetry.

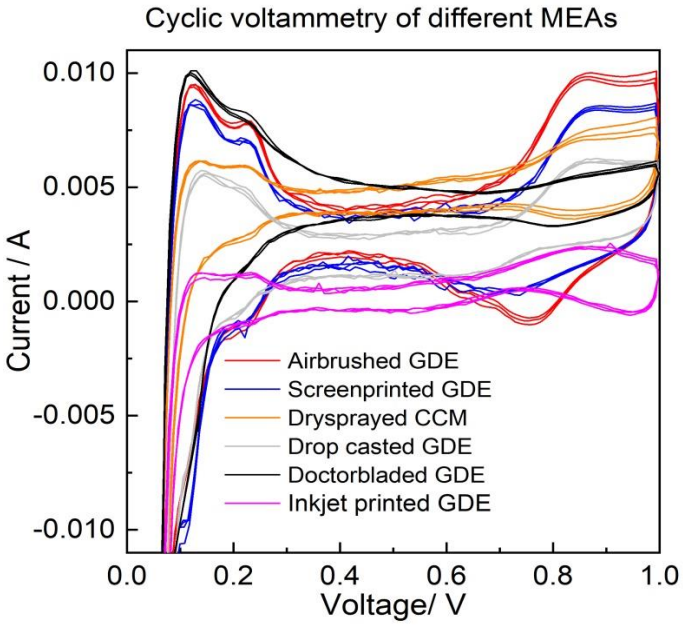

SI Figure 5: Cyclic voltammetry of the MEAs fabricated with six different coating techniques.

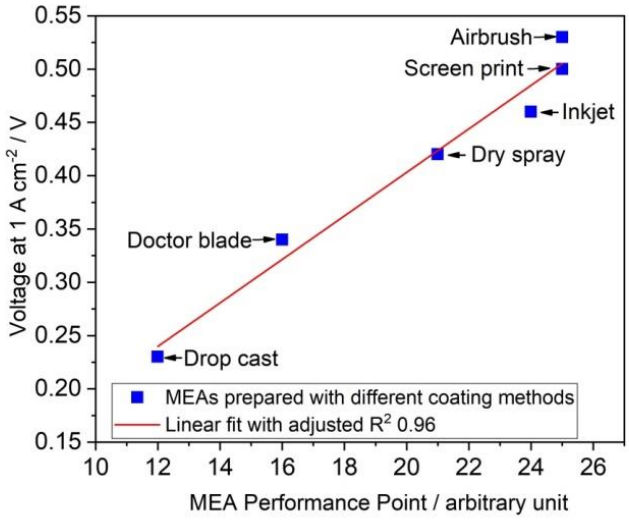

SI Figure 6: Cell voltage at 1 A cm^{-2} versus M performance points (mpp). Determination of mpp (see Table 6) is provided in the text. Correlation factor is $R^2 = 0.96$.

In SI fig. 6 membrane performance point (mpp) of each MEA is plotted against their voltage at 1 A cm^{-2} current density. All the MEAs prepared with different coating techniques are indicated with their names. Here we can observe a very good correlation between the defined characteristics and the voltage loss in the operated MEAs. A linear regression yields an R^2 value of 0.96 suggesting a significant relation between voltage loss and mpp. Additionally, this correlation is closely followed at other current densities also.

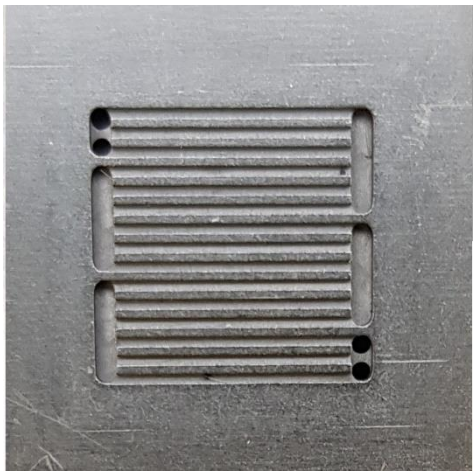

SI Figure 7: Illustration of 1 cm^2 graphite flow-field.

	Airbrush	Screen printing	Inkjet printing	Dry spray	Doctor-blade
Porosity / %	54.83	57.98	60.37	53.01	49.82
Permeability / m^2	4.36×10^{-15}	7.36×10^{15}	8.44×10^{-15}	4.66×10^{-15}	2.93×10^{-15}
Diffusivity / $m^2\ s^{-1}$	4.99×10^{-6}	5.42×10^{-6}	5.59×10^{-6}	4.95×10^{-6}	4.39×10^{-6}
Tortuosity Factor / -	1.028	1.02	1.031	1.015	1.042

SI Table 1: Effective transport parameters from FIB-SEM analysis with GeoDict.

Number of Dots	ECSA	Charge Transfer resistance	CL Proton resistance	Ohmic resistance	Porosity	Diffusion resistance
●	< 5 %	20-22 %	>20 %	> 28%	< 18 %	> 25%
●●	5-10 %	18-20 %	10-20 %	20-28 %	18-19 %	20-25 %
●●●	10-20%	16-18%	5-10 %	16-20 %	19-19.5 %	15-20 %
●●●●	20-25 %	14-16%	2.5-5 %	12-16 %	19.5 -21.5 %	10-15 %
●●●●●	25-30 %	12-14%	< 2.5 %	8-12 %	> 21.5 %	5-10 %

SI Table 2: MEA performance point measurement form the percentage scale of different characteristics

Catalyst layer and pore size distribution of electrode prepared with airbrush:

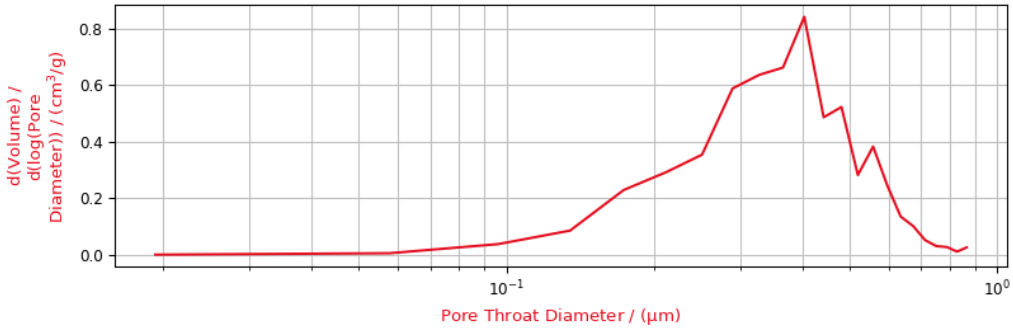

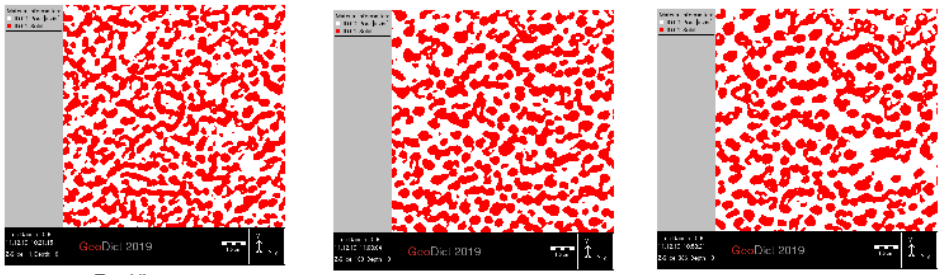

Top View Mid View Bottom View

Catalyst layer and pore size distribution of electrode prepared with screen print:

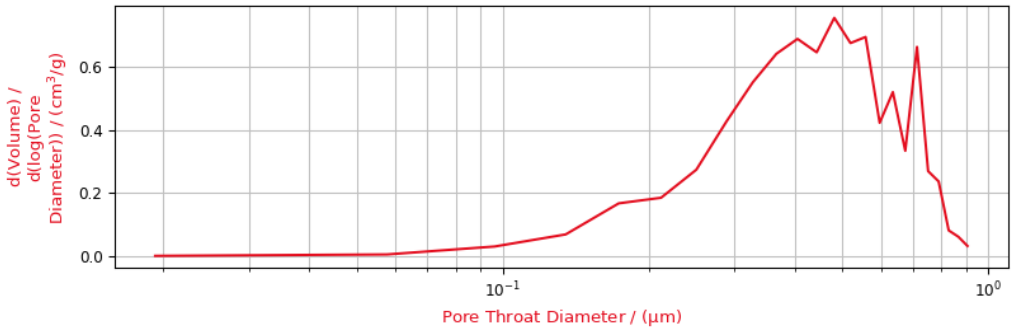

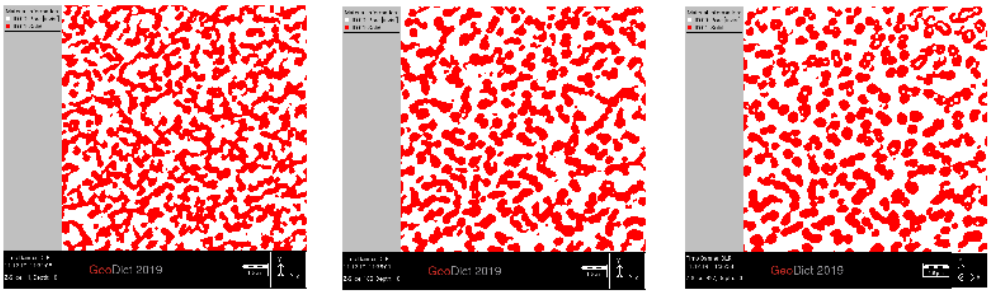

Top View Mid View Bottom View

Catalyst layer and pore size distribution of electrode prepared with inkjet print:

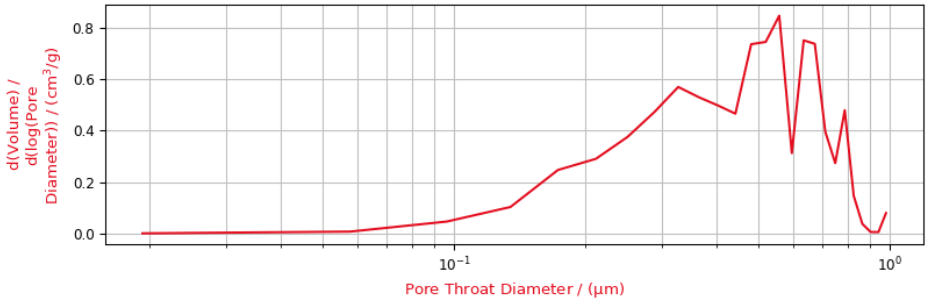

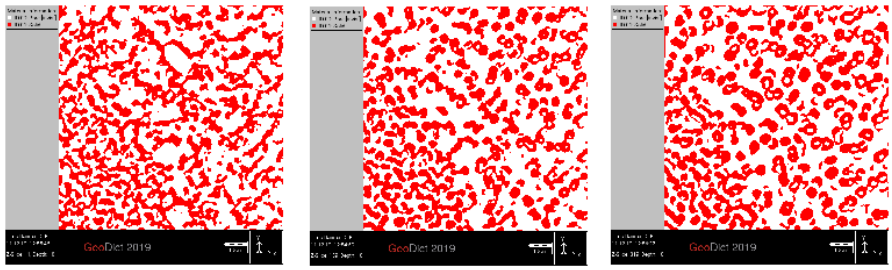

Top View Mid View Bottom View

Catalyst layer and pore size distribution of electrode prepared with dry spray:

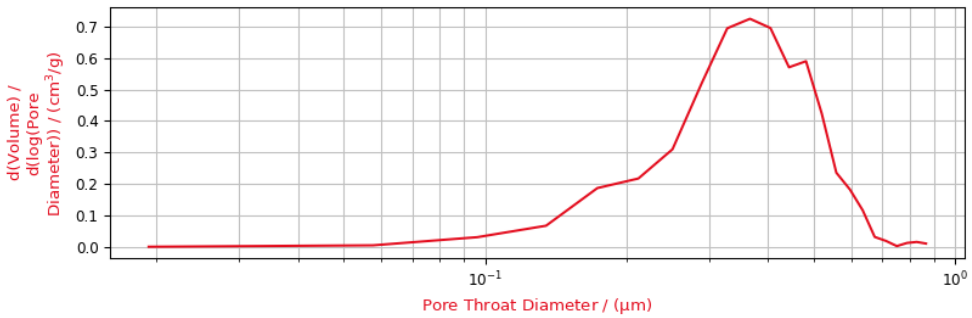

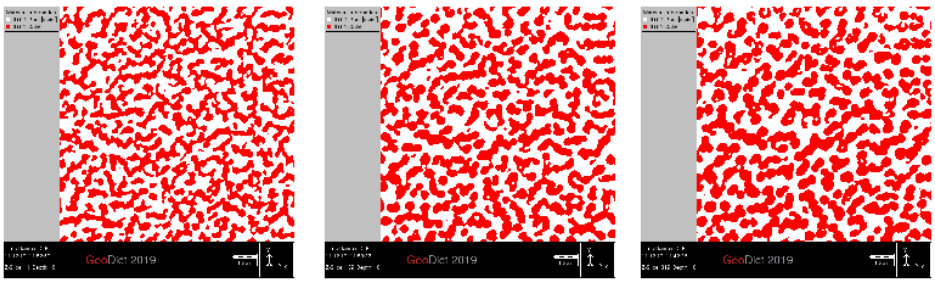

Top View Mid View Bottom View

Catalyst layer and pore size distribution of electrode prepared with doctor-blade:

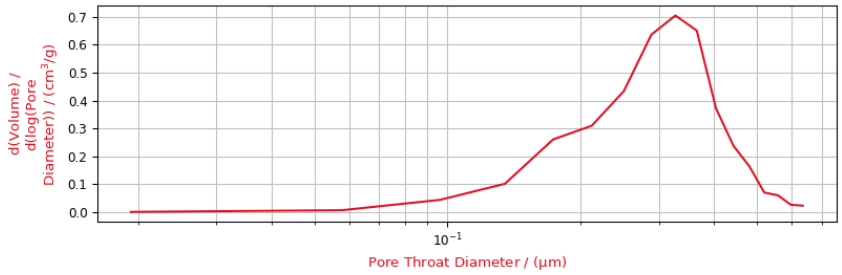

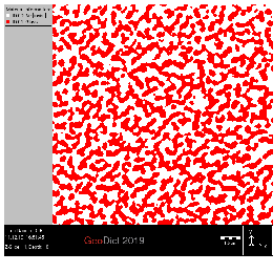

Top View

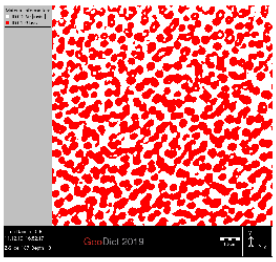

Mid View

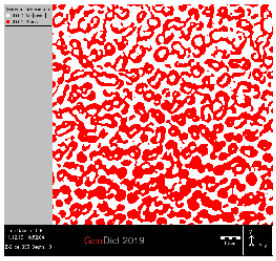

Bottom View

Journal of Power Sources 424 (2019) 82–90

Contents lists available at ScienceDirect

Journal of Power Sources

journal homepage: www.elsevier.com/locate/jpowsour

Enveloping of catalyst powder by ionomer for dry spray coating in polymer electrolyte membrane fuel cells

Krishan Talukdar[a,*], Stefan Helmly[a], Mathias Schulze[a], Daniel G. Sanchez[a], Michael Handl[b], Renate Hiesgen[b], Jürgen Kraut[b], K. Andreas Friedrich[a,c]

[a] German Aerospace Center (DLR), Institute of Engineering Thermodynamics, Pfaffenwaldring 38-40, Stuttgart, 70569, Germany
[b] University of Applied Science Esslingen, Faculty of Basic Science, Kanalstrasse 33, 75728, Esslingen, Germany
[c] University of Stuttgart, Institute of Building Energetics, Thermal Engineering and Energy Storage (IGTE), Pfaffenwaldring 31, 70569, Stuttgart, Germany

HIGHLIGHTS

- Dry spray coating is a time-saving and environment friendly way to manufacture MEA.
- Instead of solid powder, liquid ionomer was used to modify the dry catalyst powder.
- Modification of both the catalyst or it's support generates thin film of ionomer.
- This ionomer coating improves the reactive interface as well as the performance.
- Proton conductivity increases, whereas ohmic and charge transfer resistance reduces.

GRAPHICAL ABSTRACT

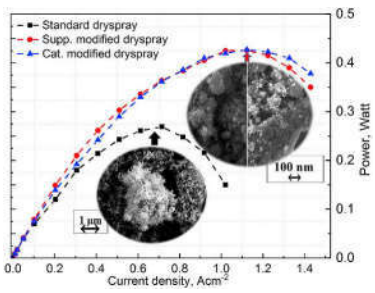

ARTICLE INFO

Keywords:
Dry spraying
Dry ink preparation
Ionomer film
Nafion® coating
PEM fuel cell

ABSTRACT

This study presents innovative concepts for improving performance of membrane electrode assemblies (MEAs) prepared by the dry-spraying method introduced by the German Aerospace center (DLR). Dry-spraying is a time and cost effective method that involves solvent-free spraying of catalyst powder on polymer electrolyte membrane. The issue which is resolved in this work is the large ionomer particle size in the conventional method. With mechanical grinding, particle size of the ionomer less than 100 nm were not been achieved. However, here the reactive interface of dry-sprayed MEA is optimized by improving ionic conductivity. Our approach is to modify a carbon support by partially enveloping with Nafion® ionomer followed by incorporating Pt black with it. Additionally, commercial catalyst powder was also modified by two-step preparation process with Nafion® dispersion. In this research, both of these modified powders were sprayed over membrane; hot-pressed; characterized, and have shown improved ionic network and distribution, which corresponds to their higher performances. The improvement in the performance does not correlate with electrode surface area but with the ionomer resistance of the catalytic layer. Therefore, with this study we demonstrate a pathway and methodology to further improve performance by optimizing ionomer structure and networks in the catalytic layer.

* Corresponding author.
E-mail address: krishan.talukdar@dlr.de (K. Talukdar).

https://doi.org/10.1016/j.jpowsour.2019.03.093
Received 6 December 2018; Accepted 22 March 2019
0378-7753/

1. Introduction

Energy demand has become one of the most serious concerns of modern society due to the problems related with greenhouse gas emissions and the depletion of fossil fuels. In this context fuel cells (FCs) in particular, Proton Exchange Membrane Fuel Cells (PEMFCs) can be considered as one vital technology to reach the goals of the European Union to reduce greenhouse gas emissions by 80% by 2050. Fuel cells convert chemical energy directly into electricity which is more efficient and environmentally friendlier than combustion engines in automotive applications [1], and fuel cells can be emission-free with green hydrogen. Moreover, fuel cells have cost and weight advantages compared to batteries at large sizes, and enable fast charging within 3 min [2]. Polymer electrolyte membrane fuel cells (PEMFCs) are attractive because of their high power density, flexibility to operate in low temperature and high dynamical response. The interior of this electrochemical cell consists of a membrane electrode assembly (MEA), a proton exchange membranes (PEM) in-between catalyst and gas diffusion layer (GDL) electrode pairs. This assembly needs to provide high intrinsic activities for the oxidation of hydrogen at the anode side and reduction of oxygen at the cathode side. In order to achieve high performance, the transport of gases as well as the conductance of electrons, and protons must be optimized to provide efficient transport to and from the interface of the electrochemical reactions. The architecture of electrodes for PEMFC's is an intricate balancing of transport media and catalytic activity. The economic competitiveness of PEMFCs is hindered by the high cost of the materials, in particular the platinum catalyst as standard material dominates the cost of mass manufacture, which may represents approximately 45% of the overall costs [3]. The costs of electrode fabrication should be reduced by different approaches such as reducing or avoiding platinum (Pt) loading on both electrodes and superior catalyst utilization. Nevertheless, even at low loading Pt electrodes still contribute significantly to the comprehensive costs of the system if mass production scenarios are evaluated. Hence, to make this technology a viable energy source, a reduction of Pt loading in the catalyst layers without loss in performance and durability is essential. Performance of fuel cells usually depends on the composition and fabrication method of catalyst layer. Thin catalyst layers can be produced by numerous coating techniques, saving expensive catalyst materials [4].

Ionomer is added to the catalyst layer to facilitate proton transfer and as binder. The effect of ionomer loading in the CL on cell performance has been examined for conventional electrodes. The state of the art Nafion® loading is approximately 30 wt% with respect to the solid catalyst particles [5–7]. Shukla et al. shows the importance of an optimal Nafion® loading with an efficient balance between proton transport and gas transport for superior fuel cells [8]. If the ratio of Nafion® decreases from the optimum level, it causes kinetic loss in low current density whereas for a higher ratio of Nafion®, it causes mass transport losses at high current densities. For state of the art idealized “model” structure of the electrode, a very thin ionomer film partly covers the Pt/C surface. This thin film of ionomer facilitates the transport of reactant gases through pores to the catalyst surface, followed by protons from the catalyst through ionomer network, and electrons via carbon support. Above-mentioned phenomena simultaneously create the indispensable ionomer catalyst interfaces to maximize catalyst utilization [9]. The transport of oxygen species as product of the oxygen reduction reaction (ORR) permeates mainly through ionomer-free parts of the Pt/C agglomerates [10]. Transport of protons [11,12] is controlled by the thickness as well as the continuity of the ionomer on the catalyst surface and hydrophilic networks in the catalyst layer (CL). Finally, the transport of electrons is related to the continuity of the carbon particle network [13] and the contact.

There are numerous catalyst coating techniques based on various substrates, particles morphology and method of coating. All of the MEA coating techniques have their own advantages and disadvantages. The PEM research group of DLR developed a dry layer preparation method for fabricating catalyst layers bound by either PTFE or Nafion® by spraying the atomized dry mixture of catalyst with the aid of nitrogen gas stream onto either GDL or membrane as described by Güzlow et al. [14]. In powder spraying, the principle of electrostatic forces, especially between electronic conductors and insulators, is used to form an adhesive powder layer onto a substrate. In the DLR process, the powder is tribologically charged initially by laboratory knife milling process,

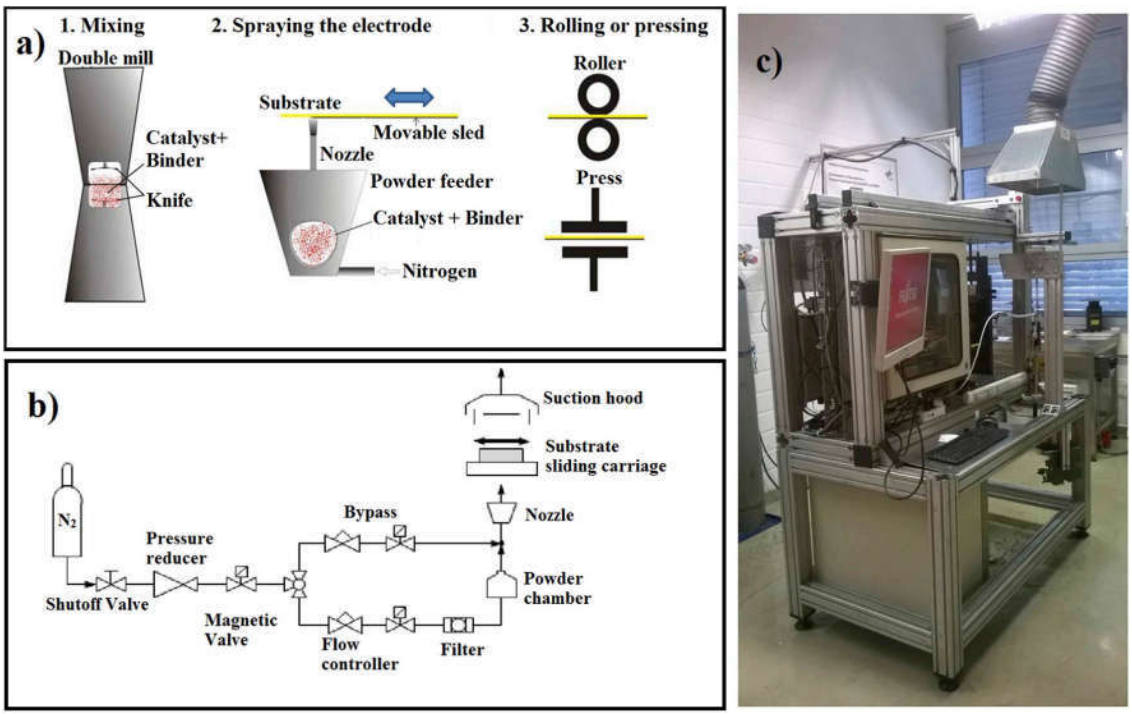

Fig. 1. a) Schema of dry powder spraying MEA manufacturing process, b) flow diagram of dry spraying facility, c) image of the DLR dry spraying machine.

while atomization takes place in the separating funnel and inside the pipes during the spray process. The charged powder is subsequently fed to the coating facility which sprays the powder via a nozzle onto the substrate, commonly the membrane. Subsequently, the assembly is hot-pressed or rolled [15,16]. Fig. 1 demonstrates the in-house dry spraying facility in DLR. This procedure is very fast and easy to handle, as a dry process avoids the use of any solvents and drying steps during MEA preparations and allows continuous production for industrial purpose. The bottleneck of this coating technique is the ionomer particle size, hydrophilicity of ionomer particles and its agglomeration. Inhomogeneous distribution and agglomeration of particles cause less active catalytic surface area in the reactive interface of the electrode compared to the conventional and commercial electrodes. Preparation of Nafion® powder is very crucial due to requirement of cryogenic grinding by means of an impactor mill in liquid nitrogen. Until now, ionomer particle sizes of down to 1 µm can be reached, and the size distribution is unsatisfactorily broad with this technique. As a consequence of large particle size and heterogeneous distribution up to 50 µm, high performance electrode membrane assemblies could not be accomplished. According to literature [13], standard electrodes should have ionic film dimension < 10 nm, which will allow sufficient proton transport and gas permeation. The resulting bigger Nafion® particles e.g. (5–50 µm) or agglomerations apparently cover many of the active catalytic sites during the hot-press procedure and as a result, uniform porosity and utilization of active area are lost. In addition, heterogeneous hydrophilic/hydrophobic regions may causes isolation of Pt, local flooding, pinholes and water-gas transport issues. Not surprisingly often dry sprayed MEAs with low Pt loading showed flooding problem and unstable performance during operation.

2. Approach

To overcome these issues of the powder spraying technique, we modified the technique with a single approach in order to achieve two following aspects; first, is to enhance the Nafion® dispersion inside the electrode, and second, is to enwrap the catalyst particles partially with a thin film of ionomer. The approach is replacing solid ionomer by introducing liquid ionomer dispersion. Consequently it facilitates catalytic activity, increased proton conductivity and gas access. This crucial approach improves the active sites of the catalyst layer and increases the performance significantly. Here we tried to eliminate the step of grinding solid Nafion® particles, and as an alternative we introduced commercially available Nafion® dispersion in the catalyst powder preparation procedure. In this article, we showed two favorable process variants, one is adding ionomer solution with carbon support, which will partially cover the carbon particles and subsequently disperse or mix the platinum black with that support to make 40% Pt on carbon support. Another is using ionomer solution to partially coat the total catalyst-support mixture purchased commercially, and eventually make a dry powder out of it. We herein fabricated MEAs by dry spraying process with standard type and modified catalyst powder with corresponding in-situ and physical characterization.

Targeting an electrode structure according to an ideal electrode architecture [17,18], we attempted to make a better network among ionomer, platinum, carbon, water and feed gasses with respect to the TPB postulation. It is assumed that, strings or filaments of ionomer attached to catalyst particles or partially coated catalyst particles with ionomer will increase the electrochemically active platinum surface for reaction. In both cases, the catalytic layer should avoid aggregation of particles and keep a good balance between hydrophilic and hydrophobic region. As our aim is to coat catalyst particles with ionomer, we will consider catalyst particles as a pigment and ionomer as a binder according to the theory of coating technology. The chief purpose of pigment dispersion is to break down aggregates and form stable dispersions of optimal sized pigment particles. Here, we introduced ionomer dispersion to partially coat the catalyst particles. A very important issue which is most of the time underestimated is the calculation of a coating ratio where ionomer acts as a binder and particles as pigments. The coating ratio and its consequence can be estimated from the pigment-volume-concentration (PVC) ratio.

$$\mathrm{PVC} = \frac{V(pigments)}{V(total)} = \frac{V(pigments)}{(V(pigments) + V(binder/Ionomer))}$$

The so-called critical-pigment-volume-concentration (CPVC) is the transition point, from the pigments being completely covered by a binder to a state where they are not [19]. It is not really possible to calculate this value, but one can easily determine this value experimentally, as the mechanical and optical properties of the coating dramatically change at that point. As the PVC value increases beyond the CPVC value, the fewer amounts of pigment particles being covered by binder and increases porosity. On the contrary, if PVC value decreases from CVPC value, the coating will lose its porosity and the binder will isolate the pigment particle completely. We computed the PVC values of our ink theoretically by calculating individually the volume of Pt-nano particle, carbon support and dry ionomer. The values are evaluated with above equation:

- PVC value of the modified commercial catalyst is 82%.
- PVC value of the modified carbon support is 82%

The value of the CPVC is governed by several factors, including particle size, particle size distribution and particle shape as well as by the chemical properties of the particle surface. Ideally for spherical particles of uniform particle size a maximum CPVC of 74% is calculated [20]. It means any coating composite of spherical particles along with binder having PVC value less than 74% will be totally covered by the binder, and a coating composite having PVC value higher than 74% will have partial covering of binder over spherical particles causing porous structure. Both of the values of our modified powders are above the average CPVC values thus ensure the partial covering of the ionomer. Due to the low binder content we ensure availability of void space, therefore enabling permeability and interface roughness. The standard dry powder preparation technique does not include liquid Nafion® as a binder, so PVC value method does not apply here.

3. Experimental

3.1. MEA preparation

DLR patented technique for the fabrication of catalyst coated membrane (CCM) is spraying a dry catalytic layer directly onto the membrane [14,15]. The preparation technique for MEAs is divided into three main steps: a) preparation of the electrode powder, b) dry spraying the powder onto the membrane, c) hot rolling or pressing the membrane with the gas diffusion layers [21,22]. Fabrication procedure of all the techniques is summarized in Table 1. Nafion® pellets/5 wt% solution/Nafion® XL membrane (Ion Power Inc.), 40 wt% Pt/C Hispec 4000 (Alfa Aesar), Pt black Hispec 1000 (Alfa Aesar), Vulcan XC-72 (CABOT), isopropanol (VWR), ultrapure water (VWR), PTFE sheets (205 µm, Bohlender) were purchased commercially. Mixing was done by S 60H Elmasonic ultrasonic bath. Nafion® XL membranes were used as substrate for powder spraying then immediately hot pressed with GDL (BC-25, SGL Carbon) at 160 °C for 5 min with 690 Ncm^{-2} by hot press (Vgot) to make CCMs.

3.2. Catalyst modification

Hispec 4000 nano powder was dispersed in ultrapure water by sonication. Afterwards, Nafion® 5 wt% solution was dropwise added to the dispersion, placed on a sonicator so that catalyst/Nafion® ratio of 70:30 is maintained. Then the mixture was sonicated again and dried at 80 °C

Table 1
Different route of catalyst powder preparation for dry spraying MEA.2

Electrode powder preparation		
Standard [15]	Catalyst modification	Support modification
*Grinding Nafion pellets to fine powder by Cryogenic Mill *Hispec 4000 + Nafion powder (Knife Milling) ►Dry powder Pt/C 40wt% : Nafion (70:30)	*Hispec 4000 + Ultrapure water (Dispersion) *Hispec 4000 catalyst dispersion +Nafion 5% dispersion (Colloidal Sol^{n}) *Drying the dispersion *Grinding it in Cryogenic Mill ►Dry powder Pt/C 40wt% : Nafion (70:30)	*Vulcan Xc-72 + Ultrapure water (Dispersion) *Vulcan XC-72 + Nafion 5% dispersion (Colloidal Solution) *Drying the dispersion *Grinding it in Cryogenic Mill *Hispec 1000, Pt-b + Modified support (Knife Milling) ►Dry powder Pt/C 40wt% : Nafion (70:30))

in air for one day in normal oven. Eventually, the solid powder was ground by means of cryogenic mill (6850 Freezer Mill) to avoid the compression molding of ionomer and sprayed via the dry spraying device to fabricate CCM.

3.3. Support modification

Vulcan XC-72 is a widespread Pt support for PEMFC application due to its high surface area and good electrical properties. It is a hydrophobic material, so it is dispersed in ultrapure water by several steps of mechanical shaking and sonication. Afterwards, Nafion® was added dropwise so that catalyst/Nafion® ratio of 70:30 is maintained and then the mixture was sonicated. Mechanical shaking followed as well as sonication for three more times. The mixture was dried at 80 °C in air for one day, and ground via a cryogenic mill to produce fine powder. Eventually, required amount of Pt black was added to the supporting powder so that the ratio of Pt to carbon support was 40:60. Then the powders were mixed via a knife mill and dry sprayed via the dry spraying device onto the membrane. For all MEAs 0.3 mgcm^{-2} Pt loading was maintained.

The MEAs were assembled in a graphite flowfield with gold coated bi-polar plate purchased from Electrochem, USA. MEAs were assembled with PTFE gaskets over the three meander two channel serpentine graphite flow field with 2 Nm torque to each four 5 mm screws. Afterwards, single cell tests were performed in the test bench built and customized by DLR. Prior to testing, MEAs were conditioned at a potential 0.6 V and 0.3 V for 4 h each. All the MEAs were examined in 50% humidification and stoichiometric flow of λ_{H2}: 1.5 - λ_{air}: 3 during conditioning, polarization curve measurement and electrochemical impedance analysis. Galvanostatic polarization was measured with the holding time 3 min in each current density. Electrochemical impedance spectroscopy (EIS) was conducted with electrochemical work station IM6e (Zahner). Nyquist and Bode plots were determined in two different current densities of 0.1 and 0.5 Acm^{-2} in the frequency range from 100 mHz to 100 KHz with the amplitude of 10 mA and 50 mA respectively. EIS at low current density shows predominantly the kinetic losses, mid current density shows dominantly the ohmic contribution, and high current density demonstrates the mass transport polarization. The ionic impedance of the electrode was also evaluated with special EIS measurement. In order to characterize ionic impedance, 10 ml/min hydrogen and nitrogen gas were fed into anode and cathode with 100% humidification. Ionic impedance was measured in 1 V potentiostatic condition with 10 mV amplitude through 500 mHz to 100 KHz frequency, stated in the concerning literature [23,24]. According to the literature, at high frequencies a Warburg-like response (45° slope) is observed, corresponding to ion conductivity in the catalyst layer. At low frequencies, the impedance plot curves up to a limiting capacitance response (vertical) which corresponds to the total capacitance and resistance of the catalyst layer. The ionic resistance, R_{ionic}, can be obtained from the length of the Warburg-like region projected onto the real impedance (Z') axis (= $R_{ionic}/3$) [24]. Three sets of MEAs were tested of each type and found that the results are reproducible for all characterizations. Cross-section of MEA was prepared by freeze-fractioning and ion cutting system (JOEL IB 19520/CCP). Catalyst powder and cross-sections were characterized by means of scanning electron microscope (JEOL JSM-7200F.) with 5 kV. We applied N_2 adsorption in order to investigate the pore structures of the catalyst powders after addition of ionomer. The N_2 physisorption, pore size distribution and B.E.T. analysis were performed by Thermo Finnigan/Sorptomatic 1990.

4. Result and discussion

Fig. 2 (a) represents the standard dry-spray powder consisting of a 6–7 μm large particle agglomeration of Nafion®. As mentioned earlier, it is challenging to avoid the substantial agglomeration of solid ionomer powder, which is hydrophilic and shows high self-adhesion. Some of the big agglomerates of Nafion® heterogeneously distributed all over the catalyst powder can be seen randomly with lower magnification of SEM which was circled in Fig. 2 (b). This heterogeneity causes the lack of active sites, uniformity and uneven thickness of the catalyst layer. Consequently, this phenomenon attributes to uneven local current density and bad performance of MEA prepared with standard catalyst powder (shown later). Fig. 2(c) shows a formation of thin ionomer coating around the Pt/C particles which increase the zone of reactive interface and thereby enhances the performance. Fine film around the Pt particles like core-shell is observable in the image, where Pt particles are bright objects covered with transparent layer of Nafion® (marked by arrow). Whereas, Fig. 2(d) shows the presence of thin ionomer film over the carbon support agglomerates, and bright platinum catalyst agglomerates are infused with them. In contrast, to standard powder, modified powders show more homogeneous distribution of platinum, carbon support and ionomer throughout the catalyst powder. As evaluated by the PVC calculation, despite that the modified catalyst (c) and support particles (d) were coated by thin film of liquid ionomer, the aggregated powders should retain enough porosity and coarseness because of their higher PVC values. Nevertheless, the ionomer coating causes many of the micro (≤ 2 nm) and mesopores (2–50 nm) to be covered by ionomer, thus reducing the porosity of the powder. However, the better ionomer connection compensates this loss by improving the network of the reactive interface, which leads to improved performance of the modifications. Nonetheless, because of the inclusion of Pt black powder (which already contains some Pt agglomerates) to prepare support modified catalyst powder, there will be less Pt active surface area compared to the standard powder. Furthermore, in case of catalyst modified powder the thin film of ionomer covered most of the Pt particles, carbon support and some of their micro/mesopores, which is the reason of reduction in surface area (explained in 4.2) shown via

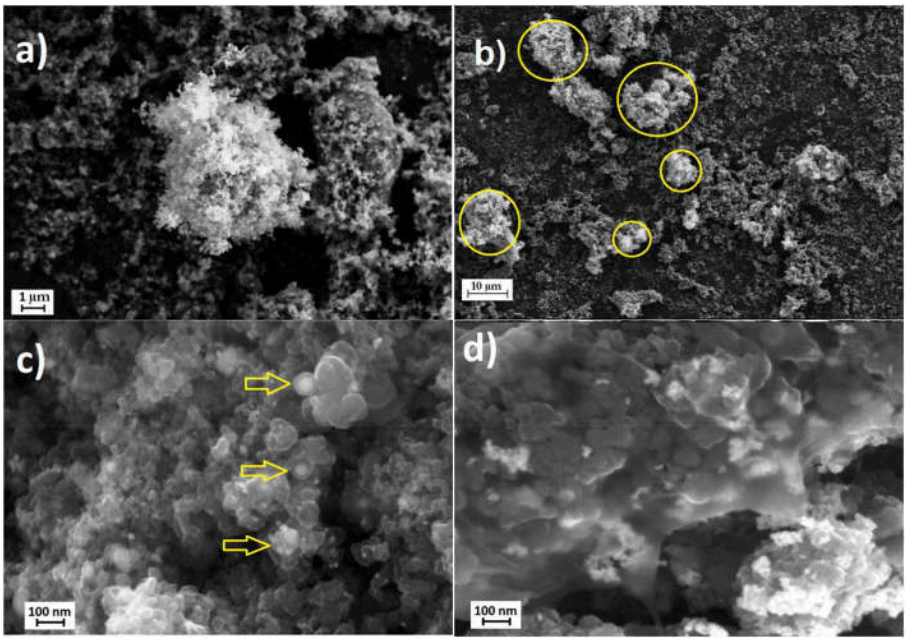

Fig. 2. SEM images of different catalyst powders; a, b: Pt/C catalyst powder mixed with solid ionomer (standard route), c: Pt/C catalyst modified with liquid ionomer (catalyst modification route)- and d: catalyst support modified with liquid ionomer mixed with Pt black (support modification route).

B.E.T. Both of the Fig. 2 (c and d) show that the thickness of ionomer films which covered the particles are well below 0.2 µm and should not cause any diffusion problem [25]. If the ionomer films are thin enough, superior electrochemical activity of Pt can be assumed; however, if the ionomer is too thick, Pt will be isolated and be inactive [19,25]. Therefore, by controlling the thickness and condition of ionomer film around the catalyst particle, we can improve the performance of the MEA.

Fig. 3(a) shows the change of N_2 adsorption isotherms of catalyst powders prepared with solid Nafion® and liquid Nafion® dispersion respectively. The amount of N_2 adsorption was reduced by the ionomer addition for both of the modified powders. When dry Nafion® powder was mixed with Pt/C powder, the mesopores and micropores of the Pt along with carbon support were intact. As a consequence, B.E.T. surface area shows a higher value 151 m^2/g. On the contrary, addition of liquid Nafion® forms an external film or coating over the Pt and carbon supports. Additionally, some of the liquid Nafion® even penetrates and blocks the internal micropores of the support which can be shown in the graph of pore size distribution in Fig. 3(b). This blockage of micropores may improve the performance by impeding Pt nanoparticles to relocate into the internal pores where they will become inactive [26,27]. As a result, both modified catalyst powders prepared with liquid Nafion® show lower B.E.T. surface area, but better distribution of ionomer which ensures higher catalytic reaction area as well as better performance.

Current-voltage graphs of the different MEAs fabricated with distinctive catalyst powders were shown in Fig. 4. IR corrected current-voltage curves are shown in Fig. 4(a) to compare the activation and mass transport losses. As the experiments were done in 1 cm^2 test station, area specific resistances were directly calculated from high

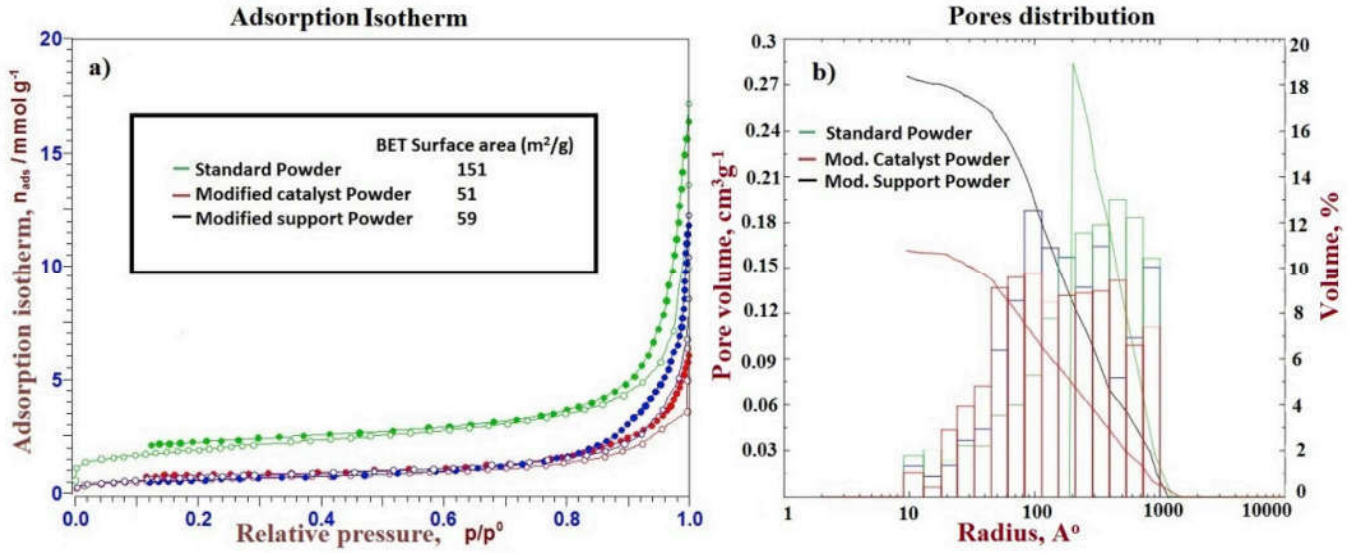

Fig. 3. a) N_2 adsorption-desorption isotherm and B.E.T. surface area measurement values (inset), b) pore size distributions of unmodified powder and powders modified by catalyst and support modifications.

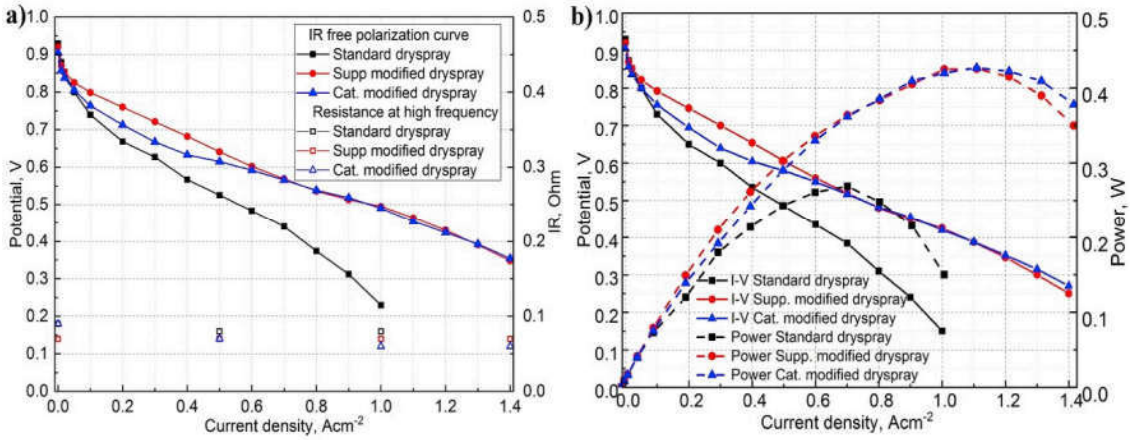

Fig. 4. a) IR compensated current/voltage characteristics of MEA's prepared with different modified powders, b) current/voltage and power characteristics; reaction condition was following: cell temp. 80 °C, 50% humidified feed gas, system pressure 150 Kpa and stoichiometry was λ_{H2}: 1.5 - λ_{air}: 3.

frequency impedance at several current density points shown on the secondary axis of Fig. 4(a). Performance and power curves of different MEAs prepared with distinctive preparation techniques are also displayed in Fig. 4 (b). Both of these polarization curves further supports the fact that MEA prepared with catalyst powders and liquid Nafion® solution exhibit better performance comparing to the standard powder. Significant difference is observed in mass transport region in higher current density where standard dry sprayed MEA shows no performance above 1 A/cm^2 current density, because of limiting diffusion. Support modified and catalyst modified powder sprayed MEAs exhibit similar performance throughout the polarization curve apart from the fact that catalyst modified MEA has poor performance at the kinetic region, but regained after 0.6 A/cm^2. In modified catalyst powder, the ionomer film covers some of the pores where some of the Pt becomes inactive inside the pores. This is the reason why support modified MEA exhibits better performance at lower current densities comparing to catalyst modified MEA where almost all the Pt is uncovered. The reason of the raising performance of catalyst modified MEA is the hydrophilicity difference of the powder before mixing ionomer dispersion. Pt/C (HISPEC-4000) powder is more hydrophilic than Vulcan Xc-72 carbon support; so that it shows better attraction to the hydrophilic part of ionomer and results in a better distribution and network of ionomer in the dispersion [27,28]. So, when current density reaches the mass-transport influenced region of the polarization curve, catalyst layer needs high proton conduction, and better distribution of ionomer facilitates the performance of the catalyst modified MEA. On the other hand, due to its high hydrophobicity, Vulcan XC-72 has inferior ionomer distribution and could not increase the power as expected despite of higher electrochemical active surface area. In this case, poor ionomer distribution causes higher ohmic loss to the support modified MEA. Nevertheless, at high current density more water is produced in the catalyst layer, and internal Pt become active when the carbon supports are fully wet. This might also be a reason for the increasing performance of catalyst modified MEA comparing to support modified one.

The above mentioned behavior is also validated by the impedance spectroscopy studies shown in Fig. 5. High frequency intersection of the Nyquist plot from the Y axis (left side) represents ohmic overpotential followed by the kinetic overpotential in the mid frequency range, and finally the low frequency region (right side) demonstrates the mass transport overpotential. Nyquist plots at two current densities reveal information for different processes; at 100 mAcm^{-2} charge transfer resistance should be significant whereas at 500 mAcm^{-2} mass transport should play an important role. All the curves in Fig. 5 were made by the raw data of the impedance spectroscopy. Considering a negligible overpotential of the anode electrode, the arcs of all MEAs should be dominated by the ORR reaction at the cathode at 100 mA/cm^2 current density. Interestingly, already at this low current density an additional arc at lower frequency appear for the standard and catalyst modified MEA demonstrating mass transport influences most probably by badly contacted catalytic region. When current density increases, impedance decreases subsequently. In the graph 5b, each arrow was illustrated as the reduced impedance of distinctive MEAs after increasing current density. The larger arrow assigns the larger reduction of impedance value, which explains better performance as well. As current density increased, the arc responsible for kinetic over potential is reduced and the arc responsible for diffusion over potential remained almost unchanged for support modified and catalyst modified MEAs. On the other hand, in case of standard dry sprayed MEA, significantly higher diffusion problem started to appear even at 500 mA current density. It is also justifiable by the polarization curve that shows total performance loss after 1000 mA/cm^2. Moreover, the Nyquist plot displays that catalyst modified powder sprayed MEA surpasses the support modified powder sprayed MEA after ohmic over potential zone and both of them retains better diffusion properties in mass transport zone compared to the standard dry sprayed MEA.

EIS-inputs of different MEAs in different current densities were fitted into the equivalent circuit which is illustrated in Fig. 6 (inset). Afterwards, we simulated the data in Zahner software with a common equivalent circuit to determine main parameters, namely the inductance of the set-up, the cell ohmic resistance, the charge transfer resistance and Nernst diffusion contribution of the cell within 2.5% statistical error on average. At higher frequency, the presence of 45° line in the Nyquist plot in Fig. 5 for all MEAs indicates that the proton transport loss (stated later) has a significant effect in these porous electrodes [23,25]. We can observe the similar behavior from the simulated value also. The constant of diffusion (Kn), which attributes to the Nernst diffusion component and proportional to the diffusion impedance, gives us a clear impression of the cathode electrode. Electrode with standard powder gives us the value Kn = 304 S^{-1} whereas; electrode with modified support gives 73 S^{-1} and modified catalyst gives 107 S^{-1} at 100 mA current density. This consequence can also be deduced from the Nyquist plot in Fig. 5(a), where we can see the biggest contribution of diffusion impedance from the electrode with standard powder, and progressively reduced in the electrode with modified catalyst powder and minimum in case of modified support. The ohmic and the cathodic charge transfer resistance were exploited to a bar chart to demonstrate the over potential in different current densities. We can observe almost similar behavior of ohmic resistance at 100 mA from the simulated value. MEA fabricated with standard dry spray shows higher charge transfer resistance at lower current density which is expected due to its poor protonic conductivity, and as we increase the current

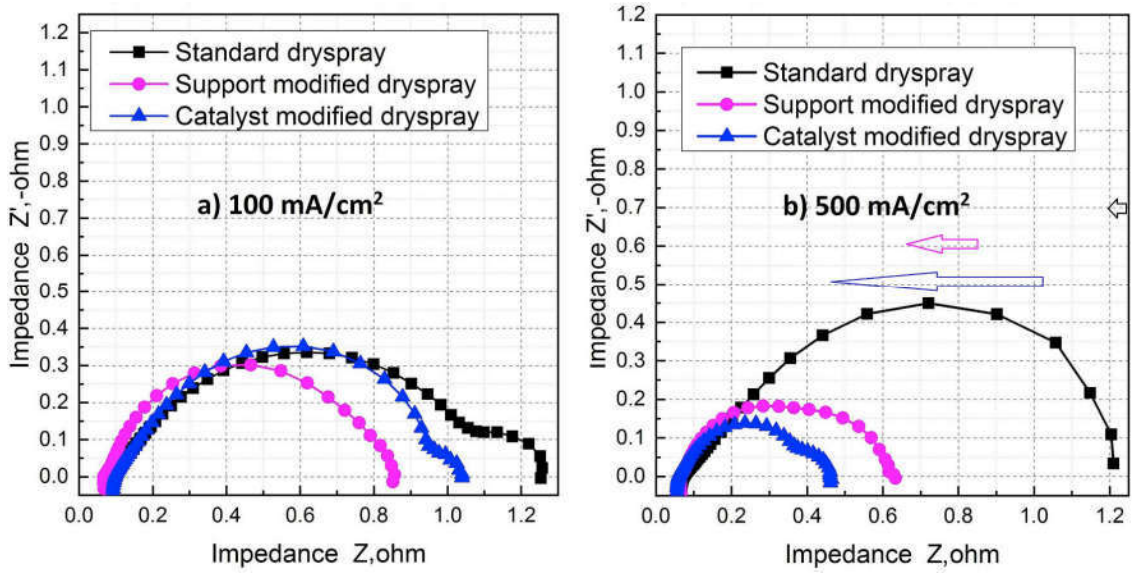

Fig. 5. EIS-Nyquist plot of MEAs prepared by unmodified, support modified and catalyst modified powder in the frequency range of 100 mHz to 100 kHz at a current density (a) 100 mA and (b) 500 mA.

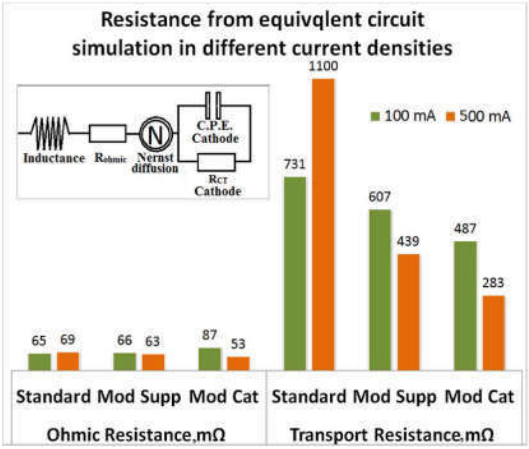

Fig. 6. (Inset) Equivalent circuit used for the evaluation of impedance spectra with the resistance values for ohmic and transport over-potential at a current densities of 100 $mAcm^{-2}$ (green) and 500 $mAcm^{-2}$ (orange). (For interpretation of the references to colour in this figure legend, the reader is referred to the Web version of this article.)

density the resistance also increases drastically. On the contrary, MEA prepared with modified catalyst shows a noteworthy recovery of both ohmic and charge transfer resistance at higher current density which is also manifested in the performance in the polarization curve.

Ionic conductivity measurement of MEA is a powerful tool considered to evaluate the ionic and electronic resistance inside the catalyst layer. The effects of the inhomogeneity of the catalyst layers [23,24] are more clearly observed in the impedance plots shown in Fig. 7(a). The high-frequency slope of the curve for the electrode impregnated with liquid Nafion® (modified powder sprayed MEAs) is markedly steeper than electrode fabricated with solid Nafion® (standard powder sprayed MEA). Higher proton conductivity and better ionomer distribution is explained by the steeper capacitance slope in Fig. 7(a). At high frequencies a Warburg-like response (45 °C slope) is observed, corresponding to ion migration through the catalytic layer, and at low frequency it is linear up to about half of the limiting capacitance and then curves up to a constant capacitance and resistance which corresponds to the total resistance and capacitance of the catalytic layer. Fig. 7(b) shows the calculated ohmic and ionic resistance of the catalyst layer. Characterization of the ionic resistance of catalyst layer can give an important measure of electrode quality and can provide valuable feedback for an optimized MEA structure [23,24]. Another advantage of Nafion® impregnation by dispersion is that more of the electrochemically active catalyst layer is accessible, as can be seen from the larger slope of the limiting capacitance observed from the modified powder sprayed electrode. These characteristics can be translated into improved performance as a fuel cell cathode in modified powder sprayed MEAs in contrast with standard powder. The distribution of ohmic and ionic resistance in the Fig. 7(b) also coincides with the performance of different MEAs. High frequency impedance (ohmic resistance) depends on the electrical connections, proton conductivity of ionomer, ratio of ionomer and MEA compression while assembling in the cell. As the comparison of the MEAs is performed with similar conditions (e.g. torque, reaction condition and ionomer ratio), it is understandable that the ohmic resistance is similar for all MEAs. The significant difference in ionic resistance is due to the different ionomer distributions within the catalytic layer and this is the important factor for performance. The drysprayed MEA has a heterogeneous ionomer distribution and poor availability of reaction interface. Agglomeration of particles plays also a vital role to reduce the electrochemically active area. When the ORR produces higher current under practical cell operating conditions, the ionomer distribution becomes more important because of the contribution of resistances to the mass transport of H^+ and O_2 through ionomer.

Fig. 8 demonstrates the SEM images of the cross-section of the electrodes after 48 h of fuel cell operation. MEA prepared with dry spray coating method shows an uneven thickness in the catalyst layer. Due to the limitation of the particle size and formation of agglomerates in the humid environment, we have not yet successfully fabricated a flat and uniform electrode layer. We expect that, “a better control of the humidity on the coating laboratory” may solve this problem. However, MEA prepared with standard powder shows a very non-uniform electrode layer with a large difference in thickness. In some areas the thickness of the CL goes down to 2 µm, in contrast to some other areas where agglomerated powder causes CCM thickness go as high as 30 µm (not in the picture). This variety of thickness is also responsible for heterogeneous current densities throughout the MEA, which causes instability of performance and hence shows higher degradation in electrodes and membrane as well. In contrast, the dispersion modified catalytic layers also show thickness heterogeneity but there microscopic

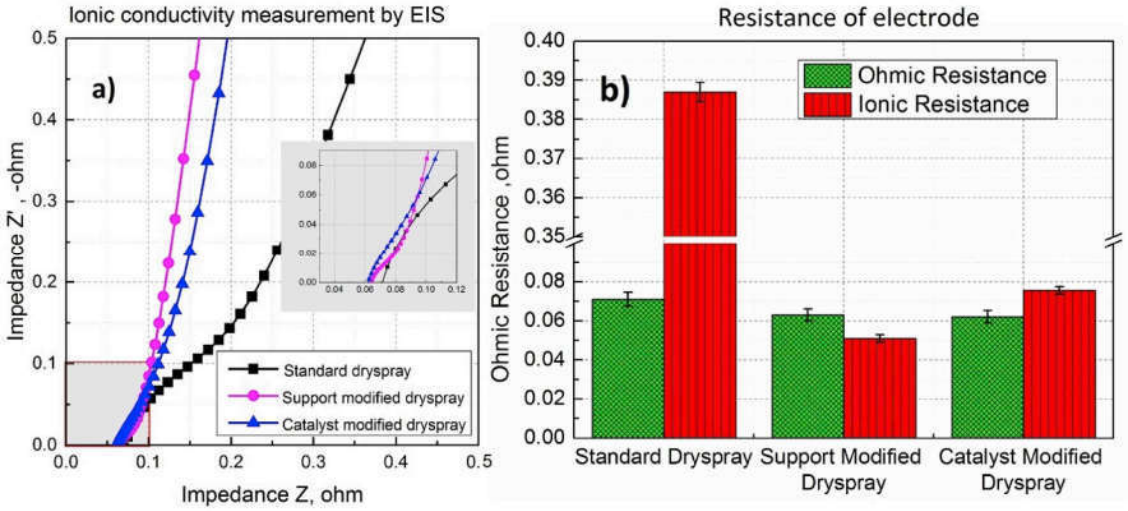

Fig. 7. a) Ionic conductivity measurement by EIS of MEAs prepared with standard (the inset represents an expansion of the high frequencies region where the curvature of approximately 90° is the representative of the limiting capacitive current), support modified and catalyst modified powder at 100% humidity with H_2/N_2 flow, b) distribution of electronic and ionic resistance.

structure is more homogeneous as reflected by better performance and stability.

It was reported by Uchida et al. that a good network and uniformity of Nafion® on Pt particles could be achieved by using "colloid" form of Nafion® in the catalyst "ink". There should be an optimum thickness of the ionomer film for superior performance [29,30]. Watanabe has reported that 0.2 μm is the critical thickness of the Nafion® film on the catalyst surface up to which the diffusion process of reactant gases to the catalyst sites is not the rate-determining step [25]. We believe that, if the Pt particle and ionomer distribution are further improved and we singularize the agglomerates during dry spraying more efficiently, it will be possible to further increase the performance of dry sprayed MEA.

5. Conclusion

This work shows how the inclusion of dispersed liquid Nafion® into catalyst powder, followed by drying and powder spraying enhances the fuel cell performance. Using liquid Nafion® instead of solid Nafion introduces ionomer films around the catalyst support as well as catalyst agglomerates hereby induces better ionomer distribution throughout the catalyst layer. It is plausible that, due to partial ionomer film forming property over catalyst particles, electrochemically active interface zone increases and so does the performance. We can justify the progression functioning as,

1) Reduction of the subsequent agglomeration of ionomer powder as well as catalyst particles and securing better distribution of ionomer by using dispersion media,
2) Thin film-ionomer structures by replacing large solid ionomer particles with Nafion® dispersion. Enhance the ionic conductivity, electrochemical properties and diffusion properties by coating catalyst and/or support particles with thin ionomer film.

However, along with better performance, the novel processes can ease the powder preparation technique by avoiding the cryogenic grinding of Nafion® which is a lengthy process. MEA prepared with dry spray coating technique has a significant potentiality in industrial manufacturing as it is a fast, easy, inexpensive and fully automatic process. Nevertheless, there are some more opportunities to enhance performance by improving catalyst-ionic structure, which should be looked into our future work.

1. Improve the distribution and homogeneity of ionomer network.
2. Fabricating 100 nm ionomer particles by spray drying the ionomer dispersion. (Spray drying is a method of producing a dry powder from a liquid or slurry by spraying and drying simultaneously).
3. Preferential non-uniform coating of ionomer over carbon support particle by spray dry technique.

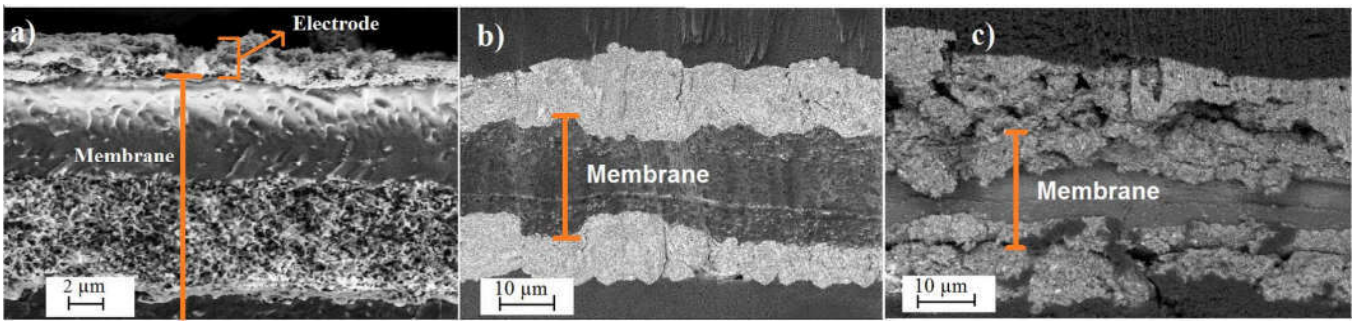

Fig. 8. SEM images of ion beam cut cross-sectional of catalyst layers with same noble metal loadings of 0.3 mg/cm^2 on one side a) inhomogeneous catalyst layer MEA sprayed with standard powder, b) sprayed with support modified, and c) sprayed with catalyst modified powder sprayed MEA; the orange bar is the thickness of membrane. (For interpretation of the references to colour in this figure legend, the reader is referred to the Web version of this article.)

Funding

Corresponding author's PhD thesis is funded by DLR-DAAD research fellowship 2015.

References

[1] N. Konno, S. Mizuno, H. Nakaji, Y. Ishikawa, Development of compact and high-performance fuel cell stack, SAE Int. J. Alt. Power. 4 (1) (2015) 123–129 https://doi.org/10.4271/2015-01-1175.
[2] R. O'Hayre, S.W. Cha, W. Colella, F.B. Prinz, Fuel Cell Fundamentals, second ed., John Wiley & Sons, New Jersy, 2009 Chapter 1. ISBN13: 9780470258439.
[3] J. Kurtz, S. Sprik, C. Ainscough, G. Saur, Annual Merit Review, Fuel Cell Electric Vehicle Evaluation, DOE Project, 20122015. National Renewable Energy Laboratory.
[4] J.H. Wee, K.Y. Lee, S.H. Kim, A. Kaufman, Fabrication method for low-Pt-loading electrocatalysts in proton exchange membrane fuel cell, J. Power Sources 165 (2007) 667–677 https://doi.org/10.1016/j.jpowsour.2006.12.051.
[5] Z. Qi, A. Kaufman, Low Pt loading high performance cathodes for PEM fuel cells, J. Power Sources 113 (1) (2003) 37–43 https://doi.org/10.1016/S0378-7753(02)00477-9.
[6] Y. Liu, M.W. Murphy, D.R. Baker, W. Gu, C. Ji, J. Jorne, Hubert A. Gasteiger, Proton conduction and oxygen reduction kinetics in PEM fuel cell cathodes: effects of ionomer-to-carbon ratio and relative humidity, J. Electrcohem. Soc. 156 (8) (2009) 970–980, https://doi.org/10.1149/1.3143965 B.
[7] S. Litster, G. McLean, PEM fuel cell electrodes, J. Power Sources 130 (2004) 61–67 https://doi.org/10.1016/j.jpowsour.2003.12.055.
[8] S. Shukla, K. Domican, K. Karan, S. Bhattacharjee, M. Secanell, Analysis of low platinum loading thin polymer electrolyte fuel cell electrodes prepared by inkjet printing, Electrochim. Acta 156 (2015) 289–300 https://doi.org/10.1016/j.electacta.2015.01.028.
[9] K.L. More, R. Borup, K.S. Reeves, Identifying contributing degradation phenomena in PEM fuel cell membrane electrode assemblies via electron microscopy, ECS Trans. 3 (1) (2006) 717–733, https://doi.org/10.1149/1.2356192.
[10] T. Muzaffer, T. Kadyk, M. Eikerling, Physical modeling of the proton density in nanopores of PEM fuel cell catalyst layers, Electrochim. Acta 245 (2017) 1048–1058 https://doi.org/10.1016/j.electacta.2017.05.052.
[11] K. Talukdar, H.J. Kim, Y.H. Kim, H.C. Lee, S.J. Choi, Polyacrylamide/Nafion® semi-interpenetrating networks as proton-conducting membrane of direct methanol fuel cell, Sci. Adv. Mater. 6 (2014) 2389–2394 https://doi.org/10.1166/sam.2014.2190.
[12] K. Talukdar, H.J. Kim, Y.H. Kim, Y.J. Park, H.C. Lee, S.J. Choi, Proton-conducting membrane from nafion®/polystyrne sulfonate composite for fuel cell applications, J. Nanoelectron. Optoelectron. 10 (2015) 535–540 https://doi.org/10.1166/jno.2015.1797.
[13] T. Morawietz, M. Handl, C. Oldani, K.A. Friedrich, R. Hiesgen, Quantitative in-situ analysis of ionomer structure in fuel cell catalytic layers, ACS Appl. Mater. Interfaces 8 (40) (2016) 27044–27054, https://doi.org/10.1021/acsami.6b07188.
[14] E. Güzlow, M. Schulze, N. Wagner, T. Kaz, A. Schneider, R. Reissner, New dry preparation techniques for membrane electrode assemblies for PEM fuel cells, Fuel Cells Bull. 15 (1999) 8–12 https://doi.org/10.1016/S1464-2859(99)80002-9.
[15] D. Bevers, N. Wagner, M. Von Bradke, Innovative production procedure for low cost PEFC electrodes and electrode/membrane structures, Int. J. Hydrogen Energy 23 (1998) 57–63 https://doi.org/10.1016/S0360-3199(97)00028-1.
[16] N. Wagner, T. Kaz, K.A. Friedrich, Investigation of electrode composition of polymer fuel cells by electrochemical impedance spectroscopy, Electrochim. Acta 53 (2008) 7475–7482 https://doi.org/10.1016/j.electacta.2008.01.084.
[17] S. Holdcroft, Fuel cell catalyst layers: a polymer science perspective, Chem. Mater. 26 (2014) 381–393, https://doi.org/10.1021/cm401445h.
[18] J. Larminie, A. Dicks, Fuel Cell System Explained, John Wiley, New Jersey, 2000 Chapter 2. ISBN-13: 978-0471490265.
[19] E.F. Hansen, S. Walston, M.H. Bishop, Matte Paint vol. 2, WAAC Newsletter, 1996 (18), http://cool.conservation-us.org/waac/wn/wn18/wn18-2/wn18-207.html.
[20] T. Brock, M. Groteklaes, P. Mischke, U. Zorll (Ed.), European Coating Handbook, Th. Schäfer, Hannover, 2000Chapter 3.3. ISBN: 3-87870-559-X.
[21] E. Gülzow, T. Kaz, New results of PEFC electrodes produced by the DLR dry preparation technique, J. Power Sources 106 (2002) 122–125 https://doi.org/10.1016/S0378-7753(01)01030-8.
[22] E. Güzlow, M. Schulze, N. Wagner, T. Kaz, R. Reissner, G. Steinhilber, A. Schneider, Dry layer preparation and characterisation of polymer electrolyte fuel cell components, J. Power Sources 86 (2000) 352–362 https://doi.org/10.1016/S0378-7753(99)00451-6.
[23] M.C. Lefebvre, R.B. Martin, P.G. Pickup, Characterization of ionic conductivity profiles within proton exchange membrane fuel cell gas diffusion electrodes by impedance spectroscopy, Electrochem. Solid St. 2 (6) (1999) 259–261, https://doi.org/10.1149/1.1390804.
[24] G. Li, G. Pickup, Ionic conductivity of PEMFC electrodes; effect of nafion loading, J. Electrochem. Soc. 150 (11) (2003) C745–C752, https://doi.org/10.1149/1.1611493.
[25] M. Watanabe, H. Igarashi, K. Yosida, An Experimental Prediction of the preparation condition of Nafion-coated catalyst layers for PEFCs, Electrochim. Acta 40 (3) (1995) 329–334 https://doi.org/10.1016/0013-4686(94)00271-2.
[26] K.R. Cooper, Experimental Methods and Data Analyses for Polymer Electrolyte Fuel Cells, Southern pinesm N.C. Schribner Associates, 2005 OCLC: 764047139.
[27] Y.C. Park, H. Tokiwa, K. Kakinuma, M. Watanabe, Effects of carbon support on Pt distribution, ionomer coverage and cathode performance for polymer electrolyte fuel cells, J. Power Sources 315 (2016) 179–191 https://doi.org/10.1016/j.jpowsour.2016.02.091.
[28] K. Malek, T. Mashio, M. Eikerling, Microstructure of catalyst layer in PEM fuel cells redefined: a computational approach, Electrocatal. 2 (2011) 141–157, https://doi.org/10.1007/s12678-011-0047-0.
[29] Z. Siroma, T. Sasakura, K. Yasuda, M. Azuma, Y. Miyazaki, Effects of ionomer content on mass transport in gas diffusion electrodes for proton exchange membrane fuel cells, J. Electroanal. Chem. 546 (2003) 73–78, https://doi.org/10.1016/S0022-0728(03)00147-5.
[30] M. Uchida, Y. Aoyama, N. Eda, A. Ohta, New preparation method for polymer-electrolyte fuel cells, J. Electrochem. Soc. 142 (2) (1995) 463–468, https://doi.org/10.1149/1.2044068.

Journal of Power Sources 439 (2019) 227078

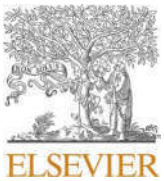

Contents lists available at ScienceDirect

Journal of Power Sources

journal homepage: www.elsevier.com/locate/jpowsour

Comparative investigation into the performance and durability of long and short side chain ionomers in Polymer Electrolyte Membrane Fuel Cells

Krishan Talukdar [a,*], Pawel Gazdzicki [a], K. Andreas Friedrich [a,b]

[a] German Aerospace Center (DLR), Institute of Engineering Thermodynamics, Pfaffenwaldring 38-40, Stuttgart, 70569, Germany
[b] University of Stuttgart, Institute of Building Energetics, Thermal Engineering and Energy Storage (IGTE), Pfaffenwaldring 31, 70569, Stuttgart, Germany

HIGHLIGHTS

- Ionomers with different side chain length are analyzed for short and long term test.
- Thinner membrane causes high gas crossover leads to higher rate of degradation.
- Gas crossover motivates the migration of Pt radical thus membrane decomposition.
- Less PTFE content of lower EW ionomer explains weaker polymeric stability.
- Longer side chain ionomer is advantageous for extended application.

ARTICLE INFO

Keywords:
Polymer electrolyte membrane fuel cell
Perfluorinated sulfonic acid membrane
Short side chain ionomer
Long side chain ionomer
Durability

ABSTRACT

Perfluorinated sulfonic acid (PFSA) ionomers have high proton conductivity and excellent mechanical-chemical stability under humid conditions in low temperature Polymer Electrolyte Membrane Fuel Cell (PEMFC) application. In this work, we compare performance and durability between long side chain (LSC) and short side chain (SSC) PFSA ionomers as a solid electrolyte membrane and as ionomer-additive in the electrodes. Membrane electrode assemblies (MEAs) are prepared combining the LSC/SSC membrane with the corresponding LSC/SSC ionomer in the catalyst layer. Thereby, their chemical compatibility could be determined. MEAs are tested in single cell test benches with segmented bipolar plate for long term degradation test with dynamic load-cycling. While maintaining uniform conditions, we have experienced that different MEAs show different behavior in short-term to long-term application. Owing to its stability in lower equivalent weight; SSC ionomer provides favorable proton conductivity leading to higher power density of the cell. Nevertheless, faster degradation of SSC than the LSC ionomer are encountered in this study likely due to the higher gas permeation of thinner SSC membranes and lower polytetrafluoroethylene content. This study contributes a significant insight in the behavior of ionomers in FC as function of time, and shows avenues for further improvement of durability.

1. Introduction

Recently, proton exchange membrane (PEM) fuel cell systems has been introduced as alternatives to the internal combustion engine in cars, trucks and buses as well as novel micro-combined heat and power devices for residential applications [1]. Polymer electrolyte membrane fuel cells (PEMFCs) are receiving more and more attention worldwide due to its advantages with respect to batteries. If hydrogen is generated from renewable energies PEM fuel cells are green energy converters for stationary and mobile applications. PEMFCs have exceptional advantages such as lightweight, high power, low operating temperature, and fast startup [2].

During last few years, Nafion®, a long side chain (LSC) ionomer, is used as electrolyte membrane for PEM fuel cell application. It is a perfluorinated sulfonic acid (PFSA) copolymer and its unique ionic property is a result of incorporating perfluorovinyl ether chains edged with sulfonate groups onto a tetrafluoroethylene (PTFE) backbone [3,4]. Furthermore, the PFSA ionomer is also added with catalyst powder to the electrodes to extend the reactive interphase among catalyst, gas phase and proton conducting membrane [5,6]. Polymer chemists are continuously developing novel structures to increase the proton conductivity at elevated temperatures and to enhance mechanical stability

* Corresponding author.
E-mail address: krishan.talukdar@dlr.de (K. Talukdar).

https://doi.org/10.1016/j.jpowsour.2019.227078
Received 2 July 2019; Received in revised form 26 August 2019; Accepted 27 August 2019

[7,8]. In the last decade, Solvay introduced a modified version of PFSA with short side chains (SSC) under the trademark "Aquivion®" [9,10]. Particularly thin SSC membranes for fuel cell applications have been developed within the FCH JU IMPACT project.[1] LSC and SSC ionomers both possess two phases, being semi-crystalline fluoropolymers they have a backbone which has hydrophobic properties and a hydrophilic sulfonic acid at the end of the side chain. The chemical structure of SSC membranes has been shown to exhibit the benefits of highest crystallinity amongst commercial PFSAs, chemical inertness and mechanical integrity up to 140–160 °C [10]. Thanks to the strong electronegative effect of fluorine atoms in its perfluorinated structure and the strong acidity of the sulfonic acid group, Aquivion® PFSA is a super-acid, with a Hammett acidity function of −12, at par with the value of pure sulfuric acid [11,12]. Furthermore, it has slightly higher glass transition temperature (Tg) than Nafion® (140–160 °C vs. 100 °C) and is thermally stable up to 230 °C. Advanced water uptake property leads to improved proton conductivity, especially at low relative humidity and higher temperature [13,14]. The distribution of ionomers is significant to optimize electrodes for PEMFC. Different levels of humidity within the catalyst layer have been associated to ionomer distribution and consequently to heterogeneous distribution of the current density in PEM fuel cell [15]. The equivalent weight (EW, unit: g mol^{-1} or g eq^{-1}) of the ionomer, by definition the weight of ionomer (in terms of molecular mass) per sulfonic acid group, is the most important value characterizing inversely the exchange capacity. Shorter side chain length of Aquivion® makes it possible to produce dispersion with lower equivalent weight and therefore higher proton conductivity. SSC ionomers show the benefits of higher proton conductivity and water retention capacity. For LSC ionomers with the prototypical Nafion®, a recasting procedure has been found to yield better films with an equivalent weight of 996 ± 24 g mol^{-1}. The lowest equivalent weight (highest exchange capacity) with stability of the ionomer matrix found for a Nafion® composite is 878 ± 8 [19]. So, most of the available commercial Nafion® dispersion, membrane or beads have EW over 900. Whereas Aquivion® has shorter PTFE side chain, which allows it to remain stable and physically stronger than Nafion® also in lower EW range [15]. According to the literature [16,17], this advantage of shorter side chain of Aquivion® makes it possible to achieve either better mechanical properties at the same ion-exchange capacity (IEC) or a higher IEC at the same mechanical properties than LSC polymers which directly influence the proton conductivity as well as performance.

It is observed that the water sorption as well as the proton conductivity increases with decreasing EW until extreme swelling indicates dissolution of the membrane and a reduction in conductivity as a consequence of dilution. Additionally, the higher amount of water in the membrane makes the membrane softer, i.e., their mechanical properties deteriorates, which affects the long term stability of membrane. From these considerations it has been derived that there should be an optimum EW to achieve the highest proton conduction while maintaining the physical integrity of polymer matrix [18,19]. Stassi et. Al. reported the performance of long and short sidechain perfluorosulfonic membrane for high temperature PEMFC operation [20]. Very recently, Shahgaldi et. Al. exhibited the impact of short side chain ionomer in PEMFC performance and durability with accelerated stress test, whereas they only focused on the application of ionomer in the catalyst layer [21]. Moreover, Wu et. Al. also studied short side chained perfluorosulfonic acid ionomer for PEM electrolyser [22]. However, a comparative study of different side chain ionomers in both short term and long term durability test as membrane and electrode application in low temperature PEMFC is still lacking.

In this work, our group demonstrates a combination of tests including both SSC and LSC ionomer in membrane as well as in catalyst layer, which will provide a deep insight regarding evaluation of ionomer. We have used stabilized Aquivion® membrane and dispersion which has the EW value around 800. All the MEAs were prepared with 0.3 mg Pt cm^{-2} loading in both anode-cathode side while maintaining uniform conditions and tested in both of the 1 cm^2 and 25 cm^2 single cell test-stations along with electrochemical impedance spectroscopy (EIS). Moreover, this article addresses the complex influence of ionomers with different side chain length for PEMFC durability with the help of load cycling test. Ex-situ characterizations such as scanning electron microscopy (SEM), infrared spectroscopy (IR) and X-ray Photoelectron spectroscopy (XPS) were also performed to determine the intrinsic properties of the ionomers and catalyst layer. Eventually, we also tried to explain the complex behavior of MEAs with the properties of the membrane and the catalytic layer. A systematic performance and durability comparison between Aquivion® and Nafion® as an electrolyte and as a proton conducting additive in the catalyst layer (CL) is the main novel feature of this work.

2. Experimental

Table 1 shows the difference in properties between LSC ionomer (Nafion®) and SSC ionomer (Aquivion®) both in membrane and dispersion form. These data are received from manufacturers. Please note the significant difference in membrane thickness (factor 2.5) between Nafion® and Aquivion®.

2.1. Electrode preparation

In this work, MEAs were fabricated by hot pressing gas diffusion electrodes (GDE) and membranes. The preparation technique we used to make GDEs is an airbrush coating technique, which is fast and very widely used [23]. We have used a commercial plastic airbrush with nitrogen gas to spray. We have taken measures like dedicated spraying equipment to avoid contamination and unwanted reactions. To make the catalyst ink the same recipe was followed: We used 40 wt% Pt/C Hispec 4000 (Alfa Aesar) as a catalyst powder and dispersed it with 100 times higher weight of ultrapure water (VWR) by means of ultra-sonication for 30 min. This suspension was put in ultrasonicator with ice cubes in it to keep the temperature low. Ionomer dispersion was added dropwise while sonication was running. The ionomer was added so that catalyst powder and ionomer reached the ratio of 70:30 in solid weight. Eventually, isopropanol (VWR) weighted 75 times higher comparing to catalyst powder was added to the final suspension to make the ink more volatile. This suspension was again sonicated for 30 min. During spraying the catalyst ink over gas diffusion layer (GDL), it was placed on the heating plate, which was kept in 105 °C to evaporate the solvents directly from the surface of the GDL. The Pt loading was measured gravimetrically. The gravimetric catalyst powder-to-ionomer 70:30 ratio ionomer was maintained, which is the optimum

Table 1
Technical information of the ionomers from the manufacturers.

Nafion® (Ion Power)		Aquivion® (Solvay)	
Membrane	Dispersion	Membrane	Dispersion
Nafion® XL	Nafion® D521	Aquivion® R79-01SX+	Aquivion® D83-25BS
Equivalent weight 1100 g eq^{-1}	Equivalent weight 1100 g eq^{-1}	Equivalent weight 790 g eq^{-1}	Equivalent weight 833 g eq^{-1}
Average thickness 28 μm	Polymer content 5.4 wt%	Average thickness 11 μm	Polymer content 5.97 wt%
Stabilized	Solvent: Alcohol and water	Stabilized	Solvent: water
Reinforced	Total acid capacity: 0.95–1.03 meq g^{-1}	Reinforced	Total acid capacity: 1.17–1.23 meq g^{-1}

[1] https://www.fch.europa.eu/project/improved-lifetime-automotive-application-fuel-cells-ultra-low-pt-loading.

composition for a catalyst loading of 0.3 mgPt cm^{-2} [24,25]. In this work, the same weight ratio of ionomer was used in the ink preparation. It is noted that keeping the gravimetric catalyst powder-to-ionomer constant means that the Nafion® based electrode with EW 1100 has lower IEC than the Aquivion® based electrode with lower EW 833. The alternative approach of keeping IEC constant, on the other hand, would mean to increase Nafion® weight ratio by 20–23% in the electrode which will impact the ink rheology and electrode structure significantly. This effect is well-known to affect cell performance and durability [25,26]. Hence, it is not possible to change just one single parameter of an electrode because the different parameters affect each other. To understand the influence of the different IEC ionomer values in the electrode a microscopic structure investigation would be necessary which is out of scope of this study.

The isopropanol (IPA) ratio was kept at 43 wt% of the total solvent because a lower IPA content in the IPA/water solvent of the Pt/C/ionomer catalyst ink solutions results in the formation of larger and higher negatively charged ionomer aggregated particles [25,26]. This leads to higher steric hindrance and higher charge repulsion of ionomer particles on the surface of Pt/C particles, thus a thinner ionomer film in contact on the surfaces of the Pt/C particles [26]. The thinner ionomer film in contact with the Pt particles in the CL of MEAs improves gas permeations and the probability of the Pt particles to come into contact with the reactant H_2/O_2 (air) fuel gases. This phenomenon enhances the generation of H^+ ions on the Pt particle surfaces in the CL, leading to higher fuel cell performance [27,28,41].

2.2. Membrane electrode assembly

GDL (25BC, SGL Carbon) was used as substrate for GDE manufacturing with airbrush spray. The resulting GDE was immediately hot pressed with Nafion® XL or Aquivion® membranes at 150 °C for 5 min by heat press (Vogt). Pressure was maintained close to 700 N cm^{-2} in the hot press. The tests were performed using a dedicated test bench. Both used fuel cell test benches were developed at German Aerospace Center (DLR). The test benches, controlled by programmable logic controller (PLC), allow automatic control of the input and output conditions, such as the pressure, temperature, flow rate of gases, and humidity of reactants. All MEAs were operated at stoichiometric flow of λ_{H2}: 1.5, λ_{air}: 2.25 during conditioning, polarization curve measurement and degradation testing.

2.2.1. Short term testing facility

To characterize the short term performance of the fabricated MEAs, they were mounted in a 1 cm^2 cell, which is a gold coated bipolar plate on top of graphite flow field purchased from Electrochem. The gas mass flow rates (H_2 and air) were controlled through the test station and could be varied between 0 and 25 ml min^{-1} on the anode side and between 0 and 75 ml min^{-1} on the cathode side in the small test bench. MEAs for 1 cm^2 were assembled over flow field with 206 μm PTFE gaskets. The following conditions for these MEAs were constant: torque: 2 Nm, humidification: 50% and, cell temperature: 80 °C, pressure: 1500 mbar (abs.).

2.2.2. Long term testing facility

To characterize long term stability and degradation mechanism, a gold coated stainless steel 25 cm^2 cell (single channel serpentine counter flow field) was used with a designated larger test bench. The 25 cm^2 cell was equipped with a segmented cell (49 segments) to monitor local current density in order to observe heterogeneous behavior during degradation tests. The gas mass flow rate was in between 0 and 500 ml min^{-1} on the anode side and between 0 and 2000 ml min^{-1} on the cathode side in the larger test bench. MEAs with 25 cm^2 had all the following conditions: torque: 4 Nm, humidification: 100% and, cell temperature: 80 °C, pressure: 1500 mbar (abs.).

2.3. Characterization facilities

The locally resolved current density measurements were performed with the 25 cm^2 cell using DLR's segmented bipolar plate (SC) based on printed circuit board (PCB) technology with integrated temperature sensors. This device allows gaining insight into the current distribution homogeneity, especially during the degradation experiments. The measurement of in-situ local current distribution (DLR segmented cell) have been successfully used as a powerful in-situ diagnostic tools during the last years for the study of local processes [29] which are influenced by heterogeneous water management [30,31], contamination effects [32] and membrane integrity [33]. A defined fuel cell dynamic load cycling protocol (FC-DLC) [34,35] was followed for each MEA for 4 weeks including one day refresh after each week. During load cycling the cells were operated at constant flow corresponding to stoichiometric flow at 1 A cm^2 current density.

Electrochemical impedance spectroscopy (EIS) was performed with an electrochemical work station IM6e (Zahner). In order to characterize the MEA by cyclic voltammograms, linear sweep voltammograms and ionic impedances, minimal flows of hydrogen and nitrogen gas were fed into anode and cathode with 100% humidification. The ionic impedance of the electrode was evaluated with EIS (complex Bode plot) in inert condition as stated in the concerning literature [36,37]. According to the literature, at high frequencies a Warburg-like response (45° slope) is observed, corresponding to ion migration through the catalyst layer. At low frequencies, the impedance plot curves up to a limiting capacitance response (vertical) which corresponds to the total capacitance and resistance of the catalyst layer. The ionic resistance, R_{ionic}, can be obtained from the length of the Warburg-like region projected onto the real impedance (Z) axis ($= R_{ionic}/3$). Shifting of the initial real impedance (Z) point in X-axis (Z) is considered as R_{ohmic}.

Pristine GDEs prepared using LSC and SSC ionomers were characterized by means of scanning electron microscope (SEM) from Ultra plus, Zeiss Corp, operated at 5 kV electron beam. For x-ray photoelectron spectroscopy (XPS) characterization, photoemission spectra were recorded using a hemispherical electron energy analyzer in an ultrahigh vacuum chamber of a base pressure of 4.10^{-10} mbar (Thermo Scientific ESCALAB250). The fresh GDE was measured first and then the gas diffusion layer (GDL) was delaminated by hand from the active layer to access the interface between catalyst layer (CL) and microporous layer (MPL) in addition to the GDL backing surface. Only samples with no apparent material transfer from the detached component were analyzed. Two MEAs were tested of each type, and it was found that the results are reproducible within less than 5% error.

2.4. Electrodes nomenclature

In this work, four types of MEAs were prepared and characterized for the comparative analysis. They are named as followed (I: ionomer in catalyst layer CL; M: membrane).

1. **I: Aquivion®, M: Aquivion®**: Aquivion® ionomer in CL, Aquivion® membrane
2. **I: Aquivion®, M: Nafion®**: Aquivion® ionomer in CL, Nafion® membrane
3. **I: Nafion®, M: Nafion®**: Nafion® ionomer in CL, Nafion® membrane
4. **I: Nafion®, M: Aquivion®**: Nafion® ionomer in CL, Aquivion® membrane

3. Result and discussion

All of the four types of MEAs were prepared for both 1 cm^2 (short term test) and 25 cm^2 (long term test). They all are characterized for comparison of their properties.

3.1. Short term test in 1 cm^2 test cell

SEM images of Fig. 1 shows the coated surface of the GDEs prepared by airbrush. Both of the electrodes were fabricated with different ionomers but same Hispec 4000 catalyst. Fig. 1a and b shows the surface of the pristine electrodes in microscale, and Fig. 1c and d shows the structure of the catalyst layer (CL) on the nanoscale. Electrodes prepared with Nafion® ionomer show higher agglomeration on the surface of the gas diffusion layer. Nevertheless, both type of electrodes show similar kind of particle distribution and almost identical porous distribution in the micro structure of the electrode. From Fig. 1c and d it is also apprehensible that the distribution of platinum nano-particle throughout both the CLs are homogeneous, which was also assured by the values from Energy dispersive X-ray spectroscopy analysis (not shown here) during the SEM analysis.

The performances characteristics of the MEAs tested in the 1 cm^2 cell are depicted in Fig. 2a and b. Fig. 2a and b illustrates the begin-of-life performance of all the MEAs with different membrane and ionomer combinations indicated in the figures. Both polarization and power curves of different MEAs in 50% humidification are presented here. From Fig. 2a and b we can determine the performance trend of the different combinations. Specifically, MEA made of electrodes with Aquivion® ionomer and Aquivion® membrane (I:Aquivion®, M:Aquivion®) exhibits highest performance. Later, I:Aquivion® M:Nafion® shows second best performance followed by I:Nafion® M:Nafion® and eventually I:Nafion®, M:Aquivion®. Catalyst layer with Aquivion® ionomer shows better performance than the equivalent with Nafion® despite of the membranes. One of the reasons for higher performance is the lower equivalent weight of Aquivion® than Nafion®, which is inversely proportional to the proton conductivity. So, the electrode made using SSC ionomer shows better performance than the one made using LSC ionomer. Furthermore, the MEA with an electrode consisting of Aquivion® ionomer displayed higher performance with thinner Aquivion® membrane than thicker Nafion® membrane because of the lower ohmic resistance. The better performance of Aquivion® membrane in particular in the ohmic dominated part of the polarization curve is also the result of higher proton conductivity and better water uptake throughout the membrane. The poor performance of I: Nafion®, M: Aquivion® comparing to I: Nafion®, M: Nafion® in the polarization curve is unexpected and demonstrates incompatibility of Nafion® ionomer with Aquivion® membrane. Nevertheless, the former outperformed the latter by better diffusion at very high current density.

Electrochemical impedance spectroscopy provides valuable insight into transport processes occurring in membrane electrode assembly during operation. Fig. 2 c clearly shows that in the kinetic region (0.1 A cm^{-2}) MEAs prepared using Aquivion® as binder in the electrode exhibit substantially lower charge transfer resistance (~0.6 Ohm) as compared to MEA with Nafion® used as binder (0.9–1.0 Ohm). This explains that, electrodes fabricated with SSC ionomer improve the reactive interphase where the electrochemical reaction takes place, and therefore reduces the kinetic polarization as well as ionic impedance (Fig. 3 c). The kinetics of an electrode improves with the good dispersion of high surface area catalyst particle and homogeneous distribution of ionomer in the CL. The isopropanol/water composition of the Pt–C/ionomer catalyst ink plays a key role in determining the morphology of the ionomer thin layer in the CLs and thus electrochemically active surface area of Pt. The dielectric constant ε of pure isopropanol, 40 wt% isopropanol and pure water are 19.9, 50.4 and 78.4 respectively [39]. Dielectric constant of a solvent is one of the major factors which determine the size of ionomer particle size or aggregation in solution. The higher the dielectric constant ε of the solvent is, the greater the probability of forming secondary aggregation. In this experiment, we received Aquivion® in water dispersion and Nafion® in 50-50 alcohol-water mixture. Eventually, they both are mixed separately with 43 wt% isopropanol-water to make the catalyst ink conveniently spray able and easily evaporable. Uchida et al. [40] found that, the ionomer penetrates only into the secondary pores between the agglomerates of the catalyst layer. The primary aggregates of Aquivion® polymer are slightly smaller than Nafion® polymer because of shorter side chain. Thus, the ionomer penetrates the secondary pore of the catalyst particles easily and is able to make good contact between catalyst and ionomer. However, Aquivion® forms larger secondary aggregates than Nafion® due to more negatively charged $-SO_3^-$ groups (Aquivion® EW < Nafion® EW) [40].

EIS in Ohmic polarization zone (500 mAcm^{-2}) is depicted by Fig. 2 d. The impedance semicircle of MEAs prepared with Aquivion® membrane becomes smaller than of MEAs with Nafion® membrane due to lower membrane thickness and higher proton conductivity of Aquivion® (see Table 1). Interestingly, at higher current density (Fig. 2 e), electrodes produced from either Aquivion® or Nafion® ionomer shows lower mass

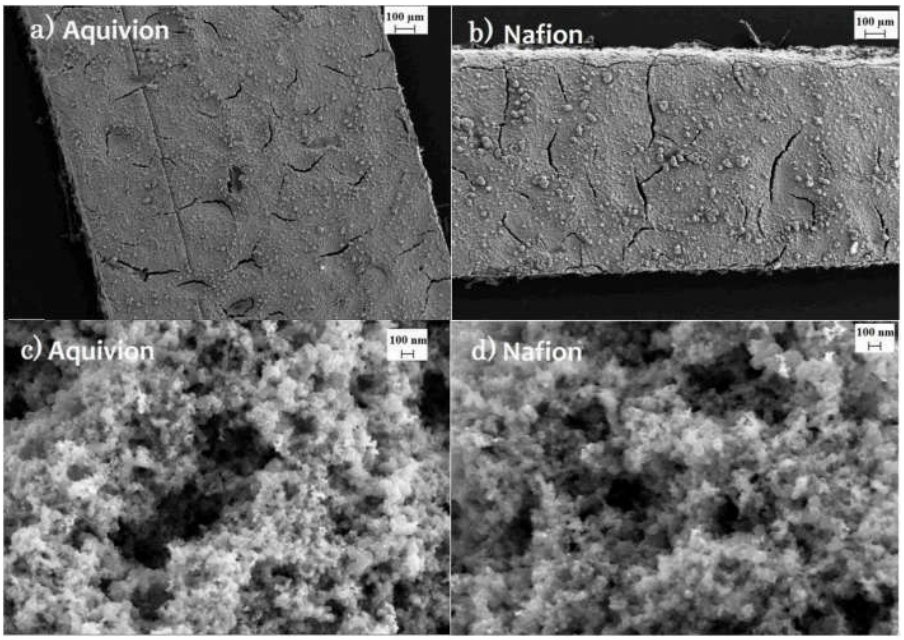

Fig. 1. SEM images of GDEs fabricated with a,c) Aquivion® and b,d) Nafion® ionomer with 40 wt% Pt/C catalyst by airbrush spray technique.

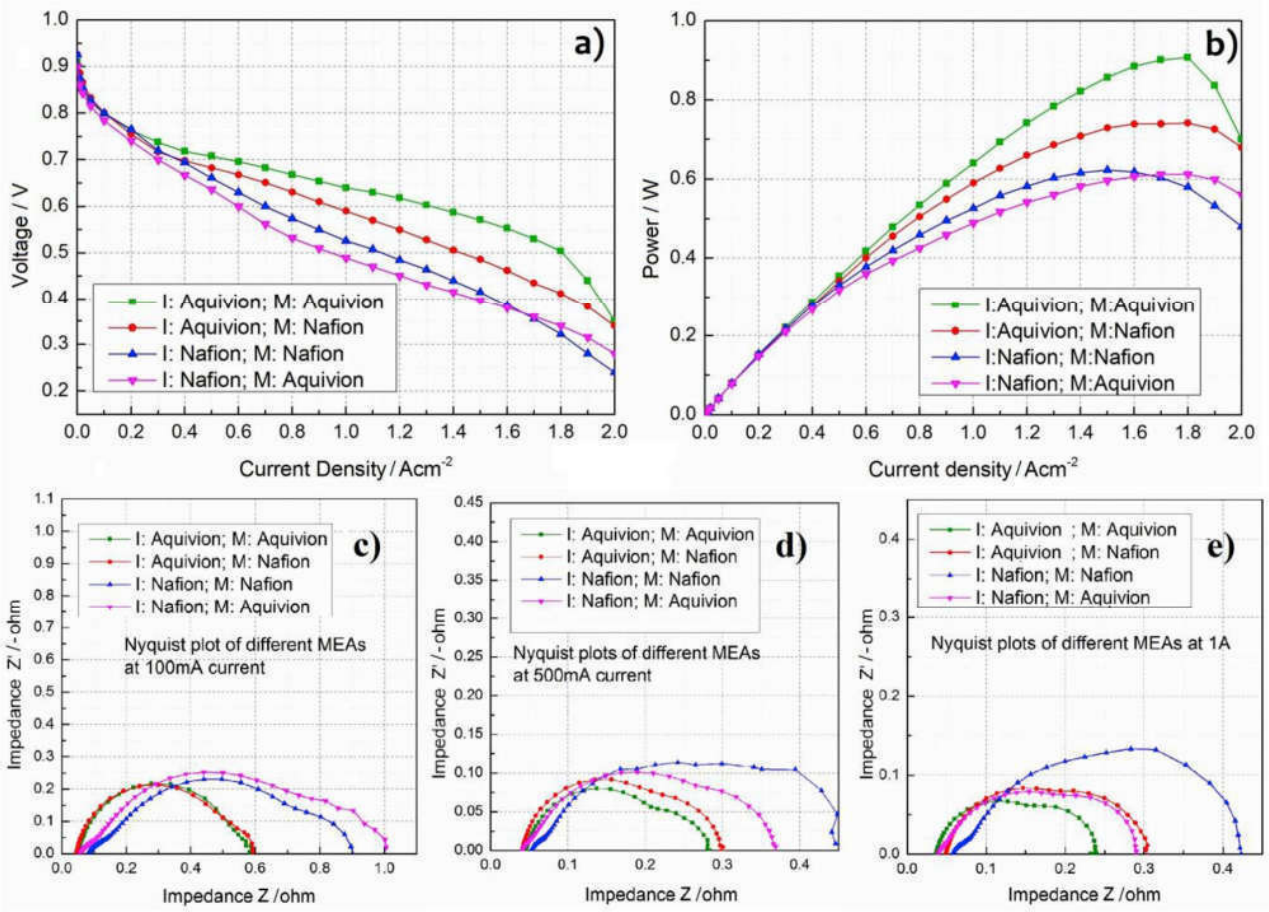

Fig. 2. a) Polarization curve and b) Power curve at begin-of-life of different MEAs measured in 1 cm^2 cell; EIS measurement: Nyquist plots of the MEAs operated in c) kinetic, d) ohmic and e) mass transport region (current densities are indicated in the figure); operated in 1 cm^2 test bench.

transport resistance with Aquivion® membrane in both EIS and polarization curve. It has to be noted, however, that also the high current region has significant ohmic contributions and as seen in Fig. 2 d,e the overall impedance of MEAs produced from Aquivion® membrane is smaller as we increase the current density. On the other hand, impedances of MEAs produced by means of Nafion® membrane do not show significant reduction at high current densities. We can conclude that the benefit of the higher water uptake of Aquivion® and lower resistance due to thinner membrane becomes especially important at higher current density. We can also speculate that during electrode preparation, the ink has a dielectric constant $\varepsilon = 50.4$ for ~40 wt % IPA-water solvent mixture. This originates higher negatively charged Aquivion® to aggregates in optimum size which results in higher steric hindrance [39]. This phenomenon causes obstacles to the deposition of large and rigid aggregates on the surfaces of the Pt/C particles that emerges voids and pores between the particles in CL. This voids and pores make the catalyst layer more permeable for feed gas and reduce the diffusion resistance. Whereas, Nafion® ionomer in the catalyst dispersion causes a higher degree of macro agglomerates and increase the polarization of the electrodes.

Mass transport diffusion of Nafion®-electrode/Nafion®-membrane in Fig. 2 e) shows the broadest arc because of the bigger size of the catalyst particle agglomeration on the GDL which was shown Fig. 1 b). On the other hand, Nafion®-electrode/Aquivion®-membrane faces less mass transport problems, due to the better water management of Aquivion® membrane. The thinner Aquivion® membrane has optimized water retention capability and water management that prevents flooding issues and reduces mass transport resistance of that MEA. Electrodes prepared with shorter side chain ionomer often shows lower mass transport diffusion in short term test compared to its alternative LSC ionomer. Park et al. has also experienced and published the similar behavior in case of short term single cell test [47,48]. The SSC ionomer covers catalyst and its support more uniformly and continuously with optimum thickness. Higher proton conductivity, uniform coverage of ionomer over carbon support, effective water trapping in the catalyst layer and better mass activity causes improved performance of MEA produced of the short side chained ionomer than the LSC ionomer [49].

Fig. 3 a) demonstrates the hydrogen crossover measured by linear sweep voltammetry. It shows us clearly the response of non-faradaic current due the crossover of hydrogen gas through the membrane [42, 44]. The thinner Aquivion® membrane causes high H_2 crossover than the thicker Nafion® membrane. It is noted that high crossover current can also play vital role in membrane degradation [38]. Consequently, thin Aquivion® membrane is responsible for both high performance and higher gas crossover due to the reduced thickness. This trade-off between low membrane resistance and high gas crossover plays a vital role in the long term performance of fuel cell which will be shown later in this article.

The measurement of electrode ionic conductivity in the MEA is an established technique, which takes into account the protonic and electronic resistance inside the catalyst layer by a transmission line model of the impedance. The effect of the inhomogeneity of the distribution and thickness of catalyst layer can be clearly observed in the capacitance value of the Nyquist plots. The effect from the distribution of ionomer and the status of the ionomer-catalyst contact through catalyst layer can be seen and clearly explained by Fig. 3-c) where the high-frequency

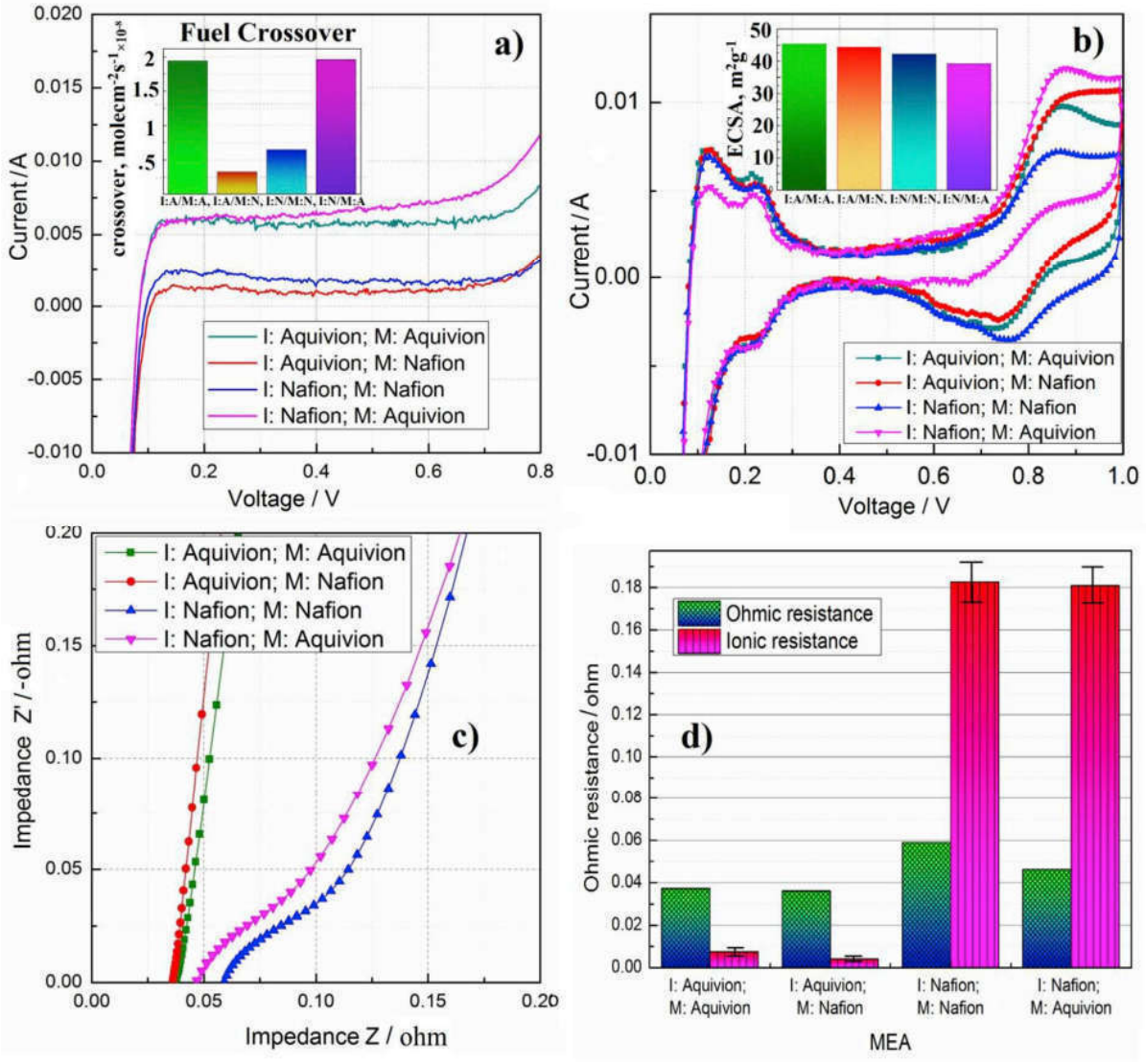

Fig. 3. a) Measurement of crossover current in MEAs with linear sweep voltammetry (inset curve illustrates amount of hydrogen crossover); b) Cyclic voltammetry graph of different MEAs (inset graph illustrates their electrochemical active surface area); c) Ionic conductivity measurement by EIS transmission line model in H_2/N_2 pumping mood; d) distribution of ionic and ohmic resistance through cathode catalyst layer.

slope of the curve associated to Aquivion®-electrode is markedly steeper than for the Nafion®-electrode indicating superior proton conductivity of Aquivion [36,37]. This phenomenon also implies that the catalyst layer consisting of Aquivion® ionomer holds tremendously less ion transport resistance comparing to Nafion® ionomer. This also explains the improved kinetics of the electrochemical reaction with better catalyst-ionomer reactive interphase which increases electrochemically active surface area of CL. The ohmic and ionic resistances of the different MEAs are reported in Fig. 3-d), according to the procedure explained in 2.3. Another advantage of electrodes with Aquivion® ionomers might be the homogenous distribution (better dispersion of the ionomer and cat and support) and substantial accessibility of catalyst over CL, as can be seen from the larger limiting capacitance observed for the Aquivion®--blended sprayed electrodes (the steepness of the curves in Fig. 3-c).

This characteristic of enhancing electrochemically active sites of the catalyst layer subjected to Aquivion®–blended gas diffusion electrodes can also be noticed via CV in Fig. 3 b). From the inset graph of Fig. 3 b), we can determine a somewhat higher electrochemical active surface area (ECSA) of Aquivion®-GDEs (independent to Aquivion®/Nafion® membrane) comparing to Nafion®-GDEs (independent to Aquivion®/Nafion® membrane) measured by the integration of the hydrogen under-potential features [42,43]. This observation again justifies the better ionomer within the catalyst layer in case of Aquivion®. Contrarily, we can spot a relative incompatibility between Aquivion®-electrode and Nafion®-membrane by their lower ECSA value in line with the lower performance in the V (j) curves.

3.2. Long term stability test by load cycling in 25 cm^2 test cell

All 25 cm^2 MEAs were operated with load cycling protocol for 600 h (approx. 4 weeks). After every test block of 150 h (approximately 1 week) they were refreshed for one day. During refresh the cell was switched off, the gas supply was interrupted, the cell temperature was brought down to room temperature, and the cell outlets were opened according to Gazdzicki et al. [35]. It is remarked that the trend observed regarding BoT performance of the different studied MEAs changes after time is considered due to the degradation behavior. Even though the properties of SSC ionomer which have been demonstrated to be advantageous regarding performance the MEAs with Aquivion® membrane showed higher performance loss upon operation.

From Fig. 4 the MEAs with thinner SSC membranes exhibit higher degradation than LSC ionomer membrane. The performance curves in Fig. 4 a, d show a drastic degradation with SSC membranes. In contrast, the curves in Fig. 4 b and c which correspond to MEAs with LSC ionomer as membrane exhibit a significantly more stable performance. Nonetheless, the data in Fig. 4 b) (SSC ionomer in CL) still shows a bit higher rate of degradation (around 3 $\mu V\,h^{-1}$) compare to data in Fig. 4 c) (LSC ionomer in CL). Moreover, the difference between the MEAs represented by the performance curves shown in Fig. 4 d) and 4 e) is the membrane thickness. In Fig. 4 d) a single Aquivion® membrane was used (11 μm). This MEA was unable to continue the load cycling test from the middle of the second week. The potential drop was so serious that it stops the test due to automatic security shut down of the test bench. In the study show in Fig. 4 e), a sandwich of two Aquivion® membranes (total 22 μm) was used. Here, we see a very stable performance after two weeks. Evidently, the higher degradation is coming from the thin SSC membrane and high gas crossover. MEA prepared with Nafion® membrane (28 μm) shows significantly less performance degradation and a higher performance at EoT compared to Aquivion®, even though the BoT performance is inferior due to the bad contact of two layer membranes. It is well-known that the thickness of the membrane plays a key role for degradation due to the high gas crossover [38,50]. Furthermore, the gas permeability co-efficient of the ionomer depends greatly on the water content, cation form and ion exchange capacity. Permeability increases with increasing water content and ion-exchange capacity. The gas permeation through a same sample varies with temperature, pressure, and membrane thickness. The hydrogen and oxygen gases that permeate through the membrane are consumed with the generation of heat and water without producing useful work which leads to fuel inefficiency. Oxygen permeates at about half of the rate of hydrogen, and is quite diluted in air. In particular, the effect of gas crossover is severe under high pressure operation and at current densities below 0.1A/cm^2 [55,56]. Critically, permeation of oxygen into the membrane can cause the formation of hyper oxide and peroxide radicals which are a major source of membrane degradation. Moreover, prolonged exposure to OCV condition causes excessive crossover and degradation due to the higher potential at cathode that leads to high rate of radical formation. To minimize this phenomenon, OCV in the fuel cell dynamic load cycling is largely replaced by 5% of maximum current density [34,52]. Moreover, thinner membrane faces more mechanical stress during operation and refresh which includes a strong change of RH when cooling down from 80 °C to room temperature. According to Fig. 4 d and e, the increased thickness of the membrane by using two sandwiched thin membranes substantially reduces performance decay.

Fig. 5 provides the cell voltage measured during load cycling as a function of time for a MEA prepared using SSC ionomer and an MEA made using LSC ionomer. Apparently, higher irreversible (overall degradation) and reversible degradation (degradation within each test block) is observed in case of the MEA prepared using SSC. After 3 weeks of load cycling operation, the degradation is very far-reaching. On the contrary, in case of LSC ionomer the irreversible degradation rate is modest. Specifically, at OCV the irreversible degradation rate for SSC (Aquivion®) MEA is ~30 $\mu V\,h^{-1}$, but at higher current density it intensified very critically. On the other hand, the irreversible degradation rate at OCV of LSC (Nafion®) MEA is also ~ 30 $\mu V\,h^{-1}$, but at higher current density the degradation rate is very minimal comparing to the former one. Again, the main affect in degradation acceleration is the thickness of the membranes. In addition, the lower PTFE content also

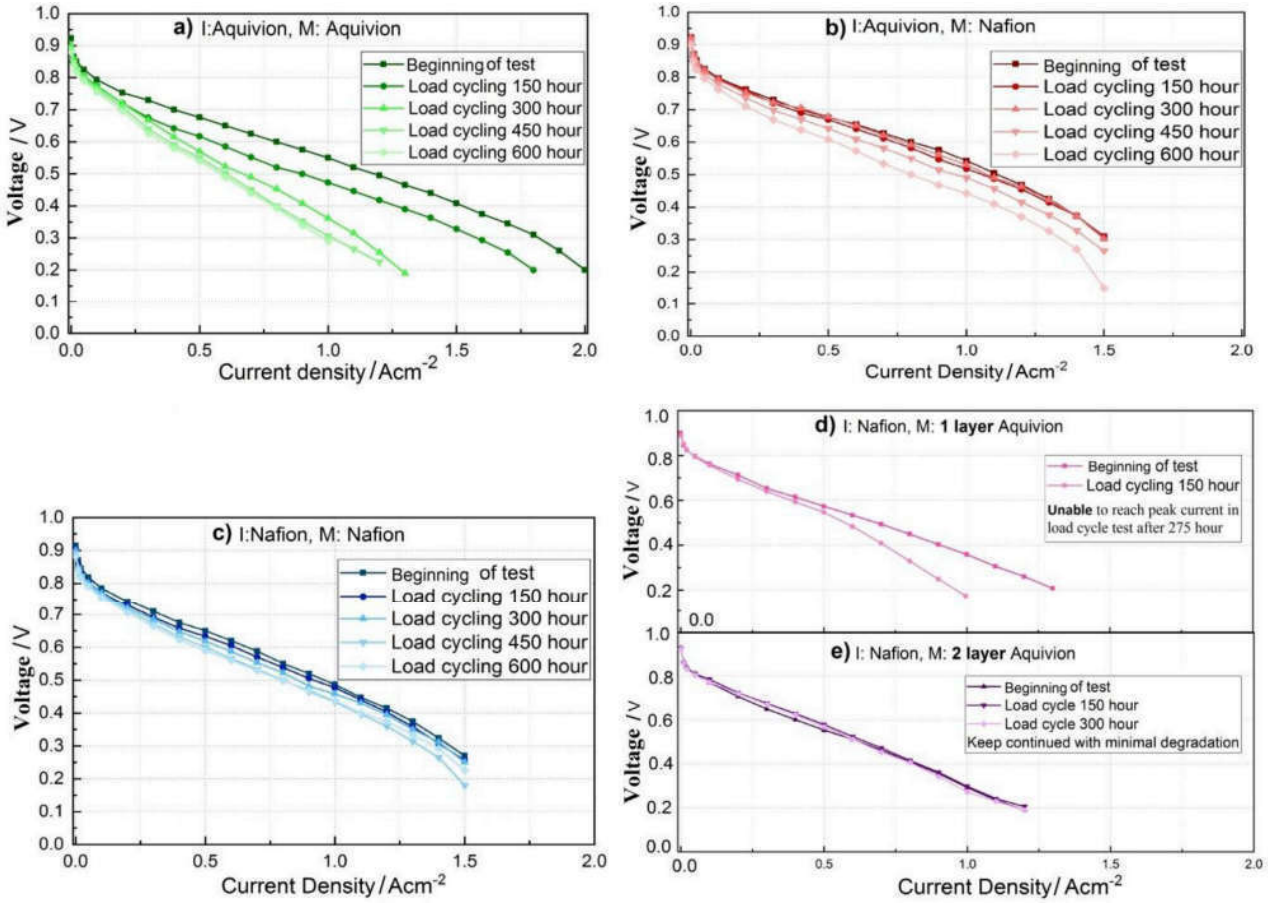

Fig. 4. Performance curves of MEAs in load cycling operation of 4 weeks in 25 cm^2 cell. Polarization curve were taken at the beginning and after every refresh (150 h of operation).

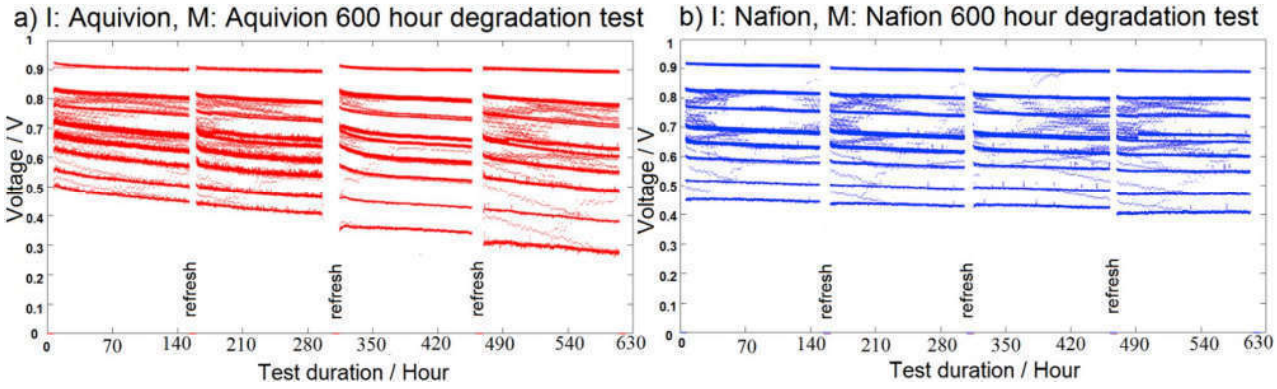

Fig. 5. Load cycling operation (fuel cell dynamic load cycle – FC-DLC) of MEAs with SSC ionomer vs LSC ionomer.

helps the degradation process in the electrode.

Current density distribution measurements obtained at BoT and EoT for the three MEAs are provided in Fig. 6. We have recorded images in every 150 h and at different current density, but here we only present the images of 25 A (1 Acm^{-2}) current. In Fig. 6, we can follow the segmented images in color before (top) and after 600 h of load cycling operation (bottom). We have not detected very significant evidence of variation in local current densities for Nafion®/Nafion® and Aquivion®/Nafion®. The MEA Aquivion®/Aquivion®, however, clearly experiences a drop of current density in the segments of column G which correspond to gas outlet. The reason is probably the higher water retention capacity of Aquivion® membrane over Nafion® membrane. Yet, some areas of MEA in Fig. 6 b-b* also gain current. This heterogeneity of current distribution may also contribute somewhat to the degradation of SSC ionomer. Furthermore, the current density distribution of the MEA Aquivion®/Nafion® (Fig. 6 c) differs from those in panels a) and b) which is due to different ionomer interphase in membrane and in electrode. In addition, no pinhole or crucial current drop has been observed after the complete load cycling operation.

Fig. 7 a) demonstrates the continuous cell voltage drop of the distinctive MEAs. Fig. 7b) shows the high frequency resistances of those MEAs measured at BoT, after 300 h and at EoT (i.e. 600 h). MEA with SSC ionomer (Aquivion®) in electrode and membrane shows higher voltage drop than MEA with LSC ionomer (Nafion®) in electrode and membrane. LSC ionomer (Nafion®) in electrode and SSC single membrane (Aquivion®) shows highest voltage drop among all tested MEAs as expected according to the performance curves in Fig. 4. However, LSC ionomer (Nafion®) in electrode and thick SSC ionomer (Aquivion®) as membrane (a sandwich of two Aquivion® membranes used) suffers substantially less voltage drop compared to the MEA where single Aquivion® membrane was used. The high frequency resistance (HFR) includes proton resistance of the membrane and of the catalyst layer as

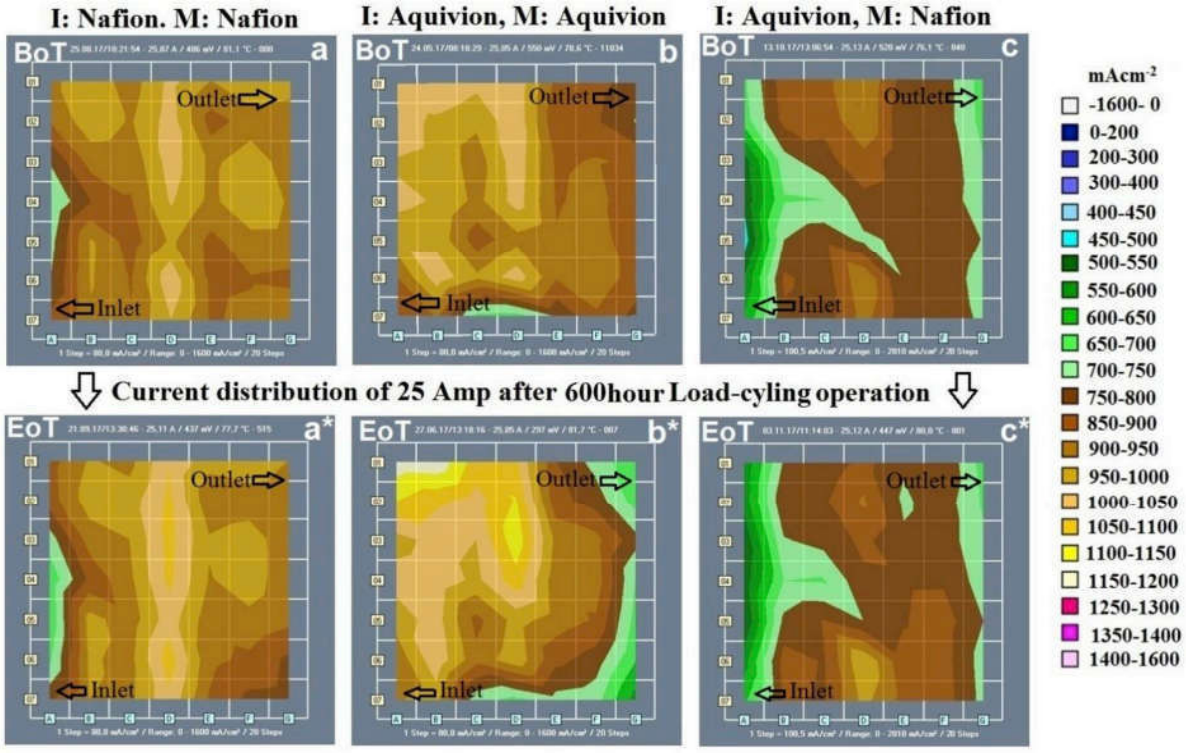

Fig. 6. Measurement of current distribution at BoT and EoT for the three different MEAs indicated in the figure. These images were taken at 1Acm^{-2} current density. Values of current distribution in color are provided in the inset. (For interpretation of the references to color in this figure legend, the reader is referred to the Web version of this article.)

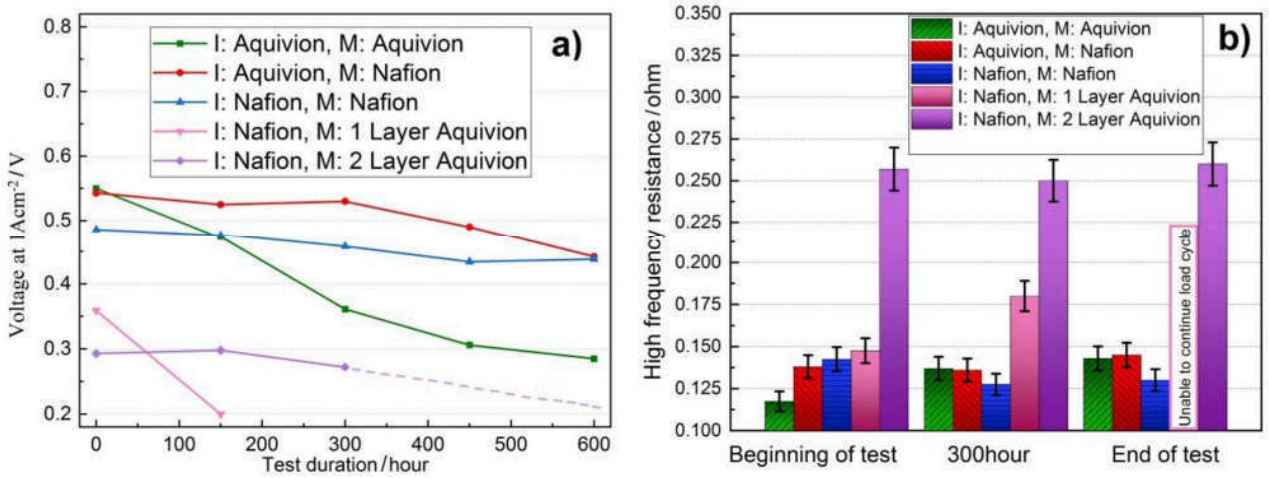

Fig. 7. a) Cell voltage values recorded at 1 Acm^2 as a function of test time for the MEAs indicated in the legend. Since the test of I: Nafion®, M: 1 Single Layer Aquivion® MEA stopped after 300 h, the voltage values were extrapolated (dashed line) until 600 h by the linear regression, b) HFR in the different MEAs at BoT, after 300 h and at EoT.

well as ohmic (electrical) resistances of MEA components and contacts between the components. In Fig. 7 b, we observe that the LSC ionomer (Nafion®) in electrode and the double Aquivion® membrane does not increase HFR value with time, whereas single Aquivion® membrane increases its HFR with time. Nafion® in electrode and double Aquivion® membrane shows very minute HFR shifting, keeping in mind that due to the application of 2 membranes the HFR of that MEA was large from the initial condition. HFR of Aquivion®/Aquivion® MEA slightly increases over longer period of application, while HFR of Nafion®/Nafion® MEA gradually decreases after even the end of test.

The XPS measurement of Fig. 8 shows us the less fluorine content in Aquivion® or SSC which is due to the shorter fluorinated side chain length. This phenomenon is justifiable for both the application of ionomer: as membrane and as binder in electrode. In our study, we have experienced a different performance behavior of LSC and SSC ionomer membrane in short and long term test. We speculate the increased degradation originates the higher gas crossover of the thinner membrane (Aquivion®). Nevertheless, the PTFE side chain portion also plays a role. The advantage of Aquivion®, which is the stability of SSC dispersion at lower EW becomes the disadvantage in long term application. Likely even though Aquivion® is well dispersed at low EW (±800), for the long term it is less stable than LSC ionomers. We suppose, because of the higher amount of CF_2 bonds (strong bond) in LSC ionomer, which is evaluated by XPS shown in Fig. 8a) and b), it is stable and less degradable in long term application. On the contrary, we can also recognize the amount of CO bonds (weaker bond) is larger in short side chain compare to long side chain ionomer. This weaker CO bond is more sensitive to the radical attack, thus shorter side chain is more susceptible to degradation than its alternative.

3.3. Synopsis

According to the literature, degradation of MEA may result from: i) carbon corrosion, ii) activity loss of the catalyst, iii) gas crossover, iv) heterogeneous current distribution and v) degradation of polymer electrolyte membrane including ionomer in the catalyst layer [51–53]. Catalyst dissolution in the cathode catalyst layer and migration and redisposition inside the membrane is a known reason for membrane degradation which is triggered by the Pt deposition [54]. Throughout the operation, catalyst particles in an MEA are gradually dissolved and migrate into the membrane phase where it is chemically reduced by crossover hydrogen from anode [38,50]. This migration of platinum causes slow degradation of ionomer. The main effect in the degradation behavior here is clearly related to gas crossover. Therefore a challenge exists to combine the higher performance of thin membranes with improved durability.

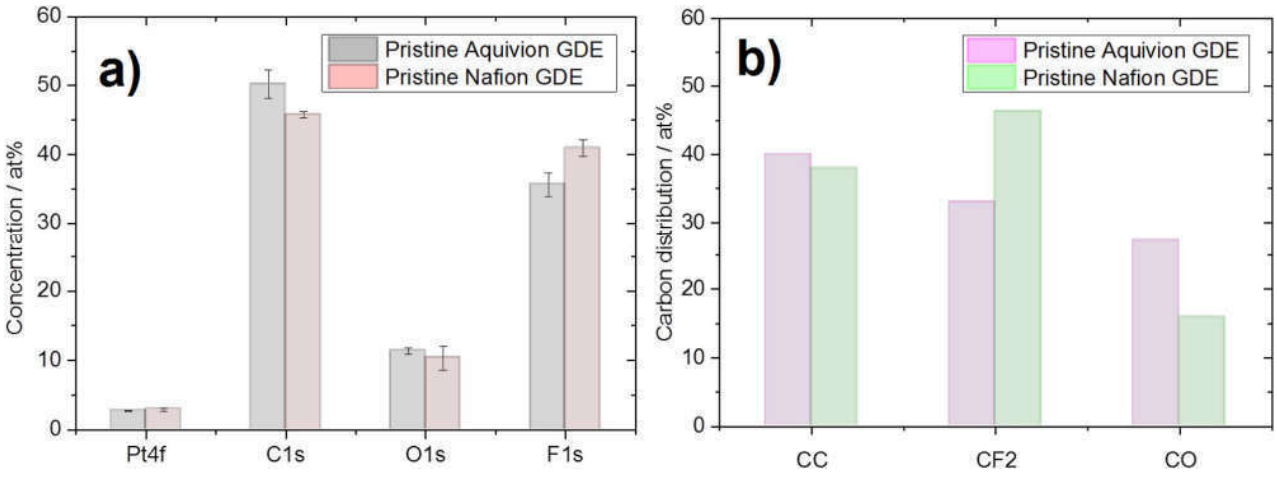

Fig. 8. a) Concentration chart of the atoms from XPS measurement, b) carbon bonding distribution curve from XPS values.

In addition to the role of membrane thickness, the operating conditions can influence the stability characteristics as well. Higher operating temperatures have numerous positive effects on fuel cell performance like a decrease of kinetic losses, an increase of diffusion and proton conduction, and an increase of hydration of membrane by accelerated electrochemical reaction (water formation). However, the last effect is counterbalanced by an increased evaporation of water leading to efficient water removal but also lower ionomer conductivity. In addition gas crossover is also enhanced by higher temperatures. On the other hand, lowering the operating temperature limits the crossover but may decrease the kinetics along with proton conductivity and facilitates the condensation of liquid water thus hindering the transport of reactants. Low gas crossover under differential pressure has been used to limit crossover and to benefit the stability of the membrane. A reduction in thickness of the membrane lowers directly the cell resistance but simultaneously increases the gas permeation. Siracusano et al. [57] demonstrated that differential pressures acting against the main permeation flux can be used to control the membrane degradation. This will have an impact on the reversible losses during durability and stability studies [55,56].

Aquivion® has shorter side chain, which facilitates higher IEC value and higher water uptake compare to Nafion® which is LSC ionomer. This phenomenon results in higher peak power density and much better electrode performance. However, we know high water uptake also causes swelling of membrane and flooding. The excessive swelling of the SSC ionomer as a result of the excess water uptake at 100% humidification may also cause an increase of the oxygen diffusion resistance from the gas phase to the catalyst sites in the cathode CLs [45,46]. A major challenge clearly demonstrated here is that the performance enhancing effects leading to higher performance (homogeneous ionomer distribution in the electrode and thin membranes) at the same time are responsible for faster degradation of the MEA. Therefore it seems an important task to reduce the gas crossover of thin membranes to limit radical attack of the ionomers. Subsequently, the degradation of the membrane is crucially influenced by the higher crossover of gases caused by the thickness of the membrane. The degeneration of ionomer in the electrode is influenced by the shorter side chain (lower equivalent weight) of the ionomer mentioned in Fig. 8. Since, CF_2 or PTFE is widely considered as one the strongest chemical bond, and CO is a weaker and more vulnerable to chemical attack, longer side chain ionomer like Nafion® shows minor degradation owing to higher CF_2 and lower CO content. A higher amount of ether groups per mass unit is an integral cause of degradation according to our hypothesis. Consequently, due to the difference in ether/fluorine content, PFSA consisting long side chain experiences slower degradation than PFSA with short side chain.

Membrane degradation is also highly dependent on mechanical stress and chemical attack; the latter being facilitated by decreasing thickness and higher gas crossover. Mechanical stress is associated with repetitive membrane swelling-shrinkage triggered by relative humidity, temperature and cycle breaks. Apparently, the thinner membrane will fail at lower stress compare to the thicker membrane which is also shown in our study. On the other hand, chemical degradation occurred due to the formation of strongly reactive radical species such as hyroxy (HO*), hyperhydroxy (HOO*) and hydrogen (H*) [55]. Radicals are considered responsible for the chemical PFSA degradation at the side chain level and even can decompose the backbone in the presence of reactive groups (carboxyl groups have been identified as a major contributor to chemical degradation) [50,58]. In our work, we assume that chemical degradation takes place in the ionomer of the electrode. In all cases we used dispersed ionomer for electrode preparation which does not have radical scavengers (e.g. ceria). To mitigate the radical attack, membranes are often incorporated with radical scavengers which use redox reactions to transform highly reactive and aggressive peroxides into water. Comparing Fig. 4 c) and 4e) we can observe that the long and short side chain membranes here shows similar rate of degradation at comparable thickness. Apart from the degradation in the electrode, Nafion and double layer Aquivion as membrane shows significantly less degradation in long term operation.

4. Conclusion

In this work, we have investigated all combinations of ionomer in the electrode as well as ionomer in the membrane. This approach is used to find trends for performance and durability of cells taking into account ionomer chemical compatibility. Moreover we also have stressed the fact that the gas crossover and the equivalent weight of ionomer are the major responsible factors for membrane degradation. This article provides a comparative study of LSC and SSC ionomers as membranes and catalyst binder in PEMFCs, evaluating the short term and long term behavior. SSC has higher ion-exchange capacity and water uptake capacity, which reflects better performance in short term test comparing to LSC. However, the lower thickness of the SSC ionomer membrane causes higher degradation compared to LSC ionomer due to gas crossover. We have experienced that very thin membrane (close to 10 μm) is the cause of additional irreversible degradation. Application of double SSC membranes demonstrated reduced degradation rate in long term test. Furthermore, LSC ionomer has higher EW, but due to longer side chain it is chemically more stable as binder and proton conductor in electrode for the long term application. The summary of this work is ionomer with SSC will be very efficient for PEMFC operation if the gas crossover and ionomer decomposition can be limited. On the other hand, though it has a lower peak power density, in long term stress application thicker membrane with LSC are presently advantageous.

Acknowledgement

Corresponding author acknowledges financial support by DAAD. The authors thank Siegfried Graf for building up and maintaining the fuel cell test benches. The research leading to these results has received funding from the European Union's Seventh Framework Program (FP7/2007–2013) for Fuel Cell and Hydrogen Joint Technology Initiative under Grant no 303452 (Impact).

References

[1] Energy, environment and new materials – F. Ioana, M.V. de Voodre (Editor.) Volume 3 Utilization of Hydrogen for Sustainable Energy, Chapter 12: Hydrogen Fuel Cell Applications, J. Mitzel and K.A. Friedrich, ISBN 978-3-11-059627-4.
[2] B.C.H. Steele, A. Heinzel, Materials for fuel-cell technologies, Nature 414 (2001) 345–352. https://doi.org/10.1038/35104620.
[3] B. Bahar, A.R. Hobson, J.A. Kolde, Integral Composite Membrane, US Patent No. 5,599,614 (1997).
[4] H. Kato, Ion Exchange and Electrode Assembly for an Electrochemical Cell, US Patent No. 6,054,230 (2000).
[5] S. Srinivasan, E.A. Ticianelli, C.R. Derouin, A. Redondo, Advances in solid polymer electrolyte fuel cell technology with low platinum loading electrodes, J. Power Sources 22 (1988) 359–375. https://doi.org/10.1016/0378-7753(88)80030-2.
[6] I.D. Raistrick, Electrode Assembly for Use in a Solid Polymer Electrolyte Fuel Cell, US patent No. 4,876,115 (1989).
[7] C. Heitner-Wirguin, Recent advances in perfluorinated ionomer membranes: structure, properties & applications, J. Membr. Sci. 120 (1996) 1–33. https://doi.org/10.1016/0376-7388(96)00155-X.
[8] K. Talukdar, H.J. Kim, Y.H. Kim, Y.J. Park, H.C. Lee, S.J. Choi, Proton-conducting membranes from Nafion/Polystyrene sulfonate compostes for fuel cell application, J. Nanoelectron. Optoelectron. 10 (2015) 535–540. https://doi.org/10.1166/jno.2015.1797.
[9] M. Gebert, A. Ghielmi, L. Merlo, M. Corasaniti, V. Arcella (Eds.), AQUIVION – the Short-Side-Chain and Low-EW PFSA for Next-Generation PEFCs Expands Production and Utilization, vol. 26, ECS Transactions, 2010, pp. 279–283, https://doi.org/10.1149/1.3428998, 1.
[10] Technical Bulletin of Solvay company, D 12/2015 (Version 1 and 1.1), (2016)-D05/2016 (Version 1), 2015.
[11] Q. Li, D. Aili, H.A. Hjuler, J.O. Jensen, High Temperature Polymer Electrolyte Membrane Fuel Cells Approaches, Status and Perspective, Springer, 2016, ISBN 978-3-319-17082-4.
[12] P. Xiao, J. Li, H. Tang, Z. Wang, M. Pan, Physically stable and high performance Aquivion/ePTFE composite membrane for high temperature fuel cell application, J. Membr. Sci. 442 (2013) 65–71. https://doi.org/10.1016/j.memsci.2013.04.014.
[13] K. Talukdar, H.J. Kim, Y.H. Kim, H.C. Lee, S.J. Choi, Polyacrylamide/Nafion Semi interpenetrating networks as proton conducting membrane of direct methanol fuel

cell, Sci. Adv. Mater. 6 (2014) 2389–2394. https://doi.org/10.1166/sam.2014.2190.
[14] H.J. Kim, K. Talukdar, S.J. Choi, Tuning of Nafion by HKUST-1 as coordination network to enhance proton conductivity for fuel cell applications, J. Nanoparticle Res. 18 (47) (2016) 1–6. https://doi.org/10.1007/s11051-016-3346-9.
[15] N.H. Jalani, R. Datta, The effect of equivalent weigh, temperature, cationic forms, sorbatesm and nanoinorganic additives on the sorption behavious of Nafion, J. Membr. Sci. 264 (1–2) (2005) 167–175. https://doi.org/10.1016/j.memsci.2005.04.047.
[16] S. Siracusano, V. Baglio, A. Stassi, L. Merlo, E. Moukheiber, A.S. Arico, Performance analysis of short side-chain Aquivion perfluorosulfonic acid polymer for proton exchange membrane water electrolysis, J.Membr. Sci. 466 (2014) 1–7. https://doi.org/10.1016/j.memsci.2014.04.030.
[17] G. Dorenbos, Y. Suga, Simulation of equivalent weight dependence of Nafion morphologies and predicted trends regarding water diffusion, J. Membr. Sci. 330 (2009) 5–20. https://doi.org/10.1016/j.memsci.2008.11.056.
[18] D. Dunwoody, J. Leddy, Proton exchange membranes: the view forward and backword, Electrochem. Soc. Interface 37 (2005). Fall, https://www.electrochem.org/dl/interface/fal/fal05/IF8-05_Pg37-39.pdf.
[19] T. Yung Chen, J. Leddy, Ion exchange capacity of Nafion and Nafion composite, Langmuir 16 (2000) 2866–2871. https://doi.org/10.1021/la991094x.
[20] A. Stassi, I. Gatto, E. Passalacqua, V. Antonucci, A.S. Arico, L. Merlo, C. Oldani, E. Pagano, Performance comparison of long and short-side chain perfluorosulfonic membranes for high temperature polymer electrolyte membrane fuel cell operation, J. Power Sources 196 (2011) 8925–8930. https://doi.org/10.1016/j.jpowsour.2010.12.084.
[21] S. Shahgaldi, I. Alaefour, X. Li, The impact of short side chain ionomer on polymer electrolyte membrane fuel cell performance and durability, Appl. Energy 217 (2018) 295–302. https://doi.org/10.1016/j.apenergy.2018.02.154.
[22] X. Wu, K. Scott, V. Puthiyapura, Polymer electrolyte membrane water electrolyser with Aquivion short side chain perfluorosulfonic acid ionomer binder in catalyst layer, Int. J. Hydrogen Energy 37–18 (2012) 13243–13248. https://doi.org/10.1016/j.ijhydene.2012.06.093.
[23] V. Mehta, J.S. Cooper, Review and analysis of PEM fuel cell design and manufacturing, J. Power Sources 114 (2003) 32–53. https://doi.org/10.1016/S0378-7753(02)00542-6.
[24] E. Passalacqua, F. Lufrano, G. Squadrito, A. Patti, L. Giorgi, Electrochim. Acta 46–6 (2009) 799–805. https://doi.org/10.1016/S0013-4686(00)00679-4.
[25] G. Shashikumar, J.W. Ihm, H. Ryu, Optimum Nafion Content in PEM Fuel Cells Electrochimica Acta, vol. 50, 2004, pp. 601–605. https://doi.org/10.1016/j.electacta.2004.01.126.
[26] T.T. Ngo, T.L. Yu, H.L. Lin, Influence of the composition of isopropyl alcohol/water mixture solvents in catalyst ink solutions on proton exchange membrane fuel cell performance, J. Power Sources 225 (2013) 293–303. https://doi.org/10.1016/j.jpowsour.2012.10.055.
[27] K. Talukdar, S. Helmly, M. Schulze, D.G. Sanchez, M. Handl, R. Hiesgen, J. Kraut, K.A. Friedrich, Enveloping of catalyst powder by ionomer for dry spray coating in polymer electrolyte membrane fuel cells, J. Power Sources 424 (2019) 82–90. https://doi.org/10.1016/j.jpowsour.2019.03.093.
[28] A. Kongkanand, M.F. Mathias, The priority and challenge of high power performance of low platinum proton exchange membrane fuel cells, J. Phys. Chem. Lett. 7–7 (2016) 1127–1137. https://doi.org/10.1021/acs.jpclett.6b00216.
[29] M. Schulze, E. Güzlow, St Schönbauer, T. Knöri, R. Reissner, Segmented cells as tool for development of fuel cells and error prevention/prediagnostic in fuel cell stacks, J. Power Sources 173 (2007) 19–27. https://doi.org/10.1016/j.jpowsour.2007.03.055.
[30] D.G. Sanchez, P.L. Garcia-Ybarra, PEMFC operation failure under severe dehydration, Int. J. Hydrogen Energy 37 (2012) 7279–7288. https://doi.org/10.1016/j.ijhydene.2011.11.059.
[31] D.G. Sanchez, D.G. Diaz, R. Hiesgen, I. Wehl, K.A. Friedrich, Oscillations of PEM fuel cells at low cathode humidification, J. Electroanal. Chem. 649 (2010) 219–231. https://doi.org/10.1016/j.jelechem.2010.04.005.
[32] D.G. Sanchez, Tiziana Ruiu, Indro Biswas, Mathias Schulze, Stefan Helmly, K. Andreas Friedrich, Local impact of humidification on degradation in polymer electrolyte fuel cells, J. Power Sources 352 (2017) 42–55. https://doi.org/10.1016/j.jpowsour.2017.03.057.
[33] R. Lin, E. Gülzow, M. Schulze, K.A. Friedrich, Investigation of membrane pinhole effects in polymer electrolyte fuel cells by locally resolved current density, J. Electrochem. Soc. 158 (2011) B11–B17, https://doi.org/10.1149/1.3504255.
[34] G. Tsotridis, A. Pilenga, G.D. Marco, T. Malkow, EU Harmonised Test Protocols for PEMFC MEA Testing in Single Cell Configuration for Automotive Applications, JRC science for Policy report, Eur 27632 EN, 2015, ISBN 978-92-79-54132-2, https://doi.org/10.2790/54653.
[35] P. Gazdzicki, J. Mitzel, A.M. Dreizler, M. Schulze, K.A. Friedrich, Impact of Platinum on performance and degradation of polymer electrolyte fuel cell Electrodes studied in a rainbow stack, Fuel Cell 18 (No 3) (2018) 270–278. http://doi.org/10.1002/fuce.201700099.
[36] M.C. Lefebvre, R.B. Martin, P.G. Pickup, Characterization of ionic conductivity profiles within proton exchange membrane fuel cell gas diffusion electrodes by impedance spectroscopy, Electrochem. Solid State Lett. 2–6 (1999) 259–261, https://doi.org/10.1149/1.1390804.
[37] G. Li, G. Pickup, Ionic conductivity of PEMFC electrodes, effect of Nafion loading, J. Electrochem. Soc. 150–11 (2003) C745–C752, https://doi.org/10.1149/1.1611493.
[38] H. Xu, R. Borup, E. Brosha, F. Garzon, Bryan Pivovar, The effect of relative humidity on membrane degradation rates and mechanisms in proton exchange membrane fuel cells, ECS Trans. 6–13 (2007) 51–62, https://doi.org/10.1149/1.2811696.
[39] T.T. Ngo, T.L. YU, HsiuL. Lin, Influence of the composition of isopropyl alcohol/water mixture solvents in catalyst ink solutions on proton exchange membrane fuel cell performance, J. Power Sources 225 (2013) 293–303. https://doi.org/10.1016/j.jpowsour.2012.10.055.
[40] M. Uchida, Y. Aoyama, N. Eda, A. Ohta, Investigation of the microstructure in the catalyst layer and effects of both perfluorosulfonate ionomer and PTFE-loaded carbon on the catalyst layer of polymer electrolyte fuel cells, J. Electrochem. Soc. 142–12 (1992) 4143–4149, https://doi.org/10.1149/1.2048477.
[41] Alireza Goshtasbi, Jixin Chen, Pablo Garcia-Salaberri, Krishan Talukdar, DanielG. Sanchez, Tulga Ersal, Through-the-Membrane transient phenomena in PEM fuel cells: a modeling study, J. Electrochem. Soc. 166–7 (2019) F-3154–F3179, https://doi.org/10.1149/2.0181907jes.
[42] K.R. Cooper, Fuel cell magazine, in: Situ PEM Fuel Cell Electrochemical Surface Area and Catalyst Utilization Measurement, Scribner Associates, 2009. Jan/Feb, http://www.scribner.com/files/tech-papers/Scribner-on-ECSA-Fuel-Cell-Magazine-2009.pdf.
[43] K. Talukdar, S. Delgado, T. Lagarteria, P. Gazdzicki, K.A. Friedrich, Minimizing mass transport loss in proton exchange membrane fuel cell by freeze drying of cathode catalyst layers, J. Power Sources 427 (2019) 309–317. https://doi.org/10.1016/j.jpowsour.2019.04.094.
[44] C. Francia, V.S. Ijeri, S. Specchia, P. Spinelli, Estimation of hydrogen crossover through nafion membranes in PEMFCs, J. Power Sources 196–4 (2011) 1833–1839. https://doi.org/10.1016/j.jpowsour.2010.09.058.
[45] L. Kim, C.G. Chung, Y.W. Sung, J.S. Chung, Dissolution and migration of platinum after long-term operation of polymer electrolyte fuel cell under various condition, J. Power Sources 183–2 (2008) 524–532. https://doi.org/10.1016/j.jpowsour.2008.05.062.
[46] J. Wu, X.Z. Yuan, J.J. Martin, H. Wang, J. Zhang, J. Shen, S. Wu, W. Merida, A review of PEM fuel cell durability: degradation mechanisms and mitigation strategies, J. Power Sources 184–1 (2008) 104–119. https://doi.org/10.1016/j.jpowsour.2008.06.006.
[47] Y.C. Park, K. Kakinuma, H. Uchida, Effects of short-side-chain perfluorosulfonic acid ionomers as binders on the performance of low Pt loading fuel cell cathodes, J. Power Sources 275 (2015) 384–391. https://doi.org/10.1016/j.jpowsour.2014.10.149.
[48] Y.C. Park, H. Tokiwa, K. Kakinuma, M. Watanabe, M. Uchida, Effects of carbon supports on Pt distribution, ionomer coverage and cathode performance for polymer electrolyte fuel cells, J. Power Sources 315 (2016) 179–191. https://doi.org/10.1016/j.jpowsour.2016.02.091.
[49] Y. Garsany, M.B. Sassin, B.D. Gould, R.M.E. Hjelm, K.S. Lyons, Influence of short side chained perfluorosulfonic acid ionomer as binder on the performance of fuel cell cathode catalyst layers, in: ECS Meeting Abstract, MA2017-02, 2017, p. 1469. http://ma.ecsdl.org/content/MA2017-02/34/1469.abstract.
[50] R. Borup, J. Meyers, B. Pivovar, Y.S. Kim, R. Mukundan, N. Garland, D. Myers, M. Wilson, F. Garzon, D. Wood, P. Zelenay, K. More, K. Stroh, T. Zawodzinski, J. Boncella, J.E. McGrath, M. Inaba, K. Miyatake, M. Hori, K. Ota, Z. Ogumi, S. Miyata, A. Nishikata, Z. Siroma, Y. Uchimoto, K. Yasuda, K. Kimijima, N. Iwashita, Scientific ascpects of polymer electrolyte fuel cell durability and degradation, Chem. Rev. 107 (10) (2007) 3904–3951, https://doi.org/10.1021/cr050182l.
[51] A. Collier, H. Wang, X.Z. Yuan, J. Zhang, D.P. Wilkinson, Degradation of polymer electrolyte membranes, Int. J. Hydrogen Energy 31 (2006) 1838–1854. https://doi.org/10.1016/j.ijhydene.2006.05.006.
[52] A.B. LaConti, M. Hamdan, R.C. McDonald, in: W. Vielstich, H.A. Gasteiger, A. Lamm (Eds.), Handbook of Fuel Cells: Fundamentals Technology and Applications, vols 3–49, John Wiley & Sons Ltd, 2003, ISBN 978-0-471-49926-8, pp. 647–662.
[53] X. Huang, R. Solasi, Y. Zou, M. Feshler, K. Reifsnider, D. Condit, S. Burlatsky, T. Madden, Mechanical endurance of polymer electrolyte membrane and PEM fuel cell durability, J. Polym. Sci. 16 (2006) 2346–2357. http://doi.org/10.1002/polb.20863.
[54] S. Helmly, M.J. Eslamibidgoli, K.A. Friedrich, M.H. Eikerling, Local impact of Pt nanodeposits on ionomer decomposition in polymer electrolyte membranes, Electrocatalysis 8–6 (2017) 501–508. https://doi.org/10.1007/s12678-017-0353-2.
[55] S.S. Kocha, J.D. Yang, J.S. Yi, Characterization of gas crossover and its implications in PEM fuel cells, AIChE J. 52–5 (2006) 1916–1925, https://doi.org/10.1002/aic.10780.
[56] T. Sakai, H. Takenaka, N. Wakabayashi, Y. Kawami, E. Torikai, Gas permeation properties of solid polymer electrolyte (SPE) membranes, J. Electrochem. Soc. 132 (1985) 1328–1382, https://doi.org/10.1149/1.2114111.
[57] S. Siracusano, C. Oldani, M.A. Navarra, S. Tonella, L. Mazzaioda, N. Briguglio, A. S. Aricò, Chemically stabilised extruded and recast short side chain Aquivion proton exchange membranes for high current density operation in water electrolysis, J. Membr. Sci. 578 (2019) 136–148. https://doi.org/10.1016/j.memsci.2019.02.021.
[58] C. D'Urso, C. Oldani, V. bagilo, L. Merlo, A.S. Aricò, Immobilied transition metal-based radical scavengers and their effect on durability of Aquivion perfluorosulfonic acid membranes, J. Power Sources 301 (2016) 317–325. https://doi.org/10.1016/j.jpowsour.2015.10.019.

Contents lists available at ScienceDirect

Journal of Power Sources

journal homepage: www.elsevier.com/locate/jpowsour

Minimizing mass-transport loss in proton exchange membrane fuel cell by freeze-drying of cathode catalyst layers

Krishan Talukdar [a,*,1], Sofia Delgado [a,b,1], Tiago Lagarteira [b], Pawel Gazdzicki [a], K. Andreas Friedrich [a,c]

[a] German Aerospace Center (DLR), Institute of Engineering Thermodynamics, Pfaffenwaldring 38-40, Stuttgart, 70569, Germany
[b] Laboratory for Process Engineering, Environmental, Biotechnology and Energy (LEPABE), Faculty of Engineering of University of Porto, Rua Roberto Frias s/n, 4200-465, Porto, Portugal
[c] University of Stuttgart, Institute of Building Energetics, Thermal Engineering and Energy Storage (IGTE), Pfaffenwaldring 31, 70569, Stuttgart, Germany

ARTICLE INFO

Keywords:
PEM fuel cell
MEA
Screen-printing
Freeze-drying
Drying electrode
Mass transport

ABSTRACT

The widespread commercialisation of proton exchange membrane fuel cell (PEMFC) for either transportation or stationary application is still hindered by cost barriers owing to the use of precious metal catalysts, as well as performance and material related insufficient durability. Therefore, it is important to enhance the platinum utilization as well as optimize the fabrication method for the production of membrane electrode assemblies (MEAs). This study demonstrates that the drying step during the electrode manufacturing directly affects the microstructure of the catalyst layer, having inherent influence on the porosity and the platinum utilization during PEMFC operation that greatly affects the performance. Freeze-drying as a novel drying technique for PEMFC electrodes is proposed for preparation of low Pt-loaded cathodes (0.160 $mg_{Pt} \cdot cm^{-2}$). This technique possesses the unique feature of solvent removal via sublimation and not only generates 3.5-fold higher effective porosities but also increases the electrochemical surface area by 1.5 times when comparing to electrode dried by regular oven drying technique. Additionally, freeze-drying of electrode also improved ionomer distribution, as evident from a reduced resistance between the pores and a reduced electrolyte resistance of the catalyst layer. Consequently, we consider freeze-drying to be a highly promising technique for future production of MEAs.

1. Introduction

Due to increasing concerns with increasing CO_2 levels in the atmosphere which are associated to global warming, many efforts are under way to replace the conventional internal combustion engines (ICEs) in transport by cleaner energy conversion technologies operated with renewable fuels or electricity. Nowadays, Proton Exchange Membrane Fuel Cells (PEMFC) are considered one of the most promising alternatives to ICEs not only due to their higher efficiency but also to the fact that the only by-product they produce is water [1]. Among many features, they include quick start-up and shut down capabilities, sustained operation at high current densities and compact design. However, to proceed with widespread commercialisation of automotive PEMFC, some technical and economic challenges must be addressed such as increasing durability and stack cost reduction.

The membrane electrode assembly (MEA) is the key component of a PEMFC which determines performance and durability of the stack and fuel cell system [2]. The MEA consists of a proton exchange membrane (typically perfluorinated sulfonic acid (PFSA) membranes), an anode and a cathode catalyst layer (CL), and two gas diffusion layers (GDL) for both anode and cathode sides. There is an intimate relation between the components of the MEA to guarantee continuous ionic and electronic conductivity and gas access to the catalyst layers. Nevertheless, the slow kinetics of the oxygen reduction reaction (ORR) that occurs at the cathode is a limiting step that strongly influences the overall performance since it represents a significant contributions to the cell potential losses [3,4]. Therefore, properties of the cathode catalyst layer have great impact on the overall MEA performance. Consequently, the cathode catalyst layer is optimized in order to maintain PEMFC performance at reduced Pt loadings. Specifically, parameters relevant for CL preparation such as: (i) the catalyst ink/powder composition (typically supported Pt catalyst mixed with PFSA ionomer and organic solvents); (ii)

* Corresponding author.
E-mail address: Krishan.talukdar@dlr.de (K. Talukdar).
[1] The first two authors contributed equally to this work.

https://doi.org/10.1016/j.jpowsour.2019.04.094
Received 24 January 2019; Received in revised form 2 April 2019; Accepted 22 April 2019
Available online 28 April 2019

Table 1
Detailed specifications of the fabricated MEAs throughout this study; including the MEA type, coating technique applied, catalyst ink components and weight ratios on total weight of the formulation, coated substrate, cathode platinum loading and further steps.

Coating Technique	Coated substrate	MEA	Catalyst ink components	wt.% ink components	Pt Loading (mg·cm-2)	Further steps
Doctorblade Gas diffusion Electrode (GDE)	**Cathode on:** gas diffusion layer, GDL Sigracet 25 BC SGL	Amount: 3 **Anode:** commercial GDE **Membrane**: Nafion XL **Cathode:** GDE	Platinum on carbon black (40 wt % Platinum)	16.54	0.18 ± 0.05	Drying; Hot-press
			Ultra-Pure water	16		
			Cyclohexanol	60.64		
			Nafion/ionomer	6.84		
Screen print Catalyst coated membrane (CCM)	**Cathode on:** membrane Nafion XL	Amount: 3 **Anode:**commercial. GDE **Membrane**: Nafion XL CCM **Cathode:** GDL	Platinum on carbon black (40 wt % Platinum)	22	0.16 ± 0.02	Drying
			Ultra-Pure water	10.26		
			Cyclohexanol	58.65		
			Nafion/ionomer	9.09		

the coating technique (iii) and the drying of the electrode (e.g. evaporation of organic solvent); are of essential importance to obtain a proper and optimized microstructure of the cathode CL. Hence, CL preparation and CL design is the most important step for further developing cells to lower loadings [5–7]. Thereby, the catalyst ink plays a vital role during the CL preparation process since it influences the rheological properties of the coating medium. Herein, in order to address these particularities, the catalyst ink properties need to be adjusted to individual coating techniques, thus guarantying the connection between the ionic and electronic phases, and access of reactants to the catalytic active sites [8–10].

The preparation of CL broadly follows two main routes, depending on the substrate of the CL which can be either (i) the gas diffusion layer or (ii) the membrane, and the resulting electrodes are then denominated either gas diffusion electrodes (GDEs) or catalyst coated membranes (CCMs), respectively, as extensively reviewed by Mehta and Cooper [11]. Numerous kinds of coating methods have been widely applied for CL preparation such as catalyst powder-suspension based methods (e.g., Inkjet-printing [12], screen-printing [13,14], doctor-blade [7,15]), decal transfer [16], wet spraying [17], vapour-based (e.g., plasma sputtering [18], helicon RF sputtering), electrical processes (e.g., pulsed electrodeposition [19]), among others. Screen-printing is one the most popular methods for PEMFC catalyst deposition due to its reproducibility and scalability [13]. Moreover, it allows catalyst layer deposition in a single printing step that is time and cost efficient [20].

An important process step during CL preparation is the drying of the electrode after printing or spraying. It is required to remove the organic or aqueous solvent used for the ink, which was added to optimize ink rheology. Most works only report the importance of drying catalyst powders rather than electrodes [21–23]. In other works, the information on electrode drying is not provided at all [24]. Thus, there is a gap in the literature in terms of elucidating the impact of the drying step on electrode properties. Since this step greatly affects the electrode porosity and pore size distribution, it has critical impacts on mass-transport limitations in the CL [25]. It is well known that electrode porosity is correlated with oxygen diffusion in the electrode; thereby, high pore volume ensures superior mass transport and proper water management in the CL, which in turn results in increased cell performances [22,23,25]. Freeze-drying, commonly known as lyophilisation, comprises the removal of the solvent directly from the solid phase to the vapour phase through sublimation [26]. Moreover, this technique is widely used in pharmaceutical and food industry [27,28]. It has been reported that the structure of nano-porous materials, such as polymers and cryogels, is kept pristine as the aggregation of particles is avoided [26,29,30] and porosity is incremented. Hence, this freeze-drying technique deserves a thorough consideration towards its implementation as a fabrication step of electrodes for PEMFC.

This work presents the advantages of freeze-drying to produce high performance yet low-loaded Pt cathodes through screen-printing and doctor blade coating methods, that also contribute to the cost effectiveness and easy-scalability of the entire manufacturing process. Moreover, to assess the effect of the drying step during the fabrication of electrodes on PEMFC performance, three drying techniques were applied after screen-printing and doctor blade coating. Furthermore, the morphological properties of the cathodes were analysed by thermogravimetric analysis (TGA), scanning electron microscopy (SEM) and porosimetry analysis.

2. Experimental

The experimental section presents technical information on (i) the used ink formulations for cathode CL preparation, (ii) applied coating and drying techniques, and performed (iii) physical and (iv) electrochemical characterization methods.

2.1. Catalyst ink formulation

The study focuses on preparation of cathode electrodes. Therefore, at the anode sides of the MEAs commercial gas diffusion electrodes (25 cm^2 active area) consisting of Pt/C catalyst (Ion Power) with 0.3 $mg_{Pt}cm^{-2}$ were used in all cases. The cathode electrodes, on the other hand, were prepared as CCMs and GDEs produced via screen-printing and doctor blade coating with different catalyst ink compositions, respectively, as summarized in Table 1.

In both cases the ink was prepared by mixing 40 wt% of Pt supported on carbon black (HiSpec 4000, Johnson Matthey), 99.99% ultra-pure water (Alfa Aesar), cyclohexanol 99% (Alfa Aesar), and 5 wt% Nafion (equivalent weight 1100) in protonic form (Ion Power). HiSpec is a common choice for supporting nano catalyst mainly due to its large surface area (232 $m^2 g^{-1}$) [31], high electrical activity and suitable pore structure [32]. Cyclohexanol was chosen as solvent since its optimum relative permittivity or dielectric constant (15 at 25 °C) that enables a great dispersion of Nafion in solution that has been reported to promote better catalyst utilization without causing the swelling of the membrane (important in case of CCM preparation which requires smooth membrane as substrate) [33]. Moreover, sublimation begins below the triple point of cyclohexanol (297 K and 14.2 Pa) [34] which can be successfully attained with the vacuum pump system available (Edwards 28 E2M28 pump – maximum vacuum: 0.1 mbar or 10 Pa). The ratio between the ionomer and the total solid particles was kept at 30 wt % in both cases [35]. The components of the inks were blended through sonication on a cold bath for 15 min (ELSER 60 Hz) and milled with a benchtop three-roll miller together with 0.3 mm zirconia grinding balls (total mass of zirconia balls corresponds to mass of the suspension) for nearly 12 h.

2.2. Coating and drying of cathodes

For screen-printing coatings, Nafion XL membranes were cut into squares (6.5 cm × 6.5 cm) and coated in an Aurel 9000 screen-printer coupled with a Koenen polyester mesh with 25 cm^2 opening area (32 threads per cm^2 with 70 μm diameter each). The printing pressure was set to 2.0 N cm^{-2} and the substrate was kept in place with a vacuum positioning system.

In case of doctor-blade coatings on GDLs the used device was a Zehntner ZAA 2300 automatic film applicator. The gap setting (height of the doctor blade from the substrate) determines the thickness of the wet coating prior to the drying step, and in this, a 65 μm gap was maintained.

After coating, the electrodes were dried using (i) oven drying at 80 °C, (ii) vacuum oven chamber (15 mbar) at 60 °C, and (iii) sublimation (0.1 mbar) with the use of liquid nitrogen as coolant [36]. Before each drying step a newly coated sample was used. Additionally, doctor bladed cathode GDEs were hot-pressed to the membrane and the anode at 160 °C and 2.5 bar for 3 min.

2.3. Physical analysis

Physical analysis section includes information about (i) scanning electron microscopy specifications (ii) gravimetric techniques applied to the substrates and (iii) porosity evaluation techniques.

2.3.1. Scanning electron microscopy

Specimens for scanning electron microscopy (SEM) were prepared by cutting a 1 × 1 cm square from both cathode CCMs and GDEs. After placing the sample inside the SEM sample holder, the fractures were made by emerging the sample in liquid Nitrogen. The measurements were carried out in a Zeiss UltraPlus, providing an electron beam range of 2.0–10 kV that allows the analysis of the surface and cross section of the different MEAs. Combined with SEM measurements, an (EDX) energy dispersive x-ray spectroscopy peltier cooled Si (Li) detector allowed the quantification of the chemical elements.

2.3.2. Gravimetry

After obtaining completely dried electrodes, both GDEs and CCMs were weighted for Pt loading calculation purposes. To determine the precise Pt loading of the CCM samples, thermogravimetric analysis (TGA) of catalyst-coated membranes was performed with a thermal gravimetric analyser (NETZSCH STA 449 C) and a DSC/TG platinum pan; the samples were heated from room temperature to 1000 °C with a heating rate of 1 K min^{-1} under air atmosphere.

2.3.3. Porosity

To measure the surface area and porosity properties of the catalyst inks, a volume of 5 mL of catalyst ink with equal composition as described in section 2.1 (screen-printing ink) was placed inside three 10 mL glass beakers. The beakers were dried for 36 h by (i) oven drying, (ii) vacuum drying, and (iii) freeze-drying (after a prior step of freezing with N_2), respectively. The masses of the dried samples equal 1 g with an uncertainty of ± 10 mg suggesting that the solvents were completely removed in all three cases. (see supplementary information 6.1). The resulting catalyst agglomerates were withdrawn from each beaker and an equal mass of material (for each drying technique applied) was then dried again, under vacuum conditions at 60 °C for 3 h, with liquid nitrogen and positioned inside a Sorptomanic 1195 chamber. Brunauer–Emmett–Telle (BET) measurements were performed using the Dollimore/Heal method for surface area determination of the approached catalyst pastes [37]. Moreover, the pore size distribution of the catalyst composite was also determined using mercury intrusion porosimetry (MIP) at 25 °C.

2.4. Electrochemical measurements

Electrochemical measurements section presents technical information on (i) the PEMFC break-in and operating conditions (ii) performance measurements (iii) electrochemical impedance spectroscopy, and (iv) cyclic voltammetry.

1. PEMFC break-in and operating conditions

The prepared MEAs were assembled in a 5 × 5 cm^2 gold foiled stainless steel single cell with serpentine flow field design (DLR) and a segmented board for electrochemical characterization. The operating temperature was 80 °C. The gas outlet pressure was kept constant at 1.5 bar (absolute). The relative humidity (RH) was set to 100% in both electrodes using bubbler humidifiers. The stoichiometric coefficients for $H_2$and air were 1.5 and 2.0, respectively. The break-in step was considered completed if the cell potential change was less than 5 mV h^{-1} at 500 mA cm^{-2}.

2. Polarization curve

After achieving nominal operating conditions, a polarization curve was recorded using a Zentro Elektrik in galvanostatic mode. The cell potential was monitored as function of the current density with a dwell time of 3 min and with increments of 25 mA cm^{-2} (range: 0–100 mA cm^{-2}) followed by steps of 100 mA cm^{-2} (range: 100 mA cm^{-2} to limiting current density).

3. Electrochemical impedance spectroscopy measurement

Electrochemical impedance spectroscopy (EIS) was performed in galvanostatic mode, using an electrochemical station with EIS module (Zahner IM6). EIS spectra were recorded at 100 mA cm^{-2} and 500 mA cm^{-2} in the frequency range 100 mHz - 100 kHz with a perturbation amplitude of 8 mA cm^{-2} and 40 mA cm^{-2}, respectively. Impedance spectra were fitted with SIM function of the Zahner software (Zahner IM6).

To measure the ionic conductivity (IC) through the cathode, a potential of 1 V was applied (potentiostatic mode), using 100% humidified $H_2$and N_2gases passing through the anode and cathode, respectively (both 100 mL min^{-1}). The applied frequency range was 500 mHz −100 kHz with a perturbation amplitude of 10 mV.

4. Cyclic Voltammetry

Cyclic voltammograms (CVs) were obtained at 1.5 bar pressure with 20 mV s^{-1} slew rate between 60 mV and 1 V to measure the electrochemical active surface area of each of the cathodes. To measure cathode CV, 100 mL min^{-1} of 100% humidified H_2 was fed into the anode compartment which corresponds to the reference and counter electrode; in parallel, 100 mL min^{-1} of 100% humidified N_2 gas was fed into the cathode compartment which corresponds to the working electrode. The cathode side of the MEA was triggered to a sweep of potentials (0–1 V) where the columbic charge for hydrogen adsorption or desorption was used to calculate the active surface area of platinum considering the charge needed to adsorb a monolayer of adsorbed H^+ on polycrystalline platinum (111). CV signal consists of the adsorption and desorption peak of hydrogen on Pt sites along with the current caused by double layer capacitance. To evaluate the ECSA only the hydrogen desorption peak was used. Thereupon it was possible to obtain the electrochemical surface area (ECSA) of the cathode through the following equation:

$$\mathrm{ECSA}\ \left(\mathrm{cm}^2_{\mathrm{Pt}}/g_{Pt}\right) = \frac{q_{Pt}}{\Gamma \cdot L} \quad (1)$$

Where q_{Pt} refers to the hydrogen adsorption/desoprtion charge density retrieved from each CV, which is the calculated desorption peak

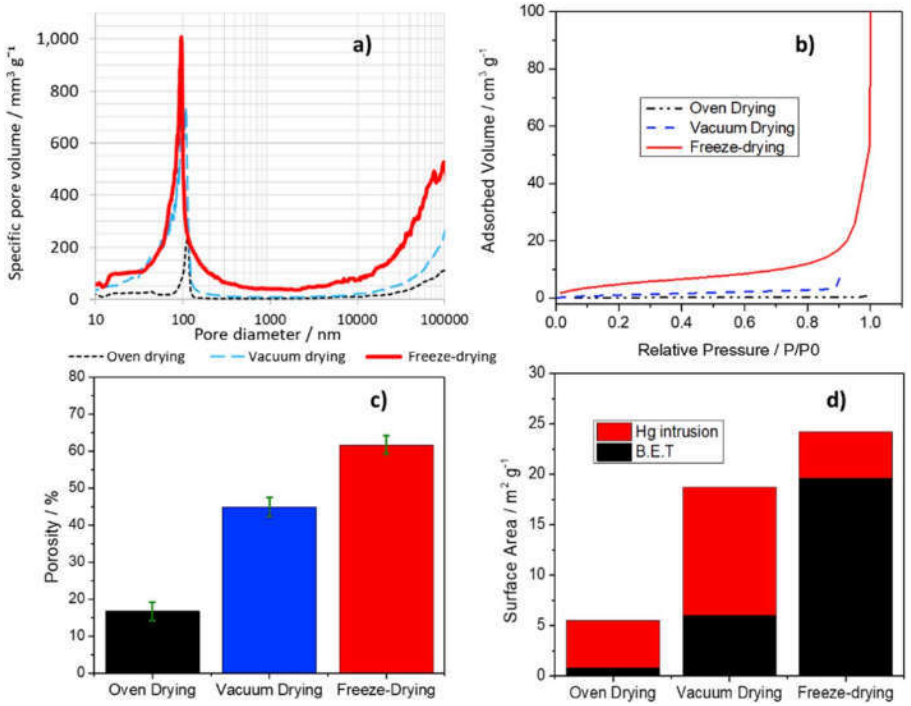

Fig. 1. Pt/C/Nafion/solvent ink dried under oven drying (—), vacuum drying - - - and freeze-drying —— **a)** Specific pore-size distribution **b)** BET isotherms **c)** porosity of the samples after oven drying (●), vacuum drying ■ and freeze-drying ▲ and **d)** BET and MIP specific surface areas.

area of the CV; Γ is equal to 210 μC·cm$^{-2}_{Pt}$ [38,39] and represents the charge required to reduce a monolayer of protons on Pt. It is a constant value. Finally, L represents the Pt loading in the electrode, $g_{Pt}cm^{-2}$. Pt utilization is a concept where we can determine how much platinum is chemically active. It was calculated from the ratio between the ECSA and the theoretical surface area (TSA) of the catalyst provided by the catalyst supplier. TSA is calculated as follows [40]:

$$TSA = 6/(\rho \cdot d) \quad (2)$$

Where ρ is the density of platinum (21.4×10^6 g m^{-3}), d is the mean diameter of the Pt particle provided from the supplier (4.5 nm).

3. Results and Discussion

Results and Discussion section presents the impact of drying techniques on (i) catalyst composites, (ii) CL morphology, and (iii) MEAs electrochemical performance. The electrochemical properties of MEAs subsection is subdivided into (i) performance analysis of the MEAs in PEMFC operation, investigation of transport properties by means of (ii) EIS and (iii) ionic conductivity measurements and (iv) investigation of cathode ECSA by using CV.

3.1. Morphological change of catalyst ink composites via drying techniques

Porosimetry measurements were performed to evaluate the three identical catalyst composites morphology under (i) oven (ii) vacuum or (iii) freeze-drying conditions to simulate the morphology of the following produced cathode catalyst layers (as described in section 2.3.3 and supplementary information 6.1). A previous study ensures that the character of carbon particle aggregation in powder form is preserved in CLs [41]. Fig. 1 a depicts the pore size-distribution of the prepared catalyst composites consisting of Pt/C and ionomer dried as approached above. The obtained solid particles and their dispersion dictate the final state of the microstructure and thus the formation of primary and secondary pores. Soboleva et al. reported that HiSpec catalyst forms

Table 2
Morphological characterization of Pt/C-Nafion powders dried to oven, vacuum and freeze-drying.

S_{BET} ($m^2 \cdot g^{-1}$)[a]	0.81	6.00	19.58	<5%
Total pore volume ($mm^3 \cdot g^{-1}$)[c]	102.5	343.2	631.28	5–7%
Average pore diameter (nm)[c]	74.5	73.26	104.1	5–7%
Type of isotherm[b]	IV	II	II	
Porosity (%)[c]	16.7	45	61.7	5%

[a] Obtained from BET measurements.
[b] From nitrogen physisorption data measurements and in accordance to the IUPAC classification.
[c] From MIP measurements.

micropores associated with the carbon primary particles (<2 nm), and mesopores ascribed to the void space inside the carbon agglomerates (ranging from 2 to 20 nm). Finally, the meso to macropores region pertain to the space between the aggregates of agglomerates, creating the secondary pores (>50 nm) [41]. Thereby, the ionomer is reported to be deposited in the pores with size < 20 nm [42]. This phenomenon reduces the loss of Pt particles into the carbon pores. Nevertheless, as noticeable in Fig. 1a, the volume of pores associated with the mesopores region below 30 nm is not negligible and greatly depends on the drying technique. In detail, the oven-dried sample shows the lowest distribution of pores in this region, followed by vacuum-dried and the freeze-dried. Furthermore, the freeze-dried specific pore volume shows a broad pore size distribution ranging from meso-to macropores. It displays a distinct peak at 90 nm and a high total pore volume in the macropores region (>100 nm). The presence of larger number of mesopores is also justified after BET experiments, with the slight hysteresis loop characteristic of capillary condensation at higher pressure [43] in case of freeze-drying as observed in Fig. 1 b.

The same behaviour is not achievable through oven-drying or vacuum-drying despite the sorption isotherms and the associated hysteresis are relatively similar in shape; However, they differ significantly in the amount of adsorbed gas. Additionally, MIP measurements allow determining the total porosity of the Pt/C-Nafion structures. The results

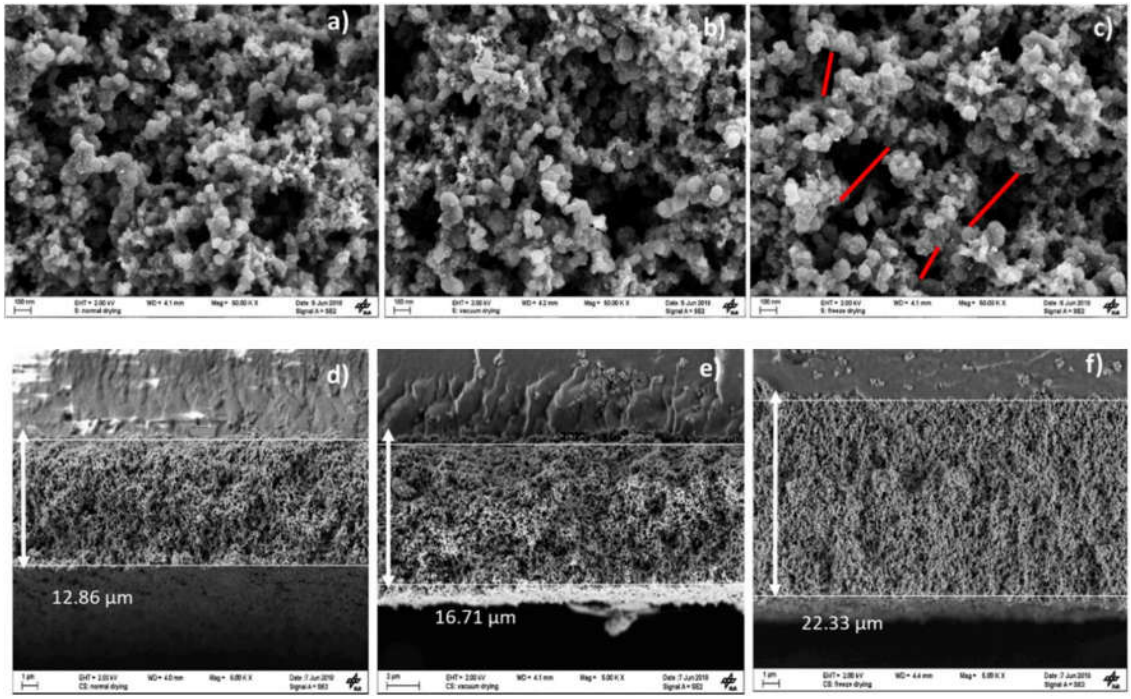

Fig. 2. SEM images of **a)** oven drying; **b)** vacuum drying and **c)** freeze-drying surfaces with 5 k magnification (red lines indicate the area of void space for pore diameters calculation); Cross sections of CCMs before operation and the indicated thickness of the CLs **d)** oven dried (CL length = 12.86 µm) **e)** vacuum dried (CL length = 16.71 µm) and **f)** freeze-dried MEA (CL length = 22.33 µm). (For interpretation of the references to colour in this figure legend, the reader is referred to the Web version of this article.)

shown in Fig. 1 c demonstrate that the freeze-dried sample has 3.5-fold higher porosity than the oven-dried sample. The effective porosity ranges from 16.7% for the oven-dried sample, 45% for vacuum-dried samples, and 61.7% for the freeze-dried sample, as summarized in Table 2 with less than 5% relative error. Moreover, the freeze-dried exhibits a significant increase in BET surface area (S_{BET}) compared to the other samples as sown in Table 2 and Fig. 1 d. Hence, it is evident that the drying step does affect the final microstructure of the catalyst and, hence, the microstructure of catalyst layer. Since freeze-drying technique is based on sublimation, the formation of larger pores relates with the direct transition from solid solvent crystals to vapour; the result is a wider network of pores. This behaviour is visible in Table 2, where the calculated average pore diameter of the freeze-dried sample is higher than of the others. In contrast it can be assumed from literature that particle size and composition is not changed in the CLs [41]. It is assumed that, the pore size and pore volume of the cathode catalyst layer increases, and the overpotential associated to diffusion of reactants is very likely to be reduced. This reduction of diffusion overpotential is in compliance with the better cell performances as verified by Yim et al. [44].

3.2. *Effect of the drying techniques in the morphology of the MEAs*

SEM images of the surface of oven-, vacuum- and freeze-dried CCMs are presented in Fig. 2 a, b and c, respectively. The catalyst layer surface is homogeneous with no sign of cracks or swelling. Beforehand, a different solvent other than cyclohexanol had been tested (isopropanol and water) and evidences of cracks were regular, after drying at the surface of the CL. The images display a typical CL surface morphology, showing a certain regularity for the small diameter pores (0–50 nm) and an irregular network of pores (that differ in shape and size) especially for larger pores. The freeze-dried electrode surface seems to show wider and more voids (black spots) that are associated to pores (red lines, Fig. 2 c) in comparison to oven- and vacuum dried electrodes in Fig. 2 a-b. Moreover, the SEM images were further analysed with automated pore recognition. The approximate average diameter of pores in each CCMs after drying were estimated. Pore volume from microscopic images were measured, and values were statistically fitted with Gaussian distribution. In comparison to oven and vacuum dried CCMs, the freeze-dried CCM displays a remarkable distribution of pores from meso to macropore region (50–150 nm) and even to pores of larger dimensions (>200 nm). Pore diameter of oven dried CL shows a peak at 65.28 ± 3.31 nm, and vacuum-dried shows two peaks at 55.26 ± 1.34 nm and 254.62 ± 1.34 nm (56% of the samples diameters fit the 0–100 nm range). Freeze-dried samples exhibit a first peak at 102.8 ± 2.35 nm and the second around 223.8 ± 2.35 nm. However, it is necessary to mention that 58% of pore sizes rely at the range of 100 up to 250 nm (**s**upplementary information 6.2 for more details).

In EDX measurements of the electrode surfaces of each CCM a prominent carbon peak is detected (~48 wt%), accounting for both the catalyst support and the molecular structure of the ionomer. Moreover, sulphur (~1 wt%), oxygen (~4 wt%) and fluorine (~19 wt%) peaks are observed due to the composition of the ionomer. The platinum mass percentage equals ~28 wt% which matches the expected wt. % of Pt amongst the total solid particles (Pt, carbon and nafion) confirming that the Pt content in each MEA is identical; (supplementary information 6.3 provides the wt.% of each ion in detail for the three CCMs). Signals associated with contaminations were not observed in the EDX signal.

Fig. 2 d-f displays the cross-section SEM analysis of the different CCMs and the catalyst layer over the membrane. Nafion XL membrane represents a thickness of ~29 µm. The oven-dried CL has ~13 µm, the vacuum-dried ~17 µm and the freeze-dried has ~23 µm thick electrode. The thickness of the freeze-dried CL is 1.8-fold higher in contrast to the other CLs. The additional thickness of the same mass of material results from an increased porosity of this sample. This suggests that, concurrently with the higher volume of pores achieved with freeze-drying and with the same solid content an increase of thickness of the catalyst layer results. This may seem detrimental as a common strategy of the scientific community is to decrease the thickness of catalyst layers, mainly to lower the Pt content [24]. According to Liu et al., at 100% RH and

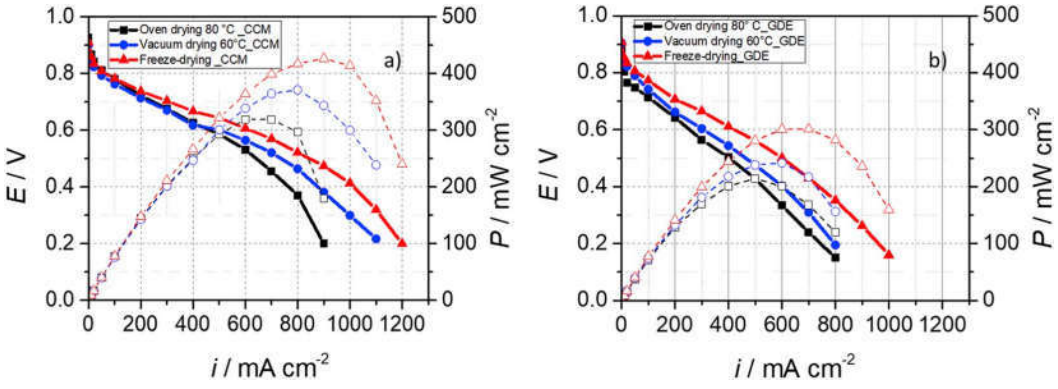

Fig. 3. Polarization curves of **a)** three CCMs (80 °C; RH: 100%; cathode: 0.160 $mg_{Pt}{\cdot}cm^{-2}$ and **b)** three GDEs (80 °C; RH: 100%; cathode: 0.183 $mg_{Pt}{\cdot}cm^{-2}$) prepared by screen-printing and dried by freeze-drying ▲, oven drying (■) and vacuum drying •; comparison were shown among the MEAs in each coating techniques individually.

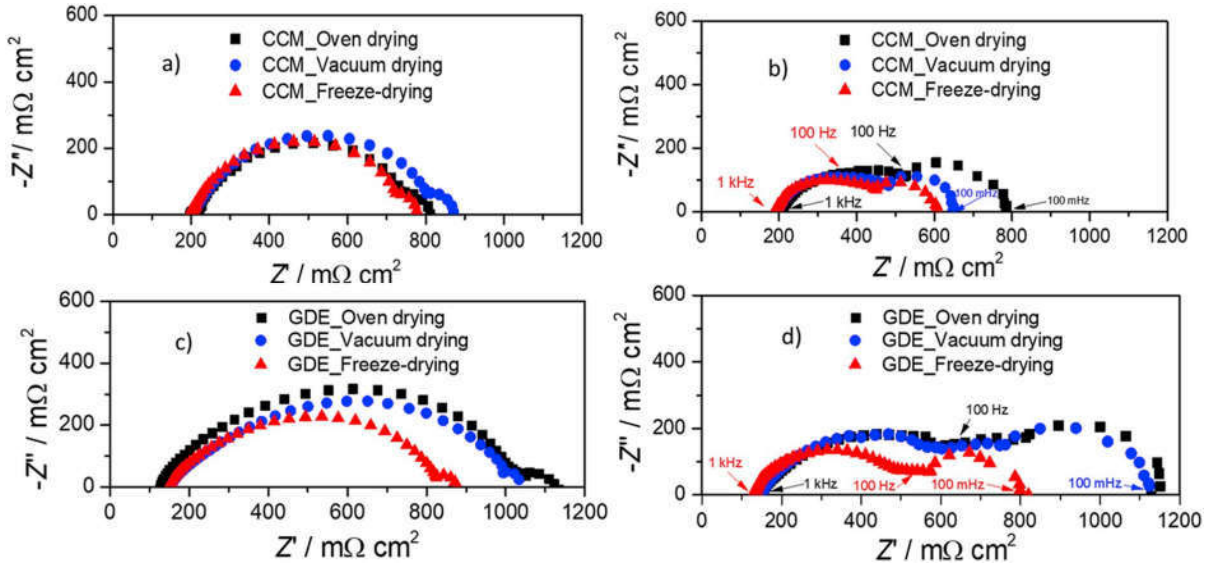

Fig. 4. Nyquist plot for the CCMs at **a)** 100 mA cm^{-2} and **b)** 500 mA cm^{-2} current densities and GDEs at **c)** 100 mA cm^{-2} and **d)** 500 mA cm^{-2} current densities.

assuming a uniform electrode, the proton resistivity is independent of the electrode thickness and the wt. % of Pt on the carbon support. As a result, there is no obstacle in using freeze-drying with the issue that this technique can increase ohmic resistances due to the increased thickness. Therefore freeze drying can be regarded as promising for low loaded MEAs if the ionomer/carbon ratio is well optimized for low Pt loadings [45]. The previous statement is confirmed with EIS data from this study, Fig. 4 a-d, where freeze-dried MEAs do not show higher ohmic resistances, despite their higher thickness. To achieve a suitable catalyst layer structure that guarantees efficient platinum utilization while ensuring a suitable porous matrix for the reactants transport is challenging. In this regard, freeze-drying is promising to provide a homogeneous geometry of the pores while influencing the dispersion of the ionomer surrounding the active sites. This features definitely impact the performance of the cell (Fig. 3 a-b).

3.3. Effect of drying in the electrochemical properties of the MEAs

3.3.1. Polarization curves

Fig. 3 a and b present the polarization curves for a set of three screen-printed CCMs and three doctor-bladed GDEs, respectively, dried by oven dying, vacuum drying and freeze-drying. The applied drying techniques along with both coating methods, generate MEAs with high reproducibility (less than 10% deviation), that in turn enables a proper assessment on the performance and morphological status of different drying techniques.

Apparently, in case of CCMs a cell voltage decrease in the current densities region > 800 mA cm^{-2} occurs due to mass transport limitations, especially for the oven-dried electrode. However, the polarization curves for freeze-dried cathodes demonstrate better performance in comparison to the other drying techniques particularly in the mass transport region at $i > 800$ mA cm^{-2}. Moreover, the ohmic loss was also reduced by the freeze-drying method, which leads to a reduced slope of the curve in the range 200–800 mA cm^{-2}.

In case of GDEs, significant polarization losses were also observed in the samples dried in different drying approaches. It is possible to justify the losses due to the poor contact between the catalyst layer with the membrane as it catalyst is coated on GDL. Additionally, the absorbing capacity of the microporous layer of the GDL may be responsible of an inferior drying process effect, where a major part of the liquid solvent penetrates into the microporous layer of GDL. This is in contrast to the observation of the CCM samples where mass transport losses were evident after each drying method. Even in this circumstances, freeze-dried GDE exhibits clear improvement in the activation region at $<$ 100 mA cm^{-2} and especially in the ohmic region at 200–800 mA cm^{-2} compared to oven-drying and vacuum-drying MEAs.

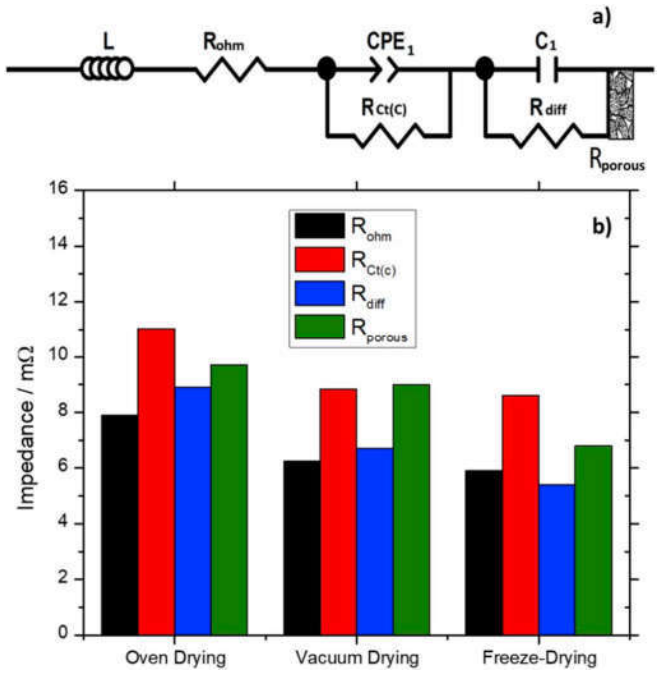

Fig. 5. a) Equivalent circuit for PEMFCs with H_2/Air gas supply; **b)** Contributions of each resistance parameter from the equivalent circuit shown in Fig. 5 a, after fitting of EIS of CCM measured at 500 mA cm^{-2}. All the capacitance values are also fitted in the simulation. The CPE_1/exponent values are 155.2 mF/0.755, 187.5 mF/0.825, 165.2 mF/0.796 for oven, vacuum and freeze-drying MEA respectively. Additionally, The C_1 value is 10.93 F, 11.9 F, 14.66 F for oven, vacuum and freeze-drying MEA respectively.

In summary, freeze-dried CCMs as well as GDEs show significantly improved performance compared to oven and vacuum-dried MEAs. Nevertheless, the MEAs prepared using GDE cathodes show lower performance than those consisting of CCM cathodes. A likely reason for this observation is that sublimation drying technique facilitates the porosity and the ionomer distribution throughout the catalyst layer. Moreover, a predictable assumption culminates a good balance of coverage of active sites by the ionomer, providing uninterrupted network to the ionic as well as electronic conductive phases. Additionally, an adequate pathway for the diffusion of the reactants and products to and from the reactive sites is likely to be achieved with this technique.

3.3.2. *Impedance spectroscopy*

EIS was performed with a potentiostat/galvanostat to examine the contributions of different drying techniques to the overall cell impedance. Fig. 4 a and c represent the electrochemical impedance spectra recorded under galvanostatic mode at 100 mA cm^{-2} for CCMs and GDEs, respectively. The corresponding spectra obtained at 500 mA cm^{-2} are provided in Fig. 4 b and d. At low current density of 100 mA cm^{-2} charge transfer polarization is a dominant factor [46]. The ohmic and mass transport issues contribute significantly at higher current densities, as depicted in Fig. 4 b and d for both CCM and GDE. In all cases, the freeze-dried electrodes exhibit the lowest impedance spectra. At 500 mA cm^{-2}, a significant reduction of charge transfer related impedances (higher frequencies) and minor mass-transport contributions (lower frequencies) are noticed for freeze-dried CCM and GDE cathodes, in comparison to oven-and vacuum-dried cathodes. However, the positive effect of freeze-drying the electrode is more evident at the mass-transport zone (lower frequencies). A likely reason relies in the improved porosity achieved by means of sublimation that provides an electrode with superior access of reactant oxygen and permeable for water transport.

For in-depth analysis, the EIS spectra of CCMs measured at

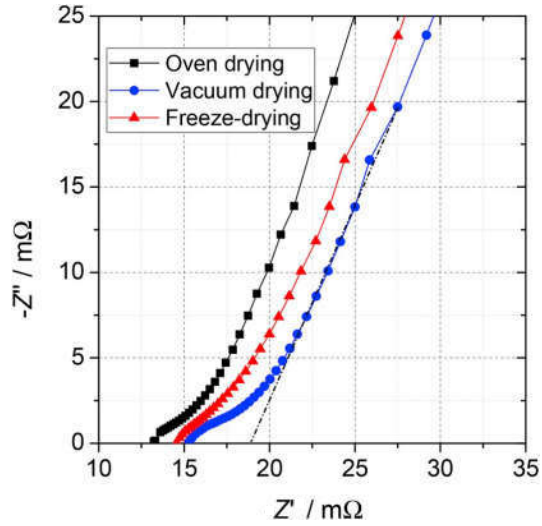

Fig. 6. Complex plane Nyquist impedance plots (500 mHz–100 kHz, 1.0 V H_2) of CCMs dried under oven, vacuum and freeze-drying conditions; The inflection of approximately 90° representative of the double-layer limiting capacitive current appears at lower frequencies (6 kHz).

500 mA cm^{-2} have been evaluated by fitting the experimental data to an equivalent circuit shown in Fig. 5 a. The detailed evaluation has not been performed for GDEs, since the same trend is observed for both cases. The contribution of the different resistance elements at 500 mA cm^{-2} is presented in Fig. 5 b. At high current density, a decreasing trend in charge transfers resistances from oven to vacuum to freeze-drying has been observed progressively. The freeze-dried CCM displays the lowest charge transfer resistance (R_{ct}(C) = ~8.6 mΩ), followed by vacuum dried that has similar contributions for the ORR (~8.8 mΩ) and the highest resistance is associated with oven dried cathodes (~9.7 mΩ). At high current densities, the most dominant overpotential is associated to the mass transport of the species to and from the active sites. Thus, depletion in oxidant at the reactive interphase or local water flooding hampers the reactants diffusion and leads to the starvation of the active sites and a subsequent sudden loss of performance. From the polarization curves (Fig. 3 a-b), it is possible to verify the major potential drop occurs in case of oven dried MEAs as the current density increases. This result is in compliance with the experimented EIS value where the highest magnitude of diffusion impedance (R_{dif} and R_{porous}) is associated with oven dried cathodes, followed by vacuum and the lowest for the freeze-dried cathodes (Fig. 5 b). This analytical result provides a hint regarding more suitable microstructure of freeze-dried electrodes with improved diffusion of the reactant and an appropriate pore structure for water elimination, in comparison to the other drying techniques investigated in this study.

3.3.3. *Ionic conductivity measurements of the catalyst layers*

Protonic conduction through the catalytic layer is a major limiting factor of the ohmic overpotential. Impedance spectroscopy under an inert atmosphere (nitrogen) was conducted to isolate the contribution of the ionic resistance across the cathode catalyst layer under the different drying conditions, following the transmission line model suggested by Pickup et al. [47] (see supplementary information 6.4). The protonic resistance, $R_{ionic,}$ through the three differently dried electrodes can be obtained from the magnitude of a Warburg-like region projected onto the real impedance (Z') axis (= R_{ionic}/3) [47,48] (Fig. 6, dotted line). The highest value of ionic resistance across the cathode catalyst layer was attained for the oven-dried (R_{ionic} of 23.3 mΩ) followed by the vacuum-dried (R_{ionic} of 20.1 mΩ) and finally for the freeze-dried cathode (R_{ionic} of 16.7 mΩ). The variations of the intercepts at high frequencies are explained by the electrode thickness and a certain experimental

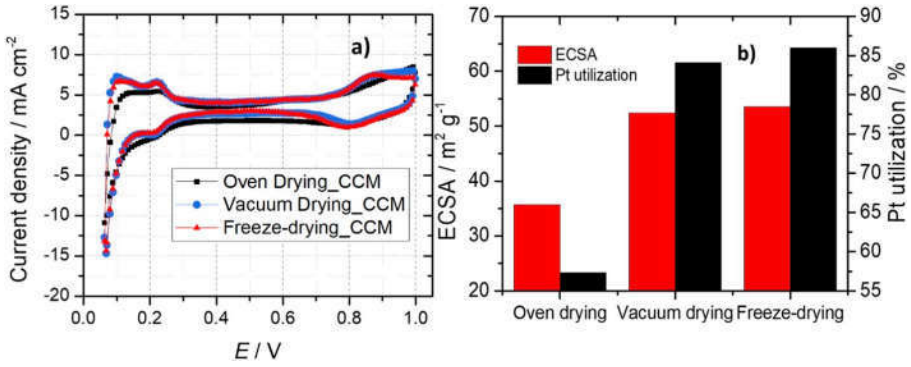

Fig. 7. a) Cyclic voltammograms for CCMs that were oven dried, vacuum dried and freeze-dried; **b)** Electrochemical active surface area (ECSA) and platinum utilization for the Pt/C catalyst in each MEA.

uncertainty related to contributions from electronic resistances associated to contact resistances. However, these contributions are negligible in this study. From the calculation, it is comprehensible that freeze-dried electrodes exhibit less protonic resistance across the CL as the dispersion and distribution of ionomer around the active sites are apparently improved.

3.3.4. Cyclic voltammetry

Fig. 7 a represents the cyclic voltammetry (CV) scans that enables the calculation of the ECSA and Pt utilization of the catalyst layer. Similar to the BET results regarding the available surface area, the freeze-dried cathode also exhibits the highest quantity of catalyst available to contribute to electrochemical reaction resulting in higher Pt utilization (~86%) compared to oven- and vacuum-dried cathodes as shown in Fig. 7 b. The TSA achieved for Pt/Vulcan-XC-72 is 62.31 $m^2 g^{-1}$. The fact that freeze-dried and vacuum-dried samples had analogous ECSA values but different single cell performances requires the consideration of an effective porosity of each of the electrodes in terms of limiting current density (higher for the freeze-dried cathode). Moreover, a rearrangement of the interphase and porous microstructure might have occurred in a matter that more active sites and highly coordinated facets of the catalyst might had been exposed by freeze-drying of the catalyst layer [49,50]. Moreover this effect may be correlated with a changed ionomer structure – possibly more homogeneous and thinner in the case of freeze drying - in the catalytic layer which may lead to this performance variation [51,52]. In summary, an increased value of ECSA coupled with higher effective porosity results in better Pt utilization along with enhanced mass transport diffusion. Consequently, a higher cell performance is obtained [38].

Furthermore, it is assumed that the porosity improved by sublimation drying techniques, also facilitates the water management. Water uptake and penetration characteristics are also enhanced by creating micro-channels throughout the electrode layer. This trade-off between thickness and porosity of the electrode provides a better performance of the cell in this study.

4. Conclusion

Freeze-drying of cathode electrodes prepared by screen printing and doctor-blade yields increased porosity compared to oven-drying and vacuum-drying. Moreover, a broader distribution of pores from micro to macro scale is observed. It is inferred from this study that the freeze-drying method of the electrode strongly influences the ionomer interactions with Pt/C catalyst and the microstructure of the catalyst layer. In contrast to oven and vacuum-drying, up to 34% and 16% higher power density is achieved with freeze-dried electrodes at Pt loadings of 0.160 mg cm^{-2}, respectively. The measured Pt utilization of nearly 86% represents an improvement of 34% comparing to the common oven drying technique. Consequently, freeze-drying not only leads to a remarkable reduction of charge transfer resistances associated to the ORR but also increases the oxygen diffusivity in the CL due to the improved interfacial properties at the catalyst/ionomer/membrane by boosting the effective porosity. Moreover, the formation of more and larger pores during the drying process is likely to aid the cell water management by preventing flooding. The improvement in power efficiency by freeze-drying CCMs and GDEs (at 0.6 mA cm^{-2} and 80 °C) is 6% and 13%, respectively, in comparison to oven-drying.

Modification of the catalyst layer microstructure with freeze-drying provides versatile opportunities to tune the intrinsic characteristics of the MEAs (e.g., water and oxygen transport through the catalyst layer). Moreover, it can be adaptable to all suspension ink coating techniques. This is a scalable technique, which could easily implement in an industrial production line of MEA. Generally, the results reported in this work clearly reveal the importance of the drying step in the MEA preparation process.

The future scope of this work will be to govern the pore size by controlling the cooling rate of the solvent during freeze-drying in a proper chamber. As the crystal size of ice decreases with increasing cooling rate, it is possible to optimize the porosity of the catalyst layer by effectively calibrating the cooling rate during the freeze-drying operation.

Acknowledgments

Krishan Talukdar acknowledges financial support by DAAD. Sofia Delgado and Tiago Lagarteira thank Professor Adélio Mendes for his support and supervision and acknowledge financial support by ERASUMS. The authors thank Siegfried Graf for building up and maintaining the fuel cell test benches, Ina Plock for her technical support with SEM images and Noriko Sata for the assistance with porosity measurements.

Appendix A. Supplementary data

Supplementary data to this article can be found online at https://doi.org/10.1016/j.jpowsour.2019.04.094.

References

[1] C.A. Rice, P. Urchaga, A.O. Pistono, B.W. McFerrin, B.T. McComb, J. Hu, Platinum dissolution in fuel cell electrodes: enhanced degradation from surface area assessment in automotive accelerated stress tests, J. Electrochem. Soc. 162 (2015) F1175–F1180, https://doi.org/10.1149/2.0371510jes.
[2] K. Park, J. Lee, H.-M. Kim, K.-S. Choi, G. Hwang, Discrete regenerative fuel cell reduces hysteresis for sustainable cycling of water, Sci. Rep. 4 (2015) 4592, https://doi.org/10.1038/srep04592.
[3] F. Gloaguen, P. Convert, S. Gamburzev, O.A. Velev, S. Srinivasan, An evaluation of the macro-homogeneous and agglomerate model for oxygen reduction in PEMFCs, Electrochim. Acta 43 (1998) 3767–3772, https://doi.org/10.1016/S0013-4686(98)00136-4.

[4] C. Marr, X. Li, Composition and performance modelling of catalyst layer in a proton exchange membrane fuel cell, J. Power Sources 77 (1999) 17–27, https://doi.org/10.1016/S0378-7753(98)00161-X.
[5] M.M. Mench, E.C. Kumbur, T.N. Veziroglu, S.S. Kocha, Electrochemical Degradation: Electrocatalyst and Support Durability, Academic Press, 2012, https://doi.org/10.1016/B978-0-12-386936-4.10003-X.
[6] X. Yu, S. Ye, Recent advances in activity and durability enhancement of Pt/C catalytic cathode in PEMFC: Part II: degradation mechanism and durability enhancement of carbon supported platinum catalyst, J. Power Sources 172 (2007) 145–154, https://doi.org/10.1016/J.JPOWSOUR.2007.07.048.
[7] G. Bender, T.A. Zawodzinski, A.P. Saab, Fabrication of high precision PEFC membrane electrode assemblies, J. Power Sources 124 (2003) 114–117, https://doi.org/10.1016/S0378-7753(03)00735-3.
[8] E. Antolini, L. Giorgi, A. Pozio, E. Passalacqua, Influence of Nafion loading in the catalyst layer of gas-diffusion electrodes for PEFC, J. Power Sources 77 (1999) 136–142, https://doi.org/10.1016/S0378-7753(98)00186-4.
[9] R. O'Hayre, D.M. Barnett, F.B. Prinz, The triple phase boundary: a mathematical model and experimental investigations for fuel cells, J. Electrochem. Soc. 152 (2005) A439–A444, https://doi.org/10.1149/1.1851054.
[10] R. O'Hayre, D.M. Barnett, F.B. Prinz, The Pt/Nafion/air triple phase boundary: model, experiment, and implications for PEM fuel cells, Proc. Electrochem. Soc. 138 (2004) 23–26.
[11] V. Mehta, J.S. Cooper, Review and analysis of PEM fuel cell design and manufacturing, J. Power Sources 114 (2003) 32–53, https://doi.org/10.1016/S0378-7753(02)00542-6.
[12] M. Mandal, A. Valls, N. Gangnus, M. Secanell, Analysis of Inkjet printed catalyst coated membranes for polymer electrolyte electrolyzers, J. Electrochem. Soc. 165 (2018) F543–F552, https://doi.org/10.1149/2.1101807jes.
[13] J.W. Ihm, H. Ryu, J.S. Bae, W.K. Choo, D.K. Choi, High performance of electrode with low Pt loading prepared by simplified direct screen printing process in PEM fuel cells, J. Mater. Sci. 39 (2004) 4647–4649, https://doi.org/10.1023/B:JMSC.0000034162.92123.96.
[14] B. Koraishy, J.P. Meyers, K.L. Wood, Manufacturing of membrane electrode assemblies for fuel cells, in: Trans. Int. Conf. Endod., 2009, pp. 1–13. https://www.sutd.edu.sg/cmsresource-/idc/papers/2009_Manufacturing_of_membrane_electrode_assemblies_for_fuel_cells.pdf.
[15] A.P. Saab, F.H. Garzon, T.A. Zawodzinski, Determination of ionic and electronic resistivities in carbon/polyelectrolyte fuel-cell composite electrodes, J. Electrochem. Soc. 149 (2002) A1541, https://doi.org/10.1149/1.1516771.
[16] M.S. Wilson, S. Gottesfeld, Thin-film catalyst layers for polymer electrolyte fuel cell electrodes, J. Appl. Electrochem. 22 (1992) 1–7, https://doi.org/10.1007/BF01093004.
[17] M.S. Wilson, High performance catalyzed membranes of ultra-low Pt loadings for polymer electrolyte fuel cells, J. Electrochem. Soc. 139 (1992) L28–L30, https://doi.org/10.1149/1.2069277.
[18] H. Rabat, P. Brault, Plasma sputtering deposition of PEMFC porous carbon platinum electrodes, Fuel Cells 8 (2008) 81–86, https://doi.org/10.1002/fuce.200700036.
[19] S. Lertviriyapaisan, N. Tantavichet, Sublayers for Pt catalyst electrodeposition electrodes in PEMFC, Int. J. Hydrogen Energy 35 (2010) 10467–10471, https://doi.org/10.1016/j.ijhydene.2010.07.112.
[20] R.N. Bonifácio, J.O.A. Paschoal, M. Linardi, R. Cuenca, Catalyst layer optimization by surface tension control during ink formulation of membrane electrode assemblies in proton exchange membrane fuel cell, J. Power Sources 196 (2011) 4680–4685, https://doi.org/10.1016/J.JPOWSOUR.2011.01.010.
[21] G. Chen, W. Wang, Role of freeze drying in nanotechnology, Dry. Technol. 25 (2007) 29–35, https://doi.org/10.1080/07373930601161179.
[22] U. Oetjen, H.-F. Schmidt, V.M. Stimming, Performance data of a proton exchange membrane fuel cell using H2/CO as fuel gas, J. Electrochem. Soc. 143 (1996) 3838, https://doi.org/10.1149/1.1837305.
[23] A. El-Himri, D. Marrero-López, J.C. Ruiz-Morales, J. Peña-Martínez, P. Núñez, Structural and electrochemical characterisation of Pr0.7Ca0.3Cr1−yMnyO3−δ as symmetrical solid oxide fuel cell electrodes, J. Power Sources 188 (2009) 230–237, https://doi.org/10.1016/J.JPOWSOUR.2008.11.050.
[24] C.M. Zalitis, D. Kramer, A.R. Kucernak, Electrocatalytic performance of fuel cell reactions at low catalyst loading and high mass transport, Phys. Chem. Chem. Phys. 15 (2013) 4329, https://doi.org/10.1039/c3cp44431g.
[25] Y.G. Yoon, G.G. Park, T.H. Yang, J.N. Han, W.Y. Lee, C.S. Kim, Effect of pore structure of catalyst layer in a PEMFC on its performance, Int. J. Hydrogen Energy 28 (2003) 657–662, https://doi.org/10.1016/S0360-3199(02)00156-8.
[26] H. Zhang, Ice Templating and Freeze-Drying for Porous Materials and Their Applications, 2018. https://www.wiley.com/enus/Ice+Templating+and+Freeze+Drying+for+Porous+Materials+and+Their+Applications-p-9783527807420.
[27] M.J. Pikal, Freeze-Drying of proteins Part I: process design, Am. Chem. Soc. (1990) 18–28, https://doi.org/10.1021/bk-1994-0567.ch008%0D10.1021/bk-1994-0567.ch008.
[28] X. Tang, M.J. Pikal, Design of freeze-drying processes for pharmaceuticals: practical advice, Pharm. Res. (N. Y.) 21 (2004) 191–200, https://doi.org/10.1023/B:PHAM.0000016234.73023.75.
[29] W. Mehnert, K. Mäder, Solid lipid nanoparticles: production, characterization and applications, Adv. Drug Deliv. Rev. 47 (2001) 165–196, https://doi.org/10.1016/S0169-409X(01)00105-3.
[30] J. Varshosaz, S. Eskandari, M. Tabbakhian, Freeze-drying of nanostructure lipid carriers by different carbohydrate polymers used as cryoprotectants, Carbohydr. Polym. 88 (2012) 1157–1163, https://doi.org/10.1016/J.CARBPOL.2012.01.051.
[31] M. Carmo, A.R. Dos Santos, J.G.R. Poco, M. Linardi, Physical and electrochemical evaluation of commercial carbon black as electrocatalysts supports for DMFC applications, J. Power Sources 173 (2007) 860–866, https://doi.org/10.1016/j.jpowsour.2007.08.032.
[32] X. Yuan, X.-L. Ding, C.-Y. Wang, Z.-F. Ma, Use of polypyrrole in catalysts for low temperature fuel cells, Energy Environ. Sci. 6 (2013) 1105, https://doi.org/10.1039/c3ee23520c.
[33] T. Lagarteira, F. Han, T. Morawietz, R. Hiesgen, D. Garcia Sanchez, A. Mendes, A. Gago, R. Costa, Highly active screen-printed IrTi4O7 anodes for proton exchange membrane electrolyzers, Int. J. Hydrogen Energy 43 (2018) 16824–16833, https://doi.org/10.1016/J.IJHYDENE.2018.02.179.
[34] Céondo GmbH, Chemical Properties of Cyclohexanol, 2016 (CAS 108-93-0), https://www.chemeo.com/cid/11-718-2/Cyclohexanol.
[35] K.H. Kim, K.Y. Lee, H.J. Kim, E.A. Cho, S.Y. Lee, T.H. Lim, S.P. Yoon, I.C. Hwang, J. H. Jang, The effects of Nafion® ionomer content in PEMFC MEAs prepared by a catalyst-coated membrane (CCM) spraying method, Int. J. Hydrogen Energy 35 (2010) 2119–2126, https://doi.org/10.1016/j.ijhydene.2009.11.058.
[36] K.P. Ryan, W.B. Bald, K. Neumann, P. Simonsberger, D.H. Purse, D.N. Nicholson, Cooling rate and ice crystal measurement in biological specimens plunged into liquid ethane, propane, and Freon 22, J. Microsc. 158 (1990) 365–378, https://doi.org/10.1111/j.1365-2818.1990.tb03008.x.
[37] D. Dollimore, G.R. Heal, An improved method for the calculation of pore size distribution from adsorption data, J. Appl. Chem. 14 (1964) 109–114, https://doi.org/10.1002/jctb.5010140302.
[38] K. Cooper, In situ PEM fuel cell electrochemical surface area and catalyst utilization measurement, in: Fuel Cell Mag, 2009, pp. 1–9. www.scribner.com.
[39] K. Kinoshita, P. Stonehart, Preparation and characterization of highly dispersed electrocatalytic materials, in: J.O.M. Bockris, B.E. Conway (Eds.), Modern Aspects of Electrochemistry, vol. 12, Plenum Press, New York, 1977, pp. 183–266. Ch. 4, https://doi.org/10.1007/978-1-4615-7452-1_4.
[40] I.H. Hafez, Mohamed R. Berber, T. Fujigaya, N. Nakashima, Enhancement of Platinum Mass Activity on the Surface of Polymer-Wrapped Carbon Nanotube-Based Fuel Cell Electrocatalysts, Scientific Report, vol. 4, 2014. Article Number: 6295 link: https://www.nature.com/articles/srep06295.
[41] T. Soboleva, X. Zhao, K. Malek, Z. Xie, T. Navessin, S. Holdcroft, On the micro-, meso-, and macroporous structures of polymer electrolyte membrane fuel cell catalyst layers, ACS Appl. Mater. Interfaces 2 (2010) 375–384, https://doi.org/10.1021/am900600y.
[42] Y.-C. Park, H. Tokiwa, K. Kakinuma, M. Watanabe, M. Uchida, Effects of carbon supports on Pt distribution, ionomer coverage and cathode performance for polymer electrolyte fuel cells, J. Power Sources 315 (2016) 179–191, https://doi.org/10.1016/J.JPOWSOUR.2016.02.091.
[43] S.-S. Chang, B. Clair, J. Ruelle, J. Beauchene, F. Di Renzo, F. Quignard, G.-J. Zhao, H. Yamamoto, J. Gril, Mesoporosity as a new parameter for understanding tension stress generation in trees, J. Exp. Bot. 60 (2009) 3023–3030, https://doi.org/10.1093/jxb/erp133.
[44] S.-D. Yim, Y.-J. Sohn, S.-H. Park, Y.-G. Yoon, G.-G. Park, T.-H. Yang, C.-S. Kim, Fabrication of microstructure controlled cathode catalyst layers and their effect on water management in polymer electrolyte fuel cells, Electrochim. Acta 56 (2011) 9064–9073, https://doi.org/10.1016/J.ELECTACTA.2011.05.123.
[45] Y. Liu, C. Ji, W. Gu, D.R. Baker, J. Jorne, H.A. Gasteiger, Proton conduction in PEM fuel cell cathodes: effects of electrode thickness and ionomer equivalent weight, J. Electrochem. Soc. 157 (2010) B1154–B1162, https://doi.org/10.1149/1.3435323.
[46] M. Schulze, N. Wagner, T. Kaz, K.A. Friedrich, Combined electrochemical and surface analysis investigation of the degradation process in polymer membrane fuel cells, Electrochim. Acta 52 (2007) 2328–2336. https://doi.org/10.1016/j.electacta.2006.05.063.
[47] M.C. Lefebvre, R.B. Martin, P.G. Pickup, Characterization of ionic conductivity profiles within proton exchange membrane fuel cell gas diffusion electrodes by impedance spectroscopy, Electrochem. Solid State Lett. 2 (1999) 259–261, https://doi.org/10.1149/1.1390804.
[48] G. Li, P.G. Pickup, Ionic conductivity of PEMFC electrodes, J. Electrochem. Soc. 150 (2003) C745–C752, https://doi.org/10.1149/1.1611493.
[49] Z. Duan, G. Wang, Comparison of reaction energetics for oxygen reduction reactions on Pt(100), Pt(111), Pt/Ni(100), and Pt/Ni(111) surfaces: a first-principles study, J. Phys. Chem. C 117 (2013) 6284–6292, https://doi.org/10.1021/jp400388v.
[50] M.K. Debe, Electrocatalyst approaches and challenges for automotive fuel cells, Nature 486 (2012) 43–51, https://doi.org/10.1038/nature11115.
[51] K. Talukdar, S. Helmly, M. Schulze, D.G. Sanchez, M. handl, R. Hiesgen, J. Kraut, K. A. Friedrich, Enveloping of catalyst powder by ionomer for dry spray coating in polymer electrolyte fuel cells, J. Power Sources 424 (2019) 82–90. https://doi.org/10.1016/j.jpowsour.2019.03.093.
[52] T. Morawietz, M. Handl, C. Oldani, K.A. Friedrich, R. Hiesgen, Quantitative in situ analysis of ionomer structure in fuel cell catalytic layers, ACS Appl. Mater. Interfaces 40 (2016) 27044–27054, https://doi.org/10.1021/acsami.6b07188.

5 Supplementary information

5.1 Preparation and analysis of catalyst ink

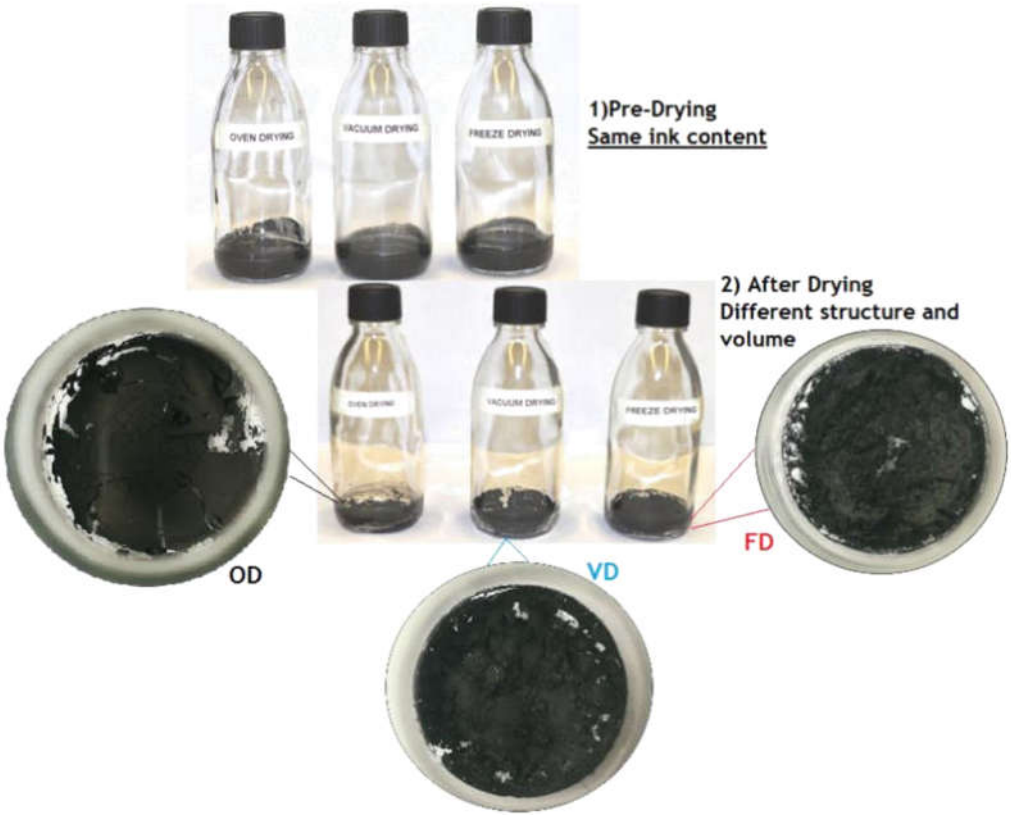

Fig. S 1. Stages of catalyst paste drying through oven drying (OD), vacuum drying (VD) and freeze-drying (FD).

The catalyst paste prepared following the routes described above (section 2.1) was placed inside three glass beakers, with the same volume, **Fig.S.1)**. The aim of this experiment was to assess and compare the surface areas and effective porosities of the resulting paste film agglomerates after being dried. It is noticeable that the microstructure of the film inside each beaker differs after different drying conditions. The foamy look surface for the freeze-dried sample is unalike to the oven dried which in turn is less porous and appears brittle. The same amount of sample was collected from each beaker. Afterwards, BET and MIP measurements were carried out to determine quantitatively the effect of drying on the catalyst paste. (**Table 2**).

5.2 Image processing and analysis – pore structures of CCMs

An approximate statistical analysis was performed to the surface of each CCM. The images obtained through SEM (at 10k and 50 k magnifications) were processed using ImageJ software. Ninety pore diameters were measured for each CCM (oven, vacuum- and freeze-dried), flat pores were excluded of the measurement through "watermark" option of the software. This estimation processing technique in 2D was used for counting pore diameters (**Fig. S 2** to **Fig. S 4**). 3D image processing would be more precise but was unavailable in this study.

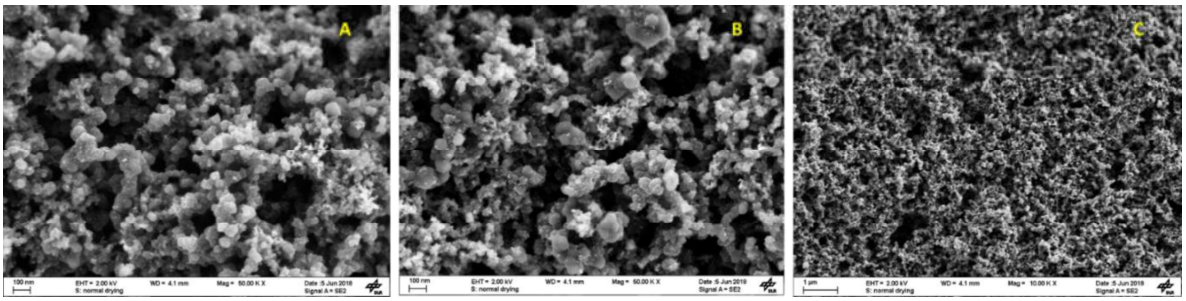

Fig. **S 2. SEM images of oven-dried surface CCM at a) and b) 50k and c) 10k magnifications.**

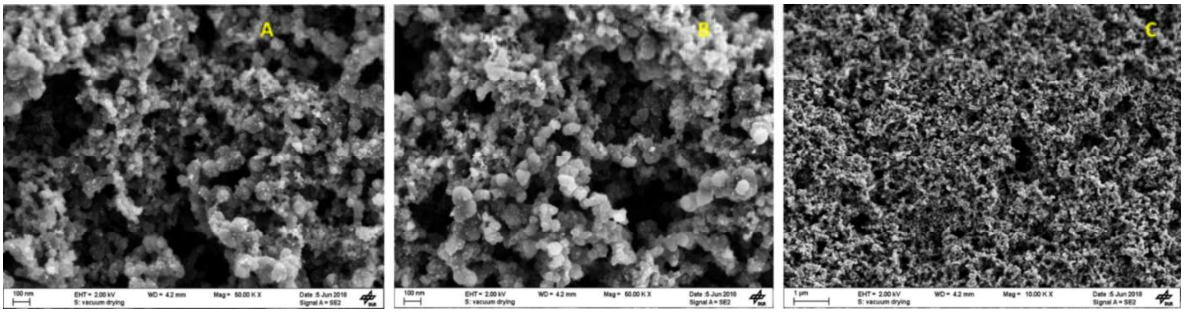

Fig. S 3. SEM images of vacuum-dried CCM surface at a) and b) 50k and c) 10k magnifications.

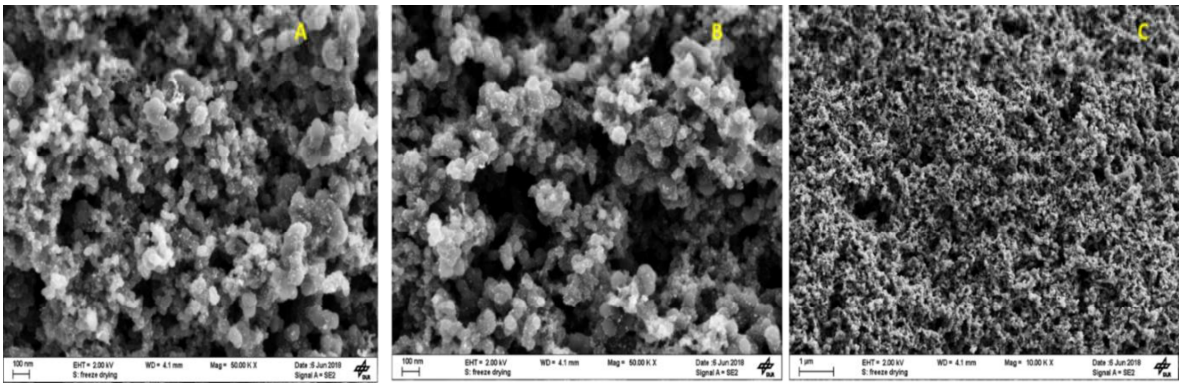

Fig. **S 4. SEM images of freeze-dried CCM surface at a) and b) 50k and c) 10k magnifications.**

Fig. S 5a-c present histograms (samples count vs. pore diameter) regarding the surface of three CCMs. shows that the most probable pore diameter for oven-dried electrodes stands at 65.28 ± 3.31 where a low number of pores with a diameter higher than 200 nm but a relatively high amount of pores with smaller diameters (micro to mesopores – 0-50 nm); Two peaks can be seen for the vacuum dried sample (**Fig. S 5b**) , hence the most probable pore diameters appear at 55.26 ± 1.34 nm and 254.62 ± 1.34 nm with many smaller pores and with more and larger pores than the former sample. **Fig. S 5c** suggests that the freeze-dried sample displays a remarkable number of pores at 102.8 ± 2.35 nm and 223.8 ± 2.35 nm with a low number of smaller pores and considerably greater larger pores than the previous oven- and vacuum-dried samples (see **table S.1** for more details).

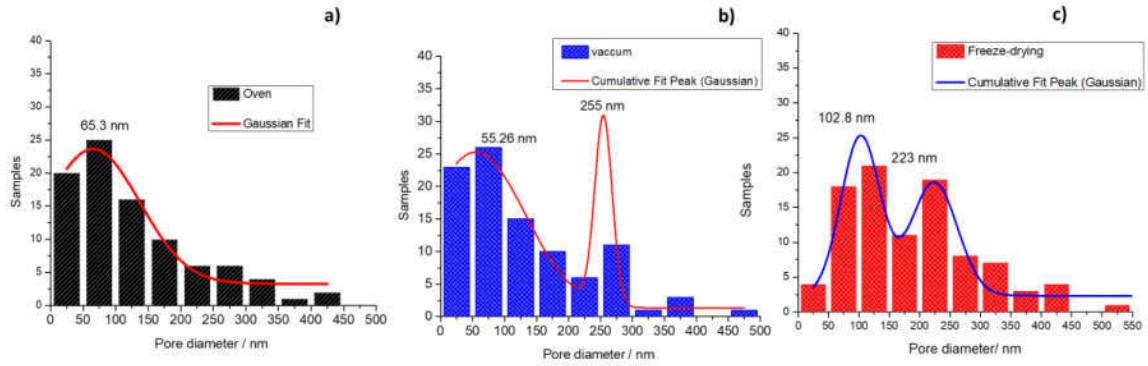

Fig. S 5. Histograms – samples count vs. pore diameter a) oven-dried b) vacuum-dried and c) freeze-dried CCMs.

Table S 1. Statistical data (concerning Fig.S5) on pore count, average equivalent pore diameter and standard deviation at specific ranges of pores.

Sample	Pore range (nm)	Equivalent pore counts (%)	Equivalent average pore diameter* (nm)	Standard deviation (± nm)
Oven drying	0-100	50	65.28	3.31
Vacuum drying	0-100	56	55.26	1.34
	100-250	34	254.62	1.34
Freeze-drying	0-100	24	---	---
	100-250	58	102.80 223.80	2.35 2.35
* Calculation based on the peaks				

5.3 EDX measurements

Table S 2 presents the expected weight percentage of each element in the CL after drying; It is considered that there are no trace of cyclohexanol and/or water. The ratio between Nafion and Pt/C is 30 %.

Table S 2. Expected weight percentage of each component in the CL after drying.

Component	Wt. %
Pt	28
Carbon	42
Nafion	30

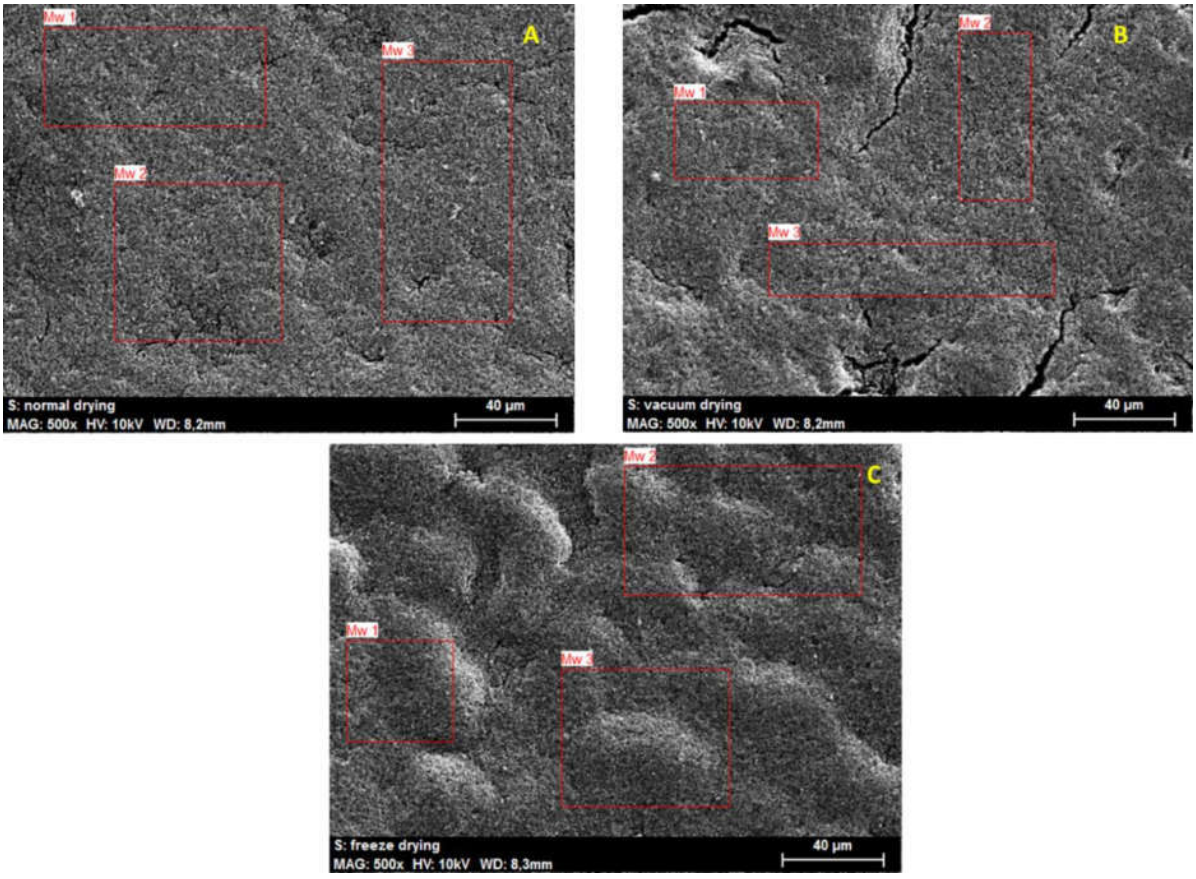

Fig. S 6. EDX images for a) oven- b) vacuum- and c) freeze-dried CCMs surface at 500 x magnification.

Table S 3. Data (concerning Fig.S6) on wt.% percentage of elements for three CCMs.

CCM	Element	Element spectrum average wt.%	Origin of the element
Oven-dried	Pt	25	Catalyst;
	C	47.54	Catalyst support (~42 %) + Nafion;
	O	4.73	Nafion;
	S	1.23	Nafion;
	F	21.57	Nafion backbone;
Vacuum-dried	Pt	27.7	Catalyst;
	C	49.52	Catalyst support (~42 %) + Nafion;
	O	3.90	Nafion;
	S	0.86	Nafion;
	F	27.7	Nafion backbone;
Freeze-dried	Pt	27.5	Catalyst;
	C	48.53	Catalyst support (~42 %) + Nafion;
	O	4.44	Nafion;
	S	0.95	Nafion;
	F	18.58	Nafion backbone;

5.4 Conductivity measurements

By purging the cathode compartment of the cell with nitrogen during the measurements, the impedance response becomes dominated by charging of the catalyst's double layer through the layer's ionic resistance [44].**Fig.6** shows the impedance spectra of the CCMs recorded according to the literature cited above. The potential was set to 1.0 V, very close to the open circuit potential for O_2/H_2O to minimize the Faradaic current due to the possible reduction of oxygen traces [45], since this experiment was performed immediately after EIS measurements on H_2/Air. It is then assumed that under an inert atmosphere, the cell impedance is determined by the cathode while the H_2 anode behaves as a reversible hydrogen electrode (RHE). Moreover, as the high frequency impedance spectra (20 kHz – 6 kHz) are dominated by the charging of the double layer (dl) capacitance between the catalyst and the ionomer/electrolyte, the Faradaic currents are negligible. The model possesses two parallel resistive trails, (i) one representing the electron transport through the carbon support and the other (ii) representing the ionic transport through the inter-particle regions. However, the electronic trail resistance is considered negligible in comparison to ionic resistances across the CL. The resistance of

the membrane is omitted since it would only cause a shift along the real impedance axis. From **Fig.6,** at high frequencies, it is visible a Warburg-like response characterized by a 45° slope corresponding to ionic migration through the catalyst layer. At lower frequencies (6kHz) the impedance plot curves up. This particular region symbolises the limiting capacitance and resistance of the CL.

Contents lists available at ScienceDirect

Journal of Power Sources

journal homepage: www.elsevier.com/locate/jpowsour

Experimental and numerical study on catalyst layer of polymer electrolyte membrane fuel cell prepared with diverse drying methods

Krishan Talukdar [a,*], Md Asaduzzaman Ripan [a], Thomas Jahnke [a], Pawel Gazdzicki [a], Tobias Morawietz [a,b], K. Andreas Friedrich [a,b]

[a] German Aerospace Center (DLR), Institute of Engineering Thermodynamics, Pfaffenwaldring 38-40, 70569, Stuttgart, Germany
[b] University of Stuttgart, Institute of Building Energetics, Thermal Engineering and Energy Storage (IGTE), Pfaffenwaldring 31, 70569, Stuttgart, Germany

HIGHLIGHTS

- Sublimation significantly improves catalyst layer porosity & ionomer distribution.
- Higher ECSA and improved diffusion properties enhance the cell performance.
- Simulation deduces an optimized oxygen transport resistance through ionomer film.
- Both experimental & simulation results acknowledge improvement due to sublimation.

GRAPHICAL ABSTRACT

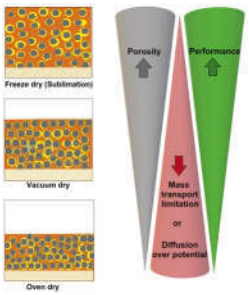

ARTICLE INFO

Keywords:
Freeze-drying
Sublimation
Microporous electrode
Mass transport
PEMFC
Drying catalyst layer

ABSTRACT

High manufacturing cost is a major challenge to commercialization of the polymer electrolyte membrane fuel cell (PEMFC) technology in high volume market. Catalyst layer (CL) of PEMFC should incorporate high effective porosity, electrochemically active surface-area, gas permeability, and favorable ionomer distribution. Drying of the CL is a very significant step of electrode fabrication, and determines most of the properties mentioned above, but is rarely a subject of investigation. From various possible drying processes of CL, freeze-drying shows some beneficial properties, such as higher porosity, better ionomer distribution, and reduces the mass transport resistance significantly by allowing more reactant gas into reactive interface. In this work, the influence of diverse drying techniques on the microstructure and performance is investigated. Complementarily, a transient 2D physical continuum-model is used to investigate the effect of the structural properties on cell performance of electrodes prepared with different drying methods. A sensitivity analysis has been also performed to determine the influence of individual parameters applied in the model. Both of the experimental and simulation results stress on the fact that the freeze-drying technique not only significantly enhances the oxygen transport properties through ionomer but also improves the porosity along with the tortuosity of the CL microstructure.

* Corresponding author.
E-mail address: krishan.talukdar@dlr.de (K. Talukdar).

https://doi.org/10.1016/j.jpowsour.2020.228169
Received 24 January 2020; Received in revised form 5 April 2020; Accepted 6 April 2020

1. Introduction

Our current energy-intensive lifestyles and population growth makes it difficult to ascertain energy supply and power generation capacity without unacceptable consequences for climate and pollution exposure. There is no doubt that polymer electrolyte membrane fuel cells (PEMFC) with their fast start-up time, high efficiency, sustained operational capacity at high power density, low weighted feature and smooth way of converting chemical energy into electrical energy can be considered as a readily available alternative power source to replace combustion engines running on fossil fuels. Apart from the high cost of the fuel cell stacks and insufficient durability under real conditions, the performance is a major concern especially at low Pt loadings. The microstructure of cathode CL must be carefully investigated considering the rate of irreversible losses in cell voltage is higher in the cathode CL whereas the rate is relatively smaller in the anode CL [1–3].

Microstructure of the catalyst layer and its porosity contributes significantly to the overall measured transport resistance. Excellent dispersion of catalyst particles, high surface area of catalyst support, homogeneously distributed thin ionomer films, favorable network between catalyst-ionomer facilitate better utilization of the catalyst and limit losses through mass and charge transport. Moreover, poor control of humidification within the membrane electrode assembly (MEA) can cause substantial loss in potential. Excess water can prevent reactant diffusion to the catalyst sites by flooding of the electrodes, gas diffusion backings, or flow channels if the water removal is inadequate. An optimized balance between porosity and thickness is required to improve the transport properties like mass transport diffusion electric as well as proton conductivity through the electrodes and precise water management [4–6]. Effective diffusivity, tortuosity, hydrophobicity and pore distribution through gas diffusion layer (GDL) along with micro porous layer (MPL) are involved in the relation between diffusion media and the performance of PEMFC. The diffusion media also play a significant role in water management with 2-phase liquid and vapor flow [7, 8].

Limited utilization of catalyst and endurance of CL is related to its heterogeneous microstructure. Carbon supported Pt and perflurosulfonic acid polymer (predominantly Nafion®) are widely used to fabricate efficient electrode [9–11]. The porous structure of catalyst layer exhibits a wide spectrum of length scales, which covers from 3 to 10 nm of carbon-supported catalyst particles to the Pt/VC agglomerates of 100–300 nm due to the binding effect of ionomer at meso-scale. Furthermore, Pt/VC aggregates are sized 1–3 μm at macro-scale, and finally the CL as porous medium exhibits a through-plane thickness of 5–50 μm. In addition to micro-pores ($\leq$2 nm), meso-pores of 2–20 nm exists within agglomerates. While the agglomerates coalesce into the aggregates, macro or secondary pores network is forged in the crevices. This heterogeneity of electrode porous structure causes imbalanced distribution of porosity and ionomer. Thus it affects both electron and proton conductivity. The interaction between the catalyst particles and ionomer plays a vital role to form efficient reactive interface which is also known as triple phase boundary (TPB). Notably, the different pore sizes and structures dominate the distribution of ionomer and diffusion co-efficient, which in turn influences the performance and durability of electrodes. Moreover, the materialized microstructure after coating and drying technique has a significant impact on water sorption and retention properties of CL which also affects critically into the performance and degradation of the electrode [12–16]. Hence, the importance of consolidating the FC performance with high microporosity or application of high-surface area supports has to be further investigated. CL fabrication is a very important process, and designing a low platinum loaded efficient electrode with durable performance requires a thin and porous coating, where the catalyst particles and ionomer are homogenously distributed with high surface area. The crucial factors of the fabrication technique are i) ink composition (catalyst/ionomer/solvent ratio), ii) coating techniques, and iii) drying of the suspension or ink (evaporation/sublimation of the solvent). The final process step, which is drying step, is immensely consequential to obtain a proper and optimized microstructure of the CL.

The paper focusses on properties of catalyst layer structure of PEM fuel cell (PEMFC). Specifically, the impact of the drying step of the catalyst layer (CL) preparation on structure of the CL is studied. Even though it has significant influence on the PEMFC performance, it has not yet fully received attention from the PEMFC community. We have used freeze–drying as a drying technique for low Pt loading electrode fabrication for PEMFC which has been reported recently [15]. The effect of higher porosity and better catalyst utilization in the catalytic layer are obvious from the former study, but the sensitivities of the drying procedure with regarding catalytic layer composition remain unclear. In this work, we have increased the catalyst loading as well as ionomer ratio to intensify the effect of freeze drying on performance as well as electric properties, and simulate the performance with a 2D model. The major characteristic of freeze-drying is the removal of solvent by sublimation from solids without sedimentation. Therefore, freeze-drying of CL prepared from suspension stimulates the porosity of the layer and the corresponding diffusivity. Also ionomer distribution is thought to be more homogeneous. Thickness of the catalyst layer can also be controlled by regulating the catalyst ink composition in this drying method [17]. In this way, it does not only enhance the effective porosity and the electrochemical surface area but also reduce the ionomer resistance inside the CL by distribution of homogeneous ionomer network [17–19]. Moreover, this technique can be adapted to other electrochemical devices also where porous network plays a significant role in the performance [15,20,21]. It is calculated by several groups that oxygen transport resistance through the ionomer coating on Pt/VC agglomerates is a dominant factor controlling rate determining step of the cathode CL activity at operating FC conditions. It is also proposed that limitations in the transport of oxygen through the ionomer can be offset by reducing the thickness of the ionomer film, and increasing the CL thickness. However, increasing the porosity of the catalyst layer by fabricating thicker catalyst layer and reducing the ionomer thickness decreases the effective proton conductance of the CL [22]. This results inadequate proton conductivity and non-uniform overpotentials in the CL leading to performance losses. Under this scenario, increasing the permeability of oxygen in the ionomer would serve an effective strategy for maintaining fuel cell performance under reduced Pt loading [23,24].

In this study, we have fabricated catalyst layers with same catalyst loading by means of screen printing technique. However, different drying methods (freeze drying, vacuum drying and oven drying) have been applied to the individual CLs to examine the effect of drying techniques into the microstructure of electrodes. Consequently, three different types of MEAs were produced consisting of different cathode CL thickness and architectures, which is reflected in their performance. To correlate their inherent microstructure yielded from distinctive drying methods, with their individual electrochemical properties, physical structural characterizations (focus ion beam scanning electron microscope and atomic force microscope) were also performed. Alongside the experimental works, numerical modeling and simulations are being conducted to get further insight into the performance limitations of the designed electrodes. So many PEMFC models are available now regarding the microstructural phenomenon of electrodes [25–28]. For these simulations a previously developed PEMFC performance model is used which is implemented in the DLR in-house modeling Framework NEOPARD-X based on Dumu^x [2,29]. This model is used to simulate the cell performance with the three different electrodes and to identify the origin of the improved performance using freeze–drying.

2. Materials and methods

2.1. Experimental method

The experimental section presents technical information on (i) ink

formulations, (ii) applied coating, (iii) drying techniques, (iv) physical characterization methods. (v) MEA fabrication, and (vi) electrochemical characterization methods.

2.1.1. Ink formulation

Since the research work is merely focused on the design and development of the cathode side electrode, a commercial GDE was used at the anode side for MEA fabrication. The materials, used for the ink formulation, are listed in Table 1. Three materials are fundamental to formulate a catalyst ink recipe: a catalyst with support, an ionomer and solvent(s). Different solvents such as Tetrahydrofuran (THF), n-butyl acetate, Ethylene glycol were tested before selecting Cyclohexanol as the most promising one to prepare suitable ink for screen-printing method [15].

The ratio between Nafion® ionomer and the total solid particles was kept as 40:60, which can be also expressed as Ionomer carbon ratio: 1.13. We have used higher ionomer-carbon ratio than our previous work [15] (0.69) due to an expected positive effect of freeze drying at higher ionomer contents. Since freeze drying leads to higher porosity we can expect that the catalytic layer can integrate more ionomer without pore blocking but with improved ionic conductivity. All the materials are added stepwise and mixed with ultra-sonication probe-sonication and ball mill. Detailed ink formulation step is discussed in "Supplementary materials".

2.1.2. Coating

Catalyst coated membrane (CCM) has been fabricated with screen printing technology. For screen-printing coatings, Nafion® XL membranes were cut into squares (6.5 cm × 6.5 cm) and coated in an Aurel 9000 screen-printer coupled with a Koenen polyester mesh with 25 cm^2 opening area (FL-190 10–20 μm EOM). The printing pressure was set to 2.0 N cm^{-2} and the substrate were kept in place with a vacuum positioning system. The loading of Pt in all CCMs is 0.3 ± 0.02 mg cm^{-2} in each CCM, which was controlled with 3 passes (pre-optimized) of simultaneous screen printing.

2.1.3. Drying techniques

After casting with screen-printing, three different drying techniques were applied to different electrodes. These techniques are explained elaborately in "Supplementary materials". The drying techniques are:

Oven drying: 70 °C for 12 h.

Vacuum drying: 70 °C with 6 mbar vacuum chamber pressure for 5 h.

Freeze drying: Cooling with liquid Nitrogen; 2 h sublimation time; secondary drying at 60 °C for 1 h [31,32].

2.1.4. Physical characterization of the CCMs

FIB-SEM: Samples prepared for Focus-Ion-Beam Scanning Electron Microscopy (FIB-SEM) were cut into 1 × 1 cm^2 from a CCM. After placing the sample inside the SEM sample holder, the fracture was made by emerging the sample in liquid Nitrogen. The measurements were carried out in 1.5 kV (electron high tension voltage) EHT (for recording image) with a 30 kV FIB probe (for ion milling). The thickness of each cut is 100 nm. A dual beam microscope integrates the features of a field emission scanning electron microscope (FESEM) with a focused Gallium ion beam (FIB) microscope (ZEISS AURIGA).

Table 1
Specification of the ink formulation for screen-printing coating method.

Platinum on Carbon black (40 wt% Pt/VC)	HiSPEC 4000 Powder	0.5 g	Ionomer to Catalyst powder (Pt/VC) mass ratio is 40:60
Ultra-Pure water HPLC grade	Alfa Aesar	3.0 g	[30] Ionomer to carbon (I/C) ratio is 1.13
Cyclohexanol 99%	Sigma-Aldrich	4.0 g	
10 wt% Solubilized Nafion®	Ion Power	3.4 g	

Atomic Force Microscopy: As AFM a Multimode 8 AFM (Bruker, Karlsruhe) was used. Conductive adhesive tape was used to glue the MEAs samples onto an AFM steel disc and to electrically connect the surface of the sample. Platinum/iridium coated AFM tips (NCHStPt, Nanoworld) were used in tapping mode with additional recorded nanomechanical information and electronic current which is averaged by a lock-in amplifier (PF-TUNA, Bruker). The 9 μm^2 measurements were recorded with 768 × 768 pixels at a scan rate of 0.326 Hz. Images with 4 μm^2 were cropped out of the measured areas. To measure the surface of the CL by AFM, we have prepared the CCM by screen printing over a membrane only with a single pass of catalyst suspension.

Scanning electron microscopy: To observe the cross section of MEAs with scanning electron microscopy (SEM), specimens were prepared by cutting a 1 × 1 cm^2 from MEAs. After placing the sample inside the SEM sample holder, the fractures were made by emerging the sample into liquid Nitrogen. The measurement was carried out in a Zeiss UltraPlus, providing an electron beam range of 2.0–10 kV that allows the analysis of the surface and the cross section of CL.

Porosity: To measure the surface area and porosity properties of the final catalyst powder, a volume of 5 mL of catalyst ink was placed inside three 10 mL glass beakers. The beakers were dried by (i) oven drying, (ii) vacuum drying, and (iii) freeze-drying respectively. 1 g of dried masses with an uncertainty of ± 10 mg (from each drying technique applied) were then dried again, under vacuum conditions at 60 °C for 3 h, with liquid nitrogen and positioned inside a Sorptomanic 1195 chamber. Brunauer–Emmett–Telle (BET) measurements were performed using the Dollimore/Heal method for surface area determination of the approached catalyst powder blended with ionomer [33]. We are using the adsorption isotherm for BET analysis [34]. Moreover, the porosity is measured from the hysteresis loop between adsorption and desorption curve. Moreover, the pore size distribution of the catalyst composite was also determined using mercury intrusion porosimetry (MIP) at 25 °C. Presently, we cannot measure the porosity with BET and MIT directly on the CCM due to insufficient reproducibility.

Additionally, the porosity of the catalyst layer in CCM was determined from the FIB-SEM images using MATLAB. The pixel count and the contrast of the FIB-SEM images were computed by image processing tool to determine the pore distribution. Pore sizes were calculated as the diameter of a circle with area equal to the detected area. Porosity was quantified by adding all the pore area dividing it by the total pixel count of the picture. It is probable that a systematic deviation between different methods to determine the value of porosity exist so that mainly a comparison between drying procedures with one method is discussed.

2.1.5. Fuel cell operation

2.1.5.1. MEA and cell preparation. The MEA was prepared by sandwiching the single side coated CCM with a GDL and a commercial GDE (Fuel Cell etc.) without hot-pressing. The GDL was placed on the coated side of the membrane, which is the cathode. The commercial GDE correspond to the anode electrode, which has a high loading to minimize their influence on performance, and is placed to the opposite side of the cathode. In between we used Nafion XL membrane to fabricate the MEAs.

Two gold coated stainless-still bipolar-plates were used as flow-field as well as current collector. The area of the flow field is 25 cm^2. The GDLs and GDEs were cut exactly same size of the active area, which means 25 cm^2. Single channel serpentine flow field was used with 1 mm channel width, 1 mm rib width and 0.8 mm depth of channel. 4 pieces 7 mm screws were used with 3 Nm torque. It is very important to set appropriate compressive stress to the cell to balance the conflicting demands of mitigating gas leaks and decreasing contact resistance without damaging the porous components so that optimal performance is obtained. The amount of compression on the GDL affects the contact resistance, the GDL porosity, and the fraction of the pores occupied by

liquid water, which, in turn, affect the performance of a PEM fuel cell [35–38]. In our experiment, we have 17–19 % compression in gas diffusion media while operating the cell in bipolar plate after clamping. The materials and the operating conditions are stated in Table 2 and Table 3 respectively.

2.1.5.2. Fuel cell testing condition. MEAs for single cell characterization were tested in an in-house developed test bench. In our test bench, we have two bubbler humidifiers for both anode and cathode gas inlet; moreover the pressure of the system is regulated after the cell. We have very minute pressure drop before the cell (anode: 5 mbar and cathode: 10 mbar). The operating conditions of the experiment are stated in Table 3. We started to test each MEA with 100% RH (relative humidity) and subsequently with 70% RH. The stoichiometry of cathode and anode were slightly increased to 2.5 and 1.7 with regard to former studies (where 2 and 1.5 was used) to avoid the flooding issue caused by higher ionomer content. 1.5 bar absolute pressure is maintained in fuel cell experiments. It is expected that this changes will lead to an intensification of the performances of the MEAs prepared by different drying methods.

2.1.6. Electrochemical characterization of the CCMs

Break-in and polarization curve: Each MEA was conditioned for 6 h in 250, 500 and 1000 mA cm^{-2} current density gradually. Break-in step is considered completed if the voltage and current are stable (where the voltage change is lower than 10 mV/hr). Polarization curve was recorded using a Zentro Elektrik electrical load in galvanostatic mode. The cell voltage was monitored as function of the current density with a dwell time of 3 min and with increments of 25 mA cm^{-2} (range: 0–100 mA cm^{-2}) followed by steps of 100 mA cm^{-2} (range: 100 mA cm^{-2} to until cell voltage drops to ~200 mV).

Electrochemical impedance spectroscopy (EIS): At normal operating condition, EIS was performed by means of galvanostatic mode using Zahner IM6 potentiostat. EIS spectra were recorded at 100 mA cm^{-2}, 500 mA cm^{-2} and 1000 mA cm^{-2} in the frequency range 100 mHz - 100 kHz with a perturbation amplitude of 5–25 mA cm^{-2}, respectively. These measurements were done at both 100% and 70% relative humidity with a stoichiometric flow of H_2 and air. Additionally, ionic conductivity (IC) through the CL was measured at a potential of 1 V (potentiostatic mode) [39], using 100% humidified H_2 and N_2 gases passing through the anode and cathode, respectively (both 100 mL min^{-1}) with a constant flow. Ionic conductivity was measured also in 100% RH for all MEAs. The applied frequency range was 500 mHz −100 kHz with a perturbation amplitude of 10 mV [40]. Impedance spectra were measured with SIM function of the Zahner software (Thales). All the EIS measurement was performed at 80 °C and 1.5 bar pressure. After adjusting the voltage or current, we have waited 10 min to perform EIS for ensuring coherent response. Moreover, 3 sets of spectra were recorded to verify the reproducibility of the EIS.

Moreover, Cyclic voltammetry (CV) of the cathode CL was measured in the potential range from 0.06 to 1 V at 80 °C cell temperature using fully humidified (100% RH) H_2 and N_2 gases passing through the anode and cathode component, respectively with a constant flow rates of both 100 mL min^{-1} [41,42]. Three consecutive CVs were recorded each time and the 2nd CV was considered. For each MEA two sets of CV measurement were performed, and the presented CV is the average of subsequent 2nd CVs from each set. H_2 desorption peak were considered to calculate the Pt ECSA of the cathode electrode [43].

Table 2
Specification of the materials used to fabricate MEAs for single cell test. Ink formulation for screen-printing, and components to assemble.

Material Components	Supplier	Specifications	Function
Nafion® XL	DuPont	27.94 μm thickness	Electrolyte, membrane
Commercial gas diffusion electrode	Fuel Cells Etc.	0.3 mg cm^{-2} Pt loading	Anode electrode and GDL
Carbon Paper GDL	SGL Carbon GmbH	25 BC non-woven 235 μm thickness	Gas diffusion layer at the cathode side
Ice cube 35 FC-PO 100 Gaskets	QuinTech	2× Frame (1.3 cm width), 5 × 5 cm^2, 0.5 mm thickness	Sealing
Bipolar plates	DLR	Gold coated SS single channel serpentine flow filed	Cell assembly, Gas distribution
Platinum on Carbon (40 wt% Pt/VC)	HiSPEC 4000 Powder	Vulcan carbon support	Cathode Catalyst
Ultra-Pure water HPLC grade	Alfa Aesar		Solvent for cathode catalyst ink
Cyclohexanol 99%	Sigma-Aldrich		Solvent for cathode catalyst ink
10 wt% Solubilized Nafion®	Ion Power	Dispersed in water Eq. wt 1100	Ionomer of the cathode catalyst layer

Table 3
Operating parameters for single cell test bench and the model simulator, (*) the minimum flow was maintained for the test station was for the current density 100 mA cm^{-2}.

Parameters	Symbol	100% RH	70% RH
Anode stoichiometry* (H_2)	λ_{an}	1.8	1.8
Cathode stoichiometry* (air)	λ_{ca}	2.7	2.7
Cell temperature	T_{cell}	80 °C	80 °C
Humidifier temperature	$T_{bubbler}$	80 °C	70 °C
Anode outlet pressure (absolute)	P_{an}	1.5 bar	1.5 bar
Cathode outlet pressure (absolute)	P_{ca}	1.5 bar	1.5 bar

2.2. Numerical method

The physical model, which has been used to conduct the research work, is an in-house model implemented in the NEOPARD-X framework [29]. This model includes:

- A 2D along-the-channel geometry with nine spatially resolved layers (anode and cathode channels, GDLs, MPLs, CLs and the membrane)
- A multiphase Darcy model for the two-phase, multicomponent transport within the porous electrodes
- Butler-Volmer kinetics for the ORR and HOR reactions
- Energy transport through all layers of the cell
- A membrane model including coupled water and proton transport as well as transport of dissolved gas species
- Proton transport through the ionomer within the CLs and electron transport through the support phase of the porous electrodes
- An ionomer film model describing the oxygen transport from the gas phase through the ionomer film to the cathode catalyst

All corresponding model equations are discussed in detail in Ref. [29]. In the following, only the modeling aspects most relevant for this work are summarized. Diffusion in the porous electrode is described by the Stefan-Maxwell equation [44].

$$\nabla x_\alpha^i = \sum_{j=1}^{N} \frac{C_\alpha^i C_\alpha^j}{C_\alpha^2 D_{eff,\alpha}^i} \left(\frac{d_\alpha^j}{C_\alpha^j} - \frac{d_\alpha^i}{C_\alpha^i} \right), \quad (1)$$

where C_α^i and C_α^j are the molar concentration of species i and j in phase α, and consecutively d_α^i and d_α^j represent diffusive flux density of species i and j in phase α. $D_{eff,\alpha}^\kappa$ is the effective diffusion coefficient, which is

calculated based on a binary diffusion coefficient, D_{α}^{κ}. The effect of porous media is taken into account by Bruggemann-correction of the diffusion coefficients

$$D_{pm,\alpha}^{\kappa} = (\varphi S_{\alpha})^{1.5} D_{\alpha}^{\kappa}, \quad (2)$$

where φ is the porosity and S_{α} is the saturation of phase α. In the gas phase, Knudsen diffusion occurs and $D_{eff,\alpha}^{\kappa}$ is calculated with a Bosanquet approximation,

$$D_{eff,g}^{\kappa} = \left(\frac{1}{D_{pm,g}^{\kappa}} + \frac{1}{D_{Knudsen,g}^{\kappa}} \right)^{-1} \quad (3)$$

$$\text{with } D_{Knudsen,g}^{\kappa} = r_{pore} \frac{2}{3} \sqrt{\frac{8RT}{\pi M^{\kappa}}} \quad (4)$$

here, $D_{Knudsen,g}^{\kappa}$ represents the Knudsen diffusion coefficient of component κ in gas phase, M^{κ} denotes the molar mass of component κ; R, T and r_{pore} express ideal gas constant, temperature and pore radius respectively. Proton transport through the CL is described by Ohm's law

$$\Psi^{H^+} = -\sigma_{eff}^{H^+} \nabla \Phi_{ion} \quad (5)$$

The amount of water activity plays a vital role in proton conductivity. A material-dependent empirical relation has been implemented to describe the influence of water activity on proton conductivity $\sigma_{eff,CL}^{H^+}$. An exponential dependence on the water activity [45] has been defined as,

$$\sigma_{eff,CL}^{H^+}(a^{H_2O}) = A \times \exp(B a^{H_2O}) \quad (6)$$

where A and B are fitting parameters. The volumetric reaction rate of Oxygen Reduction Reaction (ORR) is calculated using an ionomer film model

$$r^{ORR} = \frac{-R\kappa^{ORR} + \sqrt{4ECSA_{eff}^2 n^2 F^2 c_g^{O_2} + R^2 (\kappa^{ORR})^2}}{2\ n\ F\ ECSA_{eff}} \kappa^{ORR} \quad (7)$$

r^{ORR} = Volumetric reaction rate of ORR, R = Lumped ionomer resistance, κ^{ORR} = Rate constant of ORR, $ECSA_{eff}$ = Effective electrochemically active surface area n = Number of transferred electrons, F = Faraday's constant, $c_g^{O_2}$ = Molar concentration of oxygen. This model takes into account the oxygen transport resistance through the ionomer film,

$$R = R_{diff} + R_{int} \quad (8)$$

which consists of the resistance due to the oxygen diffusion through the ionomer film

$$R_{diff} = \frac{\delta_{ion}}{D_{ion}} \quad (9)$$

and the water activity dependent interfacial resistance which is described by the empirical relation

$$R_{int} = C\ \exp(D a^{H_2O}). \quad (10)$$

All the parameters applied in this model as well as relevant to this study are mentioned in Tables 4 and 5. Additionaly, initial conditions at the interfaces and in the electrodes are provided in the "Supplementary materials".

Table 4
The experimental parameters utilized in the numerical model.

	CCL Thickness, m	ECSA, $m^2\ g^{-1}$	Porosity, %
Freeze drying	14.58×10^{-6}	29.16	24
Vacuum drying	12.67×10^{-6}	20.28	21
Oven drying	11×10^{-6}	16.61	18

Table 5
The model parameters used in the numerical analysis.

MPL (Permeability, porosity and pore diameter)	
$K_{MPL} = 4.0 \times 10^{-15}$ [m^2]	
$\varnothing_{MPL} = 0.75$	
$r_{pore,\ MPL} = 45 \times 10^{-9}$ [m]	
Thermal conductivity(GDL, MPL, CL)	
$\lambda_{GDL} = 0.60$ [$Wm^{-1}k^{-1}$]	
$\lambda_{MPL} = 0.33$ [$Wm^{-1}k^{-1}$]	
$\lambda_{CL} = 0.3$ [$Wm^{-1}k^{-1}$]	
Exchange current density (ORR)	
$i_{ref}^{0} = 1.0e^{-4}$ [A m^{-2}]	
CL conductivity	
FD and VD	OD
A = 1.0×10^{-2} [S m^{-1}]	A = 0.80×10^{-2} [S m^{-1}]
B = 3.0	B = 3.0
Ionomer film resistance to oxygen transport	
FD and VD	OD
C = 2.5×10^{5} [s m^{-1}]	C = 2.2648×10^{4} [s m^{-1}]
D = 5.0	D = −1.5

3. Results and discussion

3.1. Experimental results

An experimental study was performed to generate sufficient data to characterize the effect of different drying techniques on the micro and macro structure of the electrode to validate the numerical model. Porosimetry study of the catalyst powder/ionomer derived from three different drying techniques but identical suspension was characterized, and demonstrated in Fig. 1a). However, the unit for the BET surface area and total pore volume are normalized to mass of total powder (Pt/VC/Nafion®). According to the BET analysis, freeze drying of the catalyst suspension yields more effective surface area than vacuum drying and oven drying. Since sublimation is the process characteristics of the freeze-drying technique, the development of larger pores is associated to the transition of solid solvent crystals directly to the vapor state, and the result is a wider network of pores. This behavior is also visible in Fig. 1a), where the calculated average pore diameter of the freeze-dried sample is higher than the others. It is assumed that the pore size and pore volume of the cathode catalyst layer increases and the over-potential associated to diffusion of reactants is likely reduced. This reduction of diffusion over-potential is in compliance with the better cell performances as verified by Yim et al. [46]. Moreover, Fischer et al. stated back on 1998 that the additional porosity across the thin film electrodes could also improve the cathode performance, in particular with air as oxidant [47]. Purple bars (3rd column) of the Fig. 1a) demonstrate the numerical value of the average pore diameter of the Pt/VC/Nafion® after drying which also follows the same trend. Therefore, it is evident that the drying step does affect the final micro/macro structure of the catalyst layer and consequently the performance of PEM fuel cell.

All the single cell tests were conducted in a 25 cm^2 active area cell and an in-house built fuel cell test bench. Three sets of experiments were conducted and an average has been used to make the figure of merits. Three CCMs produced via screen-printing technique, were physically and electrochemically characterized. A quantitative performance analysis of PEMFC is characterized by a polarization curve or I–V (current voltage characteristics) curve. The polarization curve is plotted with the error bars which were calculated from the standard deviation of the 3 independent measurements [36,48]. Please note that these I–V curves

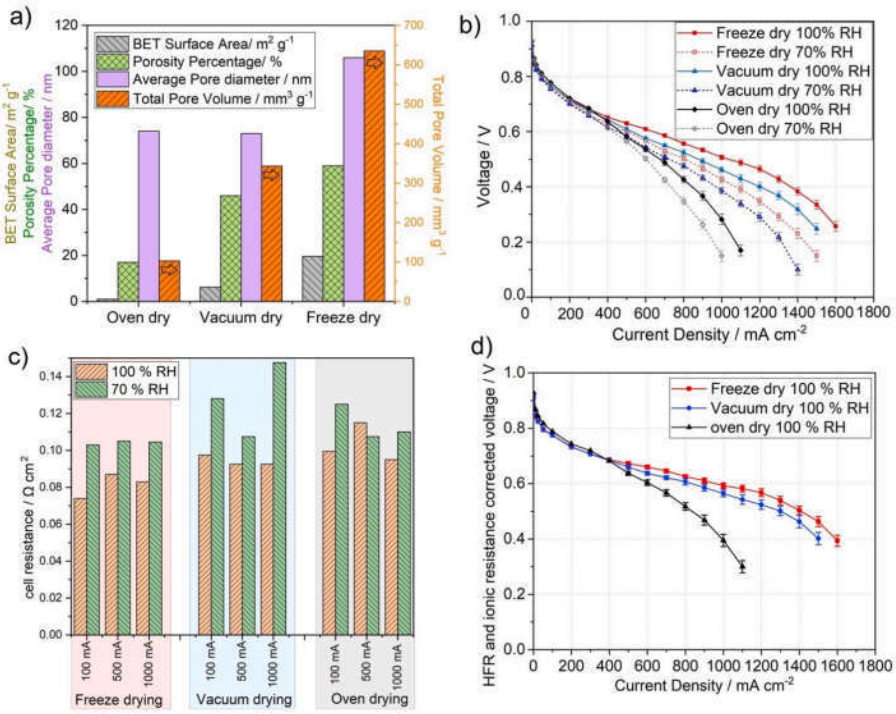

Fig. 1. a) Morphological characterization of the free standing (non-coated) Pt/VC/Nafion® powder shaped by oven, vacuum and freeze drying method. Left-axis exhibits parameters of BET surface area (Grey), porosity percentage (Green), average pore diameter (Purple) and right-axis graph exhibits parameters of total pore volume (orange); H_2/air polarization curves of MEAs with freeze, vacuum and oven dried screen-printed cathode catalyst layers with 0.3 mg cm^{-2} Pt loading at 100% RH (relative humidity) and 70% RH. The temperature was 80 °C with stoichiometric flow and the back pressure was maintained 1.5 bar for both anode and cathode; c) cell ohmic resistance or high frequency resistance (HFR) of three MEAs in different humidification; d) polarization curves with HFR and ionic resistance corrected voltage of the 3 different MEAs in 100% RH and same condition as Fig. 1b). (For interpretation of the references to color in this figure legend, the reader is referred to the Web version of this article.)

are not performed under differential conditions that mean that heterogeneous conditions leads to lower overall performances compared to measurements in differential cells. Fig. 1b) illustrates a relative humidity dependence I–V curve comparison of the MEAs fabricated with three different drying conditions. Each MEA has been tested at 100% RH along with 70% RH. Moreover, Fig. 1d) represents the polarization curves with HFR and ionic resistance (R_{ion}) corrected voltage of the 3 different MEAs in 100% RH and same condition as Fig. 1b). The HRF and R_{ion} corrected voltage $U_{cell,\ corr}(j) = U_{cell}(j) + (HFR + R_{ion})*j$ is calculated using the average HFR obtained from measured data at 100 mA cm^{-2}, 500 mA cm^{-2} and 1000 mA cm^{-2} and constant values of R_{ion} (see Fig. 2d). The open circuit voltage is commonly influenced by electrode electrochemical activity as well as the exchange current density. It is noticeable in Fig. 1b) that the open circuit voltage (OCV) does not

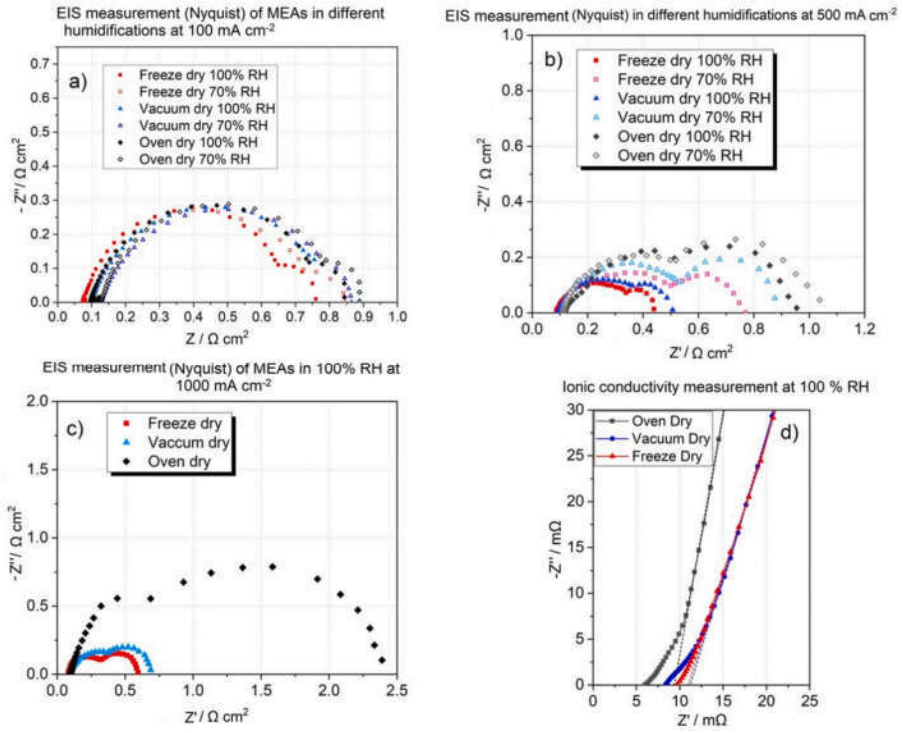

Fig. 2. Nyquist Impedance spectra a) 100 mA cm^{-2} at 100% RH and 70% RH for three different CCMs dried in three different ways, b) 500 mA cm^{-2} at 100% RH and 70% RH, c) at 1000 mA cm^{-2} only at 100% RH, d) the ionic impedance measurement of 25 cm^2 MEAs at 100% RH (not area normalized).

depend on the tested RH conditions and the drying technique. This is a consequence of the application of the same catalyst ink and coating technique during the formulation of CCMs. Moreover, the kinetics, the contact resistance, the partial pressure of the reactant gasses and the operating conditions were also indistinguishable in the I–V polarization curve in all cases. The variance starts at current densities >400 mA cm^{-2}. Moreover, diffusion loss or mass transfer limitation plays a major role at higher current density. Improved porosity and homogeneous distribution of ionomer network (will be shown in Fig. 3) facilitate the diffusion properties in the reactive interphase [15,49], which in turn reduces the concentration loss. Apparently, at higher current density the voltage loss of oven dried MEA is greater than vacuum dried MEA, and decreases to the lowest in case of freeze dried MEA. The aforementioned phenomenon is supported by a sharp drop of performance in oven dried MEA comparing to the others. The freeze dried MEA shows considerably superior performance; whereas vacuum dried MEA shows medium performance. The poor performance of the oven dried MEA is due to the higher transport limitation and the lower compression capacity of the catalyst layer. This trend is justifiable for both of the relative humidity: RH 100% and 70%. Considering that 100% RH provides more humidity into the cell, and as a consequence yields higher power due to increase proton conductivity of the ionomer leading to lower ohmic resistance of the MEA. The effect of lower relative humidity on performance is more significant for vacuum dried and freeze dried MEA compared to the oven dried MEA. We speculate that this phenomenon is due to the higher porosity of vacuum dried and freeze dried catalyst layer, which leads to a better distribution of ionomer with higher surfaces areas exposed to gas phase. With increasing porosity we expect a simultaneous decrease of ionomer film thickness. Hence, at lower RH the water content of the thinner ionomer film decreases compared to the thicker ionomer film with a concurrent loss of conductivity. This circumstance lowers the performance at 70% RH in freeze and vacuum dried MEA. Fig. 1c) represents the cell ohmic resistance or high frequency resistance (HFR) of three MEAs in different humidification. 70% RH shows higher resistance comparing to 100% RH due to the lack of water content in the membrane and electrode assembly, which in turn reduce the ionic conductivity. As will be shown next, it is very likely that also a higher transport resistance arises for thin ionomer films at reduced humidity which exacerbates performance losses at higher current densities.

A qualitative and quantitative measurement was performed by the Electrochemical Impedance Spectroscopy (EIS). Through the Nyquist plot, individual contributions to the voltage loss are attributed to the particular time constants, which are finally represented according to the distinctive arcs (overlapped semicircles in practice) [50]. High frequency resistance, which is originated from the proton conductivity of the membrane and the resistance (HFR) of the total system, is related to the left side intercepts of the horizontal axis in the Nyquist plot. As all the external parameter of the MEAs are identical, the HFR or the ohmic resistance of the all the MEAs are similar. At the medium frequency region, reaction kinetics contributes, and the first semicircle is attributed to the cathode charge transfer resistance. Fig. 2a) and b) shows a Nyquist plot of the three MEAs at 100 mA cm^{-2} and 500 mA cm^{-2}, respectively, both in 100% and 70% relative humidity.

Additionally, Fig. 2c) displays the Nyquist impedance plot at 1000 mA cm^{-2} only in 100% RH. As the first semicircle is associated with cathode kinetics, the impedance demonstrated in Fig. 2a) and b) and 2c) are mainly caused by the charge transfer. From the Fig. 2a) we can see more or less identical charge transport behavior, which is also consistent with the polarization curve in Fig. 1a). At low current density, the kinetic overpotential of all the MEAs exhibit similar behavior as they were fabricated with same catalyst loading. However, with increasing current density the behavior changes and the process associated to charge transfer for freeze dried and vacuum dried MEA shows smaller semicircles as compared to oven dried MEA. The charge transfer resistance in Fig. 2b) and c) of both freeze dried as well as vacuum dried MEAs is relatively comparable. Since, in both cases we see more or less similar type of semi-circle for freeze dried and vacuum dried MEA. On the contrary, oven dried MEA carries much higher charge transport limitation with a much bigger (first) semicircle in both current densities that can be also deduced from the current voltage curve in Fig. 1b). Besides,

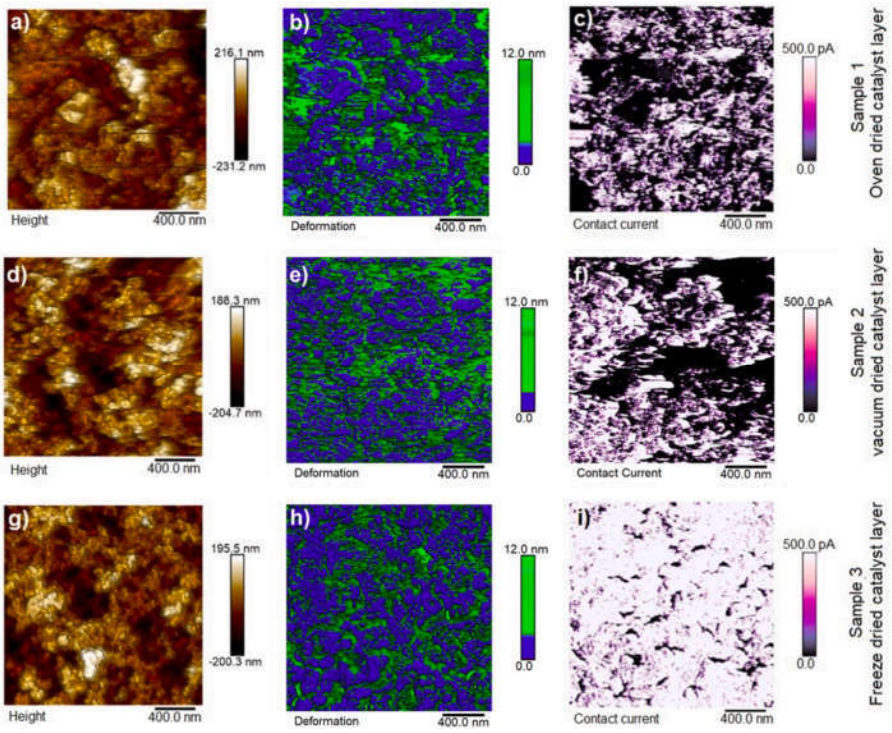

Fig. 3. AFM analysis: a/d/g) height/topography measurement of three different CL, b/e/h) deformation measurement to ionomer detection, c/f/i) electronic current measurement from three different CL by contact current.

due to the significant volume of water generates in the cathode electrode at high current density, significant amount of pores of the CL might get blocked. As a result, without sufficiently available pores, the diffusion of the reactants might get hindered if the water removal is not efficient. Therefore, at higher current densities, optimized porosity and effective water management are the key to minimize mass-transport losses [51]. It is very apparent from the Fig. 2b) and c) that oven dried MEA results in a significant mass transport loss presumably due to less porosity and flooding of water, which is demonstrated by the large second semicircle in all the cases. However, the freeze dried MEA and vacuum dried MEA show a moderate mass transport loss owing to its higher porosity and better ionomer network in the catalyst layer [52]. Bigger pore volume and homogeneous ionomer distribution make an efficient water management through the CL, and it reflects over the smaller diffusion semicircle as well as improved performance of freeze dried MEA at high current density. However, it is interesting to note that even for the MEAs with superior porosity the mass transport limitations are exacerbated significantly when reducing humidity. Since it is unlikely that ionic conductivity influences mass transport, this observation is indicative of higher oxygen transport resistance through the ionomer films. Gas transport through membranes is well-known to depend on the water content of the membranes. The significant influence of humidity on the mass transport related process indicates that the ionomer in the catalytic layer shows a similar behavior.

The ionic conductivity measurements of the catalytic layer with H_2 and N_2 (cathode) flow is shown in Fig. 2d) at 100% relative humidity. This EIS measurement is indicative of the proton conductivity through the cathode catalyst layer assuming a transmission line model. Protonic resistance, R_{ionic}, through three differently dried CCLs can be determined from the magnitude of the Warburg-like region (45°) projected onto the real impedance (Z') axis (=R_{ionic}/3) [53], which were portrayed by dotted lines in Fig. 2d). The lowest value of the protonic resistance across the CCL is obtained for the freeze dried electrode (R_{ionic} 4.08 mΩ). On the contrary, the highest protonic resistance is calculated from oven drying CCL (R_{ionic} 9.6 mΩ), followed by the vacuum dried CCL (R_{ionic} 8.4 mΩ). These values are interpreted as signaling a better ionomer distribution associated also to higher performance of the MEAs even though they have lower ECSA (see Fig. 5b). Area normalized values for oven dried, vacuum dried and freeze dried electrodes are 0.24, 0.21 and 0.1 Ω cm^2 respectively.

The AFM analysis of the different drying techniques on the surface of the CL is shown in Fig. 3. Measurements were conducted with PeakForce Tapping mode with additional recorded current. With this AFM technique one can get the topographical information along with nanoelectrics and nanomechanical properties. The height/topography, deformation and electronic current studies are shown in Fig. 3, whereas a stiffness property is shown in SI Fig. 1. The height model from AFM measurements gives the topography of the samples including the roughness and an impression of the porosity. The stiffness, adhesion (not shown) and deformation information provides clear contrast between Pt/VC and the ionomer in the catalyst layer in Fig. 3 b), e), h). The electronic current gives also an insight into the conductive network formed in Fig. 3 c), f), i). Additionally, thick ionomer layers can be detected due to no electronic current. Fig. 3 a), d) and g) are exhibiting the topographic properties by evaluating the vertical movement of the AFM tip. From the AFM height measurement, oven dried CL illustrates a high amount of catalyst particle agglomerates as visible in the topographic images in Fig. 3-a, whereas vacuum and freeze drying shows better dispersion of catalyst comparing to oven drying in Fig. 3 d), g). Hence, Fig. 3 d), g) suggests a better distribution of particles due to vacuum drying and freeze drying (well distribution of bright color). Nevertheless, integrating the information from adhesion, deformation and current measurement, we can suggest that the freeze dried CL demonstrates smaller catalyst aggregates and their well distribution over the surface. Therefore, even though Sample 2 and 3 look similar from topographic point of view in Fig. 3 d) and g), their conductivity differs significantly as shown by the right hand panels. The adhesion and deformation study provides similar behavior of ionomer distribution; however, in this article deformation is demonstrated due to having better contrast.

The deformation information along with the electronic current also depicts a high amount of ionomer agglomeration visible in green (high deformation) and no electronic current areas (dark purple). The opposite in the data is true for the catalyst. The vacuum dried CL shows a high amount of ionomer agglomeration as best seen in the electronic current channel, but as well in the stiffness (SI Fig. 1), and the deformation. Nevertheless, the ionomer structure in the non-agglomerate areas are more homogeneous than in oven dried CL. The large ionomer areas might also be a part of the exposed membrane as the electrode was kept very thin. As appeared in the Fig. 3g), the freeze dried CL (sample 3) has the most homogeneous structure with highest nanoporosity and lowest agglomeration as visible in the height channel. The ionomer is well distributed between the catalyst particles. This can be seen best in the deformation channel (Fig. 3h) between the green ionomer and the blue catalyst particles. In agreement with Fig. 3i), the ionomer layer thickness might be very small as most of the area is electronically conductive. The force (Peakforce) was kept constant for all measurements.

Three material dependent properties have been determined experimentally to understand the origin of the performance differences for the three drying techniques. The cross-sectional SEM images captured to measure the thickness of the dry electrodes are demonstrated in Fig. 4.

Pt ECSA was determined from the H_2 desorption signal from CV, while the porosity was measured by FIB-SEM. A 3D reconstruction of the catalyst layer microstructure has been obtained from a stack of SEM images, each image taken after 100 nm cut by the ion beam. An in-house MATLAB image processing tool was used to calculate the porosity and the pore size distribution from the images by calculating the difference in contrast and the resolution of the image. The porosity of the BET measurement is derived from the powder. However, the porosity will change upon coating the powder on a membrane. Therefore, we tried to implement the more realistic porosity value, and used the porosity data derived from the FIB-SEM analysis of the CCM. Porosity measurement of CL in CCM by BET/MIP (mercrury intrusion porosimetry) has been performed and reported recently [34,54], however we are still trying to adapt the CCM porosity measurement technique by BET/MIP in our facility. Fig. 5a) shows the catalyst layer captured by FIB-SEM, and the area of the pores which we counted to measure the porosity and pore diameter distribution. We observe from Fig. 5a) that the numerical

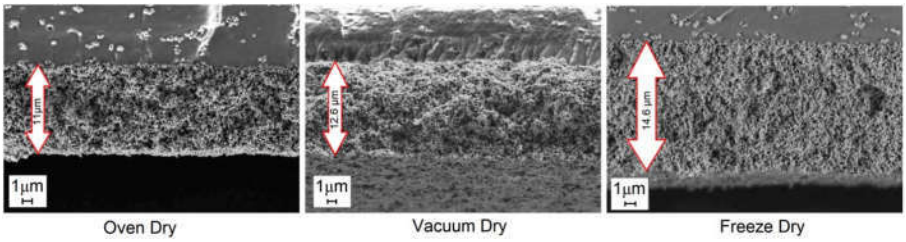

Fig. 4. The SEM images from cross-sections of MEAs prepared with different drying techniques.

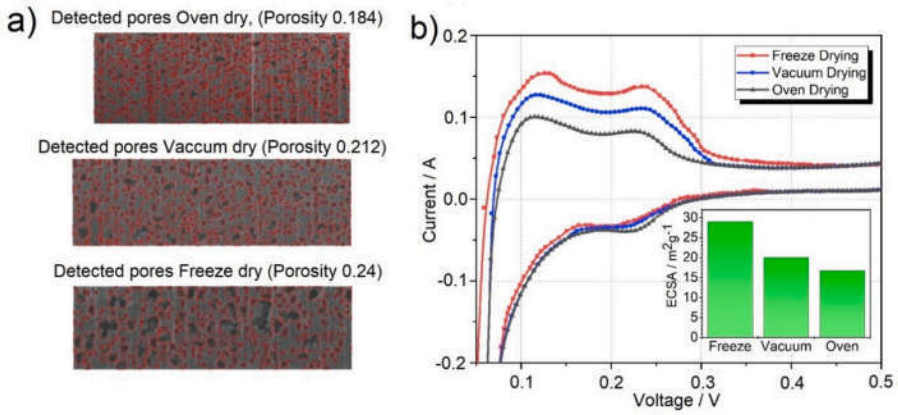

Fig. 5. a) FIB-SEM analysis along with MATLAB image processing applied on the image to measure porosity and pore size distribution, b) Cyclic voltammetry measurement of three different drying techniques including the Pt ECSA values (inset of b). These CLs are compressed to fabricate MEAs.

porosity of the catalyst layer is also increased from oven dry to freeze dry. The aforementioned values of porosity are very much compliant with the CV measurement of the MEAs. We can see from the Fig. 5b) that the freeze dried catalyst layer shows more electrochemically active surface area than the other MEAs. As CL prepared in this study has higher Nafion content when in fact higher ionomer content with inhomogeneous thickness distribution causes some of the Pt particle inaccessible. Therefore the Pt ECSA is smaller than the commonly used CL. A bar chart of calculated Pt ECSA (determined from desorption peak) values is also included as an inset image of Fig. 5b). In this article, we have measured lower ECSA value than expected, and we speculate that the reason is the higher ionomer content in the catalyst layer used compared to usual preparations. Vulcan is one of the carbon supports for Pt catalyst with reduced micro and meso porosity. Recent publications have shown that the ionomer does not penetrate the micro pores of carbon support; instead in catalyst layer ionomer covers mainly the outside of the carbon support and the aggregates [55,56]. Increasing ionomer content probably increases Pt coverage which has been shown to reduce Pt activity. It is therefore, also plausible that ECSA is reduced, but we have to further analyze the ECSA dependence on ionomer content. Higher surface area of catalyst particles and porosity are responsible for the higher ECSA value of freeze dried MEA. However, vacuum dried MEA shows a moderate ECSA value which is in between oven and freeze drying. The trend of the porosity, CV and ECSA also agrees with the performance of each MEA.

3.2. Simulation results

The main focus of the simulation work is to better understand the origin of the experimentally observed differences in performance for the three CL materials and to explore the variation of performances due to different parameters such as porosity, ECSA and CL's thickness which are likely to have important contributions on the performances. The basic experimental parameters used in numerical model are referred in Table 4.

To further investigate the origin of the different performance of the three catalyst layers we have simulated polarization curves at 100% RH and 70% RH with the physical model described in the numerical part of the experimental and method section.

The measured values for CL thickness, porosity and ECSA for each material have been used in the respective simulations. The only significant fitting parameters used are the ionic conductivity of the CL and the ionomer film resistance, which are assumed to vary depending on the drying technique due to changes in the microstructure of the CLs. Along with porosity, permeability, CL and ionomer conductivity, some modified spatial and electrochemical parameters, which are also used in the model are mentioned in Table 5. For all other model parameter the values reported in Ref. [29] have been used.

Fig. 6 shows the comparison between the simulated and experimentally measured polarization curves. A good agreement is obtained for all the cases, independently to the relative humidity and drying conditions. Interestingly, the same fitting parameters for ionic conductivity and ionomer film resistance were obtained for freeze drying and vacuum drying. This demonstrates that the difference in performance between these two drying techniques can be explained solely by the difference in CL thickness, porosity and ECSA. Instead, for oven drying a significantly higher ionomer film resistance and lower ionic conductivity was obtained which indicates a less favorable ionomer distribution within the CL in this case.

The model also allows studying the local conditions inside cell. Fig. 7a) highlights the distribution of ionic conductivity throughout the catalyst layer. The membrane is on the left and the gas inlet on the top, as shown in the schematic diagram of the model geometry. For visualization purposes the images are scaled by a factor of 10^4 in x-direction. Compared to the freeze dried and vacuum dried catalyst layers, the oven dried MEA yields a poor ionic conductivity in both humidity condition. The drying out of ionomer near the inlet reduces the ionic conductivity for all MEA simulations at 70% humidification. To get further insight into the difference between the three catalyst layers, Fig. 7b) shows the simulated spatial distribution of the ORR reaction rate within the cathode CL. As one can see, for 100% RH in case of freeze drying the higher ECSA allows for a higher reaction rate close to the membrane. Instead, for VD and especially for OD the ORR is distributed more homogeneously over the thickness of the CL which introduces additional performance losses due to the low ionic conductivity of the CL. The same holds true for 70% RH. The main difference is that in case of FD and VD the highest reaction rate shifts from the inlet towards the middle of the cell due to drying out of the ionomer close to the inlet. Instead for OD the highest reaction rate remains close to the inlet, probably due to the lower porosity which reduces the drying out effect.

To perform a sensitivity analysis of the fitting parameter fitting parameters have been altered. The goal is to investigate how the individual changed parameters influence the fitting as well as outcome of the simulation. To investigate the effect of the three material parameters CL thickness, porosity, ECSA as well as two fitting parameters the ionomer film resistance, ionic conductivity, a sensitivity analysis has been performed in which all of the parameters are varied by ±25%. Fig. 8 shows the sensitivity analysis effect on the parameters at a current density of 1500 mA cm^{-2}. It can be seen that the ECSA strongly affects the performance especially at 70% RH, while the effect of porosity and CL thickness is minor. Interestingly, a lower porosity leads to slightly lower performance at 100% RH but higher performance at 70% RH. This can

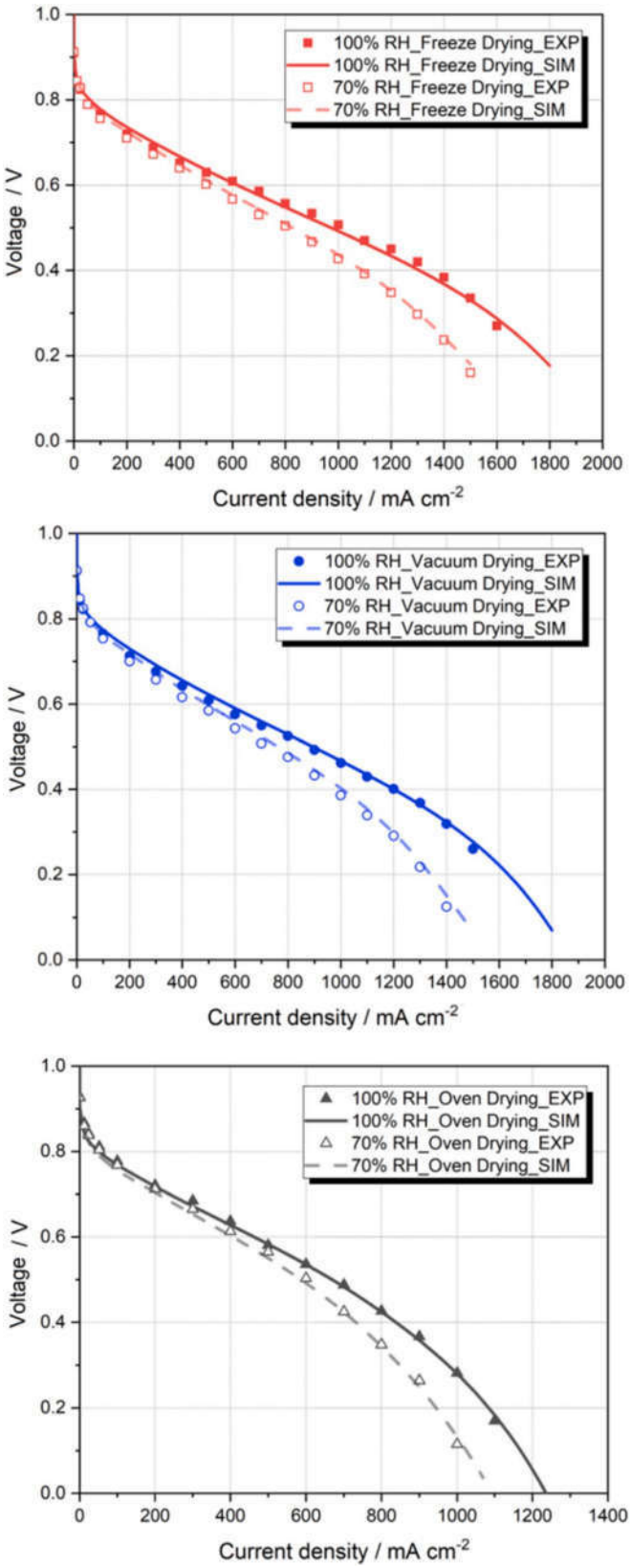

Fig. 6. Fitting of the simulation and experimental polarization curves for three different drying techniques in different relative humidity.

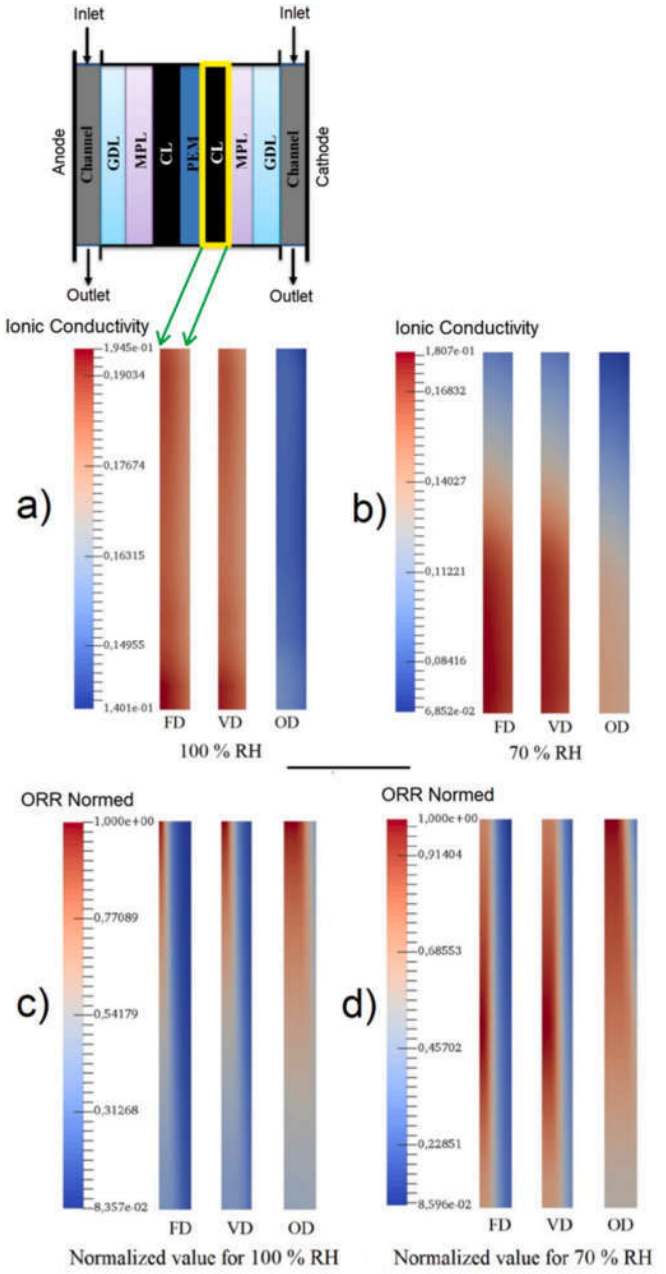

Fig. 7. a-b) Ionic conductivity (S m^{-1}) in CLs due to Freeze drying (FD), Vacuum drying (VD) and Oven drying (OD) techniques in different relative humidity; c-d) ORR rate (A m^{-3}) at 1500 mA cm^{-2} in cathode CLs for freeze drying (FD), vacuum drying (VD) and oven drying (OD) technique for different relative humidity. Normalized values have been plotted to avoid the residual effect of the measurement.

be attributed to the counterbalance between reduced oxygen transport through the pores and the reduced drying out of the ionomer at lower porosity. The figure also shows that the cell performance is very sensitive to both fitting parameters, i.e., ionic conductivity and ionomer film resistance especially at lower RH.

4. Conclusion

It is demonstrated by our work that the limitations in the transport of oxygen through the ionomer can be negate by optimizing the thickness of ionomer film by different drying methods, and increasing the CL thickness by improving its porosity. However, increased porosity,

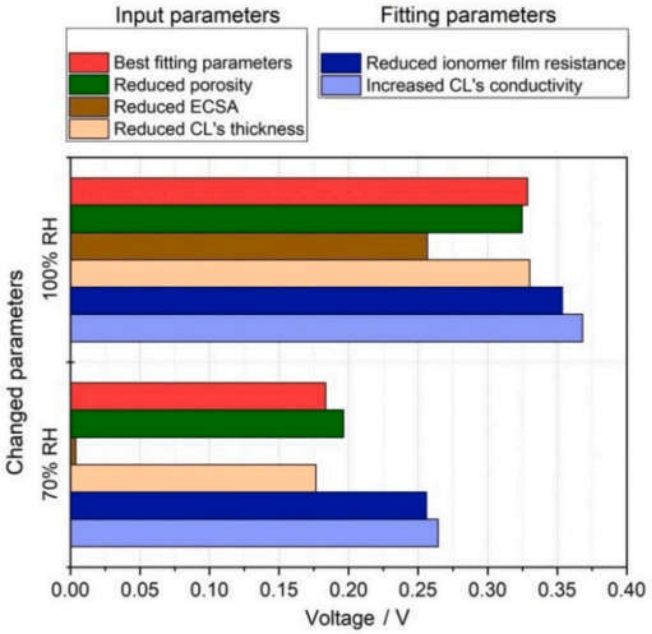

Fig. 8. Bar plots emphasizing the influence of input and fitting parameters on the freeze dried MEA (±25%) at 1500 mA cm^{-2} in both 100% and 70% relative humidity.

thicker electrode and very thin ionomer film hamper the charge transport within the CL, which counterbalances the higher permeability and diffusibility of oxidant in the reacting interface. Thus, optimized CL microstructures are needed to minimize both charge and oxygen transport losses. The electrochemical and ex-situ characterizations highlight the improved performance of freeze dried catalyst layer at high current density due to the reduced concentration polarization. This improvement in mass transport and better ionomer distribution is supported by the numerical model we have used in this study. The simulation yields a very good agreement with the experimental results, and the fit accurately explains how the improved oxygen transport behaviour triggers the performance. In summary, from both experimental and numerical points of view, we can stress on the fact that the drying technique plays a major role for the PEMFC performance due to its effect on the distribution and thickness of the ionomer layer through the catalyst layer as well as on the porosity. A well optimized catalyst layer with these above mentioned properties will raise the power density of the PEMFC application.

Nevertheless, systematic durability tests of the freeze dried CL would be the next step. Moreover, investigation of the limiting current density by means of varying oxygen concentration will give a significant clue to perceive the quantitative concentration limitation. Another future prospect is to improve our model of the CL by accommodating the drying effect more deeply, considering the rate of evaporation and rate of deposition along with the thermal conductivity of individual materials.

Declaration of competing interest

The authors declare that they have no known competing financial interests or personal relationships that could have appeared to influence the work reported in this paper.

CRediT authorship contribution statement

Krishan Talukdar: Conceptualization, Data curation, Formal analysis, Investigation, Methodology, Project administration, Supervision, Validation, Visualization, Writing - original draft, Writing - review & editing. **Md Asaduzzaman Ripan:** Data curation, Formal analysis, Investigation, Methodology, Software, Validation, Visualization. **Thomas Jahnke:** Conceptualization, Formal analysis, Investigation, Methodology, Project administration, Resources, Software, Supervision, Validation, Writing - review & editing. **Pawel Gazdzicki:** Conceptualization, Funding acquisition, Investigation, Methodology, Project administration, Resources, Validation, Visualization, Writing - review & editing. **Tobias Morawietz:** Data curation, Formal analysis, Investigation, Methodology, Visualization, Writing - review & editing. **K. Andreas Friedrich:** Conceptualization, Funding acquisition, Investigation, Methodology, Project administration, Resources, Supervision, Validation, Visualization, Writing - review & editing.

Acknowledgement

Krishan Talukdar acknowledges financial support by DAAD. The authors thank Siegfried Graf for building up and maintaining the fuel cell test benches Dr. Noriko Sata for the assistance with porosity measurements, and Julio Cesar Garcia Navarro for his contribution to determine the pore size distribution by MATLAB. Author also wants to acknowledge the kind cooperation of Professor Hermenegildo Garcia and his team from Universitat Politècnica de València for the FIB-SEM measurement. Additionally, the authors appreciate the support of the reviewers in the peer review process; the precise comments as well as critical suggestions helped to improve this manuscript.

Appendix A. Supplementary data

Supplementary data to this article can be found online at https://doi.org/10.1016/j.jpowsour.2020.228169.

References

[1] S. Litster, G. McLean, PEM fuel cell electrodes, J. Power Sources 130 (2004) 61–76, https://doi.org/10.1016/j.jpowsour.2003.12.055.
[2] T.E. Springer, M.S. Wilson, S. Gottesfeld, Modeling and experimental diagnostics in polymer electrolyte fuel cells, J. Electrochem. Soc. 140 (2016) 3513–3526, https://doi.org/10.1007/978-4-431-56042-5_22.
[3] C. Marr, X. Li, Composition and performance modelling of catalyst layer in a proton exchange membrane fuel cell, J. Power Sources 77 (1999) 17–27, https://doi.org/10.1016/S0378-7753(98)00161-X.
[4] S. Takahashi, T. Mashio, N. Horibe, K. Akizuki, A. Ohma, Analysis of the microstructure formation process and its influence on the performance of polymer electrolyte fuel-cell catalyst layers, ChemElectroChem 2 (2015) 1560–1567, https://doi.org/10.1002/celc.201500131.
[5] A. Kongkanand, M.F. Mathias, The priority and challenge of high-power performance of low-platinum proton-exchange membrane fuel cells, J. Phys. Chem. Lett. 7 (2016) 1127–1137, https://doi.org/10.1021/acs.jpclett.6b00216.
[6] V. Mehta, J.S. Cooper, Review and analysis of PEM fuel cell design and manufacturing, J. Power Sources 114 (2003) 32–53, https://doi.org/10.1016/S0378-7753(02)00542-6.
[7] F. Gloaguen, P. Convert, S. Gamburzev, O.A. Velev, S. Srinivasan, An evaluation of the macro-homogeneous and agglomerate model for oxygen reduction in PEMFCs, Electrochim. Acta 43 (1998) 3767–3772, https://doi.org/10.1016/S0013-4686(98)00136-4.
[8] S. Von Kraemer, M. Puchner, P. Jannasch, A. Lundblad, G. Lindbergh, Gas diffusion electrodes and membrane electrode assemblies based on a sulfonated polysulfone for high-temperature PEMFC, J. Electrochem. Soc. 153 (2006), https://doi.org/10.1149/1.2335979.
[9] J. Zhao, A. Ozden, S. Shahgaldi, I.E. Alaefour, X. Li, F. Hamdullahpur, Effect of Pt loading and catalyst type on the pore structure of porous electrodes in polymer electrolyte membrane (PEM) fuel cells, Energy 150 (2018) 69–76, https://doi.org/10.1016/j.energy.2018.02.134.
[10] R. O'Hayre, F.B. Prinz, The air/platinum/nafion triple-phase boundary: characteristics, scaling, and implications for fuel cells, J. Electrochem. Soc. 151 (2004) A756, https://doi.org/10.1149/1.1701868.
[11] K. Talukdar, H.J. Kim, Y.H. Kim, H.C. Lee, S.J. Choi, Polyacrylamide/Nafion® semi-interpenetrating networks as proton-conducting membrane of direct methanol fuel cell, Sci. Adv. Mater. 6 (2014) 2389–2394, https://doi.org/10.1166/sam.2014.2190.
[12] T. Soboleva, K. Malek, Z. Xie, T. Navessin, S. Holdcroft, PEMFC catalyst layers: the role of micropores and mesopores on water sorption and fuel cell activity, ACS Appl. Mater. Interfaces 3 (2011) 1827–1837, https://doi.org/10.1021/am200590w.
[13] J. Wang, Formation and Characteristics of Microstructures from PEM Fuel Cell Catalyst Ink Drying, 2015. http://hdl.handle.net/10012/9537.

[14] Krishan Talukdar, Hee Jin Kim, Young Ho Kim, Younjin Park, Ho-Chang Lee, S.-J. Choi, Proton-Conducting membranes from nafion®/polystyrene sulfonate composite for fuel cell applications, J. Nanoelectron. Optoelectron. 10 (2015) 535–540.
[15] K. Talukdar, S. Delgado, T. Lagarteira, P. Gazdzicki, K.A. Friedrich, Minimizing mass-transport loss in proton exchange membrane fuel cell by freeze-drying of cathode catalyst layers, J. Power Sources 427 (2019) 309–317, https://doi.org/10.1016/j.jpowsour.2019.04.094.
[16] K. Talukdar, S. Helmly, M. Schulze, D.G. Sanchez, M. Handl, R. Hiesgen, J. Kraut, K.A. Friedrich, Enveloping of catalyst powder by ionomer for dry spray coating in polymer electrolyte membrane fuel cells, J. Power Sources (2019) 82–90, https://doi.org/10.1016/j.jpowsour.2019.03.093.
[17] Z. Xia, S. Wang, L. Jiang, H. Sun, F. Qi, J. Jin, G. Sun, Rational design of a highly efficient Pt/graphene-Nafion® composite fuel cell electrode architecture, J. Mater. Chem. A. 3 (2015) 1641–1648, https://doi.org/10.1039/c4ta05399k.
[18] W. Abdelwahed, G. Degobert, S. Stainmesse, H. Fessi, Freeze-drying of nanoparticles: formulation, process and storage considerations, Adv. Drug Deliv. Rev. 58 (2006) 1688–1713, https://doi.org/10.1016/j.addr.2006.09.017.
[19] N. Pramounmat, C.N. Loney, C.O. Kim, L. Wiles, K.E. Ayers, A. Kusoglu, J. N. Renner, Controlling the distribution of perfluorinated sulfonic acid ionomer with elastin-like polypeptide, ACS Appl. Mater. Interfaces 11 (2019) 43649–43658, https://doi.org/10.1021/acsami.9b11160.
[20] R. Fernández, P. Ferreira-Aparicio, L. Daza, PEMFC electrode preparation: influence of the solvent composition and evaporation rate on the catalytic layer microstructure, J. Power Sources 151 (2005) 18–24, https://doi.org/10.1016/j.jpowsour.2005.02.048.
[21] H.S. Park, Y.H. Cho, Y.H. Cho, C.R. Jung, J.H. Jang, Y.E. Sung, Performance enhancement of PEMFC through temperature control in catalyst layer fabrication, Electrochim. Acta 53 (2007) 763–767, https://doi.org/10.1016/j.electacta.2007.07.046.
[22] R. Darling, Modeling air electrodes with low platinum loading, J. Electrochem. Soc. 166 (2019) F3058–F3064, https://doi.org/10.1149/2.0101907jes.
[23] S. Holdcroft, Fuel cell catalyst layers: a polymer science perspective, Chem. Mater. 26 (2014) 381–393, https://doi.org/10.1021/cm401445h.
[24] Y. Tabe, M. Nishino, H. Takamatsu, T. Chikahisa, Effects of cathode catalyst layer structure and properties dominating polymer electrolyte fuel cell performance, J. Electrochem. Soc. 158 (2011) 1246–1254, https://doi.org/10.1149/1.3624606.
[25] A.Z. Weber, R.L. Borup, R.M. Darling, P.K. Das, T.J. Dursch, W. Gu, D. Harvey, A. Kusoglu, S. Litster, M.M. Mench, R. Mukundan, J.P. Owejan, J.G. Pharoah, M. Secanell, I.V. Zenyuk, A critical review of modeling transport phenomena in polymer-electrolyte fuel cells, J. Electrochem. Soc. 161 (2014) F1254–F1299, https://doi.org/10.1149/2.0751412jes.
[26] R. Vetter, J.O. Schumacher, Free open reference implementation of a two-phase PEM fuel cell model, Comput. Phys. Commun. 234 (2019) 223–234, https://doi.org/10.1016/j.cpc.2018.07.023.
[27] K. Malek, T. Mashio, M. Eikerling, Microstructure of catalyst layers in PEM fuel cells redefined: a computational approach, Electrocatalysis 2 (2011) 141–157, https://doi.org/10.1007/s12678-011-0047-0.
[28] J. Huang, Z. Li, J. Zhang, Review of characterization and modeling of polymer electrolyte fuel cell catalyst layer: the blessing and curse of ionomer, Front. Energy 11 (2017) 334–364, https://doi.org/10.1007/s11708-017-0490-6.
[29] G.A. Futter, P. Gazdzicki, K.A. Friedrich, A. Latz, T. Jahnke, Physical modeling of polymer-electrolyte membrane fuel cells: understanding water management and impedance spectra, J. Power Sources 391 (2018) 148–161, https://doi.org/10.1016/j.jpowsour.2018.04.070.
[30] G. Sasikumar, J.W. Ihm, H. Ryu, Optimum Nafion content in PEM fuel cell electrodes, Electrochim. Acta 50 (2004) 601–605, https://doi.org/10.1016/j.electacta.2004.01.126.
[31] M.J. Pikal, S. Shah, D. Senior, J.E. Lang, Physical chemistry of freeze-drying: measurement of sublimation rates for frozen aqueous solutions by a microbalance technique, J. Pharmacol. Sci. 72 (1983) 635–650, https://doi.org/10.1002/jps.2600720614.
[32] J. Lee, Y. Cheng, Critical freezing rate in freeze drying nanocrystal dispersions, J. Contr. Release 111 (2006) 185–192, https://doi.org/10.1016/j.jconrel.2005.12.003.
[33] D. Dollimore, G.R. Heal, An improved method for the calculation of pore size distribution from adsorption data, J. Appl. Chem. 14 (1964) 109–114, https://doi.org/10.1002/jctb.5010140302.
[34] T. Soboleva, X. Zhao, K. Malek, Z. Xie, T. Navessin, S. Holdcroft, On the micro-, meso-, and macroporous structures of polymer electrolyte membrane fuel cell catalyst layers, ACS Appl. Mater. Interfaces 2 (2010) 375–384, https://doi.org/10.1021/am900600y.
[35] J. Ge, A. Higier, H. Liu, Effect of gas diffusion layer compression on PEM fuel cell performance, J. Power Sources 159 (2006) 922–927, https://doi.org/10.1016/j.jpowsour.2005.11.069.
[36] M.B. Sassin, Y. Garsany, B.D. Gould, K. Swider-Lyons, Impact of compressive stress on MEA pore structure and its consequence on PEMFC performance, J. Electrochem. Soc. 163 (2016) F808–F815, https://doi.org/10.1149/2.0291608jes.
[37] R.W. Atkinson, Y. Garsany, B.D. Gould, K.E. Swider-Lyons, I.V. Zenyuk, The role of compressive stress on gas diffusion media morphology and fuel cell performance, ACS Appl. Energy Mater. 1 (2018) 191–201, https://doi.org/10.1021/acsaem.7b00077.
[38] C. Simon, F. Hasché, H.A. Gasteiger, Influence of the gas diffusion layer compression on the oxygen transport in PEM fuel cells at high water saturation levels, J. Electrochem. Soc. 164 (2017) F591–F599, https://doi.org/10.1149/2.0691706jes.
[39] G. Li, P.G. Pickup, Ionic conductivity of PEMFC electrodes effect of Nafion loading, J. Electrochem. Soc. 150 (2003), https://doi.org/10.1149/1.1611493.
[40] K. Talukdar, P. Gazdzicki, K.A. Friedrich, Comparative investigation into the performance and durability of long and short side chain ionomers in Polymer Electrolyte Membrane Fuel Cells, J. Power Sources 439 (2019).
[41] R. Carter, S. Kocha, F. Wagner, M. Fay, H. Gasteiger, Artifacts in measuring electrode catalyst area of fuel cells through cyclic voltammetry, ECS Trans 11 (2007), https://doi.org/10.1149/1.2780954.
[42] K. Cooper, Laboratory #4 – Fuel Crossover by Linear Sweep Voltammetry & Electrochemical Surface Area by Cyclic Voltammetry, 2009, pp. 1–3, https://doi.org/10.1533/9781845694838.344.
[43] C. Breitkopf, K. Swider-Lyons, Springer Handbook of Electrochemical Energy, Springer, Berlin Heidelberg, 2016. https://books.google.de/books?id=I_qoDQAAQBAJ.
[44] R.B. Bird, W.E. Stewart, E.N. Lightfoot, Transport Phenomena, Wiley, 2006. https://books.google.de/books?id=L5FnNllaGfcC.
[45] B.P. Setzler, T.F. Fuller, A physics-based impedance model of proton exchange membrane fuel cells exhibiting low-frequency inductive loops, J. Electrochem. Soc. 162 (2015) F519–F530, https://doi.org/10.1149/2.0361506jes.
[46] S.D. Yim, Y.J. Sohn, S.H. Park, Y.G. Yoon, G.G. Park, T.H. Yang, C.S. Kim, Fabrication of microstructure controlled cathode catalyst layers and their effect on water management in polymer electrolyte fuel cells, Electrochim. Acta 56 (2011) 9064–9073, https://doi.org/10.1016/j.electacta.2011.05.123.
[47] A. Fischer, J. Jindra, H. Wendt, Porosity and catalyst utilization of thin layer cathodes in air operated PEM-fuel cells, J. Appl. Electrochem. 28 (1998) 277–282, https://doi.org/10.1023/A:1003259531775.
[48] C. Simon, F. Hasché, H.A. Gasteiger, Influence of the gas diffusion layer compression on the oxygen transport in PEM fuel cells at high water saturation levels, J. Electrochem. Soc. 164 (2017) F591–F599, https://doi.org/10.1149/2.0691706jes.
[49] S. Holdcroft, Fuel cell catalyst layers: a polymer science perspective, Chem. Mater. 26 (2014) 381–393, https://doi.org/10.1021/cm401445h.
[50] M. Eikerling, A.A. Kornyshev, Electrochemical impedance of the cathode catalyst layer in polymer electrolyte fuel cells, J. Electroanal. Chem. 475 (1999) 107–123, https://doi.org/10.1016/S0022-0728(99)00335-6.
[51] M.L.P.R. Darling, Minimizing Mass-Transport Losses in Pem Fuel Cells, n.d. 6074, https://www.electrochem.org/dl/ma/206/pdfs/1933.pdf.
[52] A.H.K. Uda, Z. Noda, K. Sasaki, Electrochemical characterization of MEAs with different Pt-loading for the efficient use of Pt, ECS Trans. Electrochem. Soc. 80 (2017) 789–799, https://doi.org/10.1149/08008.0789ecst.
[53] M.C. Lefebvre, R.B. Martin, P.G. Pickup, Characterization of ionic conductivity profiles within proton exchange membrane fuel cell gas diffusion electrodes by impedance spectroscopy, Electrochem. Solid State Lett. 2 (1999) 259–261, https://doi.org/10.1149/1.1390804.
[54] T. Suzuki, H. Tanaka, M. Hayase, S. Tsushima, S. Hirai, Investigation of porous structure formation of catalyst layers for proton exchange membrane fuel cells and their effect on cell performance, Int. J. Hydrogen Energy 41 (2016) 20326–20335, https://doi.org/10.1016/j.ijhydene.2016.09.078.
[55] V. Yarlagadda, M.K. Carpenter, T.E. Moylan, R.S. Kukreja, R. Koestner, W. Gu, L. Thompson, A. Kongkanand, Boosting fuel cell performance with accessible carbon mesopores, ACS Energy Lett 3 (2018) 618–621, https://doi.org/10.1021/acsenergylett.8b00186.
[56] Y.-C. Park, H. Tokiwa, K. Kakinuma, M. Watanabe, M. Uchida, Effects of carbon supports on Pt distribution, ionomer coverage and cathode performance for polymer electrolyte fuel cells, J. Power Sources 315 (2016) 179–191, https://doi.org/10.1016/j.jpowsour.2016.02.091.

SUPPORTING INFORMATION

2.1.1 Ink formulation:

The process of preparation started with weighting the Pt/VC inside a glass beaker and then adding the water in it. Next step is to sonicate the sample on an ELSER– 60 Hz for 30 minutes at a room temperature bath. Afterwards, 10 wt. % Nafion® ionomer was added dropwise using a micropipette. The solution was mixed simultaneously using the bath sonication step for 30 minutes again. As the last component, Cyclohexanol, which must be kept inside a regular oven for 5 minutes at 40° C (melting point of Cyclohexanol is 23° C) to liquify it before using, was added with the mixture. Later, the mixture was sonicated again for 30 minutes like previously mentioned and for 30 minute using 50 Hz (UP200S Hielscher) probe ultrasonicator with 20-50 amplitude and 0.5 cycles. Eventually, the sample was transferred to a ball mill container, which is made of stainless steel (interior container is made of zirconia), and 0.005 mm and 2 mm zirconia balls were used to ball-mill. The suspension was milled at three different rotation speeds of 200, 400 and 1100 rotation per minute (rpm) for 30 cycles. A running cycle for 200 rpm and 400 rpm were 10 minutes with 15 minutes break time between two cycles, whereas a running cycle for 1100 rpm was 5 minutes with 20 minutes break time between two cycles. Three different rpms were applied aiming towards the homogeneous mixing and size reduction of the final particles.

2.1.3 Drying techniques:

Oven Drying: In this technique, a regular laboratory oven was used and the process of drying started with implementing the sample (catalyst coated membrane) inside the oven. The dryer includes ventilation facility along with heat supply. Evaporation occurs

at 70 °C and at atmospheric pressure. The sample was kept inside the oven for approximately 12 hours.

Vacuum Drying: The methodology relies on the reduced vapor pressure conditions, which leads to faster evaporation rate at lower temperatures than the boiling point of the solvent. The dryer is attached with a membrane pump, and temperature was set to 70° C for the vacuum dryer. The sample was kept inside the dryer for 5 hours.

Freeze Drying: This drying technique consists of three key stages:

a) Freezing: two most important conditions need to be fulfilled while getting an ideal freeze drying result. The conditions are to preserve the initial physical form by freezing of the material, and to ensure that the sample temperature does not cross the melting point of the solvent. Generally, the temperature is maintained well below triple point to achieve total sublimation. The freezing process has been completed in two steps: initially, cooling the CCM with slow freezing rate for 120 minutes in the regular refrigerator, and then fast freezing using liquid nitrogen. Slow freezing rate will contribute to form bigger ice crystals, which will induce the development of macropores on the matrix of the catalyst layer, which attributes to a rapid sublimation [31,32]. Nevertheless, slow freezing secures that there is no drastic change causing dimensional stress with cracks of other defects in the sample. Then, the CCM samples were taken out from the freezer, and being allocated inside a stainless steel frame, ensuring the electrode would remain flat and stretched. Then the SS frames along with the CCMs were moved into a liquid nitrogen filled container and cooled nearly to -150 °C. Subsequently, previously non-solidified solvent formed smaller crystals due to fast freezing.

b) Primary Drying: The CCMs were then inserted inside the chamber to start sublimation. During this stage, sublimation comes into action to remove the solvent from the remaining product. Deep vacuum (0.3 mbar) is achieved with the help of a rotary pump with a cryogenic trap. The duration of this stage depends on the solvent amount, volume of the drying chamber and the capacity of the pump. Usually, it takes 2 hours for 2 CCMs in a single batch. Heat of sublimation is provided by raising the temperature of the oven very carefully while monitoring the pressure in the drying chamber. Heat of sublimation is the energy required for the solvent molecules to sublimate form solid state to vapor. This energy is provided externally by means of heat. We increase the temperature to 50° C very slowly (approximately 30 min) without sharp increase of pressure in the system. During the sublimation process the pressure increases slowly to 1 mbar and finally starts dropping to the 0.3 mbar again. When the pressure reaches to the original vacuum pressure, the primary drying is complete.

c) Secondary Drying: The solvent molecules which are bound to the product evaporate in this stage. The chamber is heated to 60° C with a heating rate of 4° C per minute to remove the remaining solvent. The entire freeze drying process takes 4 hours. This freeze drying method is easily scalable for mass production of CCMs, as most of the pharmaceutical industries use this technique to dry drugs; moreover food industries use this drying method very frequently also. After the freeze drying we can immediately use to CCM to fabricate MEA.

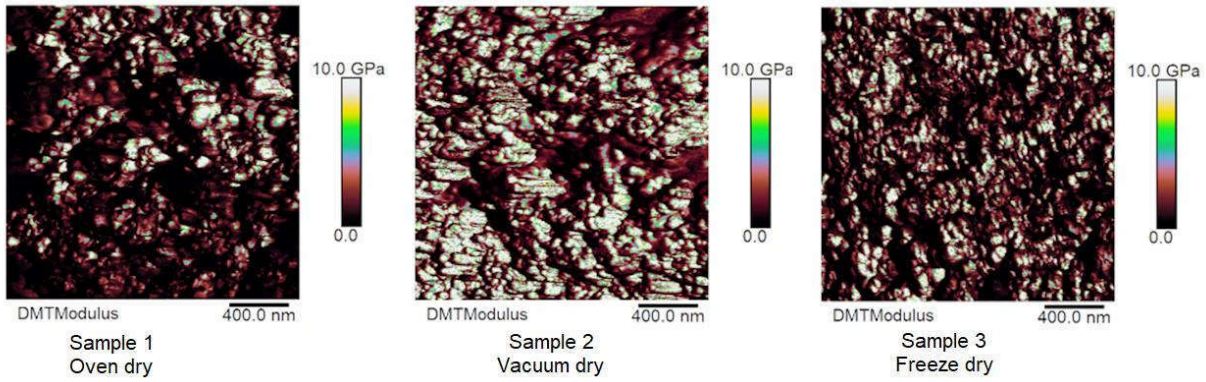

Figure SI 1: AFM stiffness measurement by DMT Module

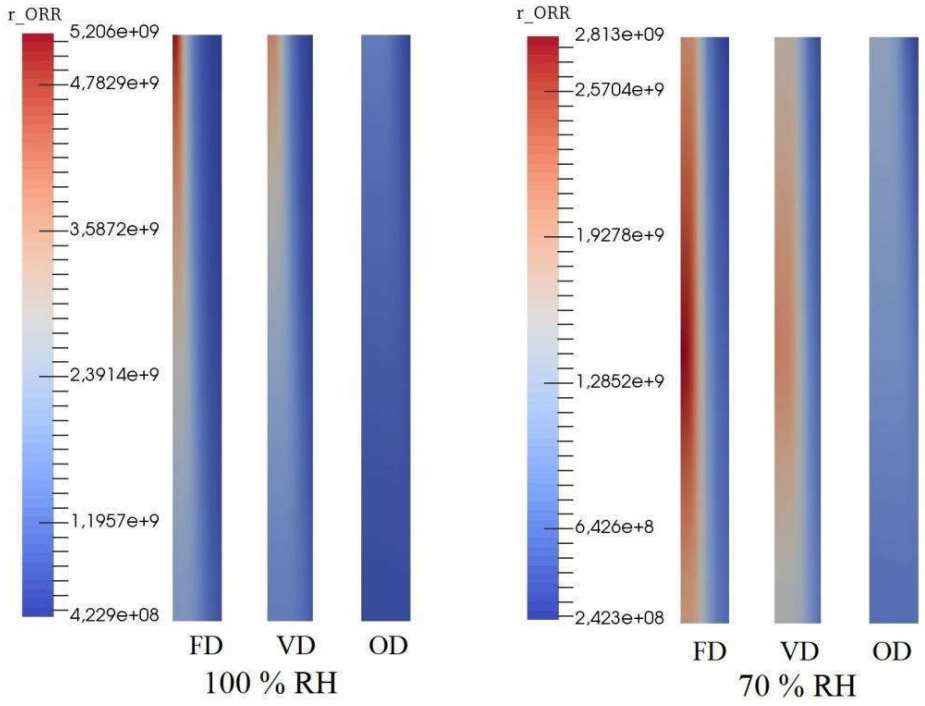

Figure SI 2: The absolute value for the concentration of ORR in both 100 % RH and 70 % RH.

Property	Oven-drying	Vacuum drying	Freeze-drying	Relative error
S_{BET} (m^2 g^{-1}) [a)]	1	6.2	19.6	<5%
Total pore volume (mm^3 g^{-1}) [b)]	103	343.5	635	5-7%
Average pore diameter (nm) [b)]	74	73	106	5-7%
Type of isotherm [a.1)]	IV	II	II	
Porosity (%) [b)]	17	46	59	5%

a) Obtained from BET measurements; [a.1)] from nitrogen physisorption data measurements and in accordance to the IUPAC classification; [b)] From MIP measurements

Table SI 1: Morphological characterization of Pt/VC-Nafion® powders dried to oven, vacuum and freeze-drying.

Features	100% RH			70% RH		
	FD	VD	OD	FD	VD	OD
OCV (mV)	915	920	928	912	913	926
Potential at 2.5 A (mV)	766	765	777	756	754	768
Potential at 12.5A (mV)	630	609	581	602	585	565
Potential at 25A (mV)	507	462	282	427	386	150

Table SI 2: Average numerical values from the polarization curve of different MEAs prepared from freeze dry (FD), vacuum dry (VD) and oven dry (OD).

Initial variable	Anode	PEM/Anode	Cathode/ PEM	Cathode
P_g	$P_{g,out,anode}$	-	-	$P_{g,out,cathode}$
S_l	0	-	-	0
$x_g^{H_2O}$	$RH_{anode}P_{sat}^{H_2O}/P_g$	-	-	$RH_{cathode}P_{sat}^{H_2O}/P_g$
$x_g^{O_2}$	0	-	-	$0.21(1 - x_{g,cathode}^{H_2O})$
$x_g^{N_2}$	-	-	-	$0.79\,(1 - x_{g,cathode}^{H_2O})$
$x_g^{H_2}$	$1 - x_{g,anode}^{H_2O}$	-	-	0
T	T_{init}	T_{init}	T_{init}	T_{init}
Φ_{ion}	0	0	0	0
Φ_{elec}	0	-	-	$\Phi_{elec,init}$
μ^{H_2O}	-	$RTln(P_{g,anode}^{H_2O}/P_{sat}^{H_2O})$	$RTln(P_{g,cathode}^{H_2O}/P_{sat}^{H_2O})$	-
P^{H_2}	-	$x_g^{H_2}P_{g,anode}$	$x_g^{H_2}P_{g,cathode}$	-
P^{O_2}	-	$x_g^{O_2}P_{g,anode}$	$x_g^{O_2}P_{g,cathode}$	-

Table SI 3: Initial conditions at the interfaces and in the electrodes.